PH.D. DISSERTATION / TESIS DOCTORAL

CHARACTERIZING THE ATMOSPHERIC AEROSOL BY ACTIVE AND PASSIVE REMOTE SENSING: MICROPHYSICAL PROPERTIES AND HYGROSCOPIC GROWTH EFFECTS

Author:

MARÍA JOSÉ GRANADOS MUÑOZ

Grupo Física de la Atmósfera

Universidad de Granada

Centro Andaluz de Medio Ambiente

Editor: Editorial de la Universidad de Granada
Autor: María José Granados Muñoz
D.L.: GR 1844-2014
ISBN: 978-84-9083-027-7

UNIVERSIDAD DE GRANADA

DEPARTAMENTO DE FÍSICA APLICADA

GRUPO DE FÍSICA DE LA ATMÓSFERA

TESIS DOCTORAL

CHARACTERIZING THE ATMOSPHERIC AEROSOL BY ACTIVE AND PASSIVE REMOTE SENSING: MICROPHYSICAL PROPERTIES AND HYGROSCOPIC GROWTH EFFECTS

Tesis presentada María José Granados Muñoz para optar al grado de Doctor.

Directores de Tesis:

Dr. Lucas Alados Arboledas
Catedrático de la UGR
Dep. Física Aplicada
Univ. de Granada

Dr. Juan Luis Guerrero Rascado
Investigador de la UGR
Dep. Física Aplicada
Univ. de Granada

Dr. Jesús Fernández Gálvez
Inv. Col. de la UGR
Dep. Física Aplicada
Univ. de Granada

Granada, Febrero de 2014

El trabajo de investigación que se expone en la presente memoria, titulado: CHARACTERIZING THE ATMOSPHERIC AEROSOL BY ACTIVE AND PASSIVE REMOTE SENSING: MICROPHYSICAL PROPERTIES AND HYGROSCOPIC GROWTH EFFECTS, para aspirar al grado de Doctor en Física que presenta María José Granados Muñoz, ha sido realizado en la Universidad de Granada gracias a la beca concedida por el Ministerio de Educación "Formación de Profesorado Universitario (convocatoria 2009)", bajo la dirección de:

VºBº

Los Directores:

Dr. LUCAS ALADOS ARBOLEDAS

Dr. JUAN LUIS GUERRERO RASCADO

Dr. JESÚS FERNÁNDEZ GÁLVEZ

Lda. MARÍA JOSÉ GRANADOS MUÑOZ

Aspirante a grado de Doctor

La doctoranda María José Granados Muñoz y los directores de la tesis Lucas Alados Arboledas, Juan Luis Guerrero Rascado y Jesús Fernández Gálvez garantizamos, al firmar esta tesis doctoral, que el trabajo ha sido realizado por la doctoranda bajo la dirección de los directores de la tesis y hasta donde nuestro conocimiento alcanza, en la realización del trabajo, se han respetado los derechos de otros autores a ser citados, cuando se han utilizado sus resultados o publicaciones.

Granada, febrero de 2014

Directores de la Tesis

Fdo.: Lucas Alados Arboledas

Fdo.: Juan Luis Guerrero Rascado

Fdo.: Jesús Fernández Gálvez

Doctoranda:

Fdo.: María José Granados Muñoz

A mis padres

“Everything should be made as simple

as possible, but not simpler”

A. Einstein.

Acknowledgements/Agradecimientos

Mientras comenzaba a escribir esta sección sin tener ni idea de qué poner ni de cómo empezar no he podido evitar que se me vengan a la cabeza un montón de recuerdos entrañables de los últimos años. Parece que fue ayer cuando vine al CEAMA por primera vez tan «cortaica» y aquí estamos, a punto de defender la tesis. En este tiempo ha sido mucha la gente que me ha ayudado y que forma parte de esos recuerdos, así que tengo mucho que agradecer.

En primer lugar me gustaría agradecer a mis directores de tesis, el catedrático D. Lucas Alados Arboledas y los doctores D. Juan Luis Guerrero Rascado y D. Jesús Fernández Gálvez, sin los cuales este trabajo no habría sido posible. A Lucas quiero agradecerle, además de todo lo que he aprendido trabajando con él, que siempre esté dispuesto a atendernos y a ayudarnos. La preocupación que muestra por sus becarios, va más allá de lo profesional. A Juanlu quiero agradecerle la ayuda que me ha prestado a lo largo de esta tesis y aún más en los últimos meses, sobre todo sabiendo llevar mis momentos de agobio. También quiero agradecer a Jesús su compañía en estos años.

Una mención especial merecen aquí Juan Antonio y Fran, por haberme enseñado, junto a mis directores, una gran parte de lo que sé sobre el lidar. Sin ellos estoy segura de que este trabajo no estaría acabado todavía. Además quiero agradecerles todo lo que me han aportado personalmente y los buenos momentos que hemos disfrutado juntos, tanto dentro como fuera del CEAMA.

También quiero dar las gracias al resto de mis compañeros puesto que siempre han estado dispuestos a prestarme su ayuda a la hora de trabajar además de hacer que venir al trabajo haya sido mucho más que simplemente eso. Espero que el ambiente que hay en este grupo se mantenga así por mucho tiempo. Quiero

agradecer a Paco Pepe, Andy, Inma e Inma Alados que hayan estado dispuestos a echar una mano y aportar su experiencia y que hagan que cada seminario y demás actividades de ocio del grupo sean irrepetibles. También quiero dar las gracias a Marian, Juan Alfredo y Luis, por su ayuda y, sobre todo, por los desayunos de La Cabaña. A Hassan y a Antonio les quiero agradecer toda su ayuda profesional y todos los buenos momentos juntos, incluido ese viaje a Marruecos —y los que ya estamos planeando…—; a Penélope sus consejos siempre optimistas y tranquilizadores y los ratos de «deporte anti-estrés»; a Alberto los buenos momentos y las charlas de la comidas; a Óscar esas alegría y esa soltura que tiene siempre; a Dani las risas que hemos compartido; y a Enrique las salidas al campo —ya sea en Yegen, Alcalá, etc.—. He querido dejar para el final a Gloria, mi flor, con la que me une una amistad de hace ya casi diez años y ahí sigue para lo bueno y para lo malo.

No me gustaría olvidar a toda la gente que a lo largo de estos años ha ido pasando por el CEAMA. A Manuel Antón, instaurador del San Manuel; Roberto, que a pesar de estar tan poco tiempo disfrutó y nos hizo disfrutar de Granada; y a Ana Calvo, por su compañía en Leipzig.

Hablando de Leipzig, no puedo olvidar expresar mi agradecimiento a la Dra. Ulla Wandinger y al Dr. Albert Ansmann por su colaboración cuando ha sido necesaria y admitirme en TROPOS durante mi estancia. Realmente hicieron esos meses allí muy agradables acogiéndome como una más del grupo.

Finalmente quiero agradecer y dedicar este trabajo a mi familia, amigos y a mi novio, porque estos años no han sido sólo trabajo y ellos han formado parte de ellos. Gracias a mis tíos, primos y amigos, por escucharme, preocuparse y aconsejarme siempre. Gracias a Lamine, por estar ahí durante toda esta tesis y sobre todo en los agobios de última hora. Y especialmente, gracias a mis padres y mi hermana, por su cariño y cuidados y porque son los que han hecho posible que yo esté hoy aquí escribiendo estas líneas y que me haya convertido en la persona que soy ahora.

Podría decir mucho más de todas y cada una de las personas que he mencionado, pero, como ya saben, no soy muy habladora ;). Espero no haber olvidado a nadie.

Para terminar, quiero expresar mi gratitud al Dr. Chaikovsky y sus colaboradores por el desarrollo del algoritmo LIRIC, el cual ha sido fundamental en esta tesis. También agradecer a la NOAA Air Resources Laboratory (ARL), Naval Research Laboratory y Barcelona Supercomputing Center por el modelo de dispersión y transporte HYSPLIT, los mapas de aerosol NAAPS y los datos de polvo del modelo DREAM, respectivamente, así como a las redes EARLINET y AERONET-RIMA, cuyos datos han sido empleados en el desarrollo de esta tesis.

Outline

Abstract

This PhD dissertation focuses on the characterization of atmospheric aerosol particles by means of active and passive remote sensing to retrieve vertically resolved optical and microphysical properties. Furthermore, the concept of retrieving information on the hygroscopic effect on the aerosol backscatter coefficient using remote sensing is tested.

For this purpose, remote sensing techniques based on a multiwavelength Raman lidar and a sun photometer data acquired at Granada experimental station, in the Southeastern Iberian Peninsula, are applied. The sun photometer is included in the AERONET network (Aerosol Robotic Network), sponsored by NASA, and is operated continuously in the radiometric station of Granada as part of the instrumentation operated by the Atmospheric Physic Group of the University of Granada (GFAT). The multiwavelength Raman lidar is also routinely operated by this group in the framework of the European Aerosol Research Lidar Network (EARLINET) which is part of the GAW Aerosol Lidar Observation Network (GALION) and is currently involved in the European project ACTRIS (Aerosols, Clouds, and Trace gases Research InfraStructure Network). For the analysis of the hygroscopic effects on the aerosol backscatter coefficient, the lidar system information is combined with radiosounding data gathered with radiosondes simultaneously launched at the same experimental site.

The analysis of aerosol microphysical properties is performed with LIRIC (Lidar Radiometer Inversion Code) algorithm developed in the National Academy of Sciences of Belarus in collaboration with the Laboratoire d’Optique Atmosphérique, Lille (France). For this purpose, LIRIC is synergistically applied to lidar and sun photometer data. The chapter devoted to methodology includes a detailed description of LIRIC and is a key point of this dissertation.

Understanding of the mathematical approach and the physics underlying LIRIC algorithm allows for the analysis of the uncertainties introduced in the output volume concentration provided by LIRIC and for the evaluation of LIRIC performance when applied to particular cases.

For the evaluation of LIRIC algorithm, three study cases are analysed in detail in order to determine the uncertainties of this algorithm due to the uncertainties in user-defined input parameters. These uncertainties are found to be below 15% for most of the cases and they are especially dependent on the vertical structure of the aerosol, being larger in cases of more complex structures. Once the uncertainties are determined, LIRIC is applied and evaluated using data from (i) two field campaigns namely CHARMEX in 2012 and CLIMARENO-GRA in 2011, and (ii) an extensive period during the summer 2012.

During CHARMEX 2012 field campaign, a dust event is monitored and LIRIC is found to be a very useful tool for the continuous monitoring of the event, allowing for the analysis of the temporal evolution of the profiles of aerosol microphysical properties. In addition, dust model mass concentration profiles of BSC-DREAM8b are compared with LIRIC results regarding the aerosol vertical structure and the aerosol load. Our results indicate a good agreement between the aerosol vertical structures obtained from both methodologies, although there are large discrepancies in the retrieved aerosol loads. CLIMARENO-GRA campaign, offers the possibility to perform an additional evaluation of LIRIC under a different dust event. In this case, LIRIC retrievals can be checked against independent data from a simultaneous flight above Granada. Furthermore, the availability of Raman lidar profiles registered the previous night to the campaign offers the possibility to check the daytime aerosol microphysical properties profiles retrieved by LIRIC with those retrieved with an inversion scheme based on the use of Raman lidar. The agreement between LIRIC retrievals and the flight measurements is rather good taking into account the uncertainties in both methodologies. On the other hand, the discrepancies between both lidar retrieval procedures evidence the temporal shift between the two retrievals that leads to changes in the vertical structure of the aerosol. Anyway, for most of the profile the volume concentration values agree within the associated uncertainties.

Besides the two field campaigns, the use of a second sun photometer located in Cerro Poyos (Sierra Nevada), in the same atmospheric column where Granada is included but at higher altitude allows for obtaining LIRIC retrievals from two different altitudes with independent sun photometer measurements. This is used to check the self-consistency and robustness of the method. This experimental setup is firstly applied to two study cases analysed in detail. Afterwards, a statistical analysis is performed based on data from summer 2012. Retrievals at both levels are compared, providing very good agreement in those cases with the same aerosol type in the whole atmospheric column. However, after our analyses it is clear that assumptions such as the height independency of the size distribution or the refractive index, or the way the incomplete overlap effects are considered in the lowermost region need to be carefully reviewed in order to improve the performance of the algorithm in some cases.

Finally, a methodology based on the combined use of active remote sensing and radiosounding to study the effects of the aerosol hygroscopic growth on the aerosol optical and microphysical properties is implemented. Thus, the effects of hygroscopic growth on aerosol optical properties, namely the aerosol backscatter coefficient, are presented here by means of two study cases corresponding to different aerosol types. The aerosol backscatter coefficient enhancement factors are calculated for both cases and lower values are obtained in the case when mineral dust was present. The Hänel parameterization is applied, obtaining for the aerosol backscatter coefficient enhancement factors results comparable to those obtained in previous studies.

Resumen

Esta tesis doctoral se centra en la caracterización del aerosol atmosférico mediante la obtención de perfiles verticales de sus propiedades ópticas y microfísicas, empleando técnicas de teledetección activa y pasiva. Además, se plantea el análisis de los efectos del crecimiento higroscópico del aerosol sobre el coeficiente de retrodispersión del aerosol atmosférico, mediante el uso de técnicas de teledetección.

A tal efecto se emplean las medidas realizadas con un lidar Raman multiespectral y un fotómetro solar, operados en la estación experimental del Grupo de Física de la Atmósfera en Granada, localizada en el sureste de la Península Ibérica. El fotómetro solar está incluido en la red AERONET (Aerosol Robotic Network), coordinada por NASA, y es operado de forma continua en la estación radiométrica de Granada como parte de la instrumentación del Grupo de Física de la Atmósfera de la Universidad de Granada (GFAT). El lidar Raman multiespectral también es operado por este Grupo en el marco de la red europea de lídares EARLINET (European Aerosol Research Lidar Network) que forma parte de la red global GALION (GAW Aerosol Lidar Observation Network) y actualmente está involucrada en el proyecto europeo ACTRIS (Aerosols, Clouds, and Trace gases Research InfraStructure Network). Para el análisis de los efectos del crecimiento higroscópico sobre el coeficiente de retrodispersión del aerosol atmosférico se ha combinado la información proporcionada por el sistema lidar con datos de radiosondeos, simultáneos a las medidas lidar y lanzados desde la misma estación experimental del GFAT.

El análisis de las propiedades microfísicas del aerosol se realiza a través del código LIRIC (Lidar Radiometer Inversion Code), desarrollado en la Academia Nacional de Ciencias de Bielorrusia, en colaboración con el Laboratoire

d’Optique Atmosphérique de Lille (France). Con este fin, LIRIC se aplica de forma sinérgica a los datos del fotómetro solar y el sistema lidar. El capítulo dedicado a la descripción de la metodología incluye una detallada descripción de LIRIC y es un punto clave en esta tesis doctoral. El conocimiento de las bases matemáticas y físicas que fundamentan LIRIC permite hacer un análisis detallado de su incertidumbre, que afecta a los perfiles de concentración en volumen proporcionados por LIRIC, así comouna evaluación de su funcionamiento cuando se aplica a casos particulares.

Para la evaluación del algoritmo LIRIC se analizan en detalle tres casos de estudio con el fin de determinar la incertidumbre debida exclusivamente a las propias incertidumbres de los parámetros de entrada definidos por el usuario. Esta incertidumbre se encuentra por debajo del 15 % para la mayoría de los casos y depende especialmente de la estructura vertical del aerosol, siendo mayor en los casos con estructuras complejas. Una vez determinada la incertidumbre, LIRIC se aplica y evalúa mediante datos correspondientes a: (i) las campañas CHARMEX en 2012 y CLIMARENO-GRA en 2011, y (ii) un amplio período correspondiente al verano de 2012.

Durante la campaña CHARMEX 2012, se realizó un seguimiento exhaustivo de un evento de polvo mineral sahariano sobre Granada. Los resultados del estudio indican que LIRIC es una herramienta muy útil para la monitorización continua del evento, permitiendo el análisis de la evolución temporal de los perfiles de propiedades microfísicas del aerosol. Además, se comparan los perfiles de concentración en masa proporcionados por el modelo BSC-DREAM8b con los proporcionados por LIRIC. Los resultados obtenidos indican un buen acuerdo entre las estructuras verticales obtenidas con ambos, aunque existen grandes diferencias en lo referente a la carga de aerosol.

La campaña CLIMARENO-GRA ofrece la posibilidad de realizar una evaluación adicional de LIRIC durante un segundo evento de polvo. En este caso, es posible contrastar los resultados obtenidos con LIRIC con datos independientes proporcionados por un vuelo instrumentado sobre Granada. Además, la disponibilidad de perfiles lidar Raman (registrados durante la noche anterior a la campaña) ofrece la posibilidad de comparar las propiedades microfísicas del aerosol obtenidas con LIRIC (durante el día) con las obtenidas a partir de un esquema de inversión diferente, basado en el uso de perfiles del lidar Raman. El acuerdo entre LIRIC y los datos del avión es bastante bueno dadaslas incertidumbres en ambas metodologías. Por otro lado, se observan algunas discrepancias entre LIRIC y el algoritmo aplicado a los datos lidar Raman. Estas discrepancias están relacionadas con el desplazamiento temporal entre los periodos en los que se realizan las medidas elásticas y Raman, y al hecho de que a lo largo de ese periodo se produzcan cambios en la estructura vertical del aerosol. Considerando esto, los perfiles de concentración en volumen obtenidos presentan buen acuerdo dentro de las incertidumbres asociadas.

Además de las dos campañas anteriores, el uso de un segundo fotómetro solar situado en la estación Cerro Poyos (Sierra Nevada), en la misma columna atmosférica que Granada pero a mayor altura, permite obtener perfiles con LIRIC a partir de dos alturas, usando medidas de fotometría solar independientes. Este dispositivo experimental ofrece la posibilidad de comprobar la auto-consistencia y estabilidad del método bajo diferentes condiciones atmosféricas. En primer lugar, se analizan exhaustivamente dos casos de estudio y, posteriormente, se realiza un análisis estadístico basado en datos del verano de 2012. La comparación de los perfiles calculados desde ambos niveles muestra que hay muy buen acuerdo en aquellos casos en los que el mismo tipo de aerosol está presente en toda la columna atmosférica. Sin embargo, de nuestro análisis se deduce que algunas de las suposiciones hechas en LIRIC, tales como la independencia con la altura de la distribución de tamaño para cada modo o del índice de refracción o la forma en que los efectos de solapamiento incompleto del lidar se consideran en la región inferior de los perfiles, necesitan ser examinadas cuidadosamente en algunos casos con el fin de mejorar los resultados del algoritmo.

Por último, se ha implementado una metodología para estudiar los efectos del crecimiento higroscópico del aerosol sobre las propiedades ópticas y microfísicas, basada en el uso combinado de la teledetección activa y radiosondeos. Los resultados obtenidos, al aplicar dicha metodología al coeficiente de retrodispersión de aerosol, se presentan aquí para dos casos de estudio, correspondientes a diferentes tipos de aerosol. Los factores de crecimiento higroscópico del coeficiente de retrodispersión de aerosol, calculados para ambos casos presentan marcadas diferencias, siendo más bajos para el caso en el que se observa presencia de polvo mineral. La aplicación de la parametrización de Hänel a nuestros datos proporciona valores del coeficiente de crecimientos higroscópico comparables a los obtenidos en estudios previos.

1 Introduction

Atmospheric aerosol particles are fundamental constituents of the Earth's atmosphere as they influence the Earth's energy budget both directly, by scattering and absorbing solar radiation [*Yu et al.*, 2006], and indirectly, by acting as cloud condensation nuclei (CCN) [*Lohmann and Feichter*, 2005]. During past years, a huge effort has been done in order to characterize the effects of atmospheric aerosol on climate. These effects are usually characterized by their influence on the radiative forcing, considered as a measure of the influence a given factor has in altering the balance of incoming and outgoing energy in the Earth-atmosphere system, being used as an index of the importance a given factor as a potential climate change mechanism [IPCC, 2007]. Thanks to this effort the uncertainties in the aerosol radiative forcing have been reduced with respect to the data in the AR4 (Fourth Assessment Report) of the IPCC 2007 (Intergovernmental Panel for Climate Change) [IPCC 2013]. However, atmospheric aerosol continue to contribute the largest uncertainty to the total radiative forcing estimate even though the level of confidence on the effects of the atmospheric aerosol has increased from low and medium to medium and high (for indirect and direct effect, respectively) [*IPCC*, 2013].

Ground based (active and passive) remote sensing techniques have proven to be quite robust and provide accurate results for atmospheric aerosol characterization [e. g. *Nakajima et al.*, 1996; *Dubovik and King*, 2000; *Mattis et al.*, 2004; *Olmo et al.*, 2006]. Nonetheless, they provide information about atmospheric aerosol properties on a local scale. In order to overcome this inconvenient, observational networks such as GALION (Global Atmospheric Watch Aerosol Lidar Observation Network), which includes EARLINET (European Aerosol Research Lidar Network, www.earlinet.org) [*Bösenberg et al.,* *2001*], MPLNET (Micro Pulse Lidar Network)[*Welton et al.*, 2005], LALINET (Latin American Lidar Network, www.lalinet.org) or ADNET (Asian Dust Network) [*Shimizu et al.*, 2004] among others; or SKYNET [*Takamura and Nakajima*, 2004] and AERONET (Aerosol Robotic Network, http://aeronet.gsfc.nasa.gov/) [*Holben et al., 1998*] have been established and are widely implemented, providing a global coverage.

Information on the vertical structure of the aerosol is of high importance, since the atmospheric aerosol effects can be very different near the surface, within the boundary layer, and in the free troposphere. In addition, estimates of radiative forcing are sensitive to the vertical distribution of aerosols [*Claquin et al.*, 1998; *Huang et al.*, 2009] and the vertical information is required for accounting the indirect effect [*McCormick et al.*, 1993; *Bréon*, 2006; *Guerrero-Rascado et al.,* 2009].

Lidar (light detection and ranging) systems have proved to be very useful tools for determining the vertical distribution of aerosols. Methods to determine aerosol optical properties with lidar systems have already been widely studied [*Klett, 1985; Ansmann et al., 1992*]. Additionally, since the 1970s several methods have been proposed in order to retrieve also aerosol microphysical properties. The retrieval of aerosol microphysical properties represents still a real challenge, especially for implementing in a relatively simple and automated way and for non-spherical particles. These microphysical properties include aerosol mean size, size distribution, volume, mass, surface-area, number concentrations and complex refractive index.

The lidar-based methods proposed to retrieve microphysical properties profiles can be classified in three different groups. The first group consists of a mathematical approach on the basis of multiwavelength Raman lidar observations [*Uthe*, 1982; *Müller et al.*, 1999; *Veselovskii et al.*, 2002; *Böckmann et al.*, 2005]. This mathematical approach has proven to be quite robust for spherical particles.

Nonetheless, recent publications extend this kind of methods to irregularly shaped particles, which are assumed to be a mixture of randomly oriented spheroids [*Veselovskii et al.*, 2010; *Müller et al.*, 2013; *Veselovskii et al.*, 2013]. These methods are mainly limited to night time operation, since most of the current lidar systems do not offer Raman capabilities at daytime. The second group requires additional information from in situ instruments carried aboard, e. g., an aircraft [*Grams et al.*, 1972] or balloon [*Wandinger et al.*, 1995], what reduces their availability. Finally, the third group is based on the synergic use of column-integrated aerosol properties information from passive remote sensing with vertical information derived from lidars. In this sense, some authors have developed methods that combine spaceborne column-integrated values with lidar vertical information [*Kaufman et al.*, 2003; *Léon et al.*, 2003], whereas in some other studies the combined use of sun photometer with lidar systems is proposed in order to derive vertically resolved aerosol microphysical properties [*Reagan et al.*, 1977; *Chaikovsky et al.*, 2012; *Lopatin et al.*, 2013; *Wagner et al.*, 2013].

The retrieval of microphysical properties from column integrated aerosol properties as provided by sun photometers is already well developed and validated through extended networks such as AERONET and SKYNET [*Dubovik and King*, 2000; *O'Neill et al.*, 2003; *Estellés et al.*, 2004; *Dubovik et al.*, 2006; *Olmo et al.*, 2006; *Campanelli et al.*, 2007; *Valenzuela et al.*, 2012a]. In addition, the use of sun photometers is widely extended since columnar integrated properties are of high importance for direct aerosol forcing estimations [*Costa et al.*, 2004; *Antón et al.*, 2011]. However, vertical information is missing. Therefore, the combination of simultaneous information about the vertical structure of atmospheric aerosol provided by the lidar system and the columnar properties provided by the sun photometer seems to be a promising synergetic tool in order to obtain improved information about atmospheric aerosol. The increasing number of stations performing these simultaneous measurements foresees an optimistic future concerning the increasing spatial coverage.

In this dissertation, a major importance will be given to the analysis of mineral dust in by means of the synergic use of lidar and sun photometer data, since the influence of mineral dust on radiative forcing is still affected by a high uncertainty due to its highly irregular shape and the chemical and physical transformations it suffers during its transport [*Sokolik and Toon*, 1999; *Formenti et al., 2011*]. Furthermore, the Mediterranean region, where our experimental site is located, is highly affected by dust transport mainly from the Sahara source region, due to the favourable synoptic conditions in this area [*LaFontaine et al.*, 1990]. Because of these reasons it is highly important to analyse the temporal and spatial variations in the aerosol properties during dust events in the Western Mediterranean Basin. Many studies have already been performed based on passive both satellite- and ground-based sensors [*Moulin et al.*, 1997; *Lyamani et al.*, 2005; *Papayannis et al.*, 2005; *Valenzuela et al.*, 2012a; *Valenzuela et al.*, 2012b]. Also, studies based on lidar systems have been addressed in order to obtain a climatology of mineral dust vertically resolved optical properties over the Mediterranean basin [e. g. *Balis et al.*, 2004; *Papayannis et al.*, 2005; *Mona et al.*, 2006] and the Iberian Peninsula [*Guerrero-Rascado et al., 2008;Guerrero-Rascado et al.*, 2009; *Córdoba-Jabonero et al.*, 2011; *Preißler et al.*, 2013].

Besides the need for systematic analyses of vertically resolved microphysical properties, it is also necessary to further investigate the effects of the aerosol hygroscopic growth in both aerosol optical and microphysical properties. Changes in the aerosol properties under high relative humidity conditions are still a quite open issue that needs to be addressed. Under high relative humidity conditions, aerosol particles size may increase due to water uptake (hygroscopic growth) altering their size distribution. Therefore, hygroscopic growth affects the direct scattering of radiation [*Hänel*, 1976; *Hegg* *et al.*, 1996] and especially the indirect effects, as the affinity of atmospheric aerosols for water vapor is highly related to their ability to act as cloud condensation nuclei (CCN)[*Charlson et al.*, 1992; *Feingold and Morley*, 2003]. Thus, an improved knowledge about aerosol hygroscopic growth is of high importance to quantify the influence of atmospheric aerosol in climate models.

In the past years, there has been an increasing interest in the hygroscopic growth effects on the aerosol optical and microphysical properties and many studies have already been performed. However, many of them are theoretical analysis performed in the laboratory using laboratory generated aerosol samples under controlled conditions [e. g. *Petters and Kreidenweis*, 2007]. Some analysis using samples of ambient aerosols have also been performed, mainly based on humidified nephelometers or humidified tandem differential mobility analysers [*Charlson et al.*, 1992; *Hegg et al.*, 1996; *McInnes et al.*, 1998]. Nonetheless, these instruments present two main problems. Firstly, they are unable to give accurate results above 85% relative humidity [*Wulfmeyer and Feingold*, 2000]. Secondly, they have to modify the ambient conditions by drying the air sample and then humidifying it again up to a certain value of relative humidity.

Lidar systems can overcome these difficulties by sampling the atmosphere without modifying the environmental conditions and also by detecting relative humidity close to saturation, which is of great importance since the range between 85 and 100% relative humidity is where the particles are more affected by hygroscopic growth. However, they present the major drawback that the sample and conditions are not controlled in anyway and cases with adequate conditions for hygroscopic growth are usually reduced. In the past years, some studies have already been performed by using lidar systems to detect aerosol hygroscopic growth with promising results [*Ferrare et al.*, 1998; *Wulfmeyer and Feingold*, 2000; *Feingold and Morley*, 2003; *Veselovskii et al.*, 2009]. Nonetheless, the number of these studies is quite reduced and most of them were based on quite limiting assumptions to retrieve the relative humidity profiles.

1.1 Objectives and outline

The main objective of this thesis is to improve the knowledge on atmospheric aerosol research, with special focus on the issues that are still quite open and are a source of uncertainty in the atmospheric and climate studies. For this purpose, two main topics are addressed. The first one is the analysis of vertically resolved microphysical properties by means of the synergic use of lidar and sun photometer data. The second one considers the analysis of the effects of aerosol hygroscopic growth on the aerosol optical and microphysical properties by means of remote sensing techniques.

The thesis dissertation is organized in several chapters, as indicated in the following outline:

Chapter 2 is devoted to the basic concepts behind the aerosol science and the theory of active and passive remote sensing used throughout this dissertation.

Chapter 3 is a brief overview of the experimental station where the measurements used in this thesis were performed together with a short description of the main instrumentation employed, namely the multiwavelength Raman lidar and the sun photometer.

Chapter 4 is devoted to the description of the methodology. A large part of this chapter focuses on the description of the Lidar Radiometer Inversion Code (LIRIC), paying special attention to methodological aspects and to the description of the algorithm, due to its extensive use throughout this thesis. A detailed analysis of the uncertainties of LIRIC algorithm is also included in this section. A second part, describes the methodology used for the detection of study cases that eventually can be used for the study of the aerosol hygroscopic growth by means of active remote sensing.

Chapter 5 presents the main results concerning the analysis of aerosol microphysical properties by the synergetic use of the lidar and the sun photometer using LIRIC. The chapter is divided in three different parts corresponding to different applications of the algorithm. The first one corresponds to CHARMEX campaign, where LIRIC is used in order to investigate its potential for studying microphysical properties profiles in both temporal and vertical dimensions with high resolution. For this purpose, a dust event measured continuously during 72 hours is investigated. The second part is focused on the analysis of CLIMARENO-GRA campaign, where the availability of information from in situ measurements on board an aircraft and the microphysical properties profiles, retrieved by a completely different approach, allows for an independent validation of LIRIC retrievals. In addition, a comparison with the profiles provided by forecast models is presented in these two sections in Chapter 5. Finally, the third part corresponds to a statistical analysis during the summer 2012, comparing LIRIC retrievals obtained from a unique experimental setup with two sun photometers, located at two different height levels in the same atmospheric column, to evaluate LIRIC performance in the vertical coordinate.

Chapter 6 analyses the effects of the aerosol hygroscopic growth on the optical properties (namely the aerosol backscatter coefficient) over Granada experimental station by means of the combined use of radiosounding data and active remote sensing. In addition, the effects of the hygroscopic growth on the volume concentration profiles retrieved with LIRIC are also analysed. Two cases of potential hygroscopic growth detected over the station are presented and compared here.

Finally, Chapter 7 presents a summary of the main conclusions of this thesis together with an outline of future research activities.

2 Fundamentals

2.1 Aerosols and climate

The Earth's atmosphere is defined as the layer of gases surrounding the planet that is retained by Earth's gravity. The atmosphere protects life on Earth by absorbing ultraviolet solar radiation, warming the surface through heat retention (greenhouse effect) and reducing the diurnal temperature variations. The Earth's atmosphere is mainly composed of two groups of gases. The first group consists of those gases with nearly steady concentrations, whereas the second one consists of gases with variable concentrations. Among other atmospheric components clouds and atmospheric aerosol particles, which are highly variable in space and time, are included.

The atmospheric aerosol is defined as the suspension of solid and/or liquid particles in the atmospheric air, excluding clouds, which are considered as a separate phenomenon [*Horvath*, 1998]. They produce perturbations in the radiative forcing, which is defined as the net change in the energy balance of the Earth system due to some agents. Specifically, the *IPCC* [2007] defines it as a measure of the influence that a factor has in altering the balance of incoming and outgoing energy in the Earth-atmosphere system. It is an accurate indicator of the importance of the factor as a potential climate change driver mechanism.

There are many classifications of the atmospheric aerosol particles, according to their origin, chemical composition or size, among others. According to their origin, aerosols are mainly classified in anthropogenic and natural. Aerosol particles from natural origin, such as mineral dust, sea spray, aerosol from forest fires, volcanoes, etc., can cause variability in the climate system and can be part of its feedbacks mechanisms [*Kaufman et al.*, 2005]. Only the atmospheric aerosol from anthropogenic origin can be considered as an external cause of climate change [*Charlson et al.*, 1992; *IPCC*, 2007]. Anthropogenic aerosol particles such as those coming from burning of fossil fuels, land use, etc are estimated to represent between 26 and 42% of the total aerosol load and are mainly concentrated in the northern hemisphere [*Charlson et al.*, 1992; *IPCC*, 2007].

Regarding their vertical distribution, the majority of the atmospheric aerosol is found in the troposphere, where they have residence times from a few days to several weeks [*Haywood and Boucher*, 2000; *Raes et al.*, 2000]. Within the troposphere, the atmospheric aerosol is not homogeneously mixed and its distribution and amount is highly variable in time and space. Because of this high variability related to their much shorter lifetime compared with the most important greenhouse gases, the quantification of the aerosol effect is more complex than the quantification of radiative forcing by greenhouse gases. Atmospheric aerosol can also be found in the stratosphere, as a permanent small contribution from the Junge layer, located in the lower stratosphere [*Junge*, 1963] or as a result of volcanic eruptions, like those of El Chichón, Mount Pinatubo or Nabro [*Barth et al.*, 1983; *Bluth et al.*, 1997; *Sawamura et al.*, 2012].

The effects of atmospheric aerosol particles are highly important for the Earth’s climate, as indicated by the Fifth Assessment Report (AR5) of the *IPCC* [2013]. According to the AR5, the total anthropogenic radiative forcing for 2011 relative to 1750 is 2.29 [1.13 to 3.33] $W \cdot m^{-2}$ (Figure 2.1), and it has increased more rapidly since 1970. The total anthropogenic radiative forcing best estimate for 2011 is 43% higher than that reported in IPCC 2007 AR4 (Fourth Assessment Report) for the year 2005. This is caused by a combination of continued growth in most greenhouse gas concentrations and improved estimates of radiative forcing by aerosols indicating a weaker net cooling effect (negative radiative forcing). The radiative forcing of the total aerosol effect in the atmosphere, which includes cloud adjustments due to aerosols (the so-called indirect effect in the AR4), is –0.9 [–1.9 to −0.1] $W \cdot m^{-2}$ (medium confidence), and results from a negative forcing from most aerosols and a positive contribution from solar radiation absorption by black carbon. There is high confidence that aerosols and their interactions with clouds have offset a substantial portion of global mean forcing from well-mixed greenhouse gases. They still contribute to the largest uncertainty to the total radiative forcing estimate, even though this is considerably reduced due to the increase in the knowledge of the aerosol properties in the last years.

The above mentioned influence of the atmospheric aerosol on the Earth's energy budget may be caused in two different ways: directly and indirectly. The so-called direct effect is the mechanism by which aerosol particles scatter and absorb shortwave and longwave radiation altering the radiative balance of the Earth-atmosphere system [*Forster et al.*, 2007]. The indirect effect is the mechanism by which aerosol particles influence cloud properties through their role as cloud condensation nuclei (CCN) and/or ice forming nuclei. The increase in aerosol particle concentrations may increase the ambient concentration of CCN and/or ice forming nuclei, therefore affecting cloud properties. A CCN increase can lead to more cloud droplets so that, for fixed cloud liquid water content, the cloud droplet size will decrease. This effect leads to brighter clouds (the so-called "cloud albedo effect", "Twomey effect" or "first indirect effect"). The term "second indirect effect" is applied to the microphysically induced effect on the liquid water content, cloud height, and lifetime of clouds [*Ramaswamy et al.*, 2001]. It is also called the "cloud lifetime effect" [*Lohmann and Feichter*, 2005] or the "Albrecht effect" [*Albrecht*, 1989]. Because of this effect, aerosol particles can also affect clouds by supressing drizzle, increasing cloud lifetime and height and hence increasing the amount of solar radiation reflected from clouds. Such effect can change precipitation patterns as well as cloud extent and optical properties. The semi-direct effect [*Menon et al.*, 2002; *Cook and Highwood*, 2004;

Johnson et al., 2004] is defined as the mechanism by which absorption of shortwave radiation by tropospheric aerosols leads to heating of the troposphere that in turn changes the relative humidity and the stability of the troposphere and thereby influences cloud formation and lifetime.

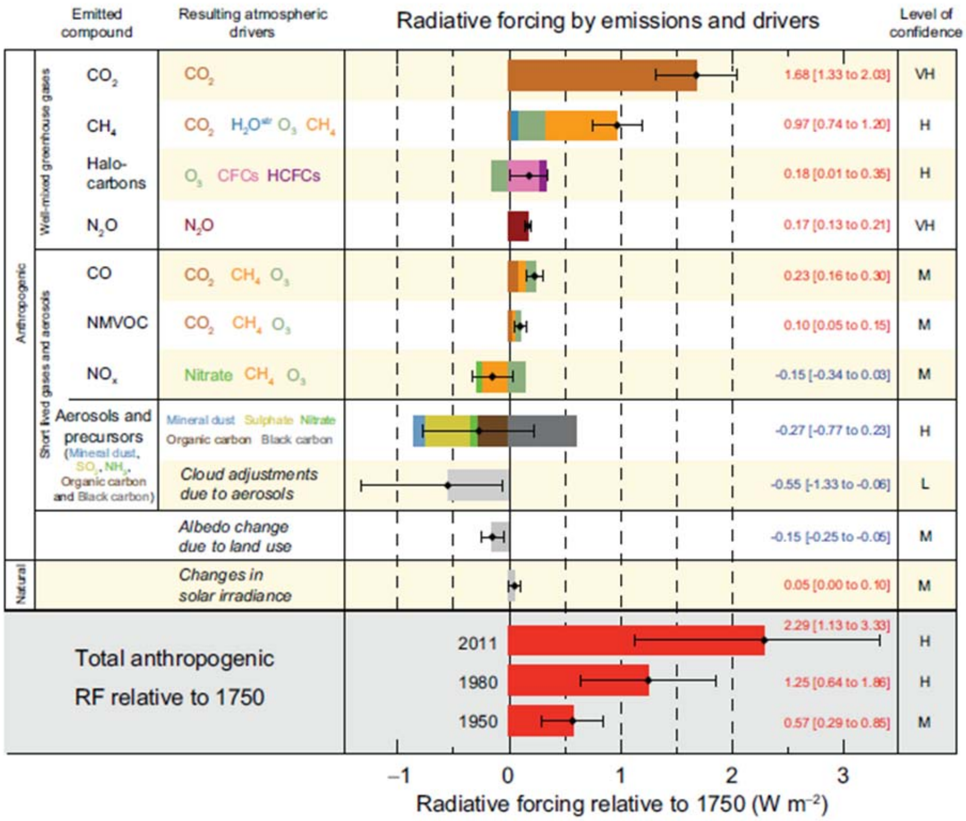

Figure 2.1. Radiative forcing estimates in 2011 relative to 1750 and aggregated uncertainties for the main drivers of climate change taken from [IPCC, 2013]. Values are global average radiative forcing, partitioned according to the emitted compounds or processes that result in a combination of drivers. The best estimates of the net radiative forcing are shown as black diamonds with corresponding uncertainty intervals; the numerical values are provided on the right of the figure, together with the confidence level in the net forcing (VH – very high, H – high, M – medium, L – low, VL – very low). Albedo forcing due to black carbon on snow and ice is included in the black carbon aerosol bar. Small forcings due to contrails (0.05 W m^{-2}, including contrail induced cirrus), and HFCs, PFCs and SF6 (total 0.03 W m^{-2}) are not shown. Volcanic forcing is not included as its episodic nature makes is difficult to compare to other forcing mechanisms. Total anthropogenic radiative forcing is provided for three different years relative to 1750. (After AR5 summary from the IPCC 2013).

2.2 Atmospheric aerosol types

Atmospheric aerosols can be classified according to different criteria. For example, according to their origin, atmospheric aerosols can be either natural or anthropogenic. Considering the mechanism of formation, the aerosol particles are classified as primary when they are emitted as such into the atmosphere and secondary when they are generated through chemical reactions. Regarding their size, the terminology may vary depending on the study area. In general, in atmospheric sciences particles of diameter <1 µm are considered as fine particles, whereas coarse particles are those with diameters > 1 µm. Within the fine mode, usually the nucleation or Aitken mode, formed by particles with diameters between 0.01 and 0.1 µm and the accumulation mode, constituted by particles from 0.1 to 1 µm of diameter are distinguished [e. g. *Seinfeld and Pandis*, 2006; *Eck et al.*, 2010].

In addition, the atmospheric aerosol is commonly classified in terms of aerosol categories for climate models. These categories are not usually composed by only one type, but they are an internal of external mixture of different components. These components may be classified as water-insoluble (mostly soil particles with some organic materials) or water-soluble (sulphates, nitrates, some organics, etc) [*Weitkamp*, 2005]. Among all the different aerosol types and mixtures, anthropogenic pollution, mineral dust and biomass burning aerosols are described in more detail in the following subsections:

2.2.1 Anthropogenic pollution

This aerosol type mainly consists of particles from the traffic and industry emissions as well as particles originated from precursor gases (SO_2, NO, NH_3 y volatile organic compounds or VOCs). They are usually in the fine mode (below 1 µm) and present spherical shape. These particles usually have their origin in local sources, but they might be transported. Regarding their chemical composition, the primary aerosol anthropogenic aerosols are mainly composed of organic carbon (OC) and black carbon (BC) aerosol from fossil fuels.

Organic aerosols are a complex mixture of chemical compounds containing carbon-carbon bonds produced from fossil fuel and biofuel burning. They might have also a natural origin, from natural biogenic emissions. Hundreds of different atmospheric organic compounds have been detected in the atmosphere [*Hamilton et al.*, 2004], which definitively makes modeling of the direct and indirect effects extremely challenging [*McFiggans et al.*, 2006].

Black carbon is a primary aerosol emitted directly at the source from incomplete combustion processes such as fossil fuel and biomass burning and, therefore, mainly from anthropogenic origin. Black carbon aerosol strongly absorbs solar radiation.

Secondary aerosol particles, originated from precursor gases, are mainly composed of sulphates, generated from the oxidation of SO_2, which is emitted e. g. in thermal power plants or in industrial activities. Nitrates, formed from oxidation of NO_x emitted by traffic and industrial activities, are also an important component of these secondary aerosol particles, together with the organic compounds emitted during biomass burning or fossil fuel combustion.

2.2.2 Biomass burning aerosol

Biomass burning describes the burning of living and dead vegetation, including anthropogenic sources, like burning of vegetation for land clearing and land-use, among others. Not all biomass burning aerosols come from anthropogenic activities, as naturally occurring vegetation fires regularly occur. The human-induced fraction is estimated to be about 90% [*Andreae*, 1991]. Biomass burning aerosol consists of two major chemical components: BC, which primarily absorbs solar radiation, and OC, which primarily scatters solar radiation. It usually has a strong fine mode contribution. However, its properties can strongly vary depending on the burning process or the processes during the transport (hygroscopic growth, coagulations or photochemical mechanisms, etc.) [*Müller et a.,* 2007; *Wandinger et al.*, 2010; *Alados-Arboledas et al.*, 2011], causing an increase of the aerosol particle size.

2.2.3 Mineral dust aerosol

Mineral dust aerosol particles mainly contribute to the coarse mode and they are highly irregularly shaped [*Freudenthaler et al.*, 2009]. Mineral dust is produced by wind erosion of soil. In this way, a large amount of mineral dust is injected every year into the atmosphere. Since 2001, different studies have reported dust emission estimates from 1000 to 3000 Tg/yr [*Zender et al.*, 2003; *Tegen et al.*, 2004; *Textor et al.*, 2007]. Besides the natural sources, dust emission is assumed to have a significant anthropogenic component mainly originating from agricultural and industrial practices [*Prospero et al.,* 2002; *Rodríguez et al.*, 2011]. *Tegen and Fung* [1994] estimated the anthropogenic contribution to mineral dust to be 30 to 50% of the total dust burden of the atmosphere. The main natural source regions of desert dust are found in the Northern Hemisphere [*Prospero et al.*, 2002], extending from the west coast of North Africa to Middle and Eastern Asia. The largest source region is the Saharan desert and its contribution to the global annual dust emission is about 50 - 70 % [*Washington et al.*, 2003]. Because mineral desert dust can be transported over thousands of kilometers, it is not only a regional phenomenon, but has a global climate effect. Dust is exported from the Saharan desert during the whole year. Once lifted into the air, mineral dust can be transported over several thousands of kilometers [*Hamonou et al.*, 1999; *Goudie and Middleton*, 2001; *Ansmann et al.*, 2003; *Ansmann et al.*, 2009].

The direct aerosol effect of dust particles is very complex. Due to their large range of sizes (from about 0.01 μm to about 100 μm) [*Sokolik et al.*, 2001] and chemical composition, they scatter and absorb not only the incoming solar light, but also have a significant impact on long-wave terrestrial radiation [*Tanré et al.*, 2003]. The magnitude and sign of the direct aerosol effect of dust strongly depends on the optical properties and the vertical and horizontal distribution of the dust plume, as well as on the albedo of the underlying surface [*Sokolik et al.*, 2001]. In addition, due to the strongly irregular shape of mineral dust particles the application of classical Mie theory is not always possible, which difficulties the study of mineral dust properties.

2.3 Basic radiometric quantities

In order to understand the processes by which the atmospheric aerosol interacts with the solar radiation, affecting the Earth's climate, it is necessary to describe some basics concepts about radiometric quantities.

The basis of the radiometric quantities is the monochromatic radiant flux Φ_λ, which is defined as the radiant energy, Q, included in an spectral interval dλ around the wavelength of interest, λ, passing through a control surface per unit time. This quantity does not provide any information about the spatial distribution of the energy. The radiant flux, $d\Phi_\lambda$, received (or emitted) at (from) the unit area on a detector (or source) without considering direction is termed the radiant flux density or irradiance:

$$E_\lambda = \frac{d\Phi_\lambda}{dS} \qquad \textit{Eq. 2.1}$$

In order to characterize the emission of point sources, the radiant intensity I_λ represents the radiant flux $d\Phi_\lambda$, propagated in a solid angle $d\Omega$, defined as

$$I_\lambda = \frac{d\Phi_\lambda}{d\Omega} \qquad \textit{Eq. 2.2}$$

For extended sources the radiance, defined as the flux emitted per unit solid angle and unit area (perpendicular to the considered direction *s*) is used. If θ is the angle between the normal to the radiating surface and the direction in which the radiant flux is emitted, the radiance is given by

$$L_\lambda = \frac{d^2\Phi_\lambda}{dS\,d\Omega\cos\theta} \qquad \text{Eq. 2.3}$$

Figure 2.2 shows a schematic diagram of the definition of radiance and

Table 2.1 summarizes the different radiometric quantities, including the symbol used and the corresponding units in the International System (IS).

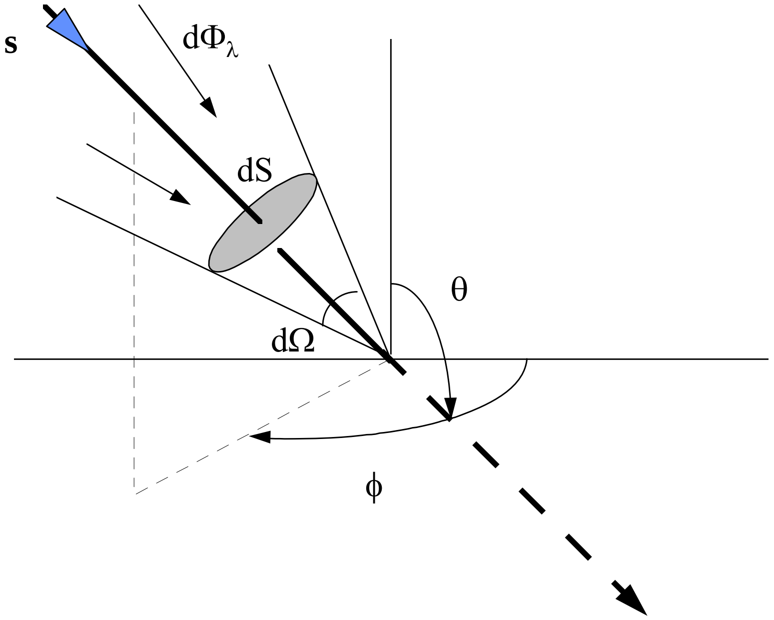

Figure 2.2. Radiance, zenith angle θ and azimuth angle ϕ define the direction of the radiant flux S.

Radiometric quantity	Symbol	Unit
Radiant energy	Q	J
Radiant flux	Φ_λ	$W \mu m^{-1}$
Radiant flux density (irradiance)	E_λ	$W\,m^{-2}\,\mu m^{-1}$
Radiant intensity	I_λ	$W\,\mu m^{-1}\,sr^{-1}$
Radiance	L_λ	$W\,m^{-2}\,\mu m^{-1}\,sr^{-1}$

Table 2.1. Radiometric symbols and units.

2.4 Light scattering and absorption by atmospheric aerosols

The direct effect of atmospheric aerosols in the Earth's energy budget is determined by the absorption and scattering processes. These processes affect the solar electromagnetic radiation propagating through the atmosphere by producing its attenuation. The attenuation of solar radiation is mainly the result of the combination of the absorption and scattering processes.

In the absorption process the energy becomes part of the internal energy of the particles. The fundamental idea of the absorption process lies in the exchanges of energy between the molecules in the atmosphere and the electromagnetic field. This absorption process depends on the energy state of the molecule, which at the same time depends on the rotational, vibrational or electronic energies. Because the energy levels associated with these different kinds of energy are quantized, the absorption process occurs only at discrete wavelengths and therefore this process is called selective absorption. When absorption takes place over a number of wavelengths very close to each other some overlap is possible and it is called absorption band [*Iqbal*, 1983]. As a consequence of the absorption process in the atmosphere, atmospheric components increase their internal energy and therefore their temperature. The absorbed radiation is used to produce a transition from one energy level to another.

The main molecular absorbers in the atmosphere are H_2O (water vapour), CO_2, O_3, N_2O, CO, O_2, CH_4 and N_2. The minor absorbers are oxides of nitrogen NO_2, N_2O_4, N_2O_5; hydrocarbon combinations C_2H_4, C_2H_6, C_3H_8; and sulphurous gas H_2S. Most of these absorbers are active mainly in the near- and far-infrared wavelengths regions (from 0.7 to 100 μm). On the contrary, atomic gases as O and N mainly absorb in the shortest wavelengths of the UV. Figure 2.3 shows the main molecular absorbers for the solar radiation spectrum.

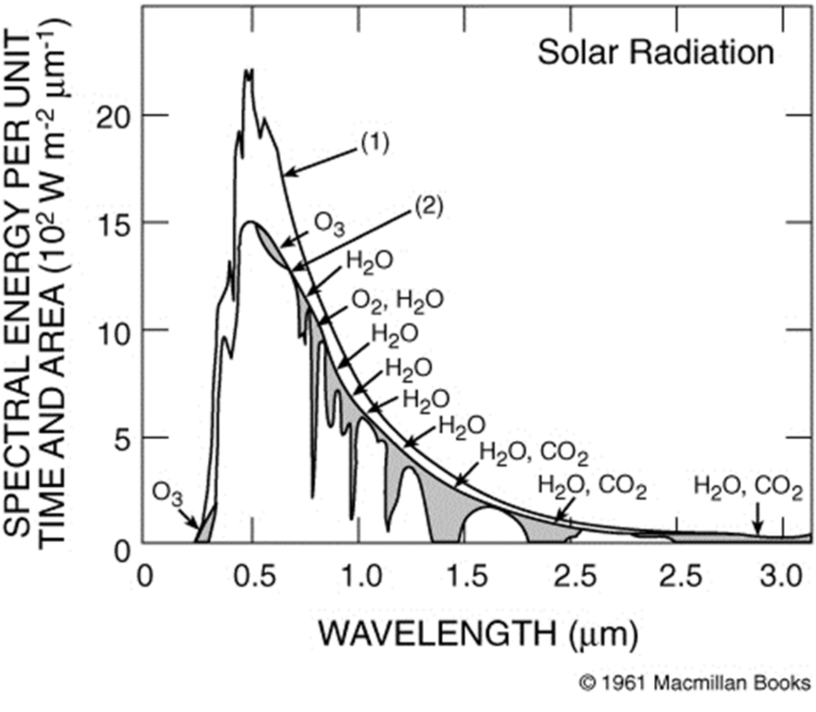

Figure 2.3. Identification of the various molecular absorbers. The graph shows the solar irradiance on top of the atmosphere, at sea level and also the corresponding irradiance for a black body at 5900 K (from Brasseur et al., [1999]).

The scattering process may be elastic or inelastic. For most of the scattered incident radiation, atmospheric components produce elastic scattering. This means that the energy and wavelength of the scattered radiation are equal to those of the incident one. In this process the energy transported by an electromagnetic wave is scattered in every direction as a consequence of the interaction of this wave with the particles in the medium.

A wavelength shift between incident and scattered frequency of the radiation is observed for a very small fraction of scattered radiation (inelastic scattering). This inelastic or Raman scattering allows for variations in the quantum state of the scatterer molecule, changing its vibrational, rotational and/or vibrational-rotational energy level. If the Raman scatterer molecule absorbs energy, being excited to a higher energy level, the frequency of the scattered radiation decreases. Therefore, the wavelength of the scattered radiation is shifted towards higher values and the process is called Stokes Raman scattering with

$$\tilde{\upsilon}_{out} = \tilde{\upsilon}_{in} - \left|\Delta\tilde{\upsilon}\right| \qquad \textit{Eq. 2.4}$$

where $\tilde{\upsilon}_{out}$ is the frequency of scattered light, $\tilde{\upsilon}_{in}$ the frequency of incident light and $\left|\Delta\tilde{\upsilon}\right|$ indicates the shift between them.

However, the scattering molecule might also lose energy and decrease its energy level. The frequency of the scattered radiation is now increased and the wavelength is shifted towards lower values. This case is called anti-Stokes Raman scattering with

$$\tilde{\upsilon}_{out} = \tilde{\upsilon}_{in} + \left|\Delta\tilde{\upsilon}\right| \qquad \textit{Eq. 2.5}$$

Because the frequency shift $\Delta\tilde{\upsilon}$ is caused by a change of the vibrational, rotational and/or vibrational-rotational energy level of the scattering molecule, it is characteristic for the scattering molecule and can be calculated as

$$\Delta\tilde{\upsilon} = \tilde{\upsilon}_{in} - \tilde{\upsilon}_{out} = \frac{\Delta E}{hc_0} \qquad \textit{Eq. 2.6}$$

$\tilde{\upsilon} = 1/\lambda = \upsilon / c_0$ in cm^{-1} is the wavenumber (usually used in spectroscopy) of the scattered radiation, ΔE is the difference between the rotational-vibrational energy levels of the scattering molecule before and after the scattering process, h is the Planck constant and c_0 the speed of light in vacuum. The frequency (wavelength) shift for changes of the vibrational energy level of the molecule is much larger than that associated to changes of the rotational energy level. Thus, electromagnetic radiation originating from vibrational-Raman scattering can be separated more easily from elastically scattered light. This effect is used in the receiver of the Raman lidar systems. However, the intensity of the Raman scattered electromagnetic radiation is much lower than the intensity of the elastic scattering. Thus, for atmospheric applications the detection of Raman signals is usually restricted to night-time when background noise is minimized.

The scattering process is highly dependent on the size parameter, *x,* defined as the relation between the particle radius and the wavelength of the incident wave ($x=2\pi r/\lambda$) and also on the refractive index *m*, which depends on the particle chemical composition:

If $x < 0.6/n$, with *n* the real part of the complex refractive index of the particles, the scattering process is described by Rayleigh theory. The Rayleigh's theory, which describes the scattering of solar radiation by air molecules, is based on the assumption that the scattering particles are spherical with radii less than 0.2 times the wavelength of the incident radiation. It only considers single-scattering processes. A key feature of this theory is that the monochromatic optical extinction varies approximately as λ^{-4}, what has been verified experimentally.

If $0.6/n < x < 5$, the scattering is explained by Mie theory. It is applied when the size of the particles is comparable to the incident wavelength (x~1), producing interference patterns with the partial waves emitted by multipoles of the particles having phase differences. For this reason there is a strong angular dependency, increasing in the forward scattering (compared to Rayleigh pattern) and the chromatic dependency of the scattering is smaller. Mie theory converges into Rayleigh theory when x decreases, therefore Rayleigh theory can be explained with Mie theory but, due to the simplicity of Rayleigh theory, they are usually applied separately.

If $x > 5$, the scattering is mainly a process of diffuse reflection that usually does not happen in the Earth's atmosphere. In this case geometric optics are used.

The scattered radiation also depends on the scattering angle, Θ, which is the angle between the incident and scattering directions. $\Theta = 0^{\circ}$ means that the scattering is fully produced in the direction of the wave propagation. For $\Theta > 90^{\circ}$ we focus on the backscattering. Figure 2.4 shows the differences in the scattering for Rayleigh and Mie theories. Rayleigh is symmetric respect to the plane perpendicular to the propagation direction and find its minimum at $\Theta = \pm 90^{\circ}$, being its maximums at $\Theta = 0^{\circ}$ and $\Theta = 180^{\circ}$. On the other hand, Mie scattering presents an asymmetry pattern, with a strong forward scattering.

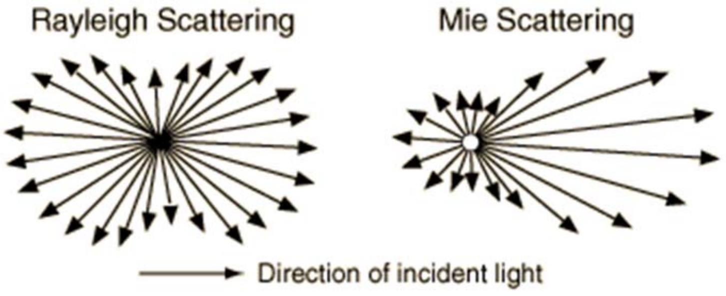

Figure 2.4. Rayleigh scattering and Mie scattering.

The medium's capacity to absorb and scatter radiation is quantified using absorption and scattering coefficients, $\sigma_{a\lambda}$ and $\sigma_{s\lambda}$. The extinction coefficient, $\sigma_{e\lambda}$, which is defined as the sum of the $\sigma_{a\lambda} + \sigma_{s\lambda}$, represents the attenuation of the radiant energy in a real medium, as inferred from the Eq. 2.7 and Figure 2.5

$$dL_\lambda = -L_\lambda \sigma_{e\lambda} ds \qquad \text{Eq. 2.7}$$

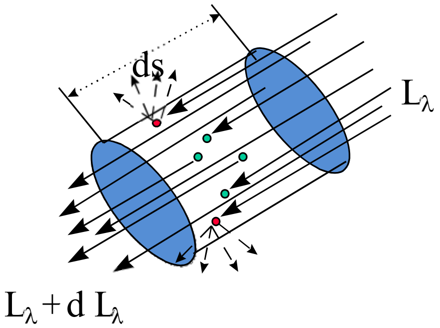

Figure 2.5. Schematic drawing of the radiance variation observed when a radiant flux beam travels through a volume dV.

The application of the Maxwell equations for the problem of the interaction of an electromagnetic wave with a sphere, assuming that the sphere is homogeneous and isotropic, was fully developed by *Mie* [1908]. A full description of Mie theory and Rayleigh theory, applied to molecules in the atmosphere, is presented in *Bohren and Huffman* [1983]. Mie expressed the extinction coefficient, $\sigma_{e\lambda}$, for a suspension of spherical particles of different radii (between r_1 and r_2) as:

$$\sigma_{e\lambda} = \int_{r_1}^{r_2} \pi r^2 Q_e(r,\lambda) n(r) dr \qquad \textit{Eq. 2.8}$$

where Q_e is the extinction efficiency factor and can be understood as the effectiveness with which the particle interacts with radiant flux. *n(r)* is the size distribution of those spherical particles. More details will be explained in the following sections.

2.5 Atmospheric aerosol properties

For the study of the atmospheric aerosol effects on the Earth's climate, the measurement and retrieval of the atmospheric aerosol properties are necessary. Aerosol optical and microphysical properties such as the aerosol optical depth, the single scattering albedo or the size distributions are used as input data for the modelling of the atmospheric aerosol, e.g [*Thomas and Stamnes*, 2002]. A description of the main aerosol properties needed for the discussion of the results in this dissertation is presented in the following subsections.

2.5.1 Optical properties

2.5.1.1 Aerosol optical depth

The optical thickness, OT, is defined as the integrated extinction coefficient between two points separated by a distance ds in the direction of the radiation propagation:

$$OT_\lambda = \int_{s_1}^{s_2} \sigma_{e\lambda} ds \qquad \textit{Eq. 2.9}$$

However, in atmospheric science the optical depth τ_λ or normal optical thickness is more commonly used. It is defined as the optical thickness measured vertically (or equivalently, the integrated extinction coefficient over a vertical column of unit cross section).

$$\tau_{e,\lambda} = \int_{z_1}^{z_2} \sigma_{e\lambda} dz \qquad \textit{Eq. 2.10}$$

The relationship between optical thickness and optical depth is

$$OT_{\lambda} = \tau_{e,\lambda} m_0 \qquad \textit{Eq. 2.11}$$

where m_0 is the relative optical air mass. In Eq. 2.11 the relative optical air mass m_0 is a function of the solar zenith angle (θ_0) defined as the angle between the zenith (the vertical direction) and the direct solar irradiance path. Its relation can be approximated with the following expression [*Kasten and Young*, 1989]:

$$m_0 = \frac{1}{\cos(\theta_0)} \qquad \textit{Eq. 2.12}$$

Eq. 2.12 assumes a uniform atmosphere with refractive index equal to one and considering a plane-parallel atmosphere [*Iqbal*, 1983]. This approximation can be applied for θ_0 smaller than 80º. Otherwise, a different approximation has to be used (i.e. [*Kasten and Young*, 1989]).

The total optical depth, $\tau_{e,\lambda}$, results of adding up the scattering and absorption processes of the different atmospheric components. Therefore, the optical depth is expressed as:

$$\tau_{e,\lambda} = \tau_{g\lambda} + \tau_{w\lambda} + \tau_{NO_2\lambda} + \tau_{O_3\lambda} + \tau_{R\lambda} + \tau_{\lambda} \qquad \textit{Eq. 2.13}$$

where the different subscripts refer to the relevant attenuation processes in the solar spectrum: g refers to the uniformly mixed gases absorption, NO_2 to the nitrogen dioxide absorption, w refers to the water vapor absorption, O_3 to the ozone absorption, R refers to Rayleigh scattering component. The last term refers to the aerosol scattering and no subscript will be used for the sake of simplicity, since in the results presented in this thesis we will focus mainly in the aerosol optical depth τ_λ.

The spectral dependence of the aerosol optical depth is parameterized by means of the Angström law [*Ångström*, 1964]:

$$\tau_\lambda = \tau_{1\mu m}\lambda^{-AE} \qquad \textit{Eq. 2.14}$$

where *AE* and $\tau_{1\mu m}$ are the Angström coefficients. The Angström exponent, *AE*, characterizes the spectral features of aerosols and is related to the size of the particles [*Shifrin*, 1995], while the $\tau_{1\mu m}$ coefficient is related to the aerosol load in the vertical column. Large values of *AE* indicate the prevalence of fine particles e. g. from anthropogenic pollution, while low values of *AE* are related with the presence of coarse particles such as desert dust and marine aerosols [*Dubovik et al.*, 2002].

2.5.1.2 Single scattering albedo

When the radiation interacts with particles, the processes of scattering and absorption occur simultaneously. The relative importance of the scattering and absorption is characterized by the single scattering albedo, defined as

$$\omega(\lambda) = \frac{\sigma_{s\lambda}}{\sigma_{s\lambda} + \sigma_{a\lambda}} = \frac{\sigma_{s\lambda}}{\sigma_{e\lambda}} \qquad \textit{Eq. 2.15}$$

It mainly depends on the relative source apportionment of the various aerosol substances and on aging during transport. Absorption of solar radiation by atmospheric aerosols mainly results from elemental carbon originated from biomass burning and fuel combustion, and from the hematite in mineral dust in the ultraviolet range. According to Mie theory, the efficiency factors of scattering and absorption expressed in terms of the size parameter *x* and the refractive index ($Q_s(x,m)$ *and* $Q_a(x,m)$), are defined analogously to the efficiency factor of extinction in Eq. 2.8. Therefore, we can calculate the scattering and absorption coefficients as [*Goody et al.*, 1989]:

$$\sigma_{s\lambda} = \int_{r_1}^{r_2} \pi r^2 Q_s(r,\lambda) n(r) dr \qquad \textit{Eq. 2.16}$$

$$\sigma_{a\lambda} = \int_{r_1}^{r_2} \pi r^2 Q_a(r,\lambda) n(r) dr \qquad \textit{Eq. 2.17}$$

The extinction coefficient $\sigma_{e\lambda}$ will be the sum of scattering and absorption coefficients $\sigma_{e\lambda} = \sigma_{a\lambda} + \sigma_{s\lambda}$.

2.5.1.3 Phase function

To describe the angular distribution of the scattered energy we define a non-dimensional variable called the phase function, $P(\Theta)$, depending on the scattering angle Θ (angle between the incident and the scattered radiation). It is defined as the fraction of the energy scattered by the aerosol in a given direction respect to the energy scattered in all directions. The phase function $P(\Theta)$ is calculated according to Mie theory [*Goody et al.*, 1989]. Some examples are shown on Figure 2.6

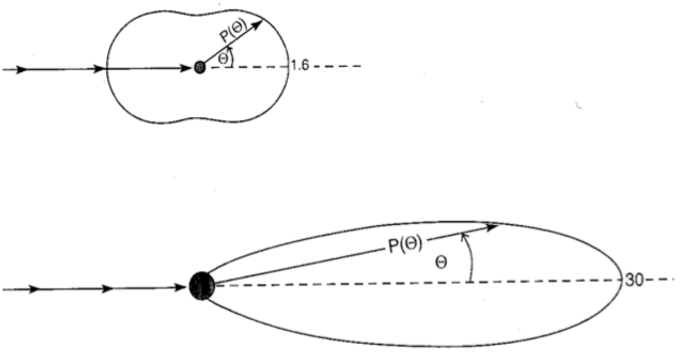

Figure 2.6 Phase function for the Rayleigh scattering (top) and Mie scattering(bottom).

The aerosol asymmetry parameter, g_{asym}, is defined as the cosine-weighted average of the phase function.

$$g_{asym} = \frac{\int_{-1}^{1} \cos\Theta \cdot P(\cos\Theta) \cdot d\cos\Theta}{\int_{-1}^{1} P(\cos\Theta) \cdot d\cos\Theta} \qquad \text{Eq. 2.18}$$

For isotropic scattering, e. g. Rayleigh scattering, g_{asym} is zero. g_{asym} increases as the forward scattering (0-90 º) is more important and can be negative if the phase function peaks in backward directions (90–180º).

2.5.2 Microphysical properties

One of the main aerosol microphysical properties is the size distribution. The size of aerosol particles ranges approximately between 0.001 and 100 μm in radius, and is described by the numeric size distribution *n(r)* as:

$$n(r) = \frac{dN}{d\ln r} \qquad \text{Eq. 2.19}$$

representing the number of particles with radius in the logarithmic interval (ln *r*, ln *r* + dln *r*). The use of logarithmic scale is useful due to the large range in size of aerosol particles. The total number of particles is obtained integrating as:

$$N = \int_{0}^{\infty} n(r)\, d\ln r \qquad \text{Eq. 2.20}$$

The equivalent surface size distribution is defined as:

$$s(r) = \frac{dS}{d\ln r} = 4\pi r^2 \frac{dN}{d\ln r} = 4\pi r^2 n(r) \qquad \text{Eq. 2.21}$$

representing the surface of particles per unity of air volume for particles with radius in the logarithmic interval (ln *r*, ln *r* + dln *r*). Therefore, the total surface *S* of the aerosol particles is defined as:

$$S = \int_0^\infty s(r)\, d\ln r \qquad \textit{Eq. 2.22}$$

Analogously, the volume size distribution is defined as:

$$v(r) = \frac{dV}{d\ln r} \qquad \textit{Eq. 2.23}$$

representing the aerosol volume in an air column of unity cross section per logarithmic particle radius unit.

Assuming only spherical particles, the volume and number size distributions can be easily related through the expression:

$$v(r) = \frac{dV}{d\ln r} = \frac{4\pi}{3} r^3 \frac{dN}{d\ln r} \qquad \textit{Eq. 2.24}$$

The relation between optical depth and the volume size distribution is indicated in the following expression:

$$\tau_\lambda = \int_0^\infty \int_{r_{\min}}^{r_{\max}} \pi r^2 Q_{e\lambda}(r) n(r,z)\, dr\, dz \qquad \textit{Eq. 2.25}$$

where r_{min} and r_{max} are the minimum and maximum radius of the particles considered. The column-integrated size distribution is expressed as:

$$n_c(r) = \int_0^\infty n(r,z)\, dz \qquad \textit{Eq. 2.26}$$

This column-integrated size distribution is related to the column-integrated volume size distribution by means of the expression:

$$v_c(r) = \frac{4}{3}\pi r^3 n_c(r) \qquad \textit{Eq. 2.27}$$

These size distributions are very useful since they allow the possibility to model certain of their characteristics. Generally, they are represented using a mathematical expression with some fitting parameters. Log-normal distributions reproduce the volume size distributions with fair accuracy [*Hegg et al.*, 1993].

2.6 Hygroscopicity of aerosol particles

The aerosol optical and microphysical properties previously explained are quite variable and even for the same aerosol type they can change due to processes such as nucleation, coagulations of photochemical mechanisms or hygroscopic growth due to water uptake. The analysis of the effects of the aerosol hygroscopic growth is also addressed in this thesis.

The increase in the diameter of the aerosol particles due to hygroscopic growth is described by the hygroscopic growth factor. In hygroscopicity studies, the hygroscopic growth factor is usually defined as

$$g(RH) = \frac{D(RH)}{D_{dry}} \qquad \textit{Eq. 2.28}$$

where D_{dry} is the particle diameter at dry conditions (RH < 40%) and *D(RH)* is the diameter at a specific relative humidity, RH. Some other aerosol properties such as the mass or the scattering coefficient can be used to study the aerosol hygroscopic properties, e. g. [*McInnes et al.*, 1996; *McInnes et al.*, 1998; *Zieger et al.*, 2013]. Variations in the aerosol properties (different from the diameter) due to water uptake are characterized by the so-called enhancement factor

$$f_{\zeta}(RH) = \frac{\zeta(RH)}{\zeta_{dry}} \qquad \textit{Eq. 2.29}$$

where ζ symbolizes any aerosol property except the diameter.

The hygroscopicity of the aerosol particles depends on particle dry diameter, on temperature, on water properties (such as density and water activity) and on the solubility of the involved chemical substances (inorganic salts, organics and soot, among others). In order to understand the hygroscopic properties of the atmospheric aerosols it is necessary to assume that they are usually concentrated aqueous solutions and their behavior is ruled by the Köhler theory. The Köhler theory is explained in detail in *Pruppacher et al.*, [1998] and *Seinfeld and Pandis*, [2012]. Nonetheless, some basics of this theory will be presented here.

In the atmosphere, water exists both in the vapor phase and in the liquid phase, i.e. as water droplets and wet aerosol particles. Expressed in a very simple way, the Köhler theory explains the conditions for water equilibrium between these two phases. Within this theory, mainly two effects have to be taken into account: the Raoult's law (or solute effect) and the Kelvin (or curvature effect).

2.6.1 The Raoult's law (solute effect)

In this context, the Raoult's law accounts for the effects on the equilibrium vapor pressure of the presence of a solute dissolved in the atmospheric water.

The relative humidity (RH) is defined as the water vapor pressure e divided by the saturation water vapor pressure for a flat surface e_0, which is also called the saturation ratio S.

$$\frac{RH}{100} = S = \frac{e}{e_0} \qquad \textit{Eq. 2.30}$$

Let us consider pure water at constant temperature and pressure in equilibrium with the atmosphere, assuming a flat surface. For this case, the equilibrium pressure of water vapor with the liquid phase is equal to the saturation water vapor pressure. Nonetheless, in the atmosphere liquid water always contains dissolved compounds. Raoult's law states that the equilibrium vapor pressure of a vapor over its solution is equal to the product of the pure component vapor pressure (saturation vapor pressure) and its mole fraction in the solution. Therefore, the equilibrium vapor pressure e_{sol} over an aqueous solution (assuming a flat surface and an ideal solution without interaction between solvent and solution) is always lower than the saturation water vapor pressure e_0 and is a linear function of the water vapor mole fraction according to the Raoult's law:

$$\frac{e_{sol}}{e_0} = \chi_w = \frac{n_w}{n_w + \sum_i n_i} \qquad \textit{Eq. 2.31}$$

where χ_w is the mole fraction of water, which is calculated by taking the number of moles of water molecules n_w and solute molecules n_i, respectively. The summation in the denominator goes over all the solutes.

In general, a solution approaches ideality as it becomes more and more dilute in all components except the solvent ($\chi_w \to 1$). However, since atmospheric aerosols are usually non ideal concentrated aqueous solutions, the deviation from ideality is taken into account by introducing the activity coefficient γ_w (water activity coefficient in our case):

$$\frac{e_{sol}}{e_0} = \chi_w \gamma_w = a_w \qquad \textit{Eq. 2.32}$$

γ_w is a function of substance, temperature, pressure and the mole fractions of all solute substances in solution and also tends to unity in cases of high dilution. The product $\chi_w \gamma_w$ is the so-called water activity a_w. Therefore according to these equations, the presence of the solute causes a reduction of the water equilibrium vapor pressure over the solution ($e_{sol} < e_0$).

2.6.2 The Kelvin effect (or curvature effect)

The Kelvin effect considers the effect of the curvature of droplets in the equilibrium vapor pressure. The Kelvin effect states that the equilibrium vapor pressure over a curved surface e_K always exceeds the vapor pressure compared to the vapor pressure of the same solution with a flat surface e_{sol}. This is expressed by the Kelvin equation as:

$$S_{Kelvin} = \frac{e_K}{e_{sol}} = exp\left(\frac{4\sigma_{sol}M_w}{RT\rho_w D}\right) \qquad \textit{Eq. 2.33}$$

where σ_{sol} is the surface tension of the solution, M_w the molecular weight of water, ρ_w the density of water, R the ideal gas constant, T the temperature, and D the droplet diameter. Note that the curvature for water droplets becomes important only for D<0.1 µm. Since $\frac{e_K}{e_{\mathrm{sol}}} > 1$, for the equilibrium of a pure water droplet with the environment the air needs to be supersaturated with water vapour. This means that the equilibrium water vapor pressure $e_K$over a curved surface is much larger than the corresponding saturation water vapor pressure for a flat surface, e_0. For larger particle diameters, lower supersaturation is needed.

2.6.3 Köhler theory

If aerosol particles are considered as droplets of aqueous solutions, the knowledge about the behavior of a pure water droplet is necessary in order to understand the behavior of aerosol particles regarding their hygroscopicity. The combination of both the modified Raoult's law for non-ideal solutions and the Kelvin effect applied to water droplets in the atmosphere is the base of the Köhler theory. This theory explains the relation between S and the droplet diameter for an aqueous solution, which is given by the following equation:

$$S = \frac{e_K}{e_0 \chi_w \gamma_w} = a_w S_K = \ a_w exp\left(\frac{4\sigma_{sol} M_w}{RT\rho_w D}\right) \qquad \textit{Eq. 2.34}$$

Taking into account the volume of the droplets and considering dilute solutions which tend to ideality ($\chi_w \rightarrow 1$) [*Seinfeld and Pandis*, 2012], it can be approximated by:

$$ln(S) = ln\left(\frac{e_d}{e_o}\right) = \frac{A}{D} - \frac{B}{D^3} \qquad \textit{Eq. 2.35}$$

$$A = \frac{4M_w\sigma_w}{RT\rho_w} \qquad B = \frac{6n_{sol}M_w}{\pi\rho_w} \qquad \textit{Eq. 2.36}$$

where the surface tension of the solute is approximated by the one of water (σ_w). The first term on the right is related to Kelvin effect whereas the second one accounts for the solute effect. As it can be inferred, the Kelvin effect tends to increase the vapor pressure whereas the solute effect tends to decrease it. Both terms increase with decreasing diameter of the aqueous solution (atmospheric aerosol), but the term related to the solute effect increases much faster.

An example Köhler curve (calculated using Eq. 2.35) is shown in Figure 2.7 for a NaCl particle with a dry size of D = 50 nm (and taking σ_w = 0.072 Jm^{-2} at T = 298K from *Seinfeld and Pandis,* [2012]). The contributions of the Kelvin effect (S always above 1) and the Raoult effect (S always below 1) are shown separately.

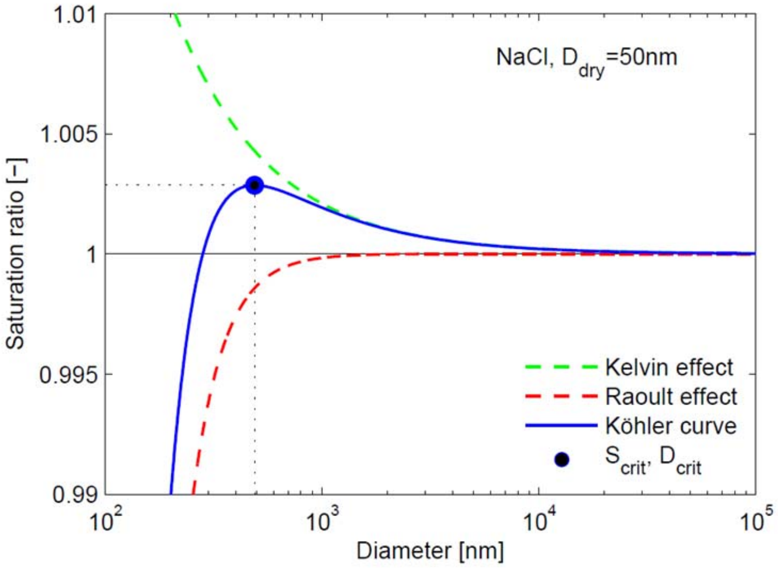

Figure 2.7. Köhler curve of NaCl particles with a dry size of D=50 nm (and taking $\sigma_w = 0.072\ Jm^{-2}$ *at T =298K from Seinfeld and Pandis, 2006).*

The Köhler curve shows a maximum at a certain diameter, which is called the critical diameter D_{crit}. The S value at the maximum is called critical supersaturation ratio S_{crit}. The Kelvin effect is the clearly dominant factor for larger droplets, while the solute effect is dominant for very small particles in relation to their dry size. On the rising part of the Köhler curve ($D < D_{crit}$), droplets are in a stable equilibrium with their environment [*Seinfeld and Pandis,* 2006]. This means that at a fixed S the droplet will stay at its original equilibrium state if it experiences small perturbations caused by the gain or loss of few water molecules. On the descending part of the Köhler curve ($D > D_{crit}$), small perturbations such as the addition of water molecules, will lead to a larger size with a decreased equilibrium vapor pressure and consequently more water will condense on the droplet which will grow even further. Perturbations that result in a loss of water molecules will lead to additional evaporation. A pure water droplet would evaporate completely, but if the droplet is a solution, it will (due to the

Raoult effect) only evaporate until it reaches the diameter that corresponds to the stable equilibrium state on the ascending branch of the Köhler curve. Therefore, droplets larger than D_{crit} are in unstable equilibrium state. Particles beyond S_{crit} are considered to be cloud droplets (or activated particles). The Kelvin effect is also responsible for the fact that the critical diameter decreases with decreasing dry particle size, while the critical supersaturation increases (for the same substance). This is also the reason why the hygroscopic growth factor decreases for smaller (dry) particles.

The hygroscopic growth described by Köhler theory is restricted to liquid and soluble particles. In the presence of insoluble compounds, the solute effect is increased in absolute terms. Besides, inorganic and also some organic compounds can also form solid particles (crystals) at low RH. The state (liquid or crystal) has to be included when describing the hygroscopic growth. If the particle is dry and solid (e. g. a single NaCl crystal) it will start taking up water at a defined RH where the particle dissolves, called the deliquescence relative humidity (DRH). The droplet will take up water if the RH is further increased to maintain thermodynamic equilibrium following the Köhler curve. The droplet will evaporate water if the RH is decreased. The phase transition from liquid to solid (crystallization) however does not occur at the DRH, the droplet rather stays supersaturated until it crystallizes at the so-called efflorescence relative humidity (ERH). This behavior is explained by nucleation kinetics: the water needs to evaporate from the supersaturated droplet and a crystal needs to be formed through nucleation at a critical supersaturation. This hysteresis phenomenon is shown in Figure 2.8 where the hygroscopic growth factor $g(\mathrm{RH})$ (Eq. 2.1) for a NaCl particle (dry size D_{dry} = 100 nm) is shown. The DRH of a substance can be significantly lower or even fully suppressed if it is mixed with other components. The ERH may be at a larger RH if the solution contains insoluble impurities (heterogeneous nucleation may take place).

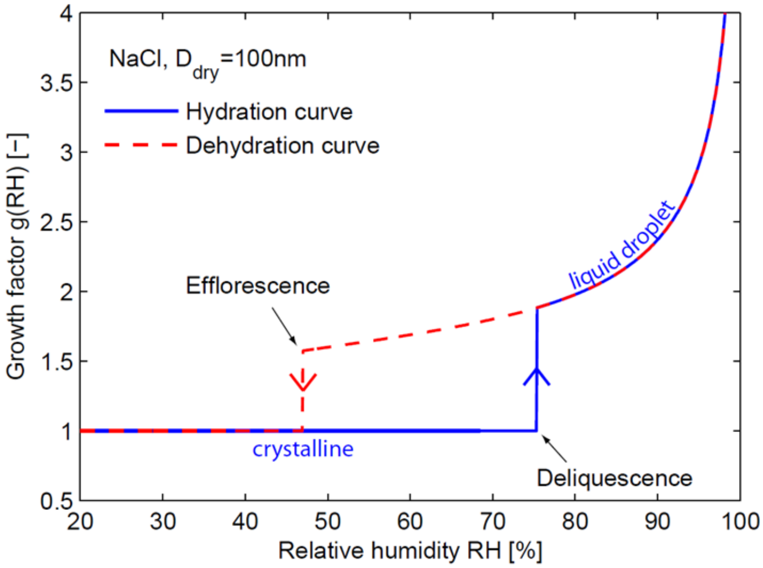

Figure 2.8. Hygroscopic growth factor g (RH) for a NaCl particle (dry size D_{dry} = 100 nm).

In the last decades, a large variety of experimental techniques have been used to measure the effects of hygroscopic growth of aerosol particles explained before, [e. g. *Hänel,* 1976*; Kotchenruther and Hobbs,* 1998*;Feingold and Morley,* 2003*; Gysel et al.,* 2004*; Fierz-Schmidhauser et al.,* 2010*; Zieger et al.,* 2013]. Together with the measurements of *g(RH)*, based on the increase in the particle diameter, these techniques are based on the detection of the effect of water absorption on particle mass or optical properties. Optical properties such as the scattering and extinction coefficients are strongly dependent on RH for hygroscopic particles. The quantification of the effect of RH on these properties is also necessary to accurately estimate the radiative forcing of atmospheric aerosols. The enhancement factor of aerosol optical properties such as the extinction, scattering or absorption coefficients was already analysed in detail some decades ago by [*Hänel,* 1976]. Since not all parameters needed to solve the Köhler equation are always known, a simplified representation of the Köhler equation is often needed to calculate or predict the hygroscopic growth of aerosol particles

Hänel [1976] already proposed a simple parameterization model for the enhancement factor of optical properties. In the chapter 1 of this thesis the aerosol optical properties are parameterized using this model proposed by Hänel, as it was previously done by [*Kotchenruther and Hobbs*, 1998; *Kotchenruther et al.*, 1999; Randriamiarisoa *et al.*, 2006; *Raut and Chazette*, 2007; *Veselovskii et al.*, 2009]. The enhancement factor due to water uptake, $f_{\zeta}(RH)$, is defined as:

$$f_{\zeta}(RH) = \left(\frac{1 - RH}{1 - RH_{dry}}\right)^{-\gamma} \qquad \textit{Eq. 2.37}$$

where ζ stands for any aerosol optical property and the γ value is an indicator of the hygroscopicity of the particles. Larger values of γ are related to more hygroscopic particles [*Randriamiarisoa et al.*, 2006].

The hygroscopic growth factor $g(RH)$ presented in Eq. 2.16 is related to the enhancement factor of the optical properties $f_{\zeta}(RH)$ by means of the Mie theory. According to *Flores et al.* [2012], this relationship in the case of $\zeta = \sigma_e$, is expressed by the following equation:

$$f_{\zeta}(RH) = \frac{N(RH)Q_e(RH)}{N\left(RH_{dry}\right)Q_e\left(RH_{dry}\right)}\, g(RH)^2 \qquad \textit{Eq. 2.38}$$

where N(RH) is the particle concentration and Q_e is the extinction efficiency.

2.7 Lidar principle and lidar equation

Lidar (Light Detection And Ranging) is an active remote sensing technique, which has proven to be an essential tool to monitor the vertical structure, composition and dynamics of the Earth’s atmosphere. Lidar systems are laser-based and operate on principles similar to that of radar (radio detection and ranging) or sodar (sound navigation and ranging). Lidar technique is described in detail in [*Measures*, 1984; *Eichinger and Kovalev*, 2004; *Weitkamp*, 2005]. Some basics are provided in this section.

Lidar systems basically detect the radiation scattered by atmospheric constituents in the backward direction (Θ=180º), the so-called backscattered radiation, from a light pulse emitted into the atmosphere. The backscattered light is collected by a telescope and focused upon a photodetector that measures the amount of backscattered light as a function of distance from the lidar system. The relation $\Delta r = c\Delta t / 2$ is used to convert Δt from the emission of the laser pulse to the detection of the photon to the distance Δr of the scattering particle from the lidar system, applying the speed of light c.

In its simplest form, the detected lidar signal can be written as

$$P(z_n) = \frac{KO(z_n)}{{z_n}^2}\beta(z_n)T(z_n)^2 + P_B \qquad \textit{Eq. 2.39}$$

For lidar applications, usually the so-called range corrected signal (RCS) is defined as:

$$RCS(z_n) = \left(P(z_n) - P_B\right)\cdot {z_n}^2 \qquad \textit{Eq. 2.40}$$

In the lidar equation $P(z_n)$ is the received power from a distance z_n and P_B is the background noise. The first factor K is a system factor that summarizes the range-independent parameters of the lidar system, $O(z_n)/z_n^2$ is the geometric term which describes the range-dependent measurement geometry. These two factors are completely determined by the lidar setup and a priori they can be controlled by the experimentalist. The information on the atmosphere and thus all the measurable quantities, are contained in the atmospheric backscatter coefficient, $\beta(z_n)$ and the transmission term $T(z_n)$. They are both wavelength dependent, but this dependence will be omitted in this section for the sake of simplicity.

Going into more detail through the lidar equation, we can write the system factor as:

$$K = P_L \frac{c\tau}{2} A\eta \qquad \textit{Eq. 2.41}$$

where P_L is the average power of a single laser pulse, and τ is the temporal pulse length. A is the area of the receiver optics responsible for the collection of backscattered light, and η is the overall system efficiency. It includes efficiency of all optical elements and the detection efficiency. The telescope area A and the laser energy E_L, or, rather, the average laser power $\bar{P} = E_L f_{rep}$, with the pulse repetition frequency f_{rep}, are primary design parameters of a lidar system.

The geometry factor

$$G(z_n) = \frac{O(z_n)}{{z_n}^2} \qquad \textit{Eq. 2.42}$$

includes the overlap function $O(z_n)$, which describes the incomplete overlap between the laser beam and the receiver field of view, and the term z_n^{-2}. The quadratic decrease of the signal intensity with distance is due to the fact that the receiver telescope area is a part of a sphere's surface with radius R that encloses the scattering volume (see Figure 2.9).

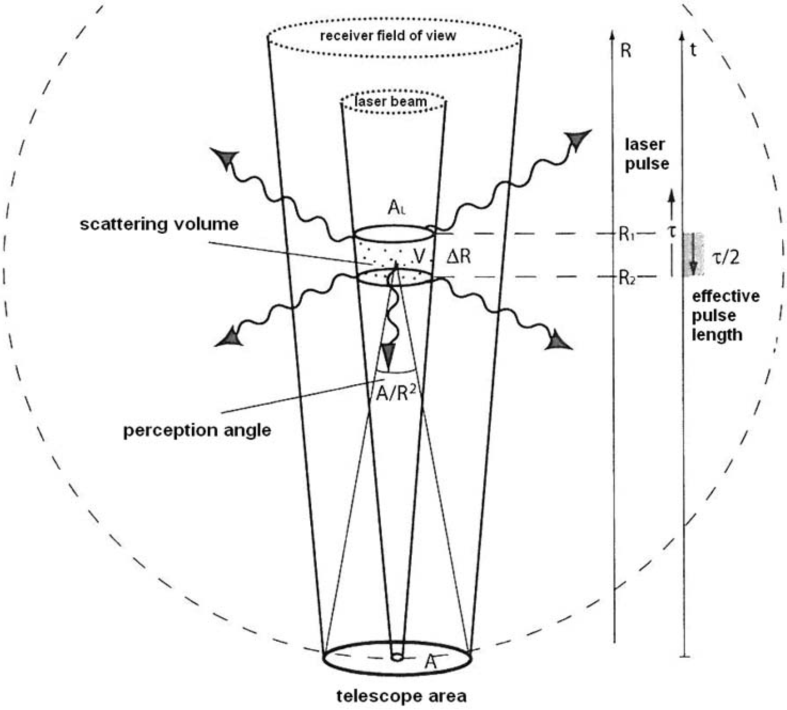

Figure 2.9. Illustration of the lidar geometry (from Weitkamp, 2005).

The atmospheric backscatter coefficient $\beta(z)$ is the primary atmospheric parameter that determines the strength of the lidar signal. It describes how much light is scattered into the backward direction, i.e., towards the lidar receiver. The backscatter coefficient is the specific value of the scattering coefficient for the scattering angle Θ = 180º. The atmospheric backscatter coefficient can then be written as

$$\beta(z_n) = \sum_j N_j(z_n) \frac{d\sigma_{j,sca}}{d\Omega}(\pi) \qquad \text{Eq. 2.43}$$

where N_j is the concentration of scattering particles of kind j in the volume illuminated by the laser pulse, and $d\sigma_{j,sca}(\pi,\lambda)/d\Omega$ the particles' differential scattering cross section for the backward direction at wavelength λ. Since the number concentration is given in units of m^{-3} and the differential scattering cross section in m^2sr^{-1}, the backscatter coefficient has the unit $m^{-1}sr^{-1}$.

The atmospheric transmittance $T(z)$ takes values between 0 and 1 and is given by

$$T(z_n)^2 = \exp\left[-2\int_0^{z_n} \alpha(r)dr\right] \qquad \textit{Eq. 2.44}$$

This term results from the specific form of the Lambert-Beer-Bouguer law for the lidar technique. The integral considers the path from the lidar to distance z_n and the factor 2 stands for the return way transmission path. The sum of all transmission losses is called light extinction, and $\alpha(z_n)$ is the lidar-retrieved extinction coefficient. It is defined similarly to the backscatter coefficient as the product of the number concentration and the extinction cross section $\sigma_{j,ext}$ for each type of scatterer j:

$$\alpha(z_n) = \sum_j N_j(z_n)\sigma_{j,ext} \qquad \textit{Eq. 2.45}$$

Summarizing the discussion of the individual terms, we can now rewrite the lidar equation (Eq. 2.37) in a more common form as

$$P(z_n) = P_0 \frac{c\tau}{2} A\eta \frac{O(z_n)}{z_n^{\ 2}} \beta(z) \exp\left[-2\int_0^{z_n} \alpha(r)dr\right] + P_B \qquad \textit{Eq. 2.46}$$

The solution of this equation is an under-determined problem with two unknown variables, the extinction and the backscatter coefficient.

Extinction can occur because of scattering and absorption of light by molecules and particles. Therefore, the extinction coefficient can be written as the sum of four components:

$$\alpha(z) = \alpha_{mol,s}(z) + \alpha_{mol,a}(z) + \alpha_{aer,s}(z) + \alpha_{aer,a}(z) \qquad \textit{Eq. 2.47}$$

where the subscripts *s* and *a* stand for scattering and absorption and the subscripts *mol* and *aer* stands for molecules and aerosol particles, respectively. Absorption of radiation by gases can be neglected at the emitted wavelengths of the lidar systems. On the other hand, laser light is scattered by air molecules and aerosol particles and therefore $\beta(z_n)$ can be written as

$$\beta(z_n) = \beta_{mol}(z_n) + \beta_{aer}(z_n) \qquad \textit{Eq. 2.48}$$

Molecular scattering is theoretically calculated from meteorological data. For this purpose, profiles of temperature and pressure are needed for the calculation of the molecular extinction and molecular backscattering (also referred to as Rayleigh extinction and Rayleigh backscattering). As previously mentioned, both $\beta(z_n)$ and $\alpha(z_n)$ depend on the wavelength of the laser light. The wavelength dependence is determined by the size, refractive index, and shape of the scatterer particles and it is usually expressed in terms of the backscatter- (or extinction-) related Angstöm exponent, β-AE(λ_1-λ_2) (or α-AE(λ_1-λ_2)).

2.8 Relation between aerosol optical and microphysical properties

In order to retrieve microphysical properties from lidar data, several methods based on a mathematical approach have already been used [*Müller et al.*, 1999; *Veselovskii et al.*, 2002; *Böckmann et al.*, 2005]. This approach is based on the Fredholm integral equation of the first kind. This equation mathematically expresses the relationship between optical data and the microphysical quantities previously described:

$$g_i(\lambda) = \int_{r_{\min}}^{r_{\max}} K_i(r, m, \lambda, s) v_c(r) dr + \varepsilon_i^{\exp}(\lambda) \qquad \textit{Eq. 2.49}$$

The term $g_i(\lambda)$ denotes the optical data at wavelengths λ at a specific height z_n. For the sake of simplicity, references to height z_n will be omitted in this subsection. The subscript i indicates the kind of information, being usually the aerosol backscatter (β_{aer}) or extinction (α_{aer}) coefficients in the case of lidar data. The subscript k may be any natural number. The expression $\varepsilon_i^{exp}(\lambda)$ is the error term. The terms denoted as $K_i(r,m,\lambda,s)$ are referred to the kernel efficiencies for the data corresponding to the subscript i, respectively. They depend on the radius r of the particles, their complex refractive index m, the wavelength λ of the interacting light, as well as the shape s of the particles. For spherical particle geometry, the kernel functions $K_i(r,m,\lambda,s)$ are calculated from the respective extinction and backscatter efficiencies $Q_i(r,m,\lambda)$ for individual particles:

$$K_i(r,m,\lambda) = \frac{3}{4r} Q_i(r,m,\lambda) \qquad \textit{Eq. 2.50}$$

Eq. 2.41 Eq. 2.49 can be more easily expressed as:

$$g_p = \int_{r_{\min}}^{r_{\max}} K_p(r,m) v(r) dr + \varepsilon_p^{\exp} \qquad \textit{Eq. 2.51}$$

with the subscript $p = (i, \lambda)$ summarizing the kind and wavelength of optical data. This equation cannot be solved analytically [*Twomey*, 1977]. The numerical solution process leads to the so-called ill-posed inverse problem [*Böckmann*, 2001], characterized by the incompleteness of the available information, the non-uniqueness of the solutions, and the non-continuous dependence of the solutions on the input data. The instability of the solutions can only be controlled by introducing meaningful boundary conditions.

The retrieval of microphysical properties based on this approach has already proved to be quite robust [*Müller et al.*, 1999; *Böckmann*, 2001; *Navas-Guzmán et al.*, 2013; *Veselovskii et al.*, 2013]. However it presents still some major drawbacks related to the fact that is an ill-posed problem. These drawbacks are especially important in the case of non-spherical particles. Different approach using complementary information, as the one used in LIRIC, may provide additional information.

3 Experimental site and instrumentation

3.1 Granada station

The station of the Atmospheric Physics Group (GFAT) is located in the Andalusian Center for Enviromental Studies (Centro Andaluz de Medio Ambiente, CEAMA) at Granada, Spain (3.61ºW, 37.16º N, 680 m a.s.l.). Most of the measurements presented in this thesis were registered at this site. Granada, located in South-eastern Spain, is a non-industrialized medium-sized city with a population of 300000 inhabitants that increases up to 600000 if the whole metropolitan area is considered. The city is situated in a natural basin surrounded by mountains with elevations between 1000 and 3500 m a.s.l. The near-continental conditions prevailing at this site are responsible for large seasonal temperature differences, providing cool winters and hot summers. The area also experiences periods of low humidity regimes especially in summer. The study area is also at a short distance, about 200 km away, from the African continent and approximately 50 km away from the western Mediterranean basin.

Due to its location in the Mediterranean basin, Granada is influenced by two major aerosol source regions: Europe as a major source of anthropogenic pollution and North Africa as a principal source of natural dust. Furthermore, the Mediterranean area is characterized by a complex meteorology that favours the aging of polluted air masses in the basin and induces high level of airborne particles. Thus, the Mediterranean basin can represent an additional source of atmospheric aerosol for the study area. In summer, the study area is isolated from travelling lows and associated frontal systems, and the intensification of the Azorean high during the warm season induces a very weak pressure gradient and strong subsidence that reduces entrainment from the free troposphere. High temperatures and low humidity in summer induce numerous forest fires in the Iberian Peninsula, whose smoke represents an additional source of atmospheric aerosol to our study area [*Alados-Arboledas et al.*, 2011].

3.2 Lidar system

A detailed description of the Raman-lidar MULHACEN LR331D400 (Raymetrics S.A.) is provided in [*Navas-Guzmán*, 2012]. The main characteristics are presented in Table 3.1.

MULHACEN (Figure 3.1) is a Raman lidar with capabilities for profiling the atmospheric aerosol and the water vapor, operating at the station since November 2004. It is configured in a monostatic biaxial alignment pointing vertically to the zenith. The transmission system consists of a pulsed Nd:YAG with fundamental emission at 1064 nm. Additional emissions at 532 and 355 nm are obtained from second and third harmonic generators. The backscattered signal is collected by a 40cm-diameter Cassegrain telescope and split into seven spectral channels using dichroic mirrors, interference filters and a polarizing beamsplitter cube. The detection and spectral selection is performed at four channels corresponding to elastic wavelengths at 1064, 532 (parallel-polarized and perpendicular-polarized) and 355 nm, and three additional channels for the Raman signals at 607 nm (N_2 Raman-shifted signal from 532 nm), 408 nm (water vapor Raman-shifted signal from 355 nm) and 387 nm (N_2 Raman-shifted signal from 355 nm). The instrument is operating with a vertical spatial resolution of 7.5 m. Due to the instrument setup, the incomplete overlap limits the lowest possible detection height at 500 m above the system [*Navas-Guzmán et al.*, 2011]. The Raman lidar was incorporated to EARLINET (European Aerosol Research Lidar NETwork, www.earlinet.org) [*Bösenberg*, 2001] in April 2005. It has taken part of the EARLINET-ASOS (European Aerosol Research Lidar Network - Advanced Sustainable Observation System) project and is currently involved in the European Project ACTRIS (Aerosols, Clouds, and Trace gases Research InfraStructure Network, www.actris.net).

Emitter	
Pulsed laser source (Class IV laser)	Nd:YAG (Quantel CFR Series)
Wavelengh	355, 532 and 1064 nm
Energy/pulse	60, 65, 110 mJ
Pulse duration	8 ns
Repetition rate	1, 2, 5 and 10 Hz
Laser beam diameter	6 mm
Laser beam divergence	<0.1 mrad
Receiver Optics	
Telescope	Cassegrain
Primary mirror diameter (mm)	400
Secondary mirror diameter (mm)	90
Focal length (mm)	3998
Telescope-laser axes distance (mm)	320
Detection Unit	
Transient Recorder	LICEL
Detectors	APD (at 1064 nm), PMT (other channels)
Wavelength Separation Unit	Dichroic mirrors, interferencial filtres and polarization cube
Detection mode	Analog and photon counting
Wavelengths (nm)	355, 387, 408, 532p, 532s, 607, 1064
Full Width at Half Maximum (nm)	1.0, 2.7, 1.0, 0.5, 0.5, 2.7, 1.0
1064 nm	Analog acquisition mode. 12 Bit-20 MHz
532, 355 nm	Analog aquisition mode: 12 Bit-20 MHz Photon-counting acquisition mode: 250 MHz
387, 408, 607 nm	Photon-counting acquisition mode: 250 MHz
Nominal spatial resolution	7.5 m

Table 3.1. Technical characteristics of the Granada lidar system.

Figure 3.1. Raman lidar system operated at Granada station.

3.3 CIMEL sun photometer

Column-integrated atmospheric aerosol properties during daytime have been obtained by means of a sun photometer CE-318-4 included in the AERONET (Aerosol Robotic Network, http://aeronet.gsfc.nasa.gov/). A complete description of the instrument can be found in Holben *et al*. [1998]. However, a brief description will be given in this section. Details are provided in Table 3.2.

The design of the sun photometer CIMEL CE318-4 consists of an optical head with two collimators, a robotic arm for sun tracking and sky positioning and an electronic box (http://www.cimel.fr). Figure 3.2 shows the CIMEL CE318-4.

Figure 3.2. Cimel CE 318-4 located at Granada experimental site.

The automatic tracking sun and sky scanning radiometer performs direct sun measurements with a 1.2° full field of view every 15 min at 340, 380, 440, 500, 675, 870, 940, and 1020 nm (nominal wavelengths). The direct Sun measurements take ~8 s to scan all 8 wavelengths (repeated three times within a minute), with a motor driven filter wheel positioning each filter in front of the detector. These solar extinction measurements are used to compute the aerosol optical depth (τ_λ) at each wavelength except for the 940 nm channel, which is used to retrieve total column water vapour (or precipitable water) in cm. The filters utilized in this instrument are ion-assisted deposition interference filters with band pass (FWHM) of 10 nm, except for the 340 and 380 nm channels at 2 nm. The estimated uncertainty in the computed τ_λ, due primarily to calibration uncertainty, is around 0.010–0.021 for field instruments (which is spectrally dependent, with the larger errors in the UV) [*Eck et al.,* 1999]. The spectral τ_λ data are screened for clouds following the methodology of Smirnov *et al.* [2000]. The sky radiances measured by the sun/sky radiometers are calibrated versus frequently characterized integrating spheres at the NASA Goddard Space Flight Center, to an absolute accuracy of ~5% or better [*Holben et al.*, 1998]. For the case of the sun photometer at Granada station, the calibration is performed through RIMA (Red Ibérica de Medida fotométrica de Aerosoles, www.rima.uva.es) network, federated to AERONET.

Radiometer CIMEL CE 318-4	
Sun photometer model	*CE 318-4*
Detector	Si Fotodiodes
Number of filters/wavelengths	8/1020-936-870-675-500-440--380-340 nm
FWHM	10-10-10-10-10-4-2 nm
Numbers of collimators	2
FOV/Aperture	1.2°
For a precise tracking on the sun	4-quadrant position detector Accuracy of 0.05
Measurement types	Direct Almucantar Principal plane
Applications	Atmospheric aerosol Water vapor
Motoring system	Motor step-by-step azimuthal y zenith
Batteries	Internal battery in electronic box External battery for both motor Solar panel or 220 VAC

Table 3.2. Characteristic of the sun photometer CE-318-4

3.4 Radiosoundings

Radiosounding data for the measurement of relative humidity profiles used in the analysis of hygroscopic properties were obtained with lightweight weather radiosondes (DFM-06, GRAW Radiosondes). The main features of the radiosonde are provided in Table 3.3. The DFM-06 is designed to provide temperature (resolution 0.01 ºC, accuracy 0.2 ºC), pressure (resolution 0.1 hPa, accuracy 0.5 hPa), humidity (resolution 1%, accuracy 2%) and wind speed and direction (resolution 0.1 m/s, accuracy 0.2 m/s) profiles from the surface up to 40 km altitude. Continuous datasets are sent to the ground station by a high quality radio-telemetry link. All the sensors are completely calibrated. They provide precise data during the ascent and are unaffected by thermal variations or errors due to solar radiation. The use of ceramic sensors allows for a rapid reaction time. Pressure measurements are calculated by means of the temperature and relative humidity profiles together with the GPS height and the ground pressure, reducing the weight of the radiosonde. Data acquisition and processing were performed by Grawmet5 software and a GS-E ground station from the same manufacturer. The ground station receives the information and provides local GPS information. The main features of the software are the initialization of the radiosonde and the evaluation and real-time display of the radiosounding data.

Figure 3.3. GRAWMET software with radiosonde and ground station.

Radiosonde DFM-09	
Weight	*<90 gr*
Size	94 mm x 94mm x 60mm
Battery	Dry Lithium
Activation	Switch
Wind finding	Differential GPS (20 channels)
Bandwidth	< 20 kHz
Frequency deviation	+/- 5kHz
Modulation	FSK
Error correction	Code-spreading, interleaving
Temperature resolution	0.1 ºC
Temperature accuracy	< 0.2ºC
Humidity resolution	1%
Humidity accuracy	< 5%
Pressure accuracy	< 1hPa
Geopotential height accuracy	< 20 m
Wind speed accuracy	< 0.2 m/s
Accuracy horizontal position	< 5 m

Table 3.3. Characteristic of the DRM-09 GRAW radiosonde.

3.5 Modelling tools

3.5.1 HYSPLIT model

The analysis of backwards trajectories performed in this thesis was performed by means of the HYSPLIT model (HYbrid Single-Particle Lagrangian Integrated Trayectory) [*Draxler and Rolph*, 2003] developed by the (National Oceanographic and Atmospheric Administration) in collaboration with the Australia's Bureau of Meteorology. HYSPLIT model can also be used for the analysis of complex dispersion and deposition simulations of pollutants and hazardous material. In addition, it provides meteorological data and allows for the tracking and forecasting of different aerosol types, such as volcanic ash. The model can be run interactively on the web through the READY system (www.arl.noaa.gov/HYSPLIT) or the code executable and the input meteorological data can be downloaded to a computer. This model combines a Langrangian approximation for resolving air mass transport with an Eulerian approximation for the diffusion of pollutants.

In this thesis, 5-day backwards trajectories of air masses arriving at the experimental site at different height levels depending on the region of interest were computed using HYSPLIT_v4 model including vertical wind information. The Global Data Assimilation System (GDAS) database was used as input meteorological database for the computations. An example is shown in Figure 3.4.

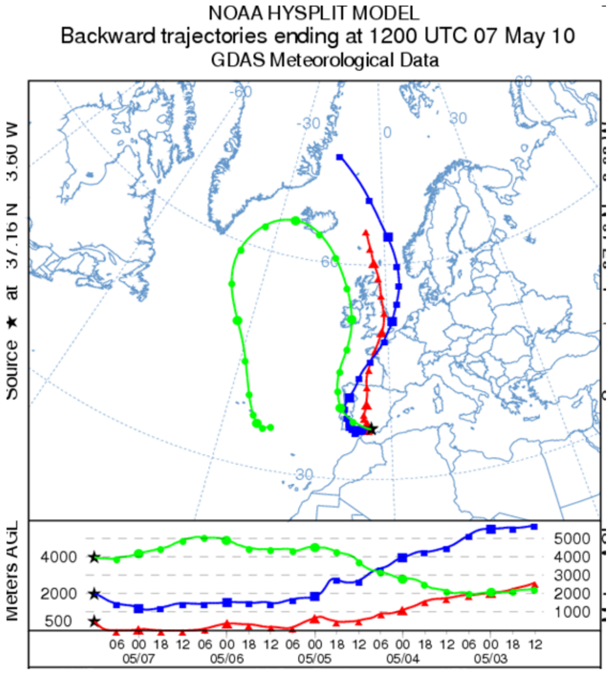

Figure 3.4. Example of 5-day backwards trajectories arriving at Granada station retrieved with HYSPLIT Model using GDAS database.

3.5.2 NAAPS model

The NAAPS (Navy Aerosol Analysis and Prediction System) [*Christensen*, 1997] model developed by the Marine Meteorology Division, Naval Research Laboratory (NRL, http://www.nrlmry.navy.mil/aerosol.html) is a multi-component aerosol analysis and modelling capability that combines satellite data streams with other available data (e. g. AERONET data, surface synoptic reports of visibility and current and past weather) and the global aerosol simulation and prediction. The model presents the advantage that is operated in near-real time with global coverage providing 120-hour forecasts. The final products of the model used in this thesis are the NAAPS Archive regional plots for Europe. These plots provide values of τ_{550nm} for mineral dust, sulphates and smoke (upper left panel of the plot). In addition, plots of the surface concentration in µg/m^3 for different aerosol types are provided, i. e. sulphates (upper right panel), dust (lower left panel) and smoke (lower right panel). Output plots are provided with a temporal resolution of 6 hours (at 00, 06, 12 and 18 UTC) and the archived data are available since March of 2000. An example is shown in Figure 3.5.

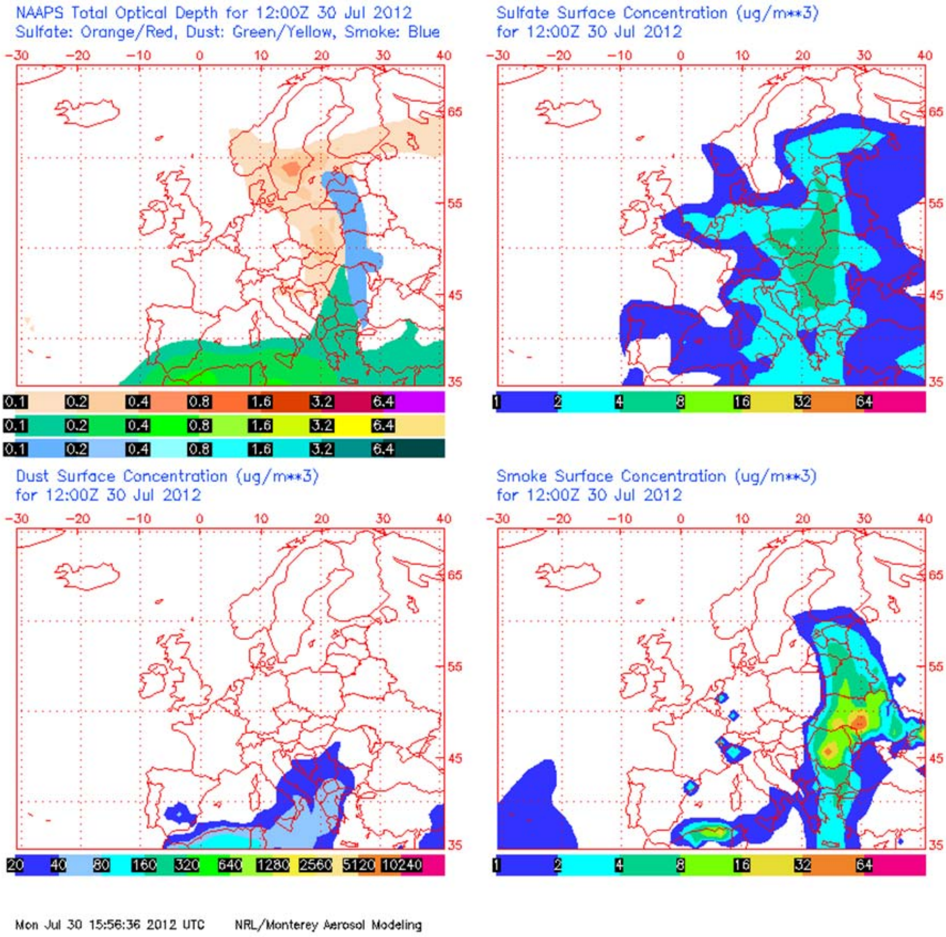

Figure 3.5 Example of NAAPS forecast model output for the European region.

3.5.3 BSC-DREAM8b model

The Dust Regional Atmospheric Model (DREAM, http://www.bsc.es/projects/earthscience/BSC-DREAM/) [*Nickovic et al.*, 2001] is an atmospheric dust forecast system operated by the Earth Sciences Divison of the

Barcelona Supercomputing Center (BSC). Currently, this BSC-DREAM dust model provides the products of an updated version of the former Dust Regional Atmospheric Model called BSC-DREAM8b [*Pérez et al.*, 2006a; *Pérez et al.*, 2006b; *Basart et al.*, 2012]. The model predicts the atmospheric life cycle of the eroded desert dust based on the solution to the Euler-type partial differential non-linear equation for dust mass continuity. Most of the different features affecting mineral dust are included in the model, such as the dust production scheme with introduced viscous sub-layer, the soil wetness effects on dust production, dry deposition and below cloud scavenging. In addition, eight size transport bins between 0.1 and 10 µm range are considered. Within each transport bin, dust is assumed to have time-invariant, sub-bin log-normal distribution employing the transport mode with mass median diameter of 2.524 µm.

The simulated dust distributions consist of daily runs in 24-hour daily forecasts. The meteorological fields are initialized every 24h (at 00 UTC) and boundary conditions are updated every 6h with the FNL/NCEP (Final Analysis/National Centers for Environmental Prediction) (1° x 1°). The resolution is set to 1/3° in the horizontal and to 24 layers extending up to approximately 15 km in the vertical. The output data presented in this thesis consists on the maps of mineral dust load in g/m^3 above North-Africa, Middle East and Europe (Figure 3.6) and the vertical profiles of mineral dust mass concentration above Granada experimental site. For the calculation of the profiles a temporal resolution of 1-hour was specifically used for the analysis in this thesis. Dust densities of 2.5 g/m^3 and 2.65 g/m^3 were assumed for the fine ($r < 1 \mu m$) and coarse modes ($r \in (1\mu m$ - $10\ \mu m]$) respectively [*Pérez et al.,* 2006a, *Basart et al.,* 2013, personal communication].

In addition, values of τ_{550nm} also provided by the model were used in this work. These values are calculated according to the equation:

$$\tau_{550nm} = \sum_{k=1}^{8} \tau_{550nm,k} = \sum_{k=1}^{8} \frac{3}{4\rho_k r_k} M Q_{e,550nm,k}$$

where k indicates the size bin, ρ_k is the mass density, r_k is the effective radius, M is the dust mass loading and $Q_{e,550nm,k}$ is the extinction efficiency factor at 550 nm obtained according to Mie theory.

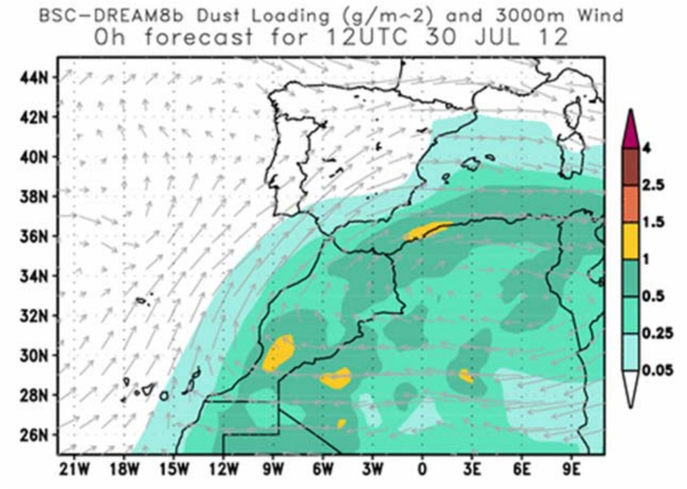

Figure 3.6. Example of BSC-DREAM8b output map of mineral dust load in g/m³ above Spain and North Africa.

4 Methodology

4.1 Lidar inversion algorithms

Lidar inversion algorithms are the techniques used to retrieve the aerosol backscatter and extinction coefficients from lidar signals. In this section, the two main inversion algorithms for retrieving optical properties are briefly described.

4.1.1 Elastic lidar technique

The algorithm used for the retrieval of elastic backscatter signals is based on the radar technology [*Hitschfeld and Bordan*, 1954]. Firstly, an analytical solution of the lidar equation for elastic signals was proposed by *Fernald et al.*, [1972]. Later on, *Klett* [1981] introduced an improved technique, which led to a more general solution proposed by *Fernald*, [1984]. The technique described here is usually referred as Klett-Fernald method and a detailed description is presented in [*Ansmann and Müller*, 2005]. Basic assumptions and the solution derivation are presented in this section.

As previously explained, the molecular terms in the lidar equation (Eq. 2.46) can be calculated using standard atmosphere conditions or an atmospheric profile from radiosondes launched nearby. Therefore, $\beta_{aer}(z_n,\lambda)$ and $\alpha_{aer}(z_n,\lambda)$ remain as the two height-dependent unknowns in the lidar equation. To solve this problem a relationship between aerosol backscatter and extinction coefficients is assumed. This is the extinction-to-backscatter ratio or lidar ratio (*LR*) of particles:

$$LR_{aer}(z_n) = \frac{\alpha_{aer}(z_n)}{\beta_{aer}(z_n)} \qquad \text{Eq. 4.1}$$

Under this assumption, the equation for $\beta_{aer}(z_n)$ can be solved following the Klett-Fernald algorithm [*Fernald et al.*, 1972; *Klett*, 1981; *Fernald*, 1984] as folows:

$$\beta_{aer}(z_n)+\beta_{mol}(z_n)=\frac{RCS(z_n)\exp\left\{-2\int_{z_0}^{z_n}\left[LR_{aer}(r)-LR_{mol}\right]\beta_{mol}(r)dr\right\}}{\dfrac{RCS(z_0)}{\beta_{aer}(z_0)+\beta_{mol}(z_0)}-2\int_{z_0}^{z_n}LR_{aer}(r)RCS(r)T_E(r,z_0)dr} \qquad \text{Eq. 4.2}$$

with

$$T_E(r,z_0)=\exp\left\{-2\int_{z_0}^{r}\left[LR_{aer}(r')-LR_{mol}\right]\beta_{mol}(r')dr'\right\} \qquad \text{Eq. 4.3}$$

where $LR_{mol}=\alpha_{mol}(z_n,\lambda)/\beta_{mol}(z_n,\lambda)=8\pi/3\ sr$.

To determine $\beta_{aer}(z_n)$ and additional assumption is needed. The aerosol backscatter coefficient has to be estimated at a specific reference height z_0 ($\beta_{aer}(z_0)$). This reference height is usually chosen such that at z_0 the aerosol backscatter coefficient is negligible compared to the known molecular backscatter value. Such clear air conditions are normally given in the upper troposphere.

4.1.2 Inelastic or Raman lidar technique

The inelastic lidar technique or Raman lidar technique is based on the Raman scattering described in section 2.4. This technique has been successfully used in lidar remote sensing techniques since the late 1960s [*Cooney*, 1972; *Melfi*, 1972]. In a Raman lidar, due to the Raman scattering, the wavelength λ_{Ra} of the scattered light is shifted with respect to emitted laser wavelength λ_0, and such a shift depends on the scatterer molecule. For detection of the Raman scattering of a gas with known atmospheric density, such as nitrogen or oxygen, the backscatter coefficient in the Raman lidar equation is known, and only the aerosol extinction and its wavelength dependence remain as unknowns [*Ansmann et al.*, 1990].

The Raman lidar equation can be written as:

$$P(z_n,\lambda_{Ra}) = K_{Ra}\frac{O_{Ra}(z_n,\lambda)}{z_n^{2}}\beta_{Ra}(z_n,\lambda)\exp\left\{-\int_0^{z_n}\left[\alpha(r,\lambda_0)+\alpha(r,\lambda_{Ra})\right]dr\right\} \qquad \textit{Eq. 4.4}$$

where $P(z_n, \lambda_{Ra})$ is the power received from distance z at Raman wavelength λ_{Ra}, K_{Ra} is a function that depends on all the range-independent system parameters, $\beta_{Ra}(\lambda, z_n) = N(z_n)\sigma_{Ra}(\lambda)$ is the Raman backscatter coefficient, where $N(z_n)$ is the atmospheric number density of the Raman scatterer and $\sigma_{Ra}(\lambda)$ is the Raman backscatter cross section, α is the range-dependent total volume extinction coefficient at wavelengths λ_0 and λ_{Ra}, and r is the range integration variable.

Assuming a wavelength dependence of the aerosol extinction $\alpha_{aer} \propto \lambda^{-k}$, the Raman lidar equation can be solved for aerosol extinction at the emitted laser wavelength as [*Ansmann et al.*, 1990]:

$$\alpha_{aer}(z_n,\lambda_0) = \frac{\dfrac{d}{dz_n}\ln\dfrac{N_{Ra}(z_n)}{RCS(z_n,\lambda_{Ra})} - \alpha_{mol}(z_n,\lambda_0) - \alpha_{mol}(z_n,\lambda_{Ra})}{1+\left(\dfrac{\lambda_0}{\lambda_{Ra}}\right)^{k}} \qquad \textit{Eq. 4.5}$$

where $d\sigma_{Ra}(\lambda)/dz = 0$ has been used. Molecular extinction can be calculated from Rayleigh scattering coefficients and atmospheric number density profiles retrieved from models or radiosonde measurements. From the detection of Raman scattered light, independent aerosol extinction profiles can be determined.

The aerosol backscatter coefficient $\beta_{aer}(z_n,\lambda_0)$ at the emitted wavelength λ_0 can then be obtained now from the ratio of the received elastically backscattered signal $P(z_n, \lambda_0)$ (Eq. 2.39) and the Raman signal $P(z_n, \lambda_{Ra})$ (Eq. 4.5) [*Ansmann et al.*, 1992b].

$$\begin{aligned}\beta_{aer}(z_n,\lambda) = {} & \left[\beta_{aer}(z_0,\lambda)+\beta_{mol}(z_0,\lambda)\right] \\ & \times \frac{P(z_0,\lambda_{Ra})P(z_n,\lambda)}{P(z_0,\lambda\ )P(z_n,\lambda_{Ra})}\frac{N_{Ra}(z_n)}{N_{Ra}(z_0)} \\ & \times \frac{\exp\left\{-\int_{z_0}^{z_n}\left[\alpha_{aer}(r,\lambda_{Ra})+\alpha_{mol}(r,\lambda_{Ra})\right]dr\right\}}{\exp\left\{-\int_{z_0}^{z_n}\left[\alpha_{aer}(r,\lambda)+\alpha(r,\lambda)\right]dr\right\}} - \beta_{mol}(z_n,\lambda)\end{aligned} \qquad \textit{Eq. 4.6}$$

Similarly to the elastic method, a reference value $\beta_{aer}(z_0, \lambda)$ is needed in order to solve Eq. 4.6. As in the Klett-Fernald retrieval, the reference height z_0 is typically set in a region with clear air or at a height where $\beta_{aer}(z_0, \lambda)$ is known.

With all the previous information, the aerosol backscatter can be derived without any assumption about the *LR*, which is an important parameter since it is directly related to the microphysical properties of the particles.

The uncertainties in the optical properties from elastic and inelastic inversions are determined by means of a numerical procedure based on the Monte Carlo technique, commonly used in the EARLINET network (European Aerosol Research Lidar Network). This procedure is based on the random extraction of new lidar signals, each bin of which is considered a sample element of a given probability distribution with the experimentally observed mean value and standard deviation. The extracted lidar signals are then processed with the same algorithm to produce a set of solutions from which the standard deviation is calculated as a function of height [*Ansmann et al.*, 1992a; *Pappalardo et al.*, 2004; *Guerrero Rascado*, 2008].

4.1.3 Depolarization measurements with lidar technique

Depolarization caused by molecules and particles can be detected by lidar systems, since they emit almost-perfect polarized light. The depolarization measurement with the lidar technique can provide useful information for the characterization of the atmospheric aerosol and can be used as input in the microphysical retrieval.

In order to quantify the depolarization capability of the atmospheric aerosol, different parameters has been defined in scientific literature [*Cairo et al.,* 1999] One of the most used is the volume linear depolarization ratio (δ^{v}), defined as the ratio between the perpendicular (⊥) and parallel (||) backscatter coefficient produced by a linear-polarized incident radiation. Low δ^{v} values are related to spherical shape whereas high δ^{v} values are related to non-spherical shapes. In order to distinguish between the depolarization caused by molecules and that caused by aerosol particles, the particle linear depolarization ratio is defined as:

$$\delta^{p}_{532nm} = \frac{\beta^{\perp}_{aer}}{\beta^{\parallel}_{aer}} \qquad \text{Eq. 4.7}$$

This parameter is used in the analysis of the results throughout this thesis and a detailed description on its retrieval and calibration can be found in *Bravo-Aranda et al.,* [2013] and *Freudenthaler et al.,* [2009].

4.2 Retrieval of microphysical properties from sun photometer measurements

Sun photometers provide column integrated information about atmospheric aerosol particles. From a very simple point of view, sun photometers are based on the principle that the incoming radiation is attenuated by atmospheric components and this attenuation is dependent on the load of aerosol particles in the atmosphere. A cloud-screening algorithm is applied to the data in order to avoid contamination by the presence of clouds. For this purpose, the triplet measurement, the smoothness and the three standard deviation criteria are applied [*Smirnov et al.*, 2000]. The triplet measurement is based on the variability of the optical depth, using the difference of τ_λ between two consecutive measurements as a criterion determining the clear-sky conditions. Strong variations within a short time period indicate the presence of clouds. The smoothness criterion is based on limiting the root mean square of τ_λ second derivative with time. Finally, the three standard deviation criterion rejects those data which fall outside three standard deviations of taken over the whole day.

The retrieval of τ_λ is done from the direct sun measurements. the τ_λ and the related AE can be retrieved based on the Beer-Bouguer-Lambert law, used in the following form [*Holben et al.*, 1998]

$$V(\lambda) = V_o(\lambda)\exp(-m_o\tau_{e,\lambda}) \qquad \text{Eq. 4.8}$$

where $V(\lambda)$ is the signal measured by the sun photometer, $V_o(\lambda)$ is the calibration constant and m_o is the relative optical air mass associated with the different extinction processes affecting the wavelengths used. By means of the term m_o the effects of aerosols, Rayleigh scattering, O_3 and NO_2 on the total extinction are accounted. $\tau_{e,\lambda}$ is the total atmospheric optical depth. Using Eq. 4.8, $\tau_{e,\lambda}$ is derived from direct sun photometer measurements using the appropriate calibration constants provided by the Aerosol Robotic Network AERONET (linear rate change in time is assumed for calibration constants). Therefore, the spectral aerosol optical depth, τ_λ, is obtained by subtracting the Rayleigh optical depth as well as the optical depths for O_3 and NO_2, which can be theoretically calculated. The uncertainty values for each wavelength are different, depending on the processes involved. For AERONET retrieved data, the total uncertainty in τ_λ is ± 0.01 for $\lambda > 440$ nm and ±0.02 for shorter wavelengths.

Besides the optical properties, the sun photometer sky radiance observations are used to retrieve microphysical aerosol properties. In order to perform these retrievals, it is necessary to perform the measurement in the principal plane and almucantar configuration in order to get a wide range of scattering angles. In the almucantar configuration, the sun photometers keep the zenith angle constant (equal to the solar zenith angle θ_s) and varies the azimuth angle, relative to the sun, from 6º to 180º. In the principal plane configuration, the azimuth angle is the one that remains constant (and equal to the solar azimuth) and the instrument takes the sky radiance measurements from the different zenith angles (Figure 4.1). From these measurements at 440, 675, 870, and 1020 nm (nominal wavelengths) together with the direct sun measured τ_λ at these same wavelengths aerosol microphysical properties are retrieved. For the retrieval of microphysical properties, the inversion algorithm from AERONET Version 2 is applied to the sun photometer sky radiance data in this study. The inversion algorithm was firstly developed by [*Dubovik and King*, 2000] and improved in [*Dubovik et al.*, 2002; *Dubovik et al.*, 2006] with the introduction of a non-spherical aerosol retrieval method, employing scattering by spheroids.

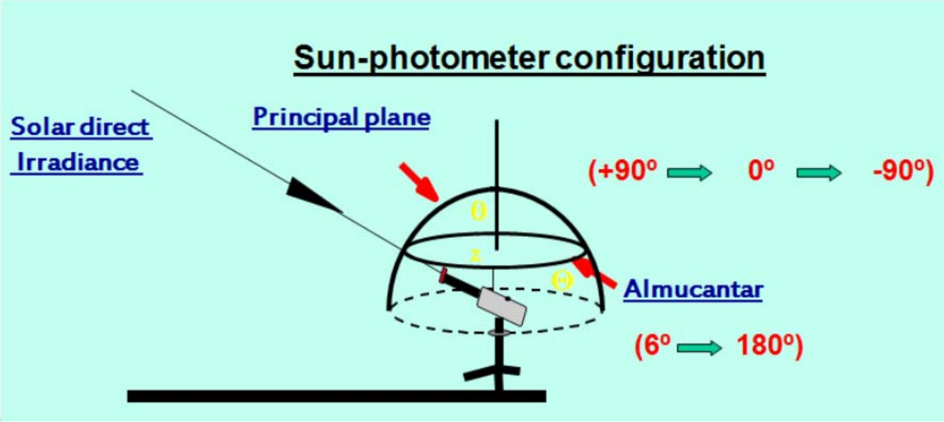

Figure 4.1. Figure describing the two geometries used for the measurements of the sky radiances (almucantar and principal plane) and solar direct irradiance configuration.

The inversion scheme applied by AERONET and its results have been tested under many different atmospheric aerosol conditions along worldwide locations, [e. g. *Dubovik et al.*, 2006]. This approach allows for retrievals and proper modeling of most optically distinct mixtures of coarse mode aerosols, and the diverse applications also demonstrated that the spheroid kernel look-up tables computed can be a useful tool for various remote sensing applications [e. g. *Dubovik et al.,* 2006]. As previously stated, the algorithm retrieves microphysical properties such as the aerosol size distribution, complex refractive index and other aerosol optical and microphysical parameters, from the almucantar spectral sky radiance distributions as measured from the ground-based sun photometers. This operational inversion algorithm significantly improved the performance of the aerosol optical properties retrievals for desert dust observations and other aerosol mixtures. Furthermore, aerosol scattering at large angles 100-140º is highly affected by the particle shape, and the difference between non-spherical and spherical scattering is near maximum at an angle of 120º. The results show that the use of spheres in modeling causes considerably larger sky-radiance errors and the effect is particularly pronounced at the top of atmosphere (TOA).

Although the inversion algorithm source code is not publicly available, further information about the development on the algorithm and a more detailed description are provided in [*Dubovik and King*, 2000; *Dubovik et al.*, 2002; *Dubovik et al.*, 2006; *Sinyuk et al.*, 2007]. For the inversion, the aerosol is modeled as an ensemble of spherical and non-spherical components, assuming a complex refractive index equal for all particle sizes [*AERONET-Homepage*, 2011b]. For the spherical part, polydisperse, homogeneous spheres are used whereas the non-spherical part is modeled by a mixture of polydisperse, randomly-oriented homogeneous spheroids [*Mishchenko et al.*, 1997]. In addition, the spheroid aspect ratio distribution is fixed to the one retrieved by *Dubovik et al.*, [2006] and fitted to the scattering matrix of mineral dust measured in laboratory by *Volten et al.*, [2001]. Additional assumptions are the vertically homogeneous distribution of the aerosol in a plane parallel atmosphere and the surface reflectance which is approximated by a bidirectional reflectance distribution function. The retrieved volume particle size distribution covers the range of radii from 0.05 up to 15 µm in 22 logarithmically equidistant bins. The percentage of spherical particles as well as the real and imaginary part of the complex refractive index are also provided, the latter ones for the different measurement wavelengths. The size distribution can be separated in fine mode and coarse mode particles. This is done by finding the minimum of the bimodal distribution between 0.439 and 0.992 µm. With the inversion algorithm, all microphysical properties as well as the $\tau_{aer,\lambda}$ are calculated not only for the total content of aerosol but also for fine-mode and coarse-mode particles separately. Besides the mentioned complex refractive index, the effective radius, the volume mean radius, the standard deviation and the volume concentrations are given. A simplified scheme of the inversion algorithm is presented in Figure 4.2.

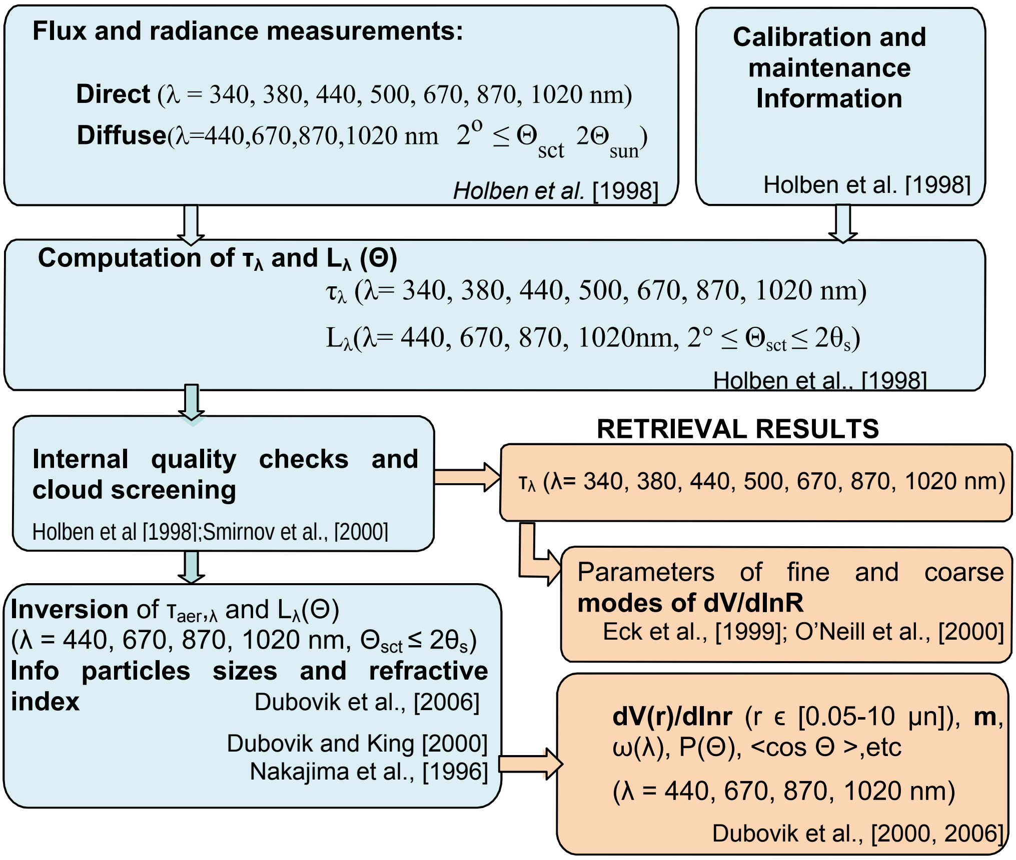

Figure 4.2. Simplified scheme of AERONET inversion retrieval procedure adapted from Dubovik et al., 2003. Flux and radiance measurements are used for the computation of τ_λ and L_λ (Θ). After quality check and cloud screening the inversion procedure based in Nakajima et al., [1996], Smirnov et al [2002] and adapted by Dubovik and King [2000] and Dubovik et al., [2006] for the spheroid aerosol model is applied to the almucantar sky radiance distributions and the retrieval results provide optical and microphysical data.

The retrieval of the particle volume size distribution was demonstrated to be adequate in practically all situations [e. g., $\tau_{400nm,} \geq 0.05$], as demonstrated by *Dubovik et al.* [2000]. According to the studies referenced in Figure 4.2, the error of the retrieved volume density $dV(r)/d \ln r$ changes as a nonlinear function of particle size, aerosol type and actual values of the size distribution. In particular, for the particle size range $0.1 \leq r \leq 7$ μm, the retrieval errors do not exceed 10% in the maxima of the size distribution and may increase up to about 35% for the points corresponding to the minimum values of $dV(r)/d\ \ln r$ in this size range. For $0.05 \le r \le 0.1$ µm and $7 < r \le 15$ µm, the accuracy of the size distribution retrieval drops significantly, because of the low sensitivity of the aerosol scattering at 440, 675, 870 and 1020 nm to particles of these sizes. Correspondingly, the retrieval errors rise up to 80%–100% (and even higher) for the sizes less than 0.1 µm and higher than 7 µm. The high errors at the edges do not significantly affect the derivation of the main features of the particle size distribution (concentration, median and effective radii, etc.) because the aerosol particle size distributions $[dV(r)/d\ \ln r]$ typically have low values at the edges of retrieval size interval. The accuracy levels drop down to 0.05–0.07 for the single scattering albedo, to 80%–100% for the imaginary part of the refractive index, and to 0.05 for the real part of the refractive index.

4.3 Microphysical properties profiles: Lidar-Radiometer Inversion Code (LIRIC)

Currently, the combination of lidar with sun photometer data in order to derive vertically resolved microphysical properties is being highly exploded within the European project ACTRIS (Aerosol, Clouds and Trace gases Research InfraStructure Network, www.actris.net). The Lidar Radiometer Inversion Code (LIRIC), developed in the Institute of Physics of Minsk (Belarus) and the Laboratoire d'Optique Atmosperique in Lille (France) [*Chaikovsky et al.*, 2008], combines lidar vertically resolved data with sun photometer column integrated values in order to retrieve vertically resolved aerosol microphysical properties.

4.3.1 LIRIC fundamentals

LIRIC is described in more detail in previous studies [*Chaikovsky et al.*, 2008; *Chaikovsky et al.*, 2012; *Wagner et al.*, 2012; *Kokkalis et al.*, 2013]. The retrieval algorithm is based on the inversions of sun photometer measurements retrieved from AERONET (Version 2, Level 1.5) combined with lidar elastic backscattered signals at three different wavelengths (355, 532 and 1064 nm). If available, the cross-polarized signal at 532 nm (532-cross) is also used. The maximum likelihood method is applied to obtain the volume concentration profiles of the fine and coarse modes. When using the fourth wavelength corresponding to the 532 cross polarized signal, it is possible to distinguish between the spherical and spheroid modes of the coarse fraction. Volume concentration profiles can be obtained with a vertical resolution as high as the vertical resolution of the lidar system. A schematic description of LIRIC is presented in Figure 4.3.

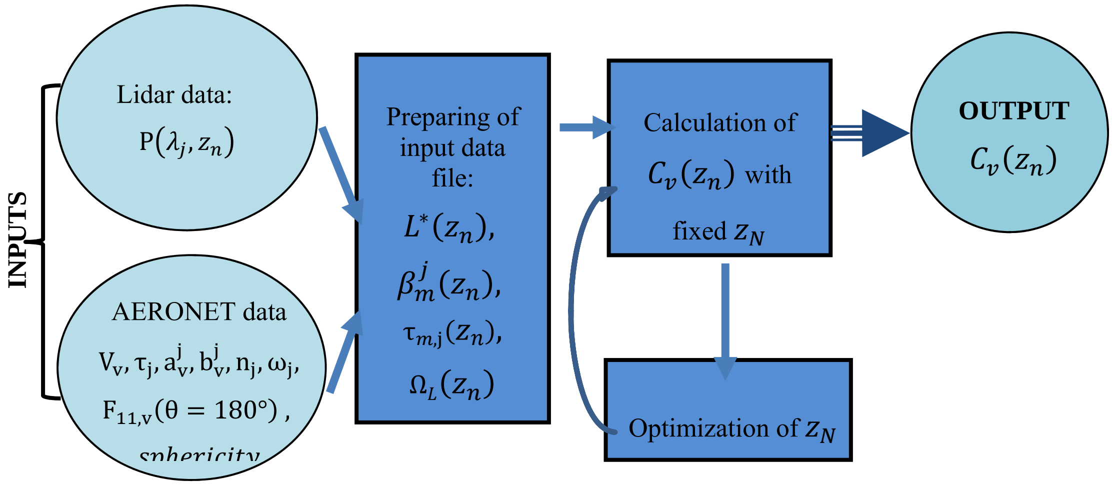

Figure 4.3. Simplified scheme of the LIRIC retrieval algorithm. Adapted from Chaikovsky et al. [2008]. $P(\lambda_j, z_n)$ *is the raw backscattered lidar signal,* V_v *is the volume concentration for each mode,* τ_j *is the aerosol optical depth for the wavelength j,* a_v^j, b_v^j *are the mean column-integrated extinction and backscatter coefficients,* n_j *is the refractive index and* ω_j *is the single scattering albedo.* $L^*(z_n)$ *represents the normalized lidar signal,* $\beta_m^j(z_n)$ *is the molecular backscatter coefficient profile,* $\tau_{m,j}(z_n)$ *is the molecular optical depth profile and* $\Omega_L(z_n)$ *are dispersion profiles.* $C_v(z_n)$ *stands for the volume concentration profiles for each mode retrieved with LIRIC and* z_N *refers to the reference height.*

The method uses an aerosol model based on a mixture of spherical and spheroid particles as described by AERONET [*Dubovik et al.*, 2006]. This model is exclusively determined from sun photometer data. Actually, the integrated volume concentrations of the fine and coarse modes, (v_c), retrieved from the radiometric measurements are the one defining the aerosol model. Separation between fine and coarse modes is made by searching the radius corresponding to the minimum of the AERONET retrieved bimodal aerosol size distribution in the range 0.194–0.576 µm [*Dubovik et al.*, 2006]. Other input variables used by LIRIC are AERONET refractive index (m), single scattering albedo (ω), integrated backscatter coefficients (b), the first element of the scattering matrices at 180º (F_{11}(180º)) and the aerosol optical depth (τ_λ). The particle size distribution (*dV/dlnr*), lidar ratio (LR), Angström exponent (AE), the ratio of spherical to spheroid particles (% sphericity) and refractive indexes (m) are also taken from the radiometric data and considered independent of the altitude for each mode. Considering that all variables are independent and that they follow a normal distribution, the maximum likelihood method [*Eadie and James*, 2006] is applied to the probability function obtained for the volume concentrations based on a set of three equations. The optimal volume concentration profiles for each mode obtained based on this method are the final output of the retrieval algorithm.

The initial set of three equations is described in detail in *Chaikovsky et al.* [2008] and presented here in Eq. 4.1-Eq. 4.3. Eq. 4.1 describes the multi-wavelength lidar equations containing information on the vertical aerosol parameters; Eq. 4.2 is related with the integral characteristics of the aerosol layer provided by sun photometer measurements; and Eq. 4.3 introduces restrictions on the vertical variability of the volume concentration profiles $C_v(z_n)$.

$$L^{*,j}(z_n) = L^j\left(C_v^j(z_n), m_j, z_n\right) + \Delta_L^j \qquad \textit{Eq. 4.1}$$

$$W_v^{*,j} = W^j\left(C_v(z_n)\right) + \Delta_F^j \qquad \textit{Eq. 4.2}$$

$$0^{*,j} = S_2 C_v^j + \Delta_{0_v}^j \qquad \textit{Eq. 4.3}$$

$L^{*,\mathrm{j}}(z_n)$ is a normalized measured lidar signal at λ_j wavelength and $L^j\left(\mathrm{C}_v^j(z_n), m_j, z_n\right)$ is a calculated nonlinear function which depends on parameters of the aerosol model. The superscript j corresponds to the different wavelengths (355, 532, 1064 nm and 532-cross when available). Hereafter, this superscript will be omitted in order to simplify the equations. The subscript υ indicates the mode and might go from 1 (fine mode) to 2 (coarse mode) or from 1 to 3 (fine, coarse spherical and coarse spheroid mode, respectively, when 532-cross channel is available). W_v^* is the total column integrated content of the aerosol fraction that is retrieved from photometer measurements and $W\left(C_v(z_n)\right)$ is the integral over an aerosol layer of the retrieved $C_v(z_n)$ profile. $0^{*,j}$ is the smoothness constraints equation, being S_2 is the matrix of second differences and Δ deviations. Next subsections described in more detail how each of the elements of these equations are calculated based on the available input data.

4.3.1.1 Multi-wavelength lidar equation

$L^*{}_n(z_n)$ is obtained from the experimental data as follows. As explained in chapter 2.7, the lidar equation and the range corrected signal are defined as

$$P(z_n) = \frac{KO(z_n)}{{z_n}^2}\beta(z_n)T(z_n)^2 + P_B \qquad \textit{Eq. 2.39}$$

$$RCS(z_n) = (P(z_n) - P_B)\cdot {z_n}^2 \qquad \textit{Eq. 2.40}$$

Eq. 2.40 is the range corrected signal and *K* is a system dependent parameter obtained from calibration at a certain range z_N, which is supposed to be an aerosol free region, as explained in section 2.7. z_N is the so-called the reference height and in LIRIC software is a user defined input parameter. *K* is then expressed as:

$$K = \frac{RCS(z_N)}{R(z_N)\beta_{mol}(z_N)T^2_{mol,N}} \qquad \textit{Eq. 4.4}$$

where $R(z_N) = \frac{\beta_{mol}(z_N)+\beta_{aer}(z_N)}{\beta_{mol}(z_N)}$

$L^*(z_n)$ is therefore defined as:

$$L^*(z_n) = \frac{RCS(z_n)}{RCS(z_N)} R^j(z_N)\beta^j_{mol}(z_N)\exp(-2\tau_{mol}(z_n, z_N)) \qquad \textit{Eq. 4.5}$$

here $RCS(z_n)$ is the measured range corrected lidar signal and $\beta^j_{mol}(z_N)\exp(-2\tau_{mol}(z_n, z_N))$ are known molecular terms which can be theoretically retrieved. Substituting Eq. 4.4 in Eq. 4.5 we obtain that

$$L^*(z_n) = \left(\beta_{era}(z_n) + \beta_{mol}(z_n)\right)\exp(2 \cdot \tau(z_n, z_N)) \qquad \textit{Eq. 4.6}$$

Therefore, the first part of the right term in Eq. 4.1 can be written as:

$$\begin{aligned} L(C_v(z_n), m, z_n) \\ &= \left(\beta_{aer}(C_v(z_n), m, z_n) + \beta_{mol}(C_v(z_n), m, z_n)\right) \\ &\cdot \exp(2\tau(C_v(z_n), m, z_n)) \end{aligned} \qquad \textit{Eq. 4.7}$$

where the aerosol backscatter and extinction coefficient profiles are obtained as:

$$\begin{aligned} \beta_{aer}(\lambda_j, z_n) &= \sum_v C_v(z_n) \cdot b_v(\lambda_j) \\ \alpha_{aer}(\lambda_j, z_n) &= \sum_v C_v(z_n) \cdot a_v(\lambda_j) \end{aligned} \qquad \textit{Eq. 4.8}$$

a_v and b_v are coefficients obtained from radiometric measurements. They are mean values of the backscatter and extinction coefficients per unit of column-integrated volume concentration V_v:

$$a_v(\lambda_j) = \frac{\tau_v(\lambda_j)}{v_{c,v}}$$

$$b_v^p(\lambda) = \frac{\tau_{\lambda,v} \cdot \omega(\lambda) \cdot F_v^p(\lambda, \theta = 180°)}{4\pi} \qquad \text{Eq. 4.9}$$

where the superscript p stands for the depolarization mode used (t = total and $\perp$ = perpendicular) $F_v^t(\lambda, \theta = 180°) = F_{11,v}(\lambda, \theta = 180°)$ and $F_v^{\perp}(\lambda, \theta = 180°) = \frac{1}{2}[F_{11,v}(\lambda, \theta = 180°) - F_{22,v}(\lambda, \theta = 180°)]$.

Therefore, the lidar ratio in LIRIC, $LR_v(\lambda_j)$, is retrieved according to the following equation

$$LR_v(\lambda_j) = \frac{4\pi}{\omega(\lambda_j) \cdot F_{11,v}(\lambda_j, \theta = 180°)} \qquad \text{Eq. 4.10}$$

The single scattering albedo $\omega(\lambda_j)$ and the first element of the scattering matrix at 180°, $F_{11,v}$, are also derived from radiometric measurements.

The term Δ_L is defined for each wavelength as

$$\Delta_L = L_n^*(z_n) - L(C_v(z_n), m_j, z_n) \qquad \text{Eq. 4.11}$$

Assuming non correlated differences, Δ_L is related to a covariance matrix Ω_L whose elements corresponds to the dispersion of differences depending on the coordinate z_n. Substituting in Eq. 4.11, the equations Eq. 4.5 and Eq. 4.7 and applying error theory we obtain that the covariance matrix elements $\Omega_L(z_n)$ depends on the dispersion of the lidar signal and the dispersion of the optical parameters α_{aer}, β_{aer} and τ_λ. The dispersion of the lidar signal takes into account dispersion effects such as synchronous and non-synchronous noise, deviation of dark current or background signal. More details about these calculations can be found in *Chaikovsky et al.*, [2008]

4.3.1.2 Sun photometer equation

The terms in Eq. 4.2 are described here. W^* is the integrated volume concentration provided by the sun photometer. The first part of the right term in Eq. 4.2 is calculated as follows:

$$W\big(C_v(z_n)\big) = \int_0^{z_N} C_v(z_n) = \sum_{n=0}^{N} C_v(z_n)\cdot\Delta z_n$$
$$= \sum_{n=N_0}^{N} C_v(z_n)\cdot\Delta z_n + C_v(z_n)\cdot z_{N_0} \qquad \text{Eq. 4.12}$$

z_{N_0} is what will be called the lower limit and is defined by the user in LIRIC software. Lidar data are considered not to be influenced by the overlap over this height. Below this lower limit, the volume concentration is assumed constant down to the surface. Therefore if $C_v(z_n) = C_v\big(z_{N_0}\big)$ if $z_n < z_{N_0}$.

The square of the errors of Eq. 4.12 is used as an estimation of the covariance matrix Ω_W , which is related to $\Delta_F = W^* - W\big(C_v(z_n)\big)$.

4.3.1.3 Smoothness constraints equation

Eq. 4.3, which takes into account the smoothness constraints, is obtained by limitation of the norm of the second order differences, defining:

$$S^2 C_v = \sum_n \frac{1}{(|\Delta z_n|)^3}\big(2C_v(z_n) - C_v(z_{n-1}) - C_v(z_{n+1})\big)^2 \qquad \text{Eq. 4.13}$$

The $0^{*,j}$ vector is used in order to avoid unrealistic strong oscillations in the output concentration profiles [*Dubovik and King*, 2000; *Dubovik*, 2005].

4.3.1.4 Application of the maximum likelihood method

Considering independent random variables which follow a normal law of distribution, the likelihood function is defined as:

$$P(C_v|L^*,W_v^*)\sim exp\left(-\frac{1}{2}\left(\begin{array}{c}\sum_{n=1}^{N-1}\sum_{j=1}^{J}\left(L_n^{*j}-L_n(C_v)\right)^T\Omega_L^{-1}\left(L_n^{*j}-L_n(C_v)\right)+\\+\sum_\psi\left(W_\psi^*-W_\psi\left(C_v(z_n)\right)\right)^T\Omega_W^{-1}\left(W_\psi^*-W_\psi\left(C_v(z_n)\right)\right)+\\+\sum_v\frac{E_v^m}{\sigma_v^2}\end{array}\right)\right)$$

Eq. 4.14

where $E_v^m=\sum_v\left(\frac{\Delta^m F_v(z_n)}{\Delta^m z_n}\right)^2\Delta z_n$ and σ_v^2 is the dispersion of finite differences estimations for height distributions $C_v(z_n)$.

The set of parameters $C_v(z_n)$ and z_N which makes maximum the probability equation or equivalently minimum the exponent of the function, is the solution of the algorithm according to the maximum likelihood method.

The exponent of Eq. 4.14 is defined as the function $\Psi(L^*,W_v^*,C_v)$,

$$\begin{gathered}\Psi(L^*,W_v^*,C_v)=\sum_{n=1}^{N-1}\sum_{j=1}^{J}\left(L_n^{*j}-L_n(C_v)\right)^T\Omega_L^{-1}\left(L_n^{*j}-L_n(C_v)\right)+\\+\sum_\psi\left(W_\psi^*-W_\psi\left(C_v(z_n)\right)\right)^T\Omega_W^{-1}\left(W_\psi^*-W_\psi\left(C_v(z_n)\right)\right)+\sum_v\frac{E_v^m}{\sigma_v^2}\end{gathered}$$

Eq. 4.15

The function $\Psi(L^*,W_v^*,C_v)$ can be separated in three different functions associated to lidar, sun photometer and smoothness constraints information respectively as follows:

$$\Psi_1\left(L^*, C_v, z_N\right) = \sum_{n=1}^{N-1}\sum_{j=1}^{J}\left(L_n^{*j} - L_n(C_v)\right)^T \Omega_L^{-1}\left(L_n^{*j} - L_n(C_v)\right)$$

$$\Psi_2\left(W_v\ \ , C_v\right) = \sum_{\psi}\left(W_\psi^* - W_\psi\left(C_v(z_n)\right)\right)^T \Omega_W^{-1}\left(W_\psi^* - W_\psi\left(C_v(z_n)\right)\right) \qquad \textit{Eq. 4.16}$$

$$\Psi_3(\,C_v) = \sum_{v}\frac{E_v^m}{\sigma_v^2}$$

After taking into account the covariance matrices, previous equations and simplifications in *Chaikovsky et al.* [2008], these three functions can be rewritten as:

$$\Psi_1\left(L^*, C_v, z_N\right) =$$

$$\sum_{n=N}^{N_0}\sum_{j=1}^{J}\left(L_n^{*j} - \left(\sum_{v} C_v(z_n)\cdot b_v(\lambda_j) + \sum_{v} C_v(z_n)\cdot a_v(\lambda_j) + \beta_m^j(z_n)\right)\right.$$
$$\left.\cdot\ \exp\left(-2\sum_{i=N}^{i=n+1}\left(\sum_{v} C_v(z_n)\cdot a_v(\lambda_j)\right)\Delta z_i\right)\right)^2 \frac{k_j^2}{\Omega_{L,n}^j}$$

Eq. 4.17

$$\Psi_2\left(W_v\ \ , C_v\right) =$$

$$\sum_{v}\frac{h_v^2}{\Omega_V}\left(W_v^* - \sum_{n=N_0}^{N} C_v(z_n)|\Delta z| - C_v(z_n)(N_0 - 1)\,|\Delta z|\right)^2$$

$$\Psi_3(\,C_v(z_n)) = \sum_{v}\sum_{n=1}^{N}\frac{d_v^2}{(|\Delta z_n|)^3}\left(2C_v(z_n) - C_v(z_{n-1}) - C_v(z_{n+1})\right)^2$$

Each of these three functions is minimized when applying the maximum likelihood method. k_j^2, h_v^2, d_v^2 are regularization parameters that can be adjusted by the user to optimise results.

4.3.1.5 Software description

Before starting the aerosol microphysical properties retrieval based on the iterative procedure, lidar data need to be preprocessed. In a first step, data are processed by LIRIC software using the Synthesizer module. In this part, data are time averaged and measurements corresponding to different detection modes (analog and photon counting) are joined for each wavelength. Next, output data from Synthesizer are processed using TropoExport, another module included in LIRIC. In this part, profiles of $\beta_{mol}^{j}(z_n)$ and $\tau_{mol}^{j}(z_n)$ are also calculated using the standard atmosphere, a custom atmosphere or radiosounding data, depending on the user's input. Lidar data are normalized in order to obtain the $L^{*}{}_{\lambda}(z_n)$ profile described in section 4.3.1.1., which will be used as input for the retrieval of microphysical properties. In this part, z_N, the reference height for calibration is indicated by the user. Also the upper and lower limits of the lidar signals, where it is considered to be reliable, are indicated. The lower limit, z_{N0}, as described in section 4.3.1. is chosen at the height above which lidar data are considered not to be influenced by the incomplete overlap. The upper limit, z_U, is set at a height where no aerosol is found and only molecular signal is expected, always over the reference height, z_N. Therefore no profiles are obtained over this upper limit. TropoExport module also calculates the statistical dispersion of $L^{*}{}_{n}(z_n)$ as explained in *Chaikovsky et al.* [2008].

The input optical and microphysical properties from sun photometer measurements previously detailed are provided by AERONET for the sun photometer detection wavelengths (340, 380, 440, 500, 675, 870 and 1020 nm). For the retrieval of the microphysical properties using LIRIC, these variables need to be recalculated for the lidar elastic wavelengths (355, 532 and 1064 nm) according to the equations in *Dubovik et al.* [2006]. This recalculation is performed by the Manual Retriever module of LIRIC.

The retrieval of the microphysical properties itself is also performed in Manual retriever using as input ${L^*}_\lambda(z_n)$ and the recalculated data from the sun photometer. The regularization parameters *k, f,* and *d* are defined by the user in this part of the code in order to optimize the retrieval of microphysical profiles.

A schematic description of the LIRIC algorithm including the software modules is shown in Figure 4.4.

In the Manual Retriever module, an iterative procedure is applied in order to obtain the minimum of the function in Eq. 4. 15. In each iteration the main aim is to reduce the differences between measured and calculated lidar signals at the wavelengths λj. The difference between column integrated volume concentrations retrieved from radiometric data and those computed from retrieved distributions $C_v(z_n)$ is also reduced. At the same time, the requirement of smoothness of the vertically resolved volume concentrations altitude distributions $C_v(z_n)$ has to be fulfilled.

As a first step of the iteration, $C_v^0(z_n)$ are calculated assuming that the profile of each mode has a constant value. In this first approach, the combination of the constant values for each mode has to provide a minimum of the function in Eq. 4.15. For the next steps, the gradient method is applied in order to obtain the increments in $C_v^i(z_n)$ as follows:

$$\frac{\partial\left(\Psi(L^*,W_v^*,C_v)\right)}{\partial C_{v(z_n)}} = F^v\left(L^*,W_v^*,C_v,z_N\right) \qquad \textit{Eq. 4.18}$$

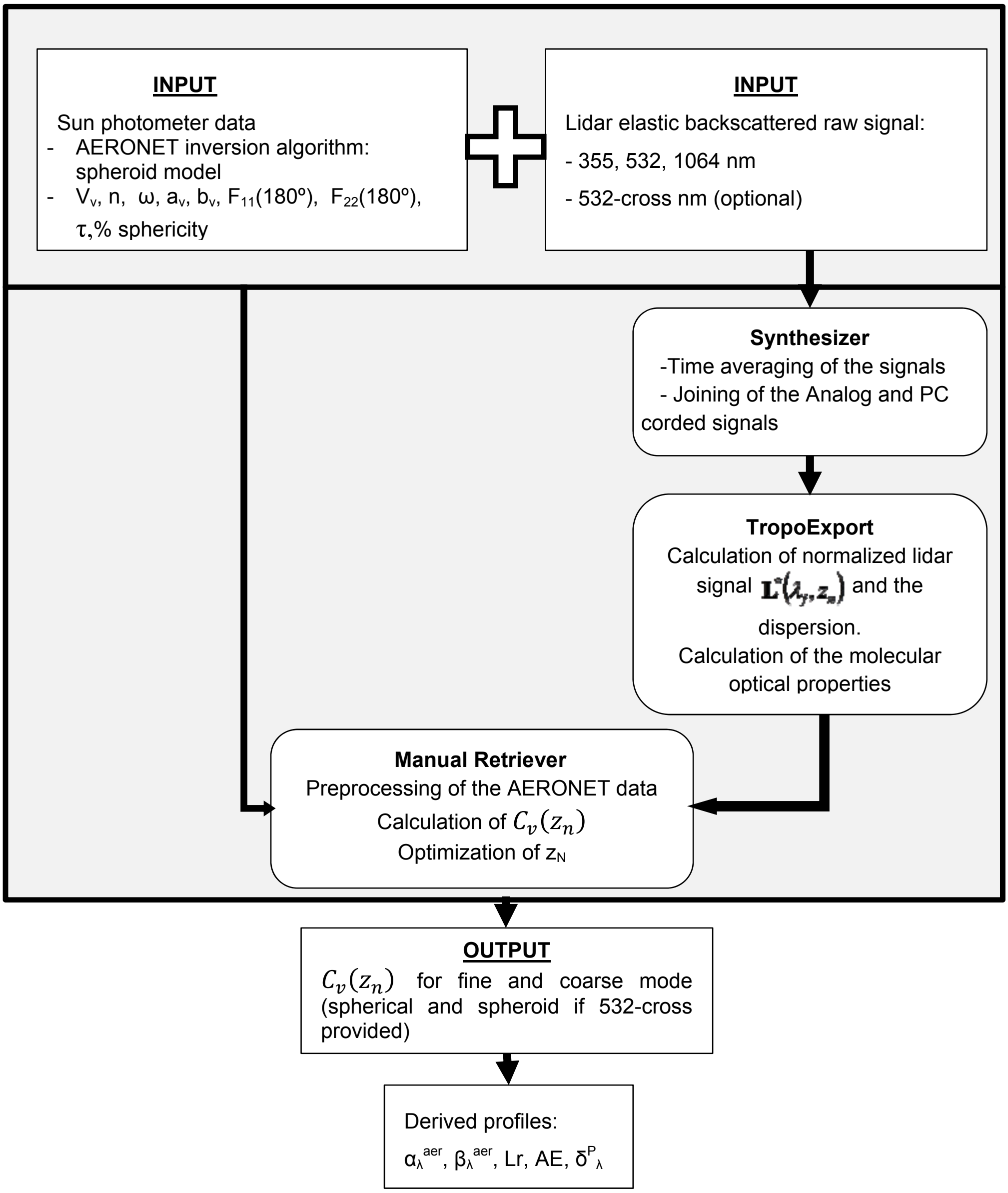

Figure 4.4. Schematic description of the LIRIC algorithm. Lidar elastic signals at different wavelengths (355, 532 and 1064 nm and if available 532 cross polarized) and AERONET inversion products are used as input data in the software. Lidar signals are pre-processed in Synthesizer and TropoExport to obtain $L^*_\lambda(z_n)$, which is used as input in Manual Retriever together with the AERONET Version 2 Level 1.5 data recalculated for the lidar wavelengths. Main outputs are the volume concentration profiles $C_v(z_n)$ for the fine and coarse mode. If 532 cross polarized lidar signal is available as input, the output $C_v(z_n)$ is retrieved for the fine, coarse spherical and coarse spheroid modes. From $C_v(z_n)$ profiles and column-integrated properties, optical properties profiles such as the aerosol backscatter coefficient β_λ^{aer}, the aerosol extinction coefficient α, the lidar ratio LR, the Angström exponent AE or the particle linear depolarization ratio δ^P_λ can also be calculated.

The iteration steps are calculated as

$$C_v^{i+1}(z_n) = C_v^i(z_n) - F^v\left(L^*, W_v^*, C_v^i, z_N\right) \frac{C_v^i(z_n)}{x_v \sqrt{\sum_v \left(F_n^v\right)^2}} \qquad \textit{Eq. 4.19}$$

where x_v is a parameter larger than 1 which assures that the increment of $C_v^i(z_n)$ is smaller than its value itself. Non-negativity criteria are also implemented in the code. The iteration continues until variations in $C_v^i(z_n)$ are smaller than a certain threshold.

Once, $C_v^i(z_n)$ profiles are obtained, LIRIC optimizes the backscatter ratio at z_N and performs an internal procedure to consider the possible contribution of aerosol backscatter from the reference layer.

4.3.1.6 LIRIC outputs

Main LIRIC outputs are volume concentration profiles $C_v(z_n)$ for the different modes (fine and coarse or fine and coarse spherical and coarse spheroid if 532-cross polarized channel is available). However, from these profiles it is also possible to obtain other derived properties such as the aerosol backscatter and extinction coefficient profiles (as in Eq. 4.8). The particle linear depolarization ratio at 532 nm (δ^P_{532nm}) can also be obtained as:

$$\delta_{532nm}^P = \frac{\beta_{532}^{\perp}}{\beta_{532}^{\parallel}} \qquad \textit{Eq. 4.20}$$

where $\beta_{532}^{\perp}$ *and* $\beta_{532}^{\parallel}$ are obtained from Eq. 4.8. as indicated below:

$$\beta_{532}^{\perp} = \beta_{aer}(532cross, z_n)$$

$$\beta_{532}^{\parallel} = \beta_{aer}(532parallel, z_n)$$

Derived properties profiles such as the lidar ratio LR or the Angström exponent profiles can also be retrieved from the output database. Aerosol backscatter coefficient profiles calculated from $C_v(z_n)$ according to equation Eq.

4.8. are compared with those calculated with the Klett-Fernald algorithm from lidar data [*Fernald et al.,* 1972; *Klett,* 1981; *Fernald,* 1984]. This algorithm retrieves the aerosol backscatter coefficient profiles corresponding to the elastic wavelengths assuming a reference height free of aerosol particles and a height-independent aerosol lidar ratio for each wavelength as explained in section 2.7.1. Additional details can be found in *Guerrero-Rascado et al.*, [2009; 2011] and *Bravo-Aranda et al.* [2013]. Lidar ratios assumed when applying the Klett-Fernald algorithm to lidar data are obtained by minimizing the difference between the integral of the aerosol backscatter coefficient profile multiplied by the LR and the $\tau_{aer,\lambda}$ provided by AERONET for each wavelength [*Guerrero-Rascado et al.*, 2008]. It is necessary to take into account that the assumption of a constant lidar ratio introduces some uncertainty in the lidar retrieved aerosol backscatter coefficient profiles [*Sasano et al.*, 1985]. In the case of LIRIC, the lidar ratio is calculated as indicated in Eq. 4.10. This value is height-independent for each mode, but is height dependent when the different modes are combined to obtain the aerosol backscatter and extinction coefficient profiles.

On other hand, δ^{P}_{532nm} profiles at 532 nm retrieved using the 532-parallel and 532-cross profiles measured with the lidar system can be compared with those retrieved from the $C_v(z_n)$ profiles obtained from LIRIC according to equation Eq. 4.22. In order to retrieve accurate δ^{P}_{532nm} profiles from lidar measurements a careful calibration of the instrument is required. Thus it is necessary to take into account the polarizing effects associated to the different optical elements (e. g., effective diattenuation of the optical systems) and the misalignment between the polarization plane of the laser and the optical devices. Then, procedures described in *Freudenthaler et al.* [2009] and *Bravo-Aranda et al.* [2013] are used. These profiles are compared with those retrieved from the $C_v(z_n)$ profiles obtained with LIRIC according to Eq. 4.22.

4.3.2 Uncertainties of the algorithm

This section discusses the methodology used to analyse the uncertainties in LIRIC output volume concentration profiles $C_v(z_n)$ due to variations in the user-defined input parameters. It is necessary to point out that the uncertainties of the input elastic lidar signals and AERONET data were not taken into account in this analysis. Therefore, only uncertainties in the output profiles due to the LIRIC algorithm itself are quantified. For this purpose, different sets of user-defined parameters have been tested for different atmospheric aerosol types and loads in order to evaluate the stability of the retrieved volume concentration profiles. Specifically, the user-defined parameters evaluated are the reference height z_N, the lower limit height z_{N0}, the upper limit z_U and the regularization parameters *k*, *f* and *d*.

a) Lower limit height z_{N0}

The lower limit is chosen at the altitude where the lidar signal is considered not to be affected by incomplete overlap. Below the lower limit of the lidar signal, retrieved volume concentration $C_v(z_n)$ profiles are assumed constant down to the Earth's surface and equal to $C_v(z_{N0})$. To study the influence of the variation in z_{N0} on the $C_v(z_n)$ profiles, three different retrievals with three different values of z_{N0} were performed for each case. These values are chosen in the altitude range between 400 and 1000 m above the lidar system, where the overlap is larger than 80% [*F Navas-Guzmán et al.*, 2011]

b) Reference height z_N

The reference height has to be chosen in an aerosol free region, where only molecular signal is expected. As in previous studies [*Wagner et al.*, 2013a,b], the reference height was chosen at a level where the backscattering ratio (total to molecular backscatter coefficient ratio) is lower than 1.1 for each wavelength, to guarantee that the aerosol backscattered signal is less than 10% of the molecular one. Three different retrievals with different values corresponding to three reference heights separated 200 m were performed for each case in order to evaluate the influence of this parameter in the final output. The difference between the z_N values was chosen to be 200 m because no significant fluctuations were expected in the volume concentration profiles for lower values. Nonetheless, tests with higher distances (up to 400 m) were performed in some cases. It was observed that the uncertainties were very similar to those obtained with 200 m, except for some specific situations that will be explained later.

The reference height z_N is a priori defined by the user, however LIRIC optimizes the backscattering ratio at this altitude and performs an internal procedure to consider the possible contribution of aerosol backscattering from the reference height range. Therefore, low variations are expected in the final output if the algorithm correctly corrects the backscatter ratio at z_N.

c) Upper limit height z_U

The upper limit is established at a height where no aerosol is found. Due to software constraints, the upper limit has to be always above the reference height z_N. Above the upper limit no profiles are retrieved anymore. In order to study the influence of the upper limit in the retrieval of $C_v(z_n)$, three different heights are used as input data for three different retrievals. As no aerosol is expected to be at heights above z_U, the output $C_v(z_n)$ are not expected to change substantially with this parameter. However, in this study it was observed that in the molecular height range above the aerosol layers, LIRIC tends to introduce a positive offset in the volume concentration profiles $C_v(z_n)$ indicating the presence of aerosol particles at these levels where there is not aerosol backscattering and affecting the entire retrieved profiles $C_v(z_n)$. This offset has also been observed in previous studies [*Wagner et al.*, 2013]. In order to avoid additional uncertainties due to the presence of this offset, the upper limit should be kept as low as possible and consequently the same for the reference height z_N.

d) Regularization parameters

Different sets of values for the regularization parameters k, f and d are used in order to perform several retrievals and evaluate the uncertainties they introduce in the final $C_v(z_n)$ profiles. The regularization parameters k and f are varied by several orders of magnitude, but always satisfying that the column integrated volume concentration values of each mode do not differ by more than 5% from those provided by AERONET. Parameter d is varied from 1 to 5.

Results of the stability tests applied to the three different cases, corresponding to different aerosol types, loads and vertical distributions, are shown in the following section.

4.3.2.1 Pollution episode: 22nd May 2011

On 22nd May 2011 a pollution episode was observed at Granada. The lidar system detected an aerosol layer up to almost 4000 m a.s.l. (Figure 4.5a). A backward trajectory analysis performed with the HYSPLIT model [*Draxler and Rolph*, 2003] indicated Southern Europe as the origin of the air masses arriving at Granada below 4000 m a.s.l (Figure 4.5b). This European region and specially the Po Valley, in Northern Italy, are highly polluted areas and important source regions of anthropogenic pollution [*Barnaba and Gobbi*, 2004]. The NAAPS model (Navy Aerosol Analysis and Prediction System) [*Christensen*, 1997] forecast the presence of sulphates over the Iberian Peninsula (Figure 4.5c), which is also an indicator of anthropogenic pollution.

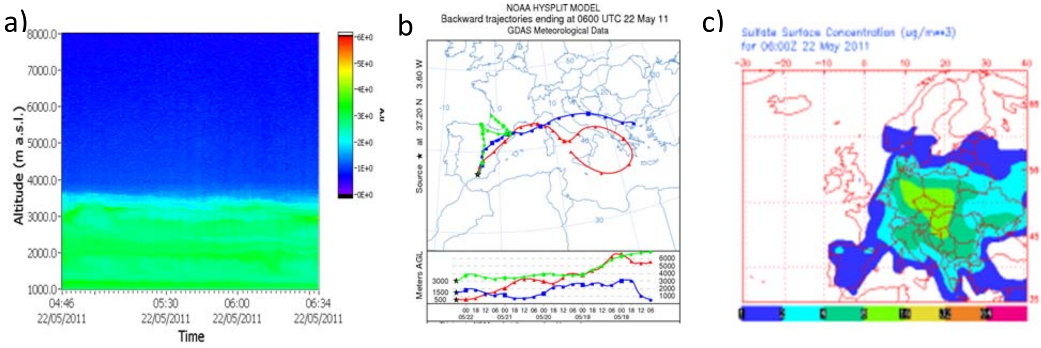

Figure 4.5. a) Time series of the lidar range corrected signal in arbitrary units at 532 nm during the morning of the 22nd May 2011. b) 5-day backtrajectories of the air masses arriving over Granada the same day at 06:00 UTC obtained by the HYSPLIT model. c) Sulphate surface concentration forecast by NAAPS for the same date at 06:00 UTC over Europe.

AERONET data obtained during this episode are presented in Figure 4.6. The Angström exponent between 440 and 870 nm, AE(440-870nm), obtained from the sun photometer data ranged from 0.9 to 1.8 during the day, indicating the predominance of small particles (Figure 4.6a). This predominance was confirmed by the aerosol size distribution retrieved at 06:25 UTC, which shows much larger concentration values for the fine mode (Figure 4.6b). The AE(440-870nm) at this time was 1.8 and the fine mode fraction was 0.85. The $\omega(\lambda)$ values retrieved at the same time showed a decreasing tendency with λ, which is typical of polluted conditions [*Dubovik et al.,* 2002; *Lyamani et al.*, 2006b] (Figure 4.6c). However, the aerosol load was not very high, as deduced from τ_{440nm} values (~ 0.20) (Figure 4.6a).

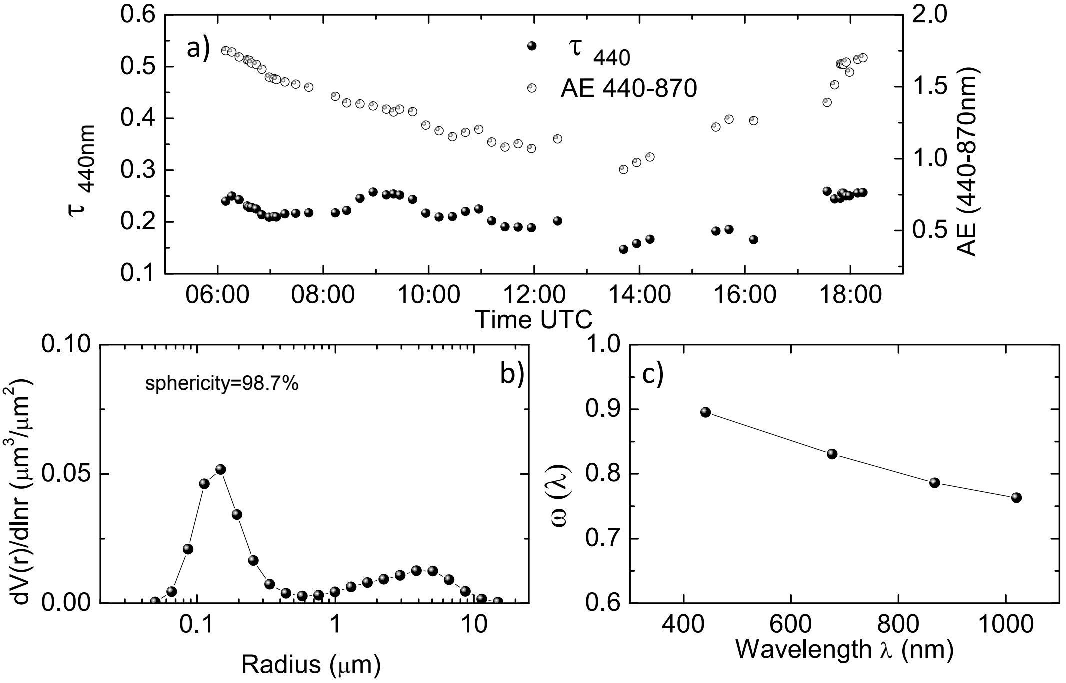

Figure 4.6. a) Time series of AERONET τ_{440} and AE(440-870nm) data on 22nd May 2011. b) Volume size distribution retrieved by AERONET inversion algorithm Version 2 the same day at 06:25 UTC. c) Single scattering albedo ω(λ) versus wavelength λ retrieved by AERONET for the same date.

Results from AERONET presented in Figure 4.6 are combined with lidar elastic signals at 355, 532 and 1064 nm and the 532-nm cross-polarized signal to retrieve the microphysical properties profiles with the LIRIC algorithm. Lidar data are averaged between 06:00 and 06:30 UTC. A first retrieval was performed using the initial set of user-defined input parameters listed in Table 4.1. The user-defined input parameters for the other two cases presented in the following subsections are also shown in this table in order to get a general overview of the values used.

Date	CASE I 22 May 2011	CASE II 3 Aug 2012	CASE III 10 Sept 2012
z_{N0} (m a.s.l.)	1010	1080	1175
z_N (m a.s.l.)	4000	6000	3750
z_U (m a.s.l.)	4150	6150	3900
k_{335}	$2.5\cdot10^{-4}$	$1.5\cdot10^{-5}$	$7.5\cdot10^{-5}$
k_{532}	$7.5\cdot10^{-4}$	$5\cdot10^{-6}$	$5\cdot10^{-5}$
k_{1064}	$2.5\cdot10^{-4}$	$2.5\cdot10^{-6}$	$2.5\cdot10^{-5}$
k_{532c}	$7.5\cdot10^{-5}$	$7.5\cdot10^{-7}$	$7.5\cdot10^{-5}$
f_{fine}	5	0.2	1
$f_{\text{spherical}}$	25	0.2	1.5
f_{spheroid}	5	0.2	0.5
d_{fine}	5	1	5
$d_{\text{spherical}}$	5	1	1
d_{spheroid}	5	1	1

Table 4.1. Initial sets of user-defined input parameters for LIRIC retrievals for the study cases I, II and III (z_{N0} = lower limit, z_N = reference height, z_U = upper limit, k_λ = lidar regularization parameters, f_v= sun photometer regularization parameters, d_v = smooth constraints regularization parameters. Heights are expressed in m a.s.l. and regularization parameters are unitless).

The variations described in section 4.3.2 were applied to this initial set of user-defined input parameters to study the influence of the different parameters in the final profiles. As the volume concentration of the coarse spheroid mode was close to zero, only results of fine and coarse spherical modes are presented here.

Firstly, the influence of variations in the user defined lower limit, z_{N0}, was analysed. Three different retrievals with LIRIC were performed using three different values of z_{N0} (1010, 1200 and 1400 m a.s.l.) while keeping constant all the other parameters as in Table 4.1. Profiles in Figure 4.7a represent the mean values of the profiles obtained from the three different retrievals and the bars indicate one standard deviation, which is considered as the uncertainty. Variations of the lower limit height value produced larger uncertainties in the lower part of the profile, with values up to 25% for the fine mode and 33% for the coarse spherical mode. In the upper part of the profile, above 1500 m a.s.l., uncertainties were around 20% for the coarse spherical mode and below 10% for the fine mode.

Uncertainties due to variations in the reference height z_N, were also analysed (Figure 4.7b). Three different retrievals were performed keeping the upper and lower limits and the regularization parameters unchanged and using three different values for z_N (4000, 4200 and 4400 m a.s.l.). The uncertainties produced by changes in the reference height are of the order of 1% in both profiles, fine and coarse spherical. The low uncertainty indicates that LIRIC internally considers the possible contribution of aerosol backscattering for the reference height and correctly converges to an optimal solution, corroborating that the algorithm is robust under these conditions.

Figure 4.7c shows profiles and uncertainties when varying the upper limit height z_U values. Three different values were used between 4150 and 4550 m a.s.l. for the three different retrievals performed. Uncertainties obtained were around 1% in the whole profile except for the upper part, above 4000 m a.s.l., where uncertainties reached 25% in the coarse spherical mode. This higher uncertainty is due to the unrealistic offset introduced by the algorithm in the molecular height that in this case affected only the spherical mode, as previously indicated.

For the regularization parameters, values were changed by increasing or decreasing one order of magnitude the original k and f parameters. Several combinations were used either simultaneously increasing (or decreasing) k and f or either simultaneously increasing k and decreasing f values (or vice versa). The regularization parameter d was varied between 1 and 5. A total of five different sets of regularization parameters were used to perform five retrievals, but always satisfying that the column integrated volume concentration of each mode did not differ more than 5% from the ones provided by AERONET, as indicated before. In this case, the variation in the regularization parameters introduced almost no uncertainties (just around 1% for the whole profile).

Summarizing, the largest uncertainties were obtained for the variations in the lower limit height z_{N0}, especially in the lower part of the profile (below 1500 m a.s.l.). Variations were larger for the coarse spherical mode. Uncertainties due to variations for the other three input parameters tested were very similar with values around 1% for both modes.

Figure 4.7e shows the mean profiles and the standard deviations obtained from the 14 previous retrievals, calculated by averaging the results of all the profiles obtained in each step of the stability test. These mean profiles and standard deviations account for the total uncertainty introduced by all the user-defined input parameters. Relative errors were very low (below 5%) in the case of the fine mode concentration values. However, in the lower part of the profile larger relative deviations were found (up to 30%). The coarse spherical mode volume concentration profile had relative errors around 20%, except for the region affected by overlap. For volume concentration values below 10 μm^3/cm^3, the relative error reached 30%.

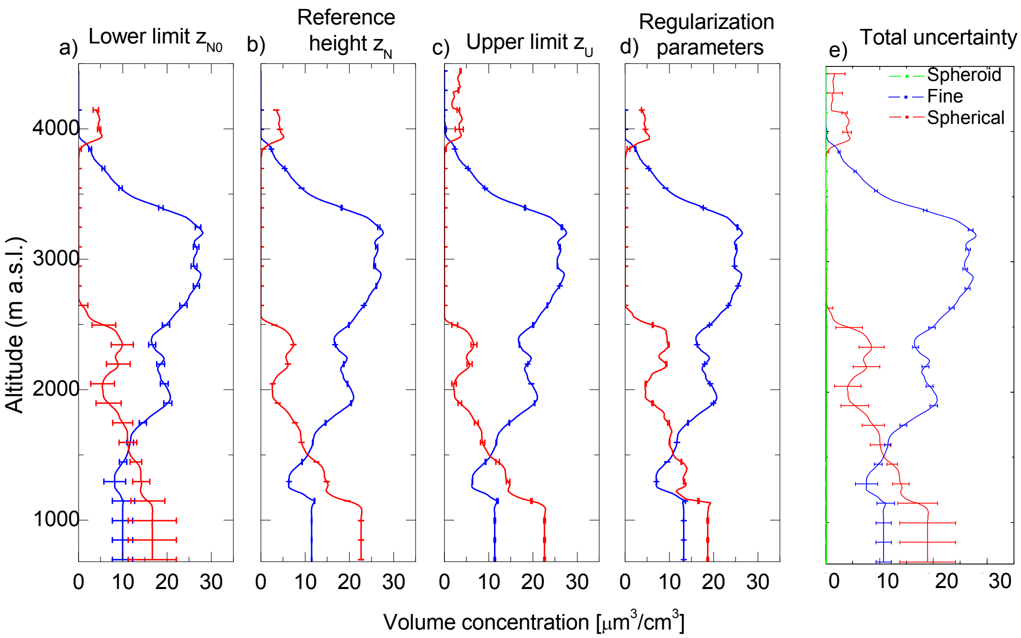

Figure 4.7. Mean fine (blue), coarse spherical mode (red) and coarse spheroid (green) volume concentration profiles and standard deviations (error bars) on 22nd May 2011 between 06:00 and 06:30 UTC obtained from different retrievals varying a) z_{N0}*, b)* z_N*, c)* z_U*, d) regularization parameters, as indicated in the text, and e) Mean profiles and standard deviation obtained by averaging all the previous profiles.*

The $C_v(z_n)$ profiles obtained indicated the existence of both fine and coarse spherical particles up to 2500 m a.s.l., whereas an absolute predominance of the fine mode is obtained from 2500 m up to 4000 m a.s.l. No concentration should be observed above the reference height z_N. However, the retrieval indicates that there are some coarse spherical particles above z_N. This is due to the unrealistic offset introduced by the algorithm in the molecular height range, as reported by *Wagner et al.* [2013]. The fine mode however is not affected by offsets in this case.

The coarse spherical mode volume concentration profile retrieved for this case is equivalent to the one obtained for the total coarse mode when performing the retrieval without using the 532-nm cross-polarized channel, with differences below 5%. The fine mode profile differences are even lower for both retrievals (with and without 532-nm cross-polarized information).

Figure 4.8 shows the comparison between aerosol optical properties retrieved by using the Klett-Fernald inversion algorithm to lidar data and those calculated from the volume concentration profiles retrieved by means of LIRIC. As explained in section 4.3.1, the lidar ratio assumed in the Klett-Fernald retrieval is obtained from comparison between the integrated aerosol extinction coefficient from lidar profiles and the sun photometer τ_λ. The agreement in the β_λ^{aer} was better for 532 and 1064 nm (~5%). For 355 nm, differences were much larger (~20%), especially around the maximum at 3000 m a.s.l. Important discrepancies were also found between the lidar ratio at 355 nm (65 sr) considered for the Klett-Fernald retrieval and the lidar ratio profile obtained from LIRIC with a mean value of around 120 sr. This lidar ratio value is very large compared to the ones in the literature [e. g. *Amiridis et al.,* 2005; *Müller et al.*, 2007; *Preißler et al.*, 2013]. Only in those cases of highly polluted episodes lidar ratios reach values above 100 sr [e. g. *Franke et al.*, 2001; *Mattis et al.*, 2004]. However, for the 532 nm channel values were quite similar for both methods (~75 sr). Differences between lidar ratios were also considerable at 1064 nm. However, as the dependence of the retrieved β_λ^{aer} on the assumed lidar ratio in the Klett-Fernald method decreases with wavelength [*Wiegner and Geiß,* 2012], this difference is not significant.

The extinction related Angström exponent profile, α-AE, provided by LIRIC and the backscatter related Angström exponent, β-AE, profile obtained with Klett-Fernald (Figure 4.8f) presented very good agreement with the AERONET column-integrated Angström exponent values (~1.5). However, β-AE profile retrieved with LIRIC presented very low values (<0.75) in comparison with that derived using the Klett-Fernald algorithm. Therefore, according to the retrieved Angström exponent profiles and taking into account Eq. 4.11, the discrepancies observed in the lidar ratios markedly affect the aerosol backscatter coefficient profiles retrieved with LIRIC. This is in agreement with the fact that α-AE is related to β-AE through the equation α-AE= β-AE + LR-AE [*Ansmann et al.,* 2002]. The unusual values obtained in the LR-AE retrieved by AERONET compared with the literature lead to inconsistent values retrieved with LIRIC for the β-AE.

The δ^{P}_{532nm} profile obtained from the lidar profiles and the appropriate calibration following *Bravo-Aranda et al.* [2013] was around 7% below 2500 m and close to 0% above this altitude, indicating a predominance of spherical particles in the whole layer. LIRIC derived δ^{P}_{532nm} was very constant, with values around 0% indicating no contribution of spheroid particles, as it can be seen in the volume concentration profiles. Above 3000 m a.s.l., the agreement between both δ^{P}_{532nm} profiles obtained was quite good, with both profiles tending to zero. However, below 3000 m a.s.l. discrepancies are higher, with δ^{P}_{532nm} provided by the lidar around 7% and the one obtained with LIRIC almost negligible. Thus, LIRIC δ^{P}_{532nm}profiles presented both lower and more constant values than those retrieved using the approach proposed in *Bravo-Aranda et al.* [2013]. These features, specially the underestimation of the LIRIC δ^{P}_{532nm} profiles, are also evident in the analyses of *Wagner et al.* [2013]. These differences are originated in the different procedures followed in each one of the retrievals. Thus, LIRIC combines AERONET information on the sphericity for the whole column and cross and parallel raw profiles at 532 nm. Meanwhile, our procedure uses these last profiles including a careful calibration, which corrects misalignment between the polarization plane of the laser and the optical system and diattenuation effects of the lidar system. This last information is not included among the system input parameters provided in LIRIC for pre-processing, although LIRIC takes into account the possibility of cross talking between the parallel and perpendicular signals. In addition, LIRIC δ^{P}_{532nm} profiles are affected by a high uncertainty in this case of very low depolarizing aerosol in the atmospheric column.

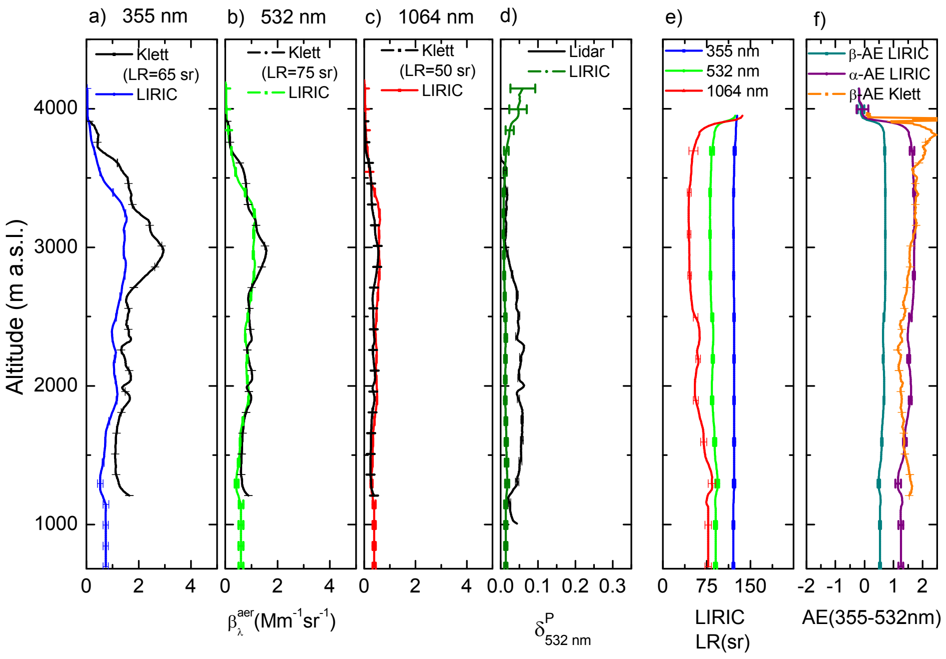

Figure 4.8. Aerosol Backscatter coefficient profiles at a) 355 nm, b) 532 nm and c) 1064 nm retrieved from LIRIC output profiles (coloured lines) and Klett-Fernald (black lines) on 22nd May 2011 between 06:00 and 06:30 UTC. d) δ^P_{532nm} profiles obtained from LIRIC (coloured line) and lidar data (black line) for the same period. e) Lidar ratio profiles obtained from LIRIC retrievals. f) Backscatter and extinction related Angtröm exponent between 355 and 532 nm profiles retrieved with LIRIC and backscatter related Angström exponent obtained with Klett-Fernald. The error bars of LIRIC profiles indicate the standard deviations obtained from the 14 retrievals performed as indicated in section 3.2.

4.3.2.2 Mineral dust event: 3rd August 2012

A mineral dust event occurred at the city of Granada on the 3rd August 2012. An atmospheric aerosol layer was observed with the lidar system up to 5.5 km a.s.l. (Figure 4.9a). Backward trajectory analysis revealed the origin of the air masses in North Africa above 3 km. However, for lower altitudes the air masses had its origin over the Atlantic Ocean and the Iberian Peninsula (Figure 4.9b). The NAAPs model forecast the presence of mineral dust over the Southeastern Iberian Peninsula and also sulphates and smoke in close areas (Figure 4.9c). The BSC-DREAM8b forecast model indicated the presence of mineral dust over the Iberian Peninsula but the dust loading values were relatively low (Figure 4.9d).

Sun photometer data (Figure 4.10) revealed high aerosol load during the whole day, with τ_{440nm} values over 0.40 during the morning and slightly decreasing to 0.2 during the afternoon. The AE(440-870nm) was around 0.1 during the whole day and the fine fraction was 0.16, indicating the predominance of coarse particles. The $\omega(\lambda)$ retrieved from AERONET inversions at 15:22 UTC presented values over 0.85 increasing with λ, which is the characteristic spectral dependence of $\omega(\lambda)$ under dust conditions [*Dubovik et al.*, 2002; *Alados-Arboledas et al.*, 2008; *Valenzuela et al.*, 2012a,b]. The aerosol size distribution for the same period showed a clear predominance of the coarse mode with high concentrations.

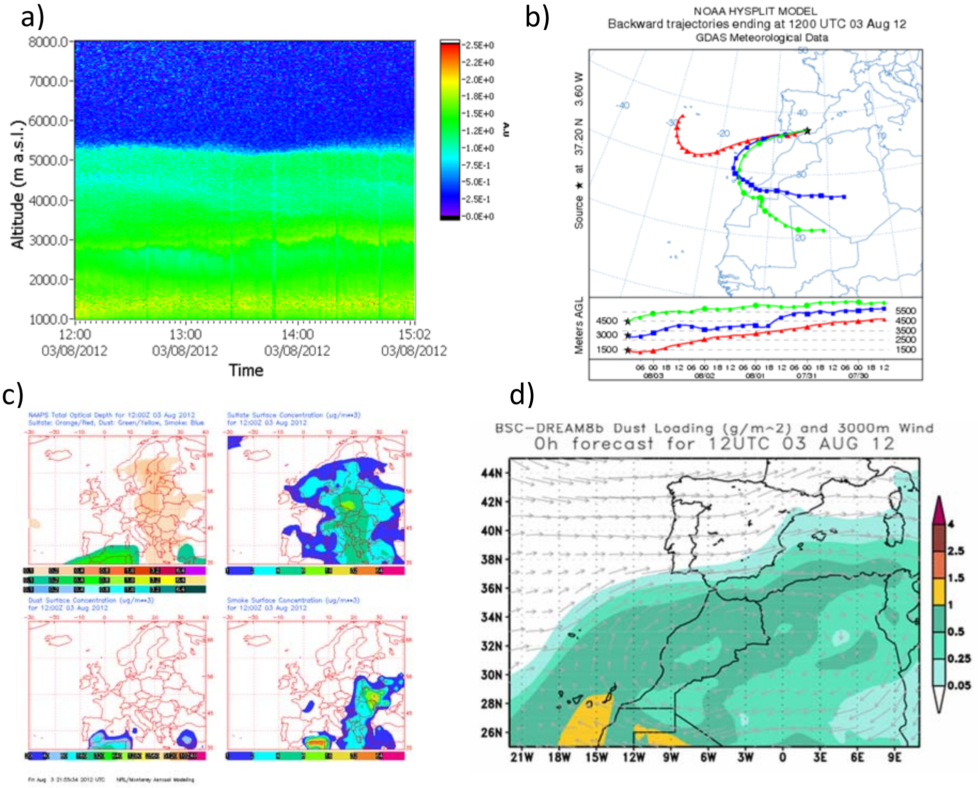

Figure 4.9. a) Time series of the lidar range corrected signal at 532 nm during the morning of the 3rd August 2012. b) 5-day backtrajectories of the air masses arriving over Granada the same day at 12:00UTC obtained with HYSPLIT model. c) NAAPS forecast for the same date at 12:00 UTC over Europe.d) BSC-DREAM8b dust loading forecast for the same period over Spain and North Africa.

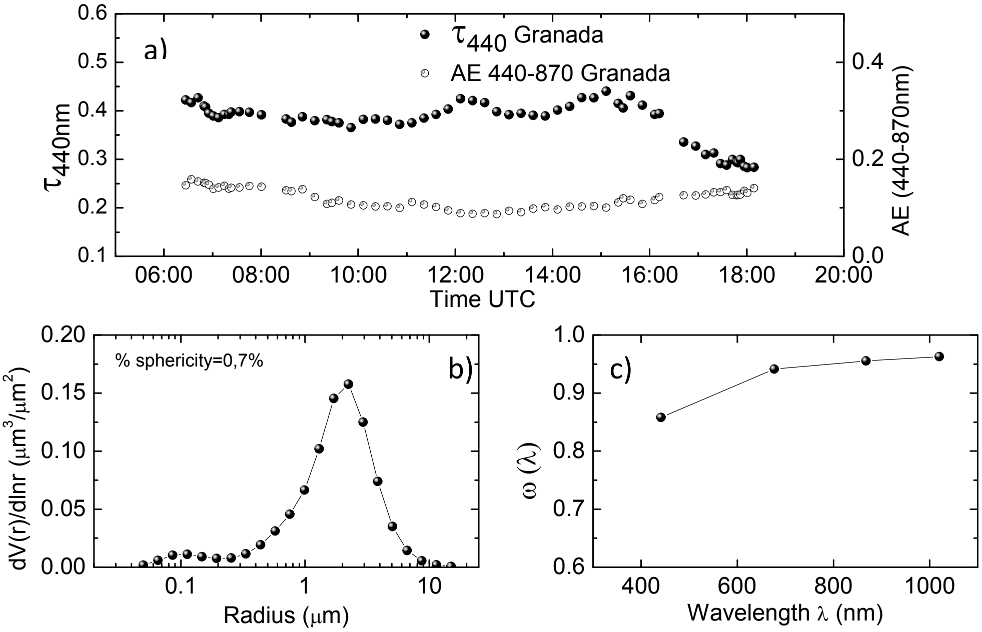

Figure 4.10. As Figure 4.6 but for the 3rd August 2012. AERONET inversion data corresponds to 15: 22 UTC.

Lidar data between 14:30 and 15:00 UTC together with AERONET inversion at 15:22 UTC were the inputs for the LIRIC retrieval. A first retrieval was performed using the input parameters described in Table 4.1 for 3rd August 2012. After that, retrievals with variations of the user-defined input parameters as described in section 3.3 were also obtained. As no coarse spherical and almost no fine particles were obtained, only results of the test applied to the coarse spheroid mode volume concentration profile are shown here. Figure 4.11a shows the mean profile and the standard deviations (error bars) of the coarse spheroid volume concentration profile obtained from three different retrievals varying z_{N0} (1080, 1280 and 1520 m a.s.l.). As in the previous case, variations of z_{N0} produced quite high uncertainties in the profile, up to 25%. However, in this case maximum uncertainties were observed at 5000 m a.s.l. where the maximum concentration was obtained and not in the lower part of the profile.

Figure 4.11b shows the uncertainties calculated varying the reference height (6000, 6200, 6400 m a.s.l.) while keeping constant the other input parameters as in Table 4.1. The uncertainties reached maximum values of ~2%, indicating that LIRIC properly corrects the possible influence of aerosol backscatter at the reference height. It is interesting to point out that in this case, when varying $\mathrm{z_N}$ up to 6800 m a.s.l. uncertainties of the order of 17% appeared in the profile. This did not occur in the other two cases presented here and could indicate that the internal correction of the backscatter ratio at height $\mathrm{z_N}$ presents some difficulties at high altitudes, due to the low signal to noise ratio.

For $\mathrm{z_U}$, 6150, 6350 and 6550 m a.s.l. values were used. Uncertainties were very similar to those obtained by varying the reference height. The unrealistic offset observed in the previous case is much lower in this case for the spheroid mode.

For the regularization parameters (Figure 4.11d), values were changed just as in the previous case by combining increases and decreases of the original *k* and *f* parameters in one order of magnitude and varying *d* between 1 and 5. Five different sets of regularization parameters were used, always satisfying that the column integrated volume concentration of each mode did not differ more than 5% of the ones provided by AERONET. The different values of the regularization parameters used lead to rather low standard deviations, with values around 10%.

For the lower limit and the regularization parameters, the largest uncertainties appeared always at the maximum located around 5000 m a.s.l. The lowest uncertainties were obtained when varying $\mathrm{z_N}$ and $\mathrm{z_U}$ and the highest were again obtained for the variations in the lower limit height $\mathrm{z_{N0}}$.

Figure 4.11e shows the averaged profiles obtained from the 14 retrievals obtained varying the input parameters as in figures 4.7a-4.7e. Relative errors are below 20% in the entire profile, with maximum values around 5 km a.s.l.

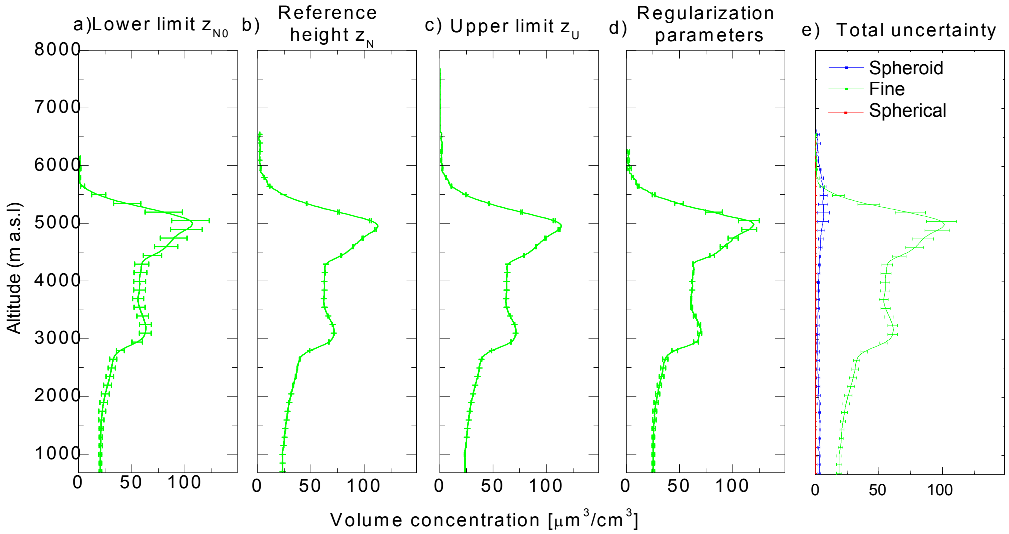

Figure 4.11. As Figure 4.7, but for the 3rd August 2012.

Volume concentration profiles clearly indicate a predominance of the coarse spheroid mode, with larger concentration values between 2.7 and 5.6 km a.s.l. A maximum of 90 $\mu m^3/cm^3$ was obtained around 5 km a.s.l. Some fine particles were also found along the profile, but its volume concentration was almost negligible (10 $\mu m^3/cm^3$ at a maximum around 5.1 km a.s.l.) compared to the coarse spheroid mode. As in the previous case, the total coarse mode retrieved without including the 532-nm cross-polarized channel is in agreement with the coarse spheroid mode shown in Figure 4.7e, with discrepancies below 2%.

Figure 4.12 shows β_{λ}^{aer} profiles obtained from the Klett-Fernald method using the lidar data and those retrieved from the volume concentration profiles retrieved from LIRIC. Agreement in this case was much better for 532 and 1064 nm than for 355 nm. An unusual increase of β_{λ}^{aer} with wavelength was observed for the profiles retrieved from LIRIC, with the largest values for 1064 nm and the lowest for 355 nm, which in turns led to negative β-AE profiles (Figure 4.12f). However, this unusual wavelength dependence was not obtained with Klett-

Fernald (β-AE~0). The α-AE obtained from LIRIC retrievals also presented positive values (Figure 4.12f). The spectral dependence of β_{λ}^{aer} obtained from LIRIC was also observed in previous studies in cases of predominance of coarse particles. *Wagner et al.* [2013] suggested that this dependence might be caused by uncertainties of the spheroids model by AERONET, especially for scattering angles of 180º. On the other hand, this dependence is in full agreement with the microphysical model used for describing the light scattering of non-spherical aerosol and no better model has been identified at present. As it was observed in the previous case, the β_{λ}^{aer} is more influenced by the assumed model than the extinction profile due to the calculations of the lidar ratio as indicated in Eq. 4.11.

The δ_{532nm}^{P} profile at 532 nm calculated from LIRIC outputs were compared with the ones obtained from the lidar data using the approach described in *Bravo-Aranda et al.*, [2013]. The δ_{532nm}^{P} values obtained from lidar data are around 17%, revealing the presence of mixed or aged mineral dust [*Freudenthaler et al.*, 2009]. Below 3 km a.s.l., the δ_{532nm}^{P} decreased, indicating higher contribution of anthropogenic or marine particles in agreement with the backward trajectory analysis performed with the HYSPLIT model. The δ_{532nm}^{P} retrieved from LIRIC outputs was also in this case lower (15%) above 2.5 km a.s.l., although the discrepancies are within the uncertainty. Below 2.5 km a.s.l. both δ_{532nm}^{P}profiles presented almost the same values, decreasing from 15 to 10%. Nevertheless, δ^{P} derived from LIRIC presented almost constant values along the profile. Discrepancies between both approaches in computing δ_{532nm}^{P} can be explained in the same terms as in the previous case.

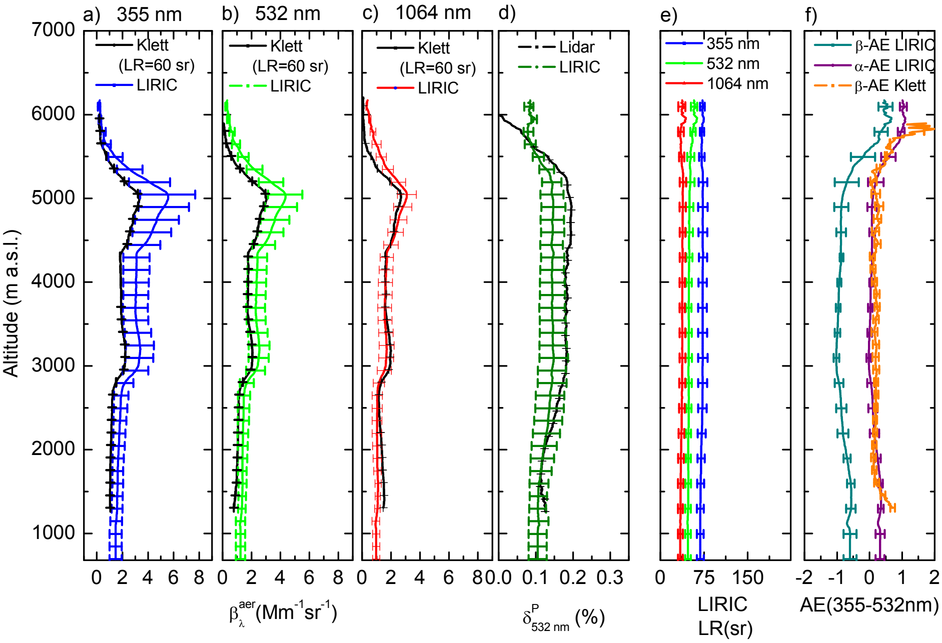

Figure 4.12. As Figure 4.8, but for the 3rd August 2012.

4.3.2.3 Mineral dust, smoke and pollution case: 10th September 2012

On 10th September 2012 a mixture of pollution, dust and smoke was observed over Granada. As can be seen from the lidar range-corrected signal time series in Figure 4.13a, the aerosol layer reached up to 4 km a.s.l. The HYSPLIT model (Figure 4.13b) indicated that the air masses came from the Mediterranean area in the lower part and from the Atlantic Ocean crossing over Africa at higher altitudes. The NAAPS forecasting model (Figure 4.13c) indicated the presence of both sulphates and smoke over Europe and the Mediterranean basin and a slight presence of dust at Granada. No BSC-DREAM8b data were available for this day. Active fire data obtained from the Web Fire Mapper of the FIRMS (Fire Information for Resource Management System, http://maps.geog.umd.edu/firms) [*Davies et al.,* 2009] are shown in Figure 4.13d. Several sources of active fires in

North Africa and the Southern Iberian Peninsula were close to the backward trajectories of the air masses arriving at Granada.

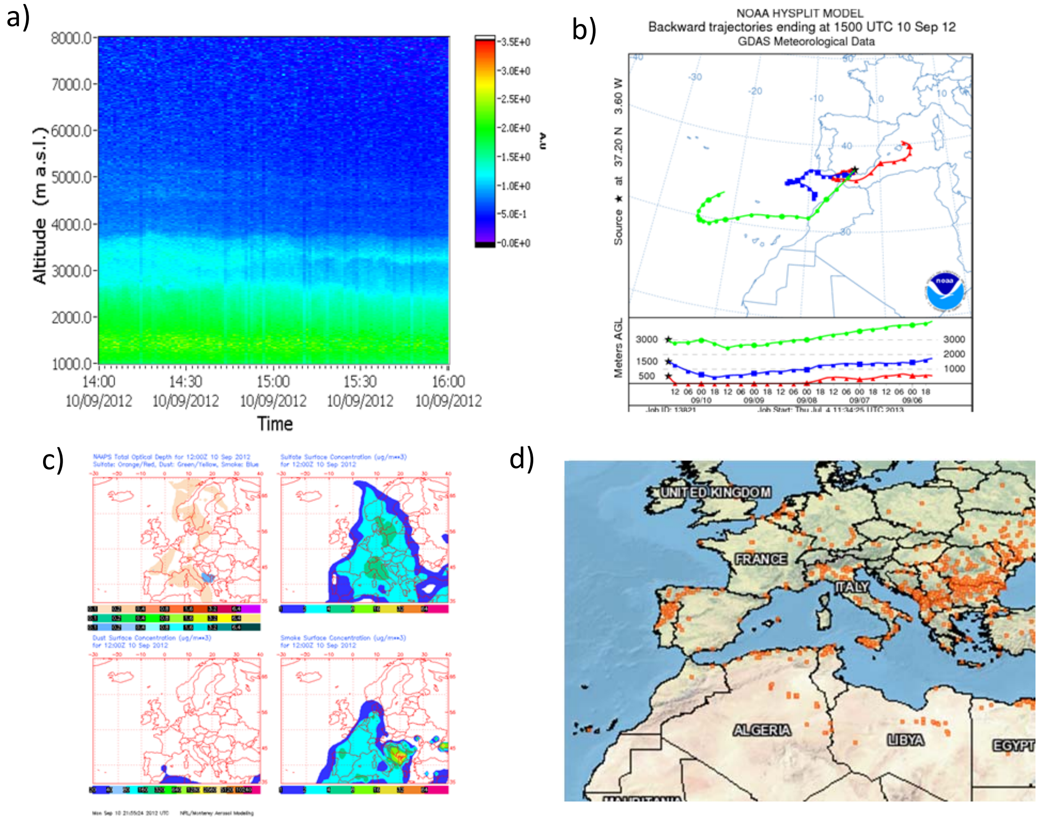

Figure 4.13. a) Time series of the lidar range corrected signal at 532 nm for the 10th September 2012. b) 5-day backtrajectories of the air masses arriving over Granada the same day at 15:00 obtained with HYSPLIT model. c) NAAPS forecast for the same date at 12:00 UTC over Europe. d) MODIS FIRMS image indicating the active fires during the three previous days to the 10th September 2012.

According to the AERONET data, the aerosol load was not very high over Granada, with τ_{440} values around 0.20 and almost constant along the day (Figure 4.14a). Values of AE(440-870 nm) were also constant oscillating between 0.9 and 1.1. The aerosol fine fraction is 0.45, indicating a mixture of both fine and coarse particles. Aerosol size distribution retrieved at 15:56 UTC (Figure 4.14b) showed that the coarse mode almost doubled the fine one, both presenting rather low values. The ω(λ) presented an almost neutral, slightly decreasing trend with λ and values around 0.85, suggesting the presence of a mixture of dust and smoke over Granada (Figure 4.14c) [*Dubovik et al.,* 2002].

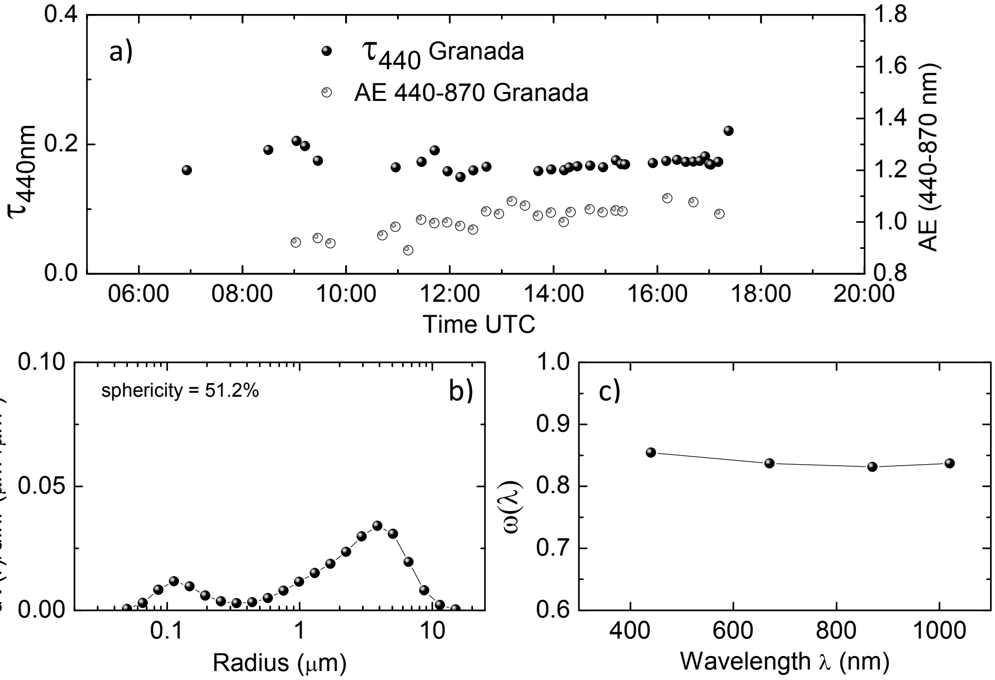

Figure 4.14. As Figure 4.6 but for the 10th September 2012. AERONET inversion data corresponds to 15: 56 UTC.

Averaged lidar data between 15:30 and 16:00 UTC were combined with AERONET inversions at 15:56 UTC to retrieve the microphysical properties of the profiles. The initial set of user-defined input parameters is summarized in Table 4.1. Retrievals with variations of the parameters in Table 4.1 were performed to test the stability of the algorithm for this case under the presence of dust, smoke and pollution, and low aerosol load. Figure 4.15a shows the uncertainties obtained from three different retrievals using the parameters from Table 4.1 but varying z_{N0}. The values provided were 1175, 1385 and 1580 m a.s.l. The highest uncertainties were obtained for the fine mode in the lower part of the profile (relative deviations around 25%). For the coarse spheroid mode the uncertainties were much lower, with maximum values around 5% in the lower part of the profile. For the coarse spherical mode the entire profile presented uncertainties around 1%.

In Figure 4.15b, the mean profiles and standard deviations were obtained from three different retrievals with the input values from Table 4.1 but varying z_N between 3750 and 4150 m a.s.l. z_N variations in this case introduced very low uncertainties, lower than 1% in the entire profile for the three modes as in the previous cases.

For this case z_U values chosen for the three retrievals varied between 3900 and 4300 m a.s.l. Variations in z_U introduced high uncertainties in the lower part of the profile, around 20% for the fine mode, 5% for the coarse spherical mode and below 1% for the coarse spheroid mode (Figure 4.15c). Fine and coarse spherical modes presented higher uncertainties when varying the upper limit due to the unrealistic offset introduced by the algorithm in the molecular height-range for these two modes.

The regularization parameters were modified as in the two previous cases, obtaining five different retrievals corresponding to five different sets of values (Figure 4.15d). They introduced very low uncertainties for the three modes (lower than 2% in the entire profile).

The LIRIC mean volume concentration profiles, obtained taking into account all the retrieved profiles with all possible variations are, shown in Figure 4.15e. The largest uncertainties were obtained for the fine mode in the lower part of the profile with uncertainties around 20%. For the coarse spherical and coarse spheroid mode uncertainties were much lower, with maximum values (~10%) also in the lower part of the profile.

For this case, the largest uncertainties were again caused by variations in the lower limit height z_{N0}. Very low uncertainties (below 2%) were obtained when varying the regularization parameters and the reference height. As in the pollution case, the largest deviations were obtainedin the lower part of the profile.

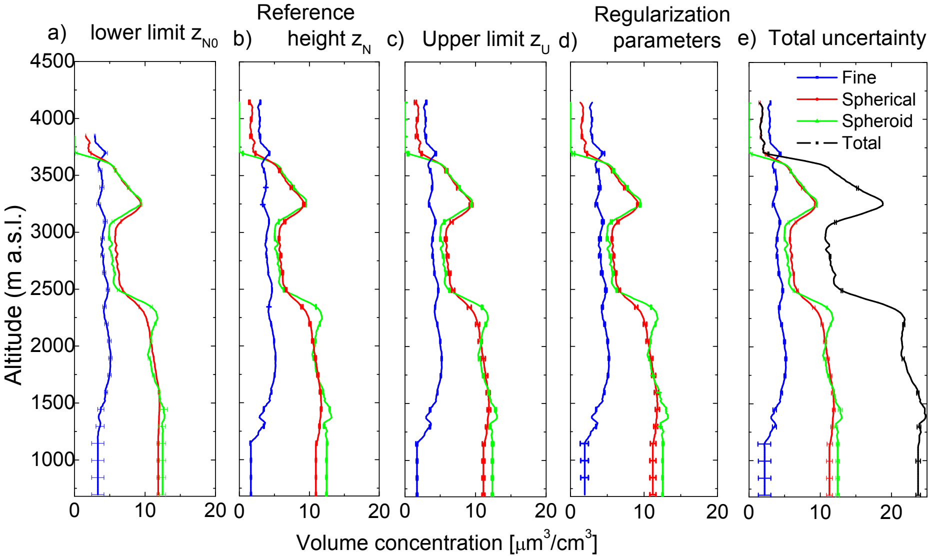

Figure 4.15. As in Figure 4.14, but for the 10th September 2012. The total coarse mode profile (black line) in e) is retrieved without using the 532-nm cross-polarized channel from lidar data.

There were mainly coarse particles of both modes (spherical and spheroids) with similar contribution. The sum of spherical and spheroid particles presented a very good agreement with the total coarse volume concentration profiles obtained without using the 532-nm cross-polarized channel, with differences lower than 4%. Maximum concentration values, reaching 12 μm^3/cm^3 for both the spherical and the spheroid modes, were obtained below 2500 m a.s.l. Above this altitude a maximum peak of 10 μm^3/cm^3 was observed around 3200 m a.s.l. A slight and almost constant (~5 μm^3/cm^3) contribution of the fine mode was observed in the entire profile. Above 3750 m a.s.l. the volume concentration was expected to be zero as indicated by the lidar elastic signals, but a positive offset was also clearly observed in this case for the fine and coarse spherical mode. This offset is larger for the fine mode, which is the one with the lowest volume concentration along the profile.

Figure 4.16 shows the comparison between optical properties of the profiles. In the case of the β_{λ}^{aer} profiles differences were larger for the infrared channel, whereas a good agreement in the visible and ultraviolet was found. The lidar ratios profiles retrieved with LIRIC presented values similar to those used in the Klett-Fernald method. For this case, negative values of the β-AE retrieved with LIRIC were obtained, especially in the part of the profile below 2500 m a.s.l. where the ratio of coarse to fine particles is larger. However, the value of α-AE retrieved with LIRIC and that of β-AE retrieved with the Klett-Fernald method were positive and closer to the column integrated value provided by AERONET.

The δ_{532nm}^{P}profile, as in the two previous cases, was lower when obtained from LIRIC outputs. Discrepancies in this case are quite remarkable, since δ_{532nm}^{P} obtained from the lidar data according to *Bravo-Aranda et al.* [2013] was twice the obtained from the LIRIC retrievals. For both profiles, values were almost constant with height, being 5% according to LIRIC retrievals and over 10% according to lidar data.

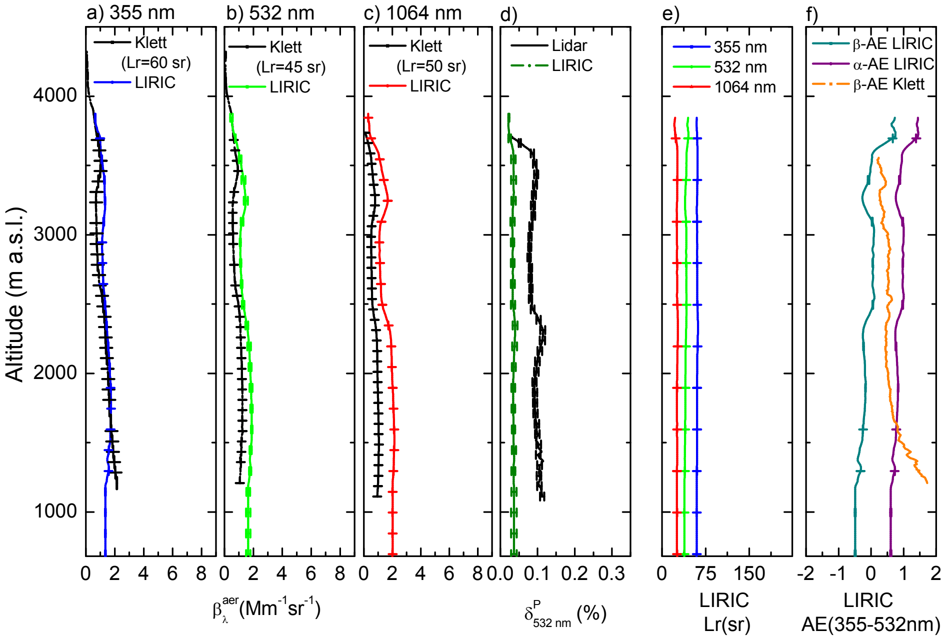

Figure 4.16 .As Figure 4.8, but for the 10th September 2012.

From the results of the analysis of the uncertainties in the volume concentration profiles, for the three different cases representatives of different atmospheric conditions, it was observed that relative uncertainties are up to 33%. However, they are usually below 15%. Uncertainties in the lower part of the profile (which is likely to be more affected by the assumption of a constant volume concentration value below z_{N0}) are highly dependent on the vertical structure of the aerosol layers. In the absence of aerosol layering in this part of the profile, close to the surface, the uncertainties are not very high, as in the dust case from the 3rd of August 2012. However, uncertainties can reach very large values if the aerosol in the lower region is not well mixed and presents a complex layering, as occurred on 22nd May 2011 and 10th September 2012. A way to reduce the uncertainty produced by this parameter could be the use of a near field telescope in order to reduce the effects of the incomplete overlap. For those cases with low aerosol load (τ_{440nm}<0.25) and the aerosol restricted to a lower altitude (<4000 m a.s.l.) uncertainties due to the regularization parameters and the reference height are very low, with values below 2%. However, for the dust case, with a larger aerosol load (τ_{440}=0.45) and located from the surface up to 5500 m a.s.l. the influence of these two parameters are much higher (~15%). Low uncertainties are expected when varying the reference height z_N since the algorithm considers the possible influence of aerosol backscatter in this molecular region and corrects it at the end of the process. For the pollution and smoke cases the algorithm correctly processes the backscattering ratio at z_N in the different retrievals and the uncertainties were actually very low. However, for the dust case the convergence is lower due to the larger signal to noise ratio at higher altitudes.

The unrealistic offset introduced by the algorithm in the upper part of the profile was observed in the three study cases. The presence of this offset may be related to underestimations in the molecular extinction profiles in TropoExport, which may lead to an overestimation of the aerosol volume concentration in the molecular height range. The unrealistic offset usually presented larger values for those modes with lower concentrations. The uncertainties due to variations in the upper height limit of the profile z_U were highly dependent on this offset, being almost negligible when the offset was not observed.

When comparing the sum of the coarse spherical and coarse spheroid volume concentration profiles retrieved using the 532-nm cross-polarized channel as input data with the total coarse mode retrieved without the 532-nm cross-polarized information the agreement is very high, with differences below 5% in the whole column. The fine mode profiles are almost equivalent.

The aerosol backscatter coefficient profiles retrieved from LIRIC outputs and the ones obtained from the Klett-Fernald method presented some discrepancies, especially related to differences in the lidar ratio. Negative β-AE retrieved with LIRIC were obtained in the dust case and mixed dust, smoke and pollution case. This spectral dependence was also observed by *Wagner et al.*, [2013]. It appears only in those cases with a predominance of the coarse mode. If the volume concentration profiles of the fine mode present larger values, LIRIC retrieved β-AE presents positive values, as in the pollution episode analysed here. *Wagner et al.* [2013] suggested that this unusual increase of the aerosol backscatter coefficient with wavelength is caused by the AERONET spheroids model which used to account for difference of light scattering by non-spherical particles for large scattering angles (θ > 120º) [*Dubovik et al.*, 2006]. In case of lidar, θ = 180°, the AERONET data do not have observations at this scattering angle and cannot be used to validate the performance of the spheroid model in backscattering. On the other hand, *Dubovik et al.* [2006] showed that the spheroid model accurately reproduces laboratory measurements of mineral dust phase function for scattering angles from 5° to 173° and, at present, no other model has been suggested as a better alternative. It is also clear, that the spheroid model improves the accuracy in the retrieval of both columnar properties from AERONET measurements and vertical aerosol profiles from lidar observation compared to the model of spheres. At the same time, more efforts are needed for clarifying the validity and limitations of the spheroid model used in the lidar applications and for identifying alternative and superior microphysical models.

δ^{P}_{532nm} profiles retrieved from LIRIC outputs and those retrieved from lidar data presented important discrepancies. In general, larger values were obtained from the lidar data. As indicated before, these differences can be explained by the approach followed in LIRIC.

4.4 Hygroscopic properties

The study of water uptake by atmospheric aerosol is of high importance since it affects the aerosol optical and microphysical properties. There are already several studies about aerosol hygroscopicity, but they were mostly performed in laboratory using in-situ instrumentation and controlled conditions. Lidar systems can also provide useful information about aerosol hygroscopic properties under the right conditions. Opposite to the in-situ measurements, lidars present a main advantage as they can provide vertically resolved measurements without modifying the aerosol sample or its surroundings. They also detect RH close to saturation, which is of great importance since the range between 85 and 100% relative humidity is where the particles are more affected by hygroscopic growth. In the past years, some studies have already been performed using lidar systems to detect aerosol hygroscopic growth obtaining satisfying results [*Ferrare et al.*, 1998; *Wulfmeyer and Feingold*, 2000; *Feingold and Morley*, 2003; *Veselovskii et al.*, 2009]. However, all these studies present the major drawback that some assumptions were necessary to obtain the relative humidity profiles. In this work, a methodology to study aerosol hygroscopic growth based on lidar data and collocated radiosounding relative humidity profiles is established. The availability of collocated radiosounding data allows for reducing the number of assumptions. In addition, radiosounding presents the advantage of a higher vertical resolution in comparison with some other instrumentation, i.e. microwave radiometers. However, the availability of radiosounding data is quite reduced since most of the stations only perform radiosounding launches during some specific campaigns. Furthermore, stations with daily radiosounding data available perform only one or two launches per day (usually at midday and midnight). In this study, a total of 50 radiosondes were launched in the period 2011 to 2013 during specific campaigns in summer and winter, together with some occasionally launches when adequate conditions for hygroscopic growth were expected.

To retrieve the aerosol hygroscopic properties from lidar data, it is necessary to get measurements in an atmospheric column where there is an increase in RH large enough to observe an increase in the aerosol optical (or microphysical) properties detected by the lidar system due to the aerosol water uptake. Therefore, for the study of hygroscopic properties, simultaneous lidar data together with the RH profiles obtained from collocated radiosoundings are needed.

From the lidar data, β_{λ}^{aer} profiles are obtained by applying the Klett-Fernald inversion algorithm explained in section 4.1.1 [*Fernald*, 1984; *Fernald et al.*, 1972; *Klett*, 1981, 1985]. β-AE(355-532nm) and the δ^{P}_{532nm} are also calculated.

Only those cases with a simultaneous increase in the atmospheric aerosol optical properties (i.e. β_{λ}^{aer}) and the RH profiles are considered as potential cases of hygroscopic growth.

For these potential cases, it is necessary to verify that in the height range analysed the aerosol presents certain degree of homogeneity. In this way we can assume that the increase in the aerosol properties is caused by the increase in the aerosol size due to water uptake and not due to changes in the aerosol composition. That means that the same aerosol type or mixture must be present along the analysed height range and no variations in the aerosol load must exist. For this purpose, ancillary information such as the backward trajectories of the air masses, the profiles of potential temperature, θ, or the water vapour mixing ratio profiles, *r,* are used.

Backward trajectories analyses with the HYSPLIT model [*Draxler and Rolph*, 2003] are performed. These analyses are mainly used as a selection criterion. If the origin and the trajectory of the air masses are independent of the altitude in the height range analysed, it is considered that the same aerosol type might have been advected above the experimental site and, therefore, a homogenous aerosol composition might be expected. Otherwise, variations in the aerosol composition are expected and the case is not considered for the analysis, as indicated in *Veselovskii et al.* [2009].

In addition, good mixing is required as a boundary condition in order to guarantee the homogeneity of the aerosol composition and load in the investigated layer. Constancy in θ and r profiles is considered as an indicator of well mixed conditions within the layers. Both atmospheric variables are obtained from the radiosounding data.

If the requirements of homogeneity on the atmospheric aerosol composition and load are fulfilled, the selected cases are analysed to study the hygroscopic properties of the atmospheric aerosol. For this purpose, the enhancement factor is computed in the selected height range from a combination of aerosol optical (or microphysical) properties and the corresponding RH values at the same height. The enhancement factor is defined in an analogous way to Eq. 2.37:

$$f_{\zeta}(RH) = \frac{\zeta\,(RH)}{\zeta\,(RH_{ref})} \qquad \textit{Eq. 4.21}$$

where ζ represents a certain optical (or microphysical) aerosol property. RH_{ref} is the reference relative humidity and in the it is usually chosen as the lowest value of RH in the profile from the radiosounding. For this study, $f_{\zeta}(RH)$ is obtained for β_{λ}^{aer} profiles ($f_{\beta}(RH)$) and the volume concentration profiles retrieved with LIRIC ($f_{VC}(RH)$).

For the different cases, the ranges of RH and, as a consequence, RH_{ref} values are different since they are dependent on the ambient conditions. Therefore, in order to make the different results comparable it is necessary to use a common RH_{ref} value. For this purpose, the Hänel model [*Hänel*, 1976] defined in section 2.6. is used to parameterize the experimental enhancement factor curves. As explained in section 2.6, several parameterizations of the Hänel model have been proposed in previous studies [*Kotchenruther and Hobbs*, 1998; *Kotchenruther et al.*, 1999; *Raut and Chazette*, 2007; *Veselovskii et al.*, 2009]. In this study, the one described in *Veselovskii et al.* [2009] is the one that provides the best fit, being the one selected in this study. The general form of the Hänel equation (Eq. 2.37) is particularized here for the lidar-retrieved backscatter coefficient β_{λ}^{aer}, and expressed as:

$$f_{\beta}(RH) = \left(\frac{1 - RH}{1 - RH_{ref}}\right)^{-\gamma} \qquad \textit{Eq. 4.22}$$

where the γ value is an indicator of the hygroscopicity of the particles, as previously explained.

5 LIRIC applications

5.1 CHARMEX campaign

CHARMEX (Chemistry-Aerosol Mediterranean Experiment) is an international project involving several Mediterranean countries which aims at developing and coordinating regional research actions for a scientific assessment of the present and future state of the atmospheric environment in the Mediterranean Basin, and of its impacts on the regional climate, air quality, and marine biogeochemistry (http://charmex.lsce.ipsl.fr/). This region is of huge interest since multiple studies indicate that aerosol radiative forcing over the Mediterranean region is one of the largest in the world [*Lelieveld et al.*, 2002; *IPCC*, 2007]. Through seven work packages, CHARMEX addresses: (i) emissions and source apportionment; (ii) chemical ageing of air masses with focus on the formation of secondary organic aerosols; (iii) transport processes and their effect on air quality; (iv) direct radiative forcing by aerosols and its consequences on the water budget and regional climate; (v) deposition of nutrients and contaminants; (vi) recent trends in atmospheric composition and variability; and (vii) future evolution of atmospheric chemistry at the horizon 2030 and 2050. In the case of lidar data there is a special interest in obtaining a real database with vertical resolution for checking 3-D modelling of African mineral dust aerosol radiative impact over the Mediterranean basin.

Partners involved in CHARMEX project include primarily French institutions as it is a French initiative. These institutions are namely the CNRS-INSU (National Institute for Earth Sciences and Astronomy of the National Centre of Scientific Research), ADEME (French Environment and Energy Management Agency), CNES (the French national scientific research centre) and Météo-

France, among others. Another institutions involved are IDAEA (Instituto de Diagnóstico Ambiental y Estudios del Agua), Polytechnic University of Catalonia, the University of Granada and the University of the Balearic Islands in Spain, Italian National Agency for New Technologies, ENEA (Energy and Sustainable Economic Development) and the University of Florence in Italy, University of Malta, KIT (Karlsruhe Institute of Technology) in Germany, the University of Cork in Ireland, the University of Bucharest in Romania, CNR-IMAA (Consiglio Nazionale delle Ricerche - Istituto di Metodologie per l'Analisi Ambientale) in Italy, among others.

5.1.1 CHARMEX 2012: Temporal evolution of a dust event

In the context of CHARMEX campaign, in July 201272-hour intensive measurements were performed simultaneously at twelve ground-based lidar stations. The main aim of this exercise was to characterize dynamic processes of polluted air masses transport from source regions over the Mediterranean coast and to quantify the exchanges between the boundary layer and free troposphere above the Mediterranean basin [*Mona et al.*, 2012]. The exercise was held from 9th July at 06:00 UTC to 12th July at 05:00 UTC. Eleven out of the twelve stations are included in ACTRIS/EARLINET network. One additional non-EARLINET station was performing ground-based lidar measurements in Messinia, Greece. Besides the lidar measurements, seven of the stations performed coincident sun photometers measurements following AERONET protocols, i.e. Granada, Évora, Madrid, Barcelona, Bucharest, Potenza and L'Aquila. The raw data from EARLINET stations were automatically treated by the Single Calculus Chain (SCC) developed by the lidar network EARLINET to generate temporal integrated profiles of RCS under cloud-free conditions. Figure 5.1 shows the lidar and sun photometers stations measuring during this 72-hour intensive measurement period.

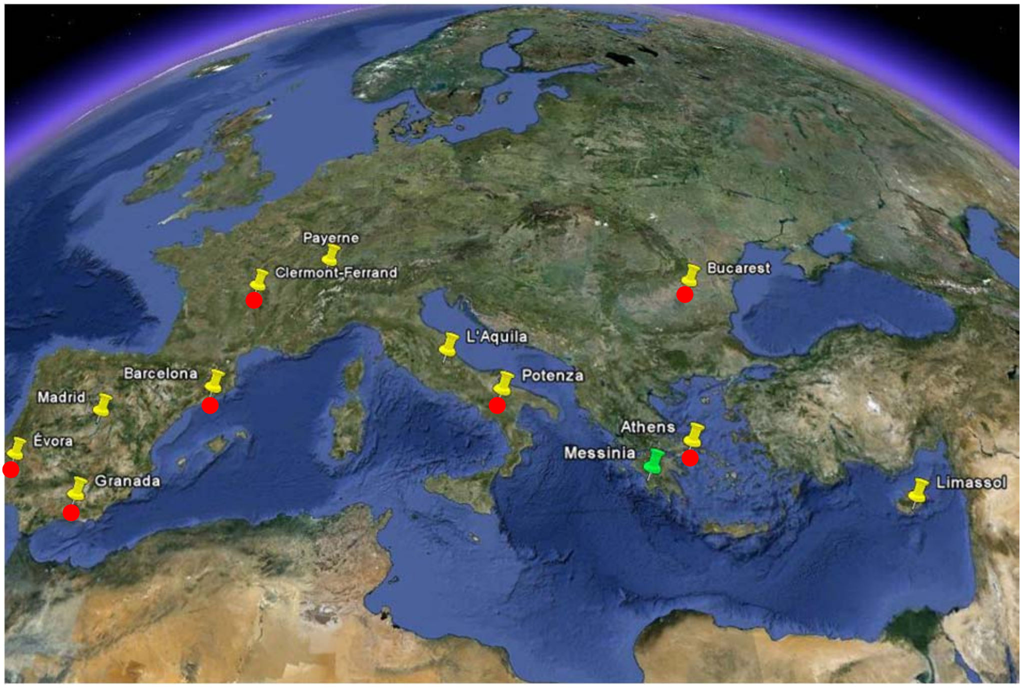

Figure 5.1. Stations measuring during CHARMEX 2012 intensive measurement period on July 2012 campaign. The yellow label indicates EARLINET stations, the green label non-EARLINET stations and the red dots collocated AERONET stations.

In this chapter, the data collected during this CHARMEX 72-hour intensive measurement effort on July 2012 were used to analyse vertical profiles of microphysical properties. By combining lidar measurements and AERONET inversion retrievals at Granada experimental site, volume concentration profiles of fine, coarse spherical and coarse spheroid were retrieved by means of LIRIC algorithm. The main aim of this analysis was to study the temporal evolution of the microphysical properties during the 3-day intensive measurement period.

During this 72-hour measurement period a dust event was observed over the Western Mediterranean Basin, as revealed by different forecast models and by the analysis of the lidar and sun photometer data. According to experimental data, from Granada station, and the model forecast, from the days previous to 9th July (not shown), the dust outbreak over our station started several days before. In this way, it was already well developed when the intensive measurement period started. The dust event was correctly forecast by the NAAPS and BSC-DREAM8b models (Figure 5.2). Both models indicated a stronger presence of dust over Granada station during the first day of the measurements. Then it decreased until 11th July. The 5-day backward trajectories analysis performed with HYSPLIT v.4.9 model indicated that the air masses arriving at Granada on 9th and 11th July came from Africa close to the African coast over 2500 m a.s.l. and from the North Atlantic Ocean through South-western Iberian Peninsula below this altitude (Figure 5.3). On 10th July the air masses came from Central Africa through the North African coast for heights above 5000 m a.s.l.. Furthermore, the air masses came from the Atlantic Ocean going along the coast of Africa over 2500 m a.s.l. while below this altitude they came from the North Atlantic Ocean overpassing South-western Iberian Peninsula.

Figure 5.4 shows the time series of the lidar RCS (arbitrary units) for the 72-hour period. As it is observed, clouds were present above Granada during the whole morning on 9th July. A strong backscattered lidar signal corresponding to aerosol layers was observed during most of the time. These aerosol layers reached altitudes up to 6000 m a.s.l., except for the evening of the 10th of July from 18:00 UTC to 00:00 UTC, when the aerosol layer was confined below 2500 m a.s.l.

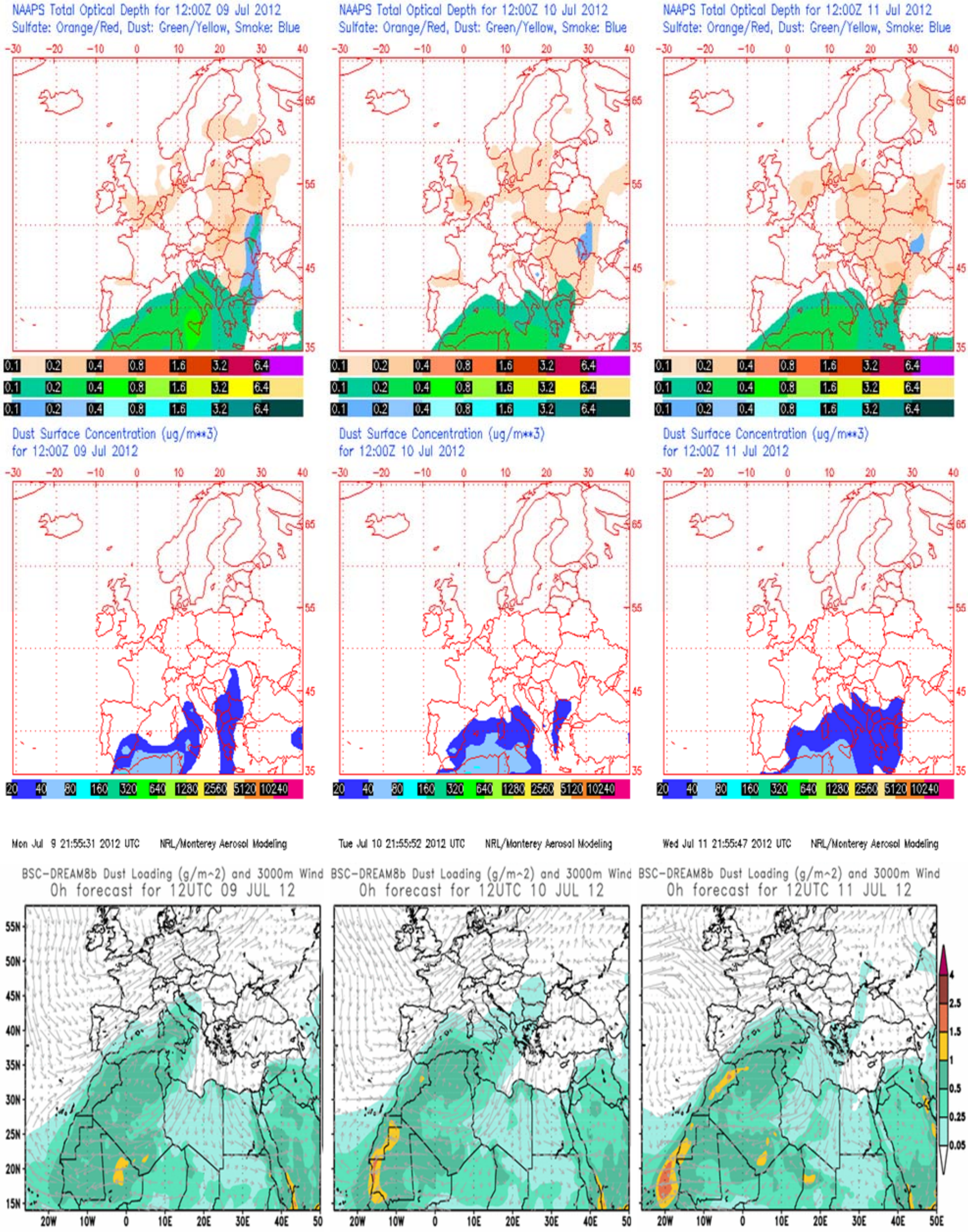

Figure 5.2. a) NAAPS forecast model for 9th, 10th and 11th July 2012 at 12:00 UTC. The upper panels show the total optical depth for dust, smoke and sulphates and the lower panels show the dust surface concentration (units) over Europe. b) BSC-DREAM8b forecast model for 9th, 10th and 11th July 2012 at 12:00 UTC over Europe and North Africa.

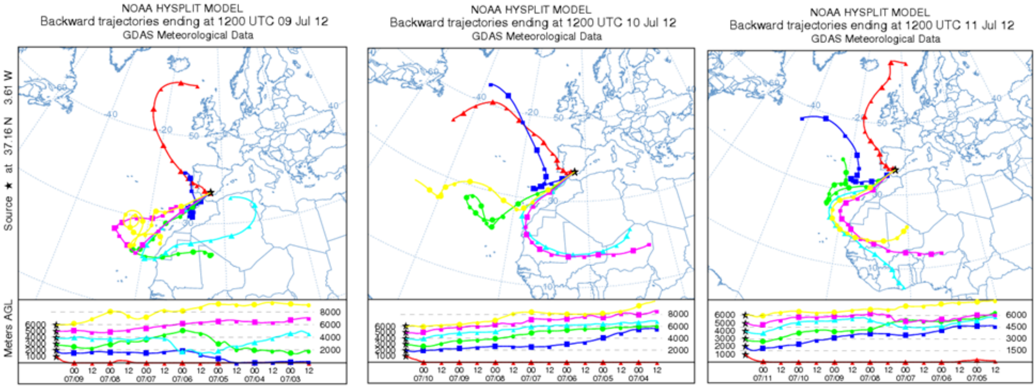

Figure 5.3. 5-day backward trajectories arriving over Granada on 9th, 10th and 11th July 2012 (from left to right) computed by HYSPLIT model.

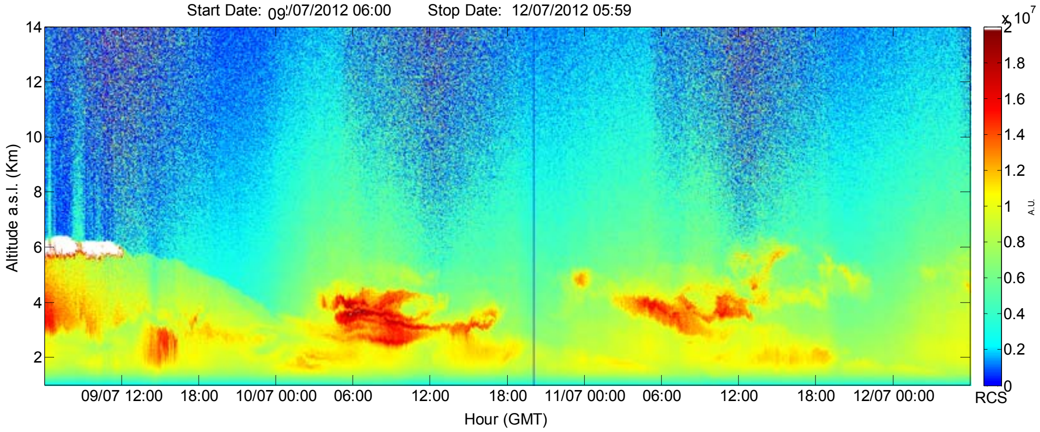

Figure 5.4. Time series of the lidar RCS at 532 nm (arbitrary units) from 9th to 11th July 2012.

Because of the presence of clouds, AERONET Level 1.5 data were not retrieved during the morning on 9th July (Figure 5.5a). However, they were available during the rest of the exercise. τ_{440nm} was larger on 9th July than on 10th and 11th July, with values above 0.20 and reaching a maximum value of 0.40

around 16:00 UTC. During 10th and 11th July, τ_{440nm} values were between 0.10 and 0.20, except for the late afternoon of 10th July from 17:00 UTC, when the aerosol load decreased and τ_{440nm} below 0.10 were observed. The sun photometer AE(440-870nm) was below 0.5 during the whole period except for the 10th July late afternoon, in coincidence with the decrease in τ_{440nm}. The column-integrated volume concentration was decreasing along the whole period with minimum values on 10th July in the late afternoon, as it can be observed in the size distribution plots in Figure 5.5b. There was a predominance of the coarse mode during the whole period, with maximum values of 0.13 $\mu m^3/\mu m^2$ during the first day. The wavelength dependence of $\omega(\lambda)$ indicated a clear predominance of mineral dust on 9th July. During 10th and 11th July $\omega(\lambda)$ values indicated the presence of more absorbing particles in the aerosol mixture. Furthermore, the values of $\omega(\lambda)$ obtained in the afternoon on 9th and 11th presented a different spectral dependence, suggesting aging processes of the mineral dust or mixing with anthropogenic pollution [*Dubovik et al.*, 2002].

The combined use of the lidar data and the AERONET inversion retrievals allowed for an exhaustive 3-day analysis of microphysical properties retrieved with LIRIC. The retrieval of microphysical properties was performed using 30-min averaged lidar data (in order to reduce noise on the lidar profiles) and the closest (in time) AERONET retrieval, considering only those data with time differences lower than two hours. A total of 60 different retrievals were performed based on 60 lidar datasets and 21 AERONET inversion products.

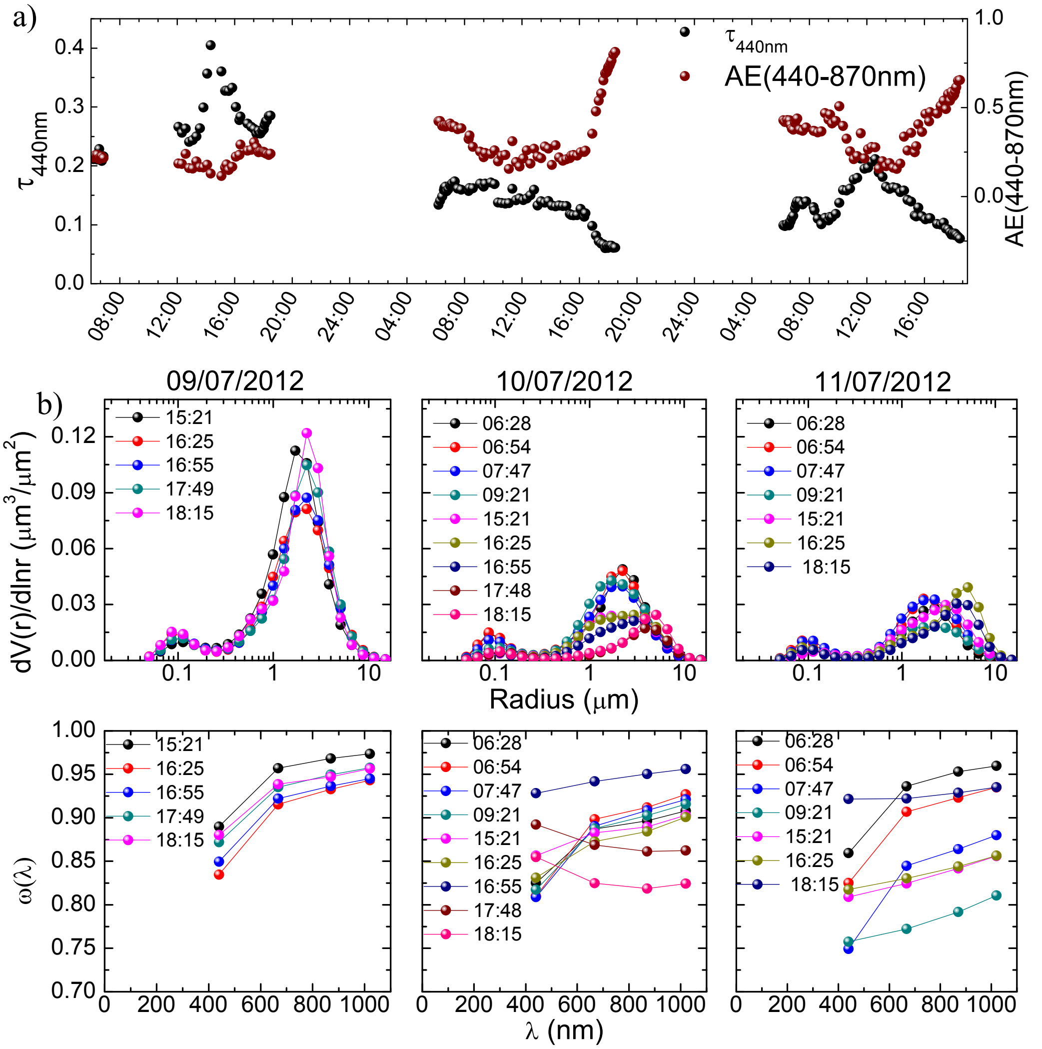

Figure 5.5. a) AERONET Level 1.5 retrieved τ_{440nm} and AE(440-870nm) during CHARMEX 2012 campaign. b) AERONET Version 2 Level 1.5 size distributions and ω(λ)retrieved for 9th, 10th and 11th July (from left to right).

Figure 5.7 shows the time series of the volume concentration profiles retrieved with LIRIC. It is clearly observed that the dust event was decreasing its intensity along the whole study period with the largest aerosol concentrations retrieved on 9th July (~35 $\mu m^3/cm^3$) and the lowest concentrations on 11th July (~15 $\mu m^3/cm^3$), in agreement with AERONET data and model predictions. Maximum values of total volume concentration were around 60 $\mu m^3/cm^3$ on 9th

July. There was a strong predominance of the coarse spheroid mode during the whole period with maximum values on 9th July afternoon, reaching values up to 55 $\mu m^3/cm^3$. Some fine particles were also observed, with larger volume concentrations during the first day (~10 $\mu m^3/cm^3$). For this first day of measurements, fine particles reached altitudes around 6000 m a.s.l, whereas on 10th and 11th July larger volume concentration values were confined to the lowermost region from surface up to 3 km a.s.l. The presence of this fine mode in the upper layers might be related to the advection of anthropogenic pollutants coming from Moroccan industrial activity in the North of Africa mixed with the mineral dust as reported in previous studies [*Rodríguez et al.*, 2011]. Figure 5.6 reveals that air masses overpassed North African industrial areas before reaching Granada. However, it is also possible that this fine mode volume concentration is due to the fine particles from mineral dust. A more detailed analysis with additional data would be needed in order to make out this point.

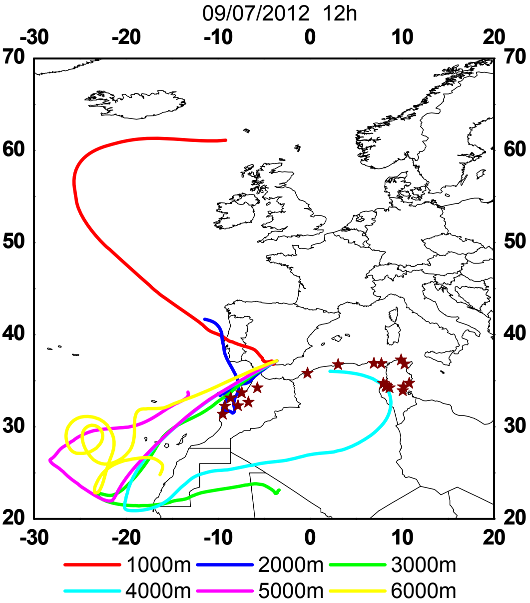

Figure 5.6 Map of location of the main industrial activity in the North of Africa (stars)taken from Rodriguez et al., [2011] together with the 5-day backwards trajectories arriving at Granada experimental site on 9th July 2012 at 12:00 UTC.

The contribution of the fine mode in the lowermost part may be due mainly to anthropogenic sources of local origin. From 11th July around 12:00 UTC up to the end of the study period, an increase in the coarse spheroid mode concentration was observed. This is in agreement with the information provided by the particle linear depolarization profiles δ_{532nm}^{p} obtained from the lidar data according to *Bravo-Aranda et al.,* [2013] (Figure 5.8). On 9th July the values of δ_{532nm}^{p} were around 0.30 in the layer between 3 and 5 km a.s.l. These values are representative of pure Saharan dust [*Freudenthaler et al.*, 2009]. However, they decreased down to 0.25 during the following days, indicating a possible mixing of dust particles or aging processes affecting the mineral dust. During the 11th of July the decrease in the fine mode in coincidence with the increase in the coarse spherical mode suggests the possibility of a coating of the mineral dust particles by the fine ones. This could be associated to the aging of the mineral dust since there is no input of fresh mineral dust particles. On 10th July 2012 this behaviour is also faintly observed in the late afternoon.

According to δ_{532nm}^{p} profiles depicted in Figure 5.8 the mineral dust layer is clearly located above 2500 m a.s.l. or even at higher altitudes depending on the analysed period. In the region closer to the surface, values are lower indicating more contribution of anthropogenic particles. In the case of LIRIC, these vertical structures were not so clearly defined, as very constant contributions of fine and coarse particles with height were observed. This vertical homogeneity is related to the assumption of height independency of properties such as the refractive index, size distribution of the modes or the sphericity, which according to the results presented throughout this dissertation is an issue that needs to be improved in the following versions of LIRIC.

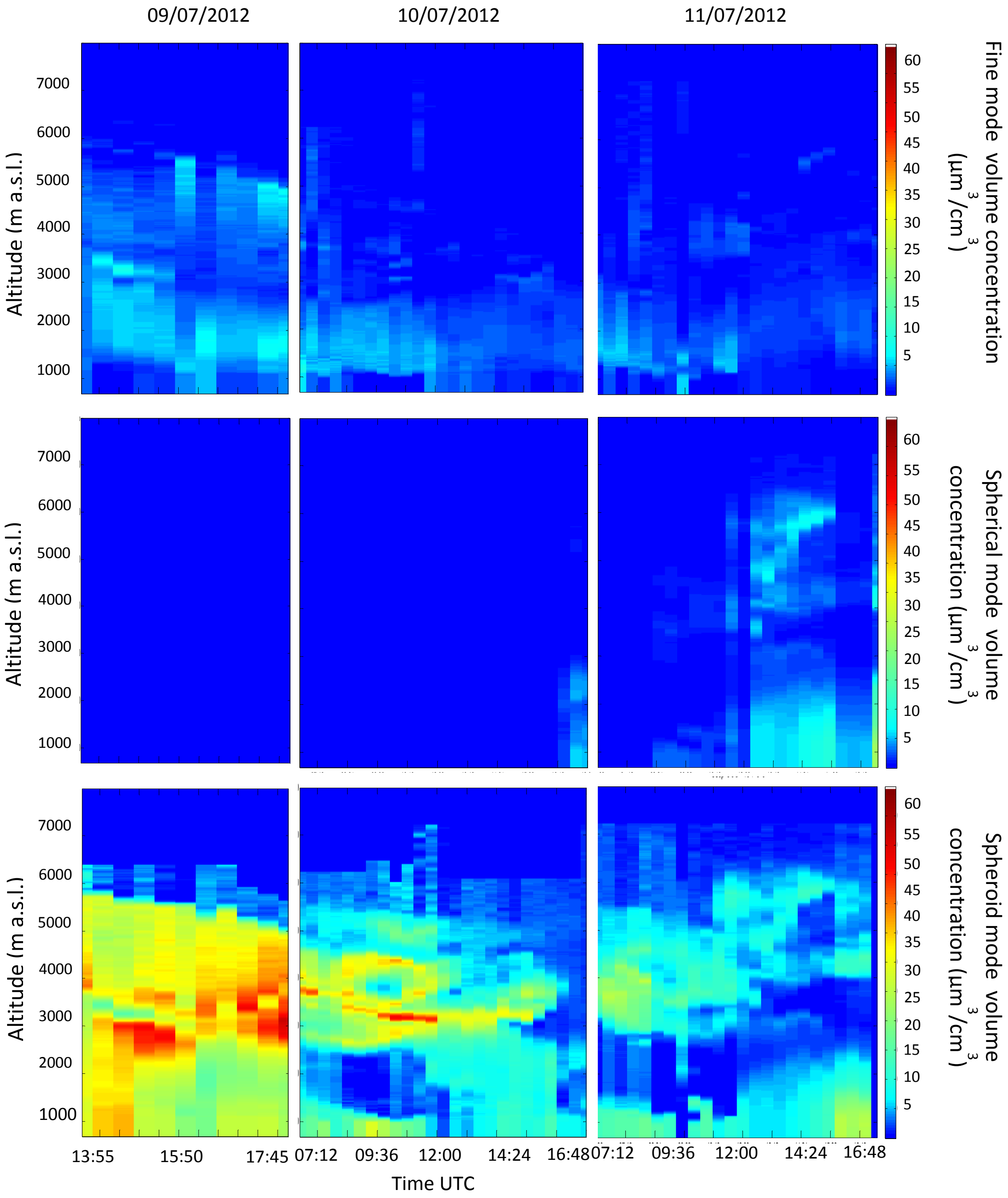

Figure 5.7. Time series of the volume concentration profiles (in µm³/cm³) for the fine mode (upper part), coarse spherical mode (middle part) and coarse spheroid mode (lower part) for days 9th, 10th and 11th of July 2012 (from left to right).

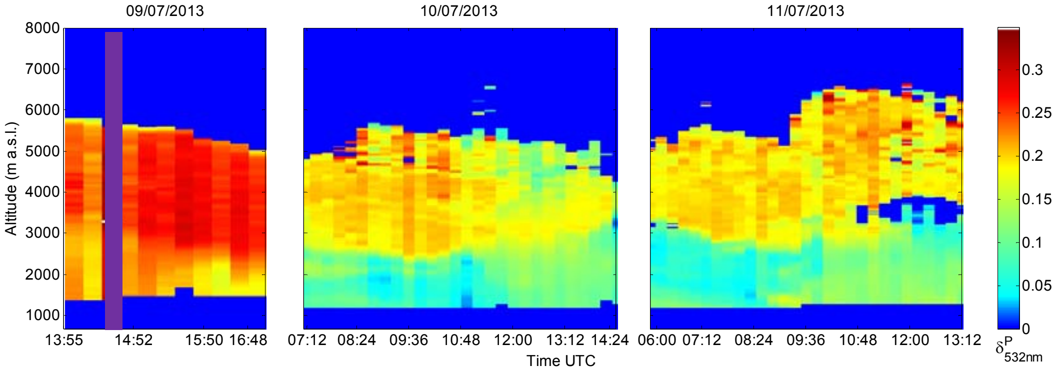

Figure 5.8. Time series of the δ^{P}_{532nm} *profiles retrieved at different time intervals during CHARMEX 2012 intensive measurement period.*

BSC-DREAM8b forecast model data were available during this 72-hour measurement period. Mass concentrations profiles provided by the model were compared with those retrieved with LIRIC. Since LIRIC provides volume concentration profiles a conversion factor was needed to obtain mass concentration. This conversion factor was the density of the aerosol particles used by BSC-DREAM8b model, namely 2.65 g/cm^3 for the coarse mode (1-10 μm) and 2.5 g/cm^3 (0.1-1 μm) for the fine mode [*Pérez et al.*, 2006b, Basart, personal communication]. In addition, the initial vertical resolution of LIRIC was degraded to the one provided by BSC-DREAM8b model by linear interpolation. After this processing, the mass concentration profiles modelled by BSC-DREAM8b were compared with the total volume concentration profiles retrieved with LIRIC since the model considers also the range corresponding to the fine mode. Because mineral dust is usually assumed as spheroid, an additional comparison with the sum of the coarse spheroid mode and the fine mode was performed.

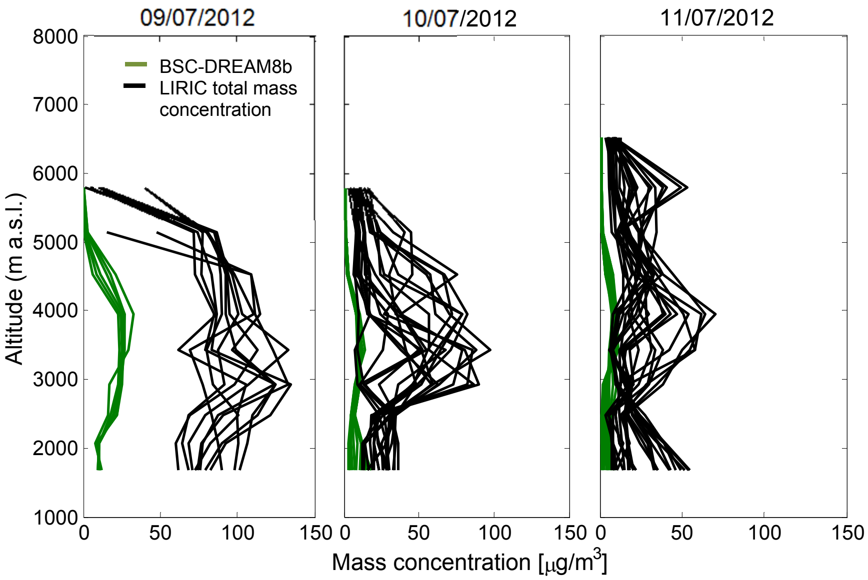

Figure 5.9. Daily evolution of BSC-DREAM8b mass concentration profiles and LIRIC total mass concentration profiles for days 9th, 10th and 11th July 2012.

In a general overview, we can see in Figure 5.9 that during the three days analysed the mass concentration forecast by BSC-DREAM8b was much lower than the one retrieved with LIRIC. This underestimation is clearly related to the underestimation of τ_{550nm} values provided by BSC-DREAM8b model in comparison with AERONET retrieved data (Figure 5.10). As it was pointed out in previous studies [*Basart et al.*, 2012], τ_{550nm} values are underestimated by BSC-DREAM8b model over the Iberian Peninsula. The mean bias value obtained in our analysis is -0.11±0.06, which is in agreement with the value obtained by [*Basart et al.*, 2012] for the Eastern Iberian Peninsula. Aside from the underestimation, Figure 5.9 shows that on 10th and 11th July, BSC-DREAM8b mass concentration was reduced to half with respect to 9th July, as it occurred also with LIRIC mass concentration values. However, the temporal variation of the dust load during the day was not properly followed by BSC-DREAM8b, with very similar column-integrated values of the profiles along the whole day, whereas LIRIC profiles presented a much larger variability, as it occurred also with the τ_{550nm} retrieved with AERONET data (Figure 5.10). As indicated by BSC-DREAM8b forecast model in Figure 5.2, Granada is located at the edge of the event. The non-homogeneity in the horizontal distribution of the dust event may be an additional source for the discrepancies found in this comparison.

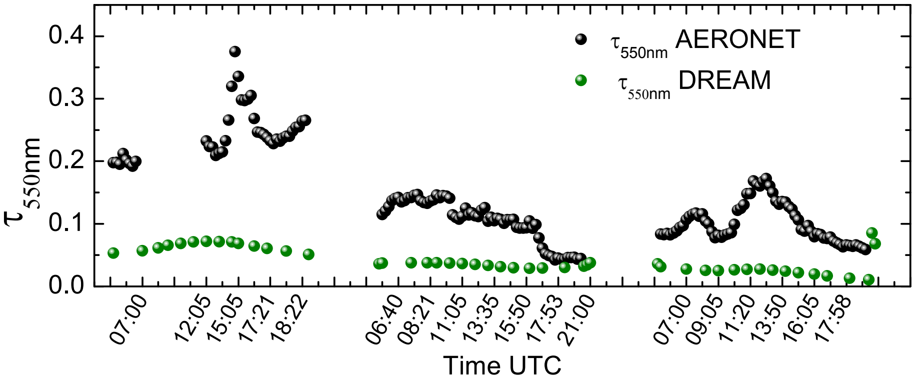

Figure 5.10. Time series of τ_{550nm} provided by BSC-DREAM8b and AERONET data during CHARMEX 2012 campaign.

The mean profiles for the each day and the mean absolute deviations in µg/m^3 are shown in Figure 5.11. On 9th July absolute deviations were much larger (~70 µg/m^3) than on 10th and 11th July (~24 and 18µg/m^3 respectively), when the mineral dust load was much lower. Differences between the LIRIC total volume concentration and the sum of fine and spheroid particles were almost negligible for 9th and 10th July. Nonetheless, on 11th July differences around 5 µm^3/cm^3 are evident since the load of coarse spherical particles on this day was higher as observed in Figure 5.7. The profiles corresponding to the sum of fine and spheroid particles were very similar to the profiles of total volume concentration with the largest differences (only 4µg/m^3) on 11th July.

Once a strong underestimation of the BSC-DREAM8b compared to LIRIC mass concentration values was observed, in order to check if the model correctly retrieves the vertical structure of the dust layers, a supplementary evaluation was performed using normalized profiles. The profiles were normalized to their maximum values and results are shown also in Figure 5.11. The normalized profiles showed that the model determines the structure of the dust layers fairly well on 10th July, with absolute deviation values below 0.1 (in normalized units) except for the lowermost part of the profiles. On 9th and 11th July absolute deviations were much larger (reaching up to 0.5 in normalized units) and it is worthy to point out that BSC-DREAM8b model determined the top of the dust layer around 5000 m a.s.l. whereas LIRIC indicated that the dust layer reached up to 6000 m a.s.l.

Table 5.1 presents the main statistical parameters obtained from the comparisons between the BSC-DREAM8b modelled data and LIRIC retrieved profiles (total volume concentration and spheroid + fine modes) for each day. Slope, intercept and correlation coefficients were obtained from linear fit whereas the absolute deviation and relative deviation were calculated as:

$$AD = \frac{\sum_n \left(C_{mass}^{LIRIC}(z_n) - C_{mass}^{DREAM}(z_n)\right)}{n}$$

$$RD = 100 \cdot \frac{\sum_n \left(C_{mass}^{LIRIC}(z_n) - C_{mass}^{DREAM}(z_n) \big/ C_{mass}^{LIRIC}(z_n) \right)}{n}$$

where n is the number of height levels.

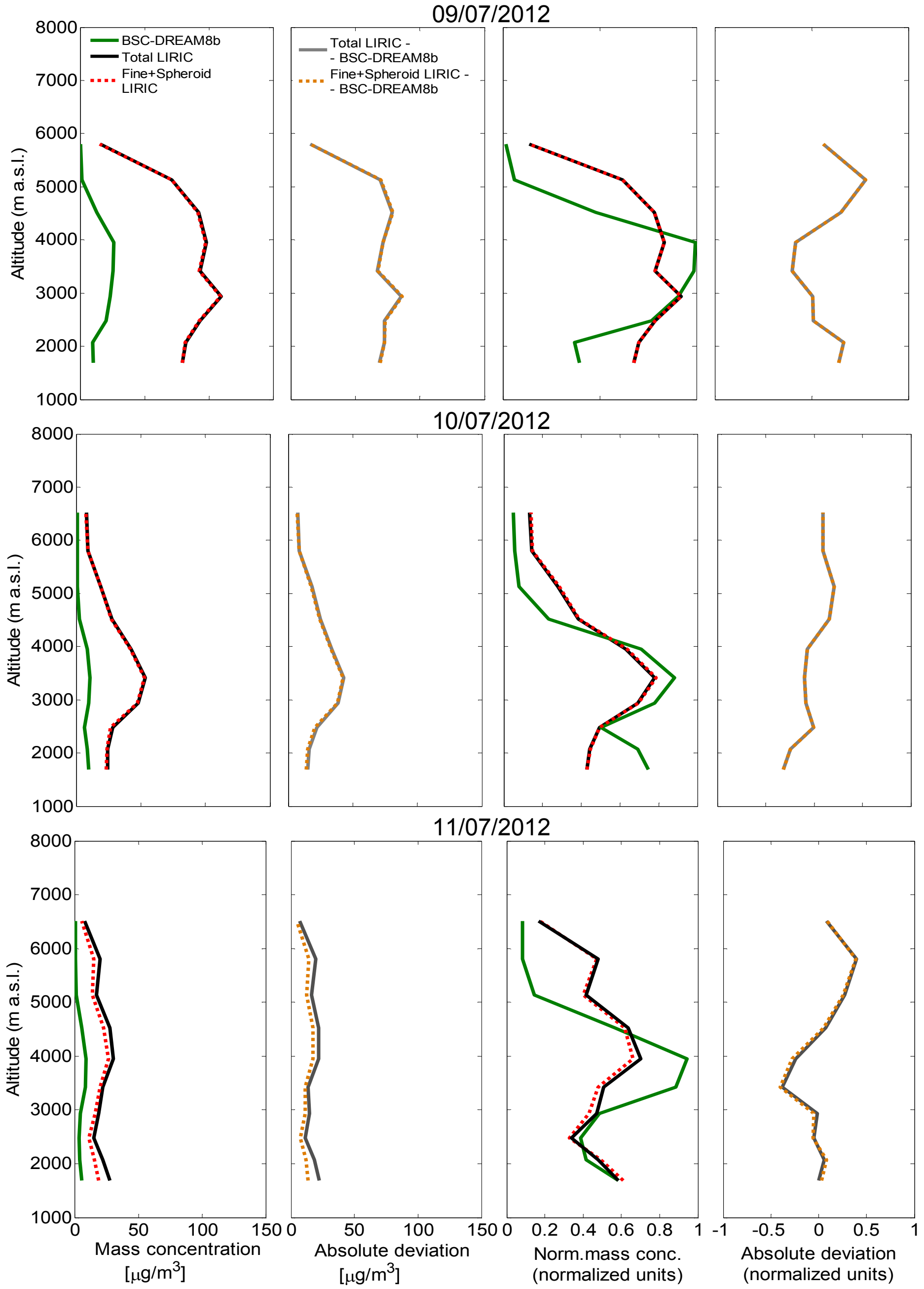

Figure 5.11. (from left to right) Mean BSC-DREAM8b mass concentration (green line), LIRIC total mass concentration (black line) and LIRIC fine + spheroid modes mass concentration (orange line) and the corresponding absolute deviation profiles on 9th, 10th and 11th July 2012. Idem for normalized profiles.

		Slope	Intercept (µg/ m^3)	Correlation coefficient (R)	Absolute deviation (µg/m^3)	Relative deviation (%)	RMSE (µg/m^3)
Day 9	Total	0.22	-3.3	0.64	68	83	72
	Spheroid	0.22	-3.2	0.64	67	83	71
	Total normalized	0.98	-0.1	0.64	0.14	24	0.31
	Spheroid normalized	0.98	-0.1	0.64	0.14	24	0.31
Day 10	Total	0.09	3.5	0.43	24	73	30
	Spheroid	0.09	3.5	0.43	23	71	29
	Total normalized	0.52	0.3	0.43	-0.04	-33	0.34
	Spheroid normalized	0.52	0.3	0.43	-0.04	-33	0.34
Day 11	Total	0.03	4.0	0.14	16	70	21
	Spheroid	0.06	3.8	0.17	12	60	16
	Total normalized	0.19	0.4	0.17	0.02	34	0.40
	Spheroid normalized	0.19	0.4	0.17	0.02	34	0.40

Table 5.1. Statistical parameters obtained from the comparison between LIRIC total mass concentration profiles and LIRIC mass concentration profiles on 9th, 10th and 11th July 2012.

The correlation coefficients presented values between 0.64 on 9th July and 0.17 on 11th July, indicating a low correlation of the profiles. The values obtained on 9th and 10th are similar to those obtained by *Basart et al.,* [2012] for the time series of τ_{550nm} compared to AERONET τ_{550nm} values. However, on 11th July the correlation obtained here is much lower. The slopes obtained are closer to unity for the normalized profiles than for the non-normalized ones, which indicate that BSC-DREAM8b profiles better forecast the aerosol vertical structure than the aerosol load. According to these slope values of the normalized profiles, it is observed that the disagreement between BSC-DREAM8b and LIRIC was getting worse as time progressed, indicating that BSC-DREAM8b better forecast dust events in earlier stages. On 9th July the sloped even reached 0.98 for the normalized profiles. However, in the other cases they were all quite below one, indicating a strong underestimation of the model compared to LIRIC. The relative deviation for the profiles varied between 60 and 83% indicating large discrepancies and a strong underestimation of the model compared to the data retrieved with LIRIC. However, for the normalized profiles the relative deviation in the range between -33% and 34%. The root mean square error (RMSE) is also much lower for the normalized profiles, as observed in Table 5.1. This also indicates that the model reproduces better the aerosol vertical layering than the aerosol load.

To summarize, 60 microphysical properties profiles retrieved with LIRIC during the 72-h CHARMEX intensive measurement period summer 2012 were analysed in this thesis in order to study the temporal evolution of a dust event. During the study period, the observed dust event was decreasing its intensity, with larger concentrations on 9th July decreasing towards 11th July, in agreement with AERONET data and model predictions. On 9th July it is evident that there werea strong predominance of the coarse spheroid mode with maximum values in the afternoon while on 11th July it is observed an increase in the concentration of the coarse spheroid mode during the afternoon,. The comparison of the LIRIC retrieved mass concentration with BSC-DREAM8b model profiles indicated that the model underestimated LIRIC retrievals. However, from the normalization of the profiles, it could be inferred that the model reproduced better the aerosol vertical layering than the aerosol load.

5.2 CLIMARENO-GRA campaign

The CLIMARENO-GRA campaign was held at the University of Granada during the summer of 2011 in collaboration with the National Institute of Aerospace Technique in Spain (INTA). The main goal of this campaign was to study and compare dust and non-dust conditions above the city of Granada. For this purpose, special attention was paid to the retrieval of vertical profiles of optical and microphysical aerosol properties.

A dust event was detected on 27th June of 2011 whereas as a reference day, with non-dust conditions 14th June 2011 was chosen. During these two days all the available instrumentation at CEAMA station was simultaneously operating and a detailed analysis of the optical properties and in-situ measurements was presented in *Bravo-Aranda et al*. [in preparation]. In this section, we will focus mainly on 27th June because of the availability of simultaneous airborne data provided by INTA C-212-200 scientific aircraft.

The forecast modelling tools confirmed the presence of mineral dust above Granada station on 27th June 2011. As indicated by NAAPS forecast model (Figure 5.12a), mineral dust was present above Granada in the atmospheric column, even though los surface dust concentration was forecast. BSC-DREAM8b model (Figure 5.12c) also indicated the presence of mineral dust over most of the Iberian Peninsula, although with medium to low concentrations above Granada experimental site. A 5-day backward trajectories analysis performed with HYSPLIT model using GDAS meteorological database (Figure 5.12b) indicated that the air masses were coming from Northern Africa below 3000 m a.s.l. and passed by Northern African coast at higher altitudes.

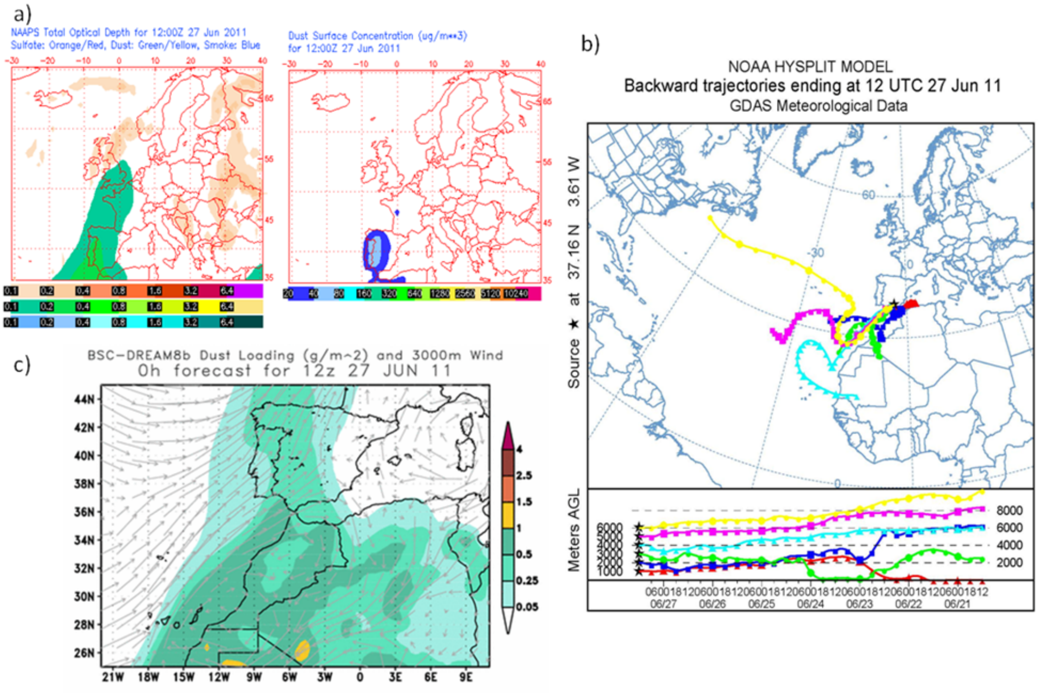

Figure 5.12. a) NAAPS forecast model for 27th June 2011 at 12:00 UTC. b) HYSPLIT 5-day backward trajectory analysis for the same period. c) BSC-DREAM8b dust loading forecast for 12:00 UTC on 27th June 2011.

Lidar measurements were performed from 06:00 to 12:00UTC, as observed in Figure 5.13, which shows a strong backscattered signal associated to the presence of atmospheric aerosol was observed up to 4.5 km a.s.l. AERONET Level 1.5 data shown in Figure 5.14a indicated that the aerosol load was quite high with τ_{440nm} values larger than 0.30 during the whole day. The AE(440-870nm) presented values between 0.40 and 0.70, indicating the predominance of coarse particles during the entire study period. Several AERONET inversion retrievals were available during different periods of the day, allowing for the calculation of microphysical properties profiles with LIRIC. Size distributions are shown in Figure 5.14b. As it can be observed, there was a predominance of the coarse mode during the whole day, although the aerosol load was lower from

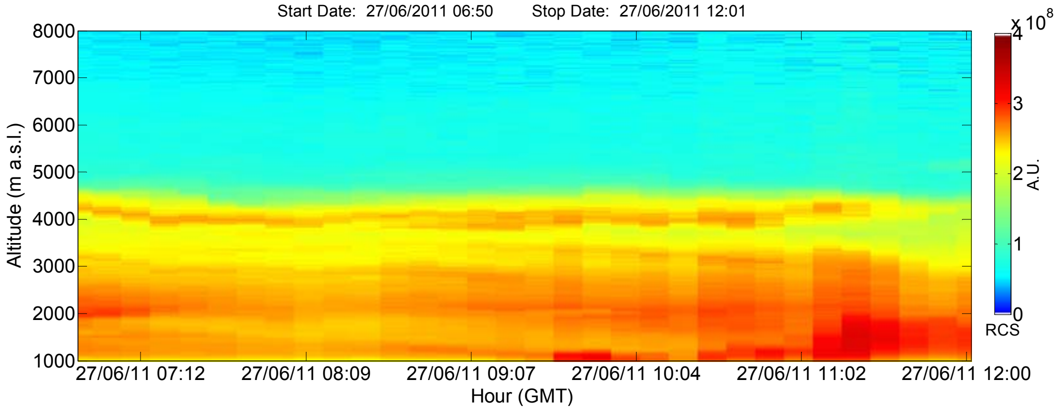

Figure 5.13. Time series of the lidar RCS on 27th June 2011 between 07:00 UTC and 12:00 UTC.

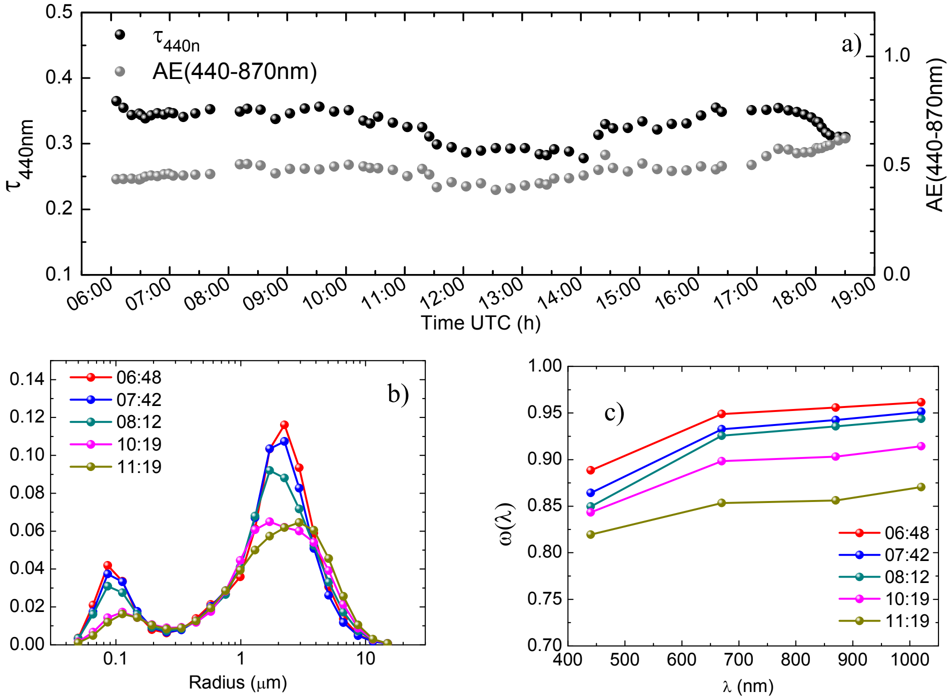

Figure 5.14. a) Time series of τ_{440nm} and AE(440-870nm) from AERONET level 1.5 data. b) Size distributions from AERONET inversion retrievals at the different time periods indicated in the legend. c) $\omega(\lambda)$ corresponding to the AERONET inversion retrievals of the size distributions.

10:19 UTC, in coincidence with a decrease of the τ_{440nm} from 0.40 to 0.35. $\omega(\lambda)$, shown in Figure 5.14c, presented the typical behaviour of mineral dust, with slightly positive spectral dependence [*Dubovik et al.,* 2002]. Values were decreasing along the morning, indicating an increase of absorbing particles in the atmospheric column.

A detailed analysis of the optical properties retrieved by means of Klett-Fernald retrieval will be presented in *Bravo-Aranda et al.,* [in preparation] (Figure 5.15). However, some hints are provided in this section in order to analyse the coherence between aerosol optical and microphysical properties. As it can be observed in Figure 5.15, β_{532nm} values were decreasing during the morning in the height layer between 3500 and 4800 m a.s.l. In this height range, β-AE(355-532nm) profiles indicated the predominance of coarse particles with values close to zero during the entire period, in coincidence with δ^{P}_{532nm} values that suggested an important contribution of non-spherical particles (δ^{P}_{532nm} in the range 0.23-0.28). However, in the lowermost part of the profiles, below 2000 m a.s.l., β-AE(355-532nm) was decreasing from 2 down to ~0.5 and δ^{P}_{532nm} was increasing from 0.08 up to 0.2, indicating a possible entrainment of the mineral dust to the boundary layer throughout the morning. Anyhow, values of δ^{P}_{532nm} were larger than 0.2 above 2000 m a.s.l. during the whole analysed period. In this sense, LIRIC retrievals (Figure 5.16), indicated a clear predominance of the coarse spheroid mode from the surface up to 5000 m a.s.l. In addition, a decrease of the volume concentration values was observed during the morning, in agreement with the decrease in $\beta_{532nm.}$ A maximum peak of the volume concentration of the coarse spheroid mode was observed between 4000 and 4500 m a.s.l., depending on the analysed period. The location of the maximum was the same for β_{532nm} profiles, as observed in Figure 5.15. Some fine particles were also observed during the different periods as indicated by the volume concentration profiles, but in low concentrations (~6 $\mu m^3/cm^3$). These particles might correspond to fine particles

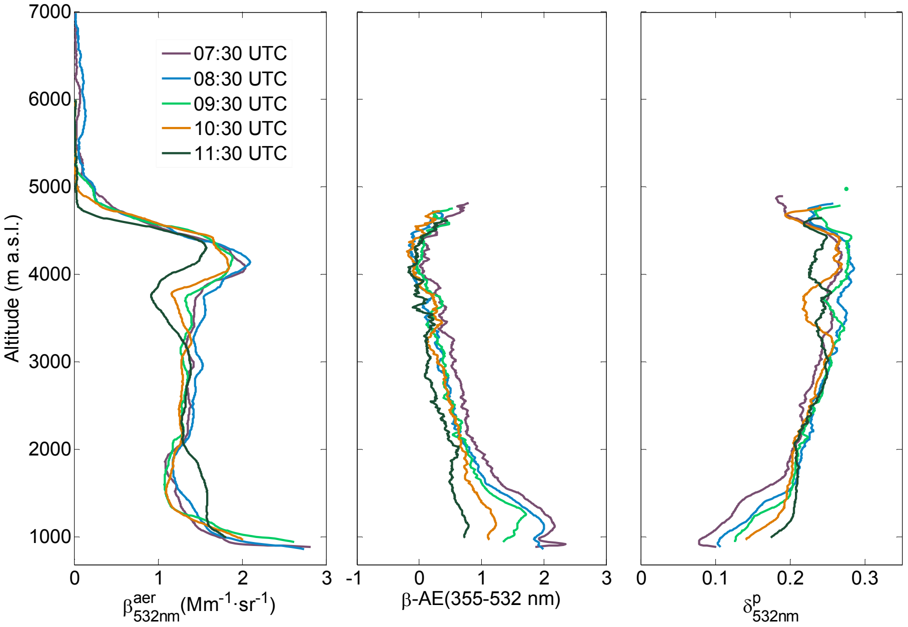

Figure 5.15. β^{aer}_{532nm}, *β-AE(355-532nm) and* δ^{P}_{532nm} *for the different time periods indicated in the legend on 27th June 2011 (adapted from Bravo-Aranda et al., [in preparation])*

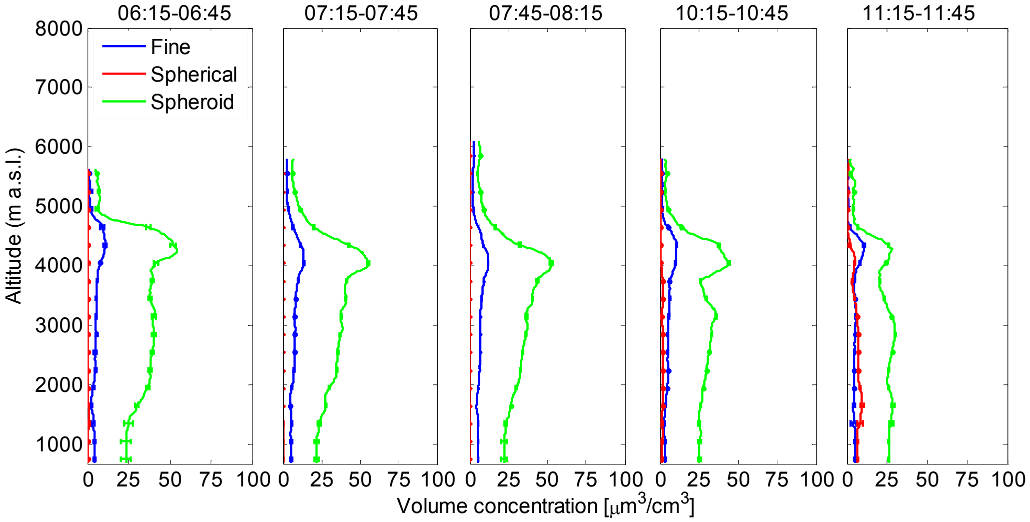

Figure 5.16. LIRIC inversion retrievals obtained for different periods on 27th June 2011 during the morning. The error bars are obtained as indicated in section 4.3.2.

from mineral dust or they could have been advected from the industrial areas in the North of Africa together with the mineral dust [*Rodriguez et al.,* 2011], but more data would be needed in order to determine this (i. e. vertical profiles of $\omega(\lambda)$). The coarse spherical mode was slightly increasing reaching its maximum values (~ 7 $\mu m^3/cm^3$) between 11:15 and 11:45 UTC. This slight increase in the volume concentration of the coarse spherical mode (from 0 to 5 $\mu m^3/cm^3$) around 4500 m a.s.l. was in agreement with a slight decrease in δ^{P}_{532nm} values (from 0.28 to 0.23) in the same height range.

The good agreement between aerosol optical and microphysical properties was expected since LIRIC retrievals are based on lidar data also. However, in the layer closer to the surface, below 2000 m a.s.l., the agreement was not so good. This can be explained by the fact that LIRIC makes the assumption that the volume concentration is constant below z_{N0} and uncertainties of the algorithm are higher in this region. Also, it is necessary to consider that LIRIC assumes several AERONET retrieved properties as height-independent and therefore results are much more vertically homogeneous than those retrieved from the lidar data with Klett-Fernald.

5.2.1 Comparison of LIRIC with airborne data

Airborne data provided by INTA aircraft were available over Granada in the analysed period. Airborne measurements were carried out by the INTA CASA C-212-200 (Figure 5.17) atmospheric aircraft. Measurements of temperature, relative humidity, GPS position and aerosol size distribution were performed during the flight on 27th June 2011.

Figure 5.17. Picture of the INTA CASA C-210-200 aircraft for atmospheric research (from www.eufar.org) and the CAPS (right top) and PCASP-100X (right bottom), taken from www.dropletmeasurement.com.

The airborne platform developed a vertical profile following a pseudo spiral centred at 3.57°W, 37.19°N, close to CEAMA experimental site, and having a diameter of about 4500 m. The aircraft overpass around the lidar systems was performed at several altitudes between 1200 and 5200 m a.s.l. A gentle ascent and descent rate was used of about 2.5m/s in order to increase vertical resolution and avoid problems with the inlets. Figure 5.18 shows the ascending track of the INTA-C212-200 aircraft during this flight. The flight took place around 10:30 UTC and CASA C-212-200 atmospheric research aircraft was equipped with two optical particle counters designed by Droplet Measurement Technologies (DMT) PCASP-100X and CAPS, from which microphysical properties profiles were derived allowing the comparison with LIRIC output profiles (Figure 5.19). The instruments were fixed at two hard points located under the aircraft wings.

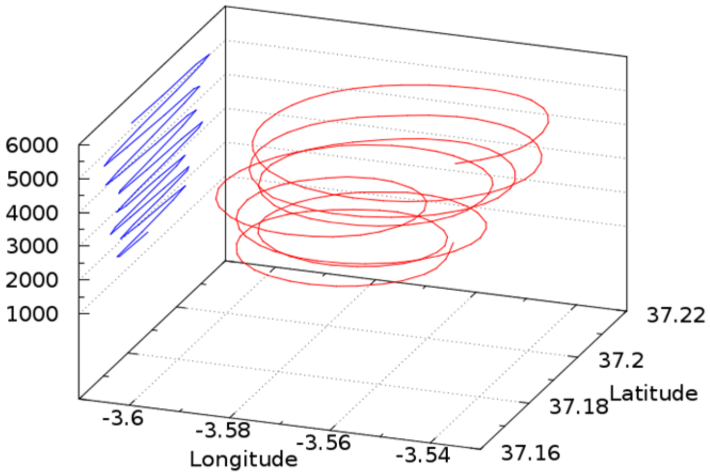

Figure 5.18. a)Ascending track of the INTA-C212-200 aircraft above CEAMA experimental site during the flight on 27th June 2011 around 10:30 UTC. b) Aircraft imaga (from www.eufar.org)

The CAPS (Cloud, Aerosol, and Precipitation Spectrometer) sonde located on board the C-212-200 combines five different instruments in one flight canister, covering a sizing range with diameters from 0.51 µm to 1550 µm. The five instruments included in the CAPS are the Cloud Imaging Probe (CIP), the Cloud and Aerosol Spectrometer (CAS), the Hotwire Liquid Water Content Sensor (Hotwire LWC), a GPS system and meteorological sensors. For the purposes of our analysis, data corresponding to the CAS optical counter were used. The CAS measures in the range 0.51-50 µm of diameter in 30 different size bins. Its measuring principle is based on light-scattering, i.e. particles scatter light from an incident laser, and collecting optics guide the light scattered in the 4° to 12° range into a forward-sizing photodetector. This light is measured and used to infer particle size. Backscatter optics also measure light in the 168° to 176° range, which allows for the determination of the real component of the refractive index for spherical particles. The uncertainty of this sonde varies between 15 and 20% for the size distributions [*Feingold et al.*, 2006].

The PCASP-100X (Passive Cavity Aerosol Spectrometer Probe) provides size distributions of aerosol particles in the range 0.1- 3 µm of diameter in 15 different bins. The measuring principle is similar to the CAS. A laser beam illuminates the particles and light is scattered in all directions. Some of the scattered light is collected by a mirror within a scattering angle from about 35^o - 135^o. This collected light is focussed onto a photodetector and then amplified, conditioned, digitized and classified into one of fifteen size channels. The size of the particle is determined by measuring the light scattering intensity and using Mie scattering theory to relate this intensity to the particle size for a fixed refractive index. Size distributions are provided with an uncertainty of 20% [*Baumgardner et al.*, 2005]

From the combination of the data from the CAS and PCASP-100X instruments, volume concentration profiles for the fine mode (radius between 0.05 and 0.5 µm) and coarse mode (radius from 0.5 to 25 µm) were obtained to perform the comparison with LIRIC retrieved profiles. In order to retrieve the volume concentration profiles from the on-board instrumentation, Mie theory was applied considering aerosol particles as spheres and a refractive index correction was performed, in a similar way to that explained in [*Andrey et al.*, 2014]. Results from the comparison are shown in Figure 5.19. For the fine mode, the volume concentrations were very low, with values below 5 $\mu m^3/cm^3$. For the coarse mode, similar layering was detected with both LIRIC and the airborne data, presenting two maximum peaks around 3500 and 4200 km a.s.l. The dust layer geometrical thicknesses observed and the location of the highest aerosol layer (between 3800 and 4600 m a.s.l.) were very similar for both LIRIC and the aircraft data. However, the height of the first maximum was located at higher altitude according to the aircraft (3400 m a.s.l., whereas LIRIC located it at 3200 m a.s.l.). Up to 3000 m a.s.l. absolute differences were below 5 $\mu m^3/cm^3$, but discrepancies were larger in the maximum peaks, reaching up to 25 μm^3/cm^3 (~50% in relative difference).

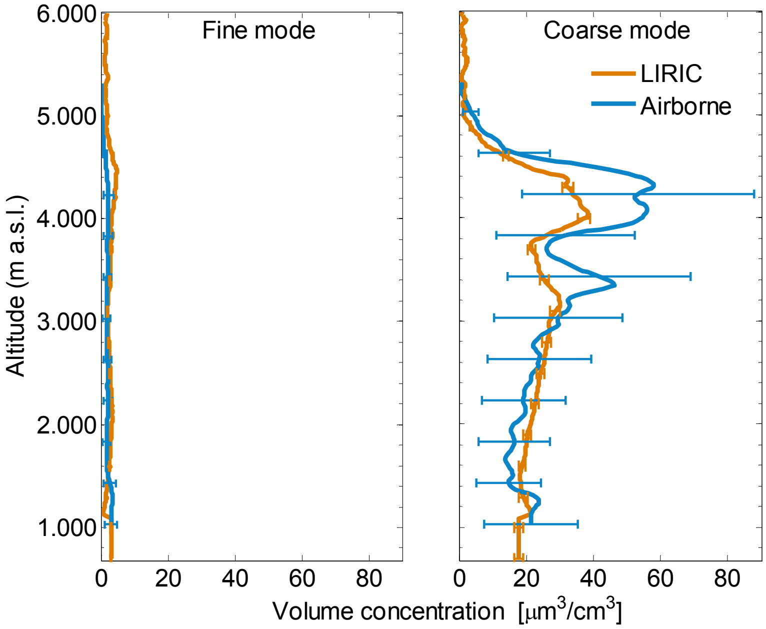

Figure 5.19. Volume concentration profiles retrieved with LIRIC (orange line) and the onboard in-situ instrumentation (blue line) during the flight on 27th June 2011 at 10:30 UTC for the fine and coarse modes.

According to the results, the aircraft measurements and LIRIC profiles agreed both in magnitude and vertical structure of the volume concentration profiles for both fine and coarse modes. Nevertheless, some discrepancies were observed. These discrepancies may have been partly caused by nonuniform spatial distribution of the aerosol, since the volume air sampled were not exactly the same. Nonetheless, considering the RCS time series in Figure 5.13 it seems that the atmosphere was rather homogenous and this error might be negligible. The application of Mie theory in order to retrieve the volume concentration profiles from the measured size distributions on-board the CASA C-212-200 aircraft may be an important source of error for this case of mineral dust, which are non-spherical aerosol particles. The sphericity assumption in Mie theory may introduce large uncertainty for particles in the size range 3-8 µm of radius [*Ginoux*, 2003]. In addition, the aircraft inlets may introduce some inaccuracies in the measurements too. Another possible cause for the discrepancies observed may be due to the aircraft in-situ measurements and LIRIC retrievals which are based on different inversion methodologies, which already present certain uncertainties. Therefore, considering this previous information, the agreement between the airborne measurements and LIRIC profiles was quite good during this flight on 27th June 2011.

5.2.2 Comparison of LIRIC with BSC-DREAM8b model

Dust concentration profiles provided by the BSC-DREAM8b model were also available during this CLIMARENO-GRA campaign and were compared with the profiles retrieved with LIRIC and with the aircraft measurements. In order to retrieve the dust mass concentration the coarse mode retrieved with LIRIC was multiplied by the dust density. For this purpose, we considered the value used in the BSC-DREAM8b model (2.5 g/cm^3 for the fine mode and 2.65 g/cm^3 for the coarse mode), as it was explained in section 5.1.1. Comparison is shown in Figure 5.20. Values obtained for the three datasets were of the same order. However, LIRIC and the aircraft indicated the presence of dust up to 4000 m a.s.l. and BSC-DREAM8b forecast it up to 5000 m a.s.l. In general, larger mass concentration values were observed with BSC-DREAM8b model up to 4500 km a.s.l. As indicated in the previous section, two maximum values for the mass concentration were obtained with LIRIC at 3500 and 4200 m a.s.l. and with the aircraft at 3800 and 4600 m a.s.l., whereas this complex layering was not properly predicted by BSC-DREAM8b, with only one maximum peak at 800 m a.s.l. The altitude of the dust layer corresponding to this maximum was therefore highly underestimated by the model. Consequently, for this case it seems that the model did not correctly forecast the vertical structure of the aerosol layers, although a discrepancy with

LIRIC of only 30% is obtained for the column-integrated dust mass concentration values.

The results obtained from the comparison in this case are quite different from those obtained during CHARMEX campaign in 2012 (see section 5.1). Results from section 5.1 indicated that BSC-DREAM8b model did not correctly forecast the values of the mass concentration, but better results were obtained regarding the vertical structure of the aerosol layers. The different results obtained in these two campaigns may be due to the fact that during CHARMEX 2012 the dust event was already well developed at the time of the measurements, whereas during CLIMARENO-GRA campaign the dust event was just at the beginning. Also the horizontal homogeneity of the aerosol plume in the closer regions may influence the results. In addition, the horizontal distribution of the dust event as modelled by BSC-DREAM8b forecast models for the two cases may also influence in the different obtained results in both cases.

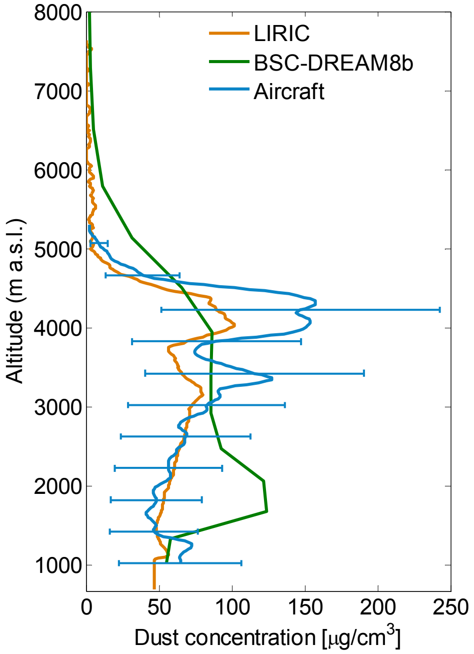

Figure 5.20. Dust mass concentration profiles retrieved with LIRIC, from the aircraft data and forecast by BSC-DREAM8b model for 27th June 2011 at 10:30 UTC.

5.2.3 Retrieval of microphysical properties from Raman lidar signals

The use of the Raman channels during the night previous to the flight, between 00:00 and 01:00 UTC, allowed us to investigate microphysical properties by using the algorithm developed by *Veselovskii et al.* [2013]. Combined with LIRIC retrieval for the period 07:15-07:45 UTC, this retrieval allowed us to study the development of the dust event during that night.

The inversion algorithm developed by *Veselovskii et al.,* [2013] provides aerosol microphysical properties such as the mean effective radius, number, surface area, and volume concentration, and complex refractive index from multiwavelength lidar data. The method consists on a mathematical approach based on the concept of Tikhonov's regularization [*Tikhonov and Arsenin*, 1979]. A simple modification to this inversion with regularization by applying the minimum discrepancy criterion is made [*Sabatier*, 1987]. Optical aerosol properties are used as input data in order to obtain the microphysical properties by means of the Fredholm integral equations described in section 2.8. At least β_λ at three different wavelengths and α_λ at two wavelengths are needed as input data. The use of the depolarization information allows for retrieving the spheroids volume fraction (SVF), extending the use of the algorithm to those cases with non-spherical particles, e. g. mineral dust events.

Results corresponding to two different retrievals using Veselovskii's algorithm applied to non-spherical particles are shown in Figure 5.21. In the first retrieval, the depolarization information was used and the spheroids volume fraction (SVF) was obtained according to these data. In the second retrieval, SVF was assumed to be 100% and depolarization information was not used. As it can be seen, discrepancies between both retrievals were very low since the SVF obtained using the depolarization information is never below 80% for this case of mineral dust.

Volume concentration profiles retrieved with LIRIC at 07:15-07:45 UTC are also shown in Figure 5.21. In the case of LIRIC, the use of depolarization data allowed to obtain profiles of fine, coarse spherical and coarse spheroid model, whereas with Veselovskii's algorithm only the total volume concentration was obtained at the different layers. As it can be observed in the data, there are discrepancies between both retrievals, but it is worthy to note that the period analysed were different and the discrepancies can be explained by the temporal evolution of the dust event during the night. For this purpose, optical properties were analysed and results are shown in Figure 5.21. As it can be inferred from the data, β_{532nm} values, retrieved using the Raman technique during night-time and Klett-Fernald inversion algorithm during daytime, were decreasing in the layer between 2500 and 3700 m a.s.l. going from 1.8 $Mm^{-1}·sr^{-1}$ at 00:00-01:00 UTC to 1.4 $Mm^{-1}·sr^{-1}$ at 07:15-07:45 UTC. The volume concentration profiles retrieved with Veselovskii's algorithm at night and LIRIC at daytime presented a similar temporal evolution in this height range, with values around 75 $\mu m^3/cm^3$ at 00:00-01:00 UTC and 50 $\mu m^3/cm^3$ at 07:15-07:45 UTC. At 2000 m a.sl. and in the height range 3900-4500 m a.s.l., where β_{532nm} presented similar values during night and day, the agreement between LIRIC and Veselovskii's results was really high with similar volume concentration values obtained from both retrievals. Nonetheless, in the case of Veselovskii's retrieval, the complex structure with two aerosol layers above 2500 m a.s.l. observed in the β_{532nm} profile during the night was detected as a single layer in the volume concentration profile due to the low vertical resolution of the algorithm. However, LIRIC reproduces fairly well the vertical structure observed in the β_{532nm} profile corresponding to daytime.

Therefore, according to the analysis of the optical properties the mineral dust event was developing during the night and the aerosol properties were changing. In this context, discrepancies between Veselovskii's and LIRIC retrieved volume concentration profiles were expected and they were likely due to the temporal evolution of the aerosol properties, not to discrepancies in the methodology applied. Because of the coherence of the results obtained with both LIRIC and Veselovskii's inversion algorithms with the optical properties in this section, it seems that the combined use of both techniques is very appropriate for the continuous monitoring of aerosol microphysical properties during both day and night-time.

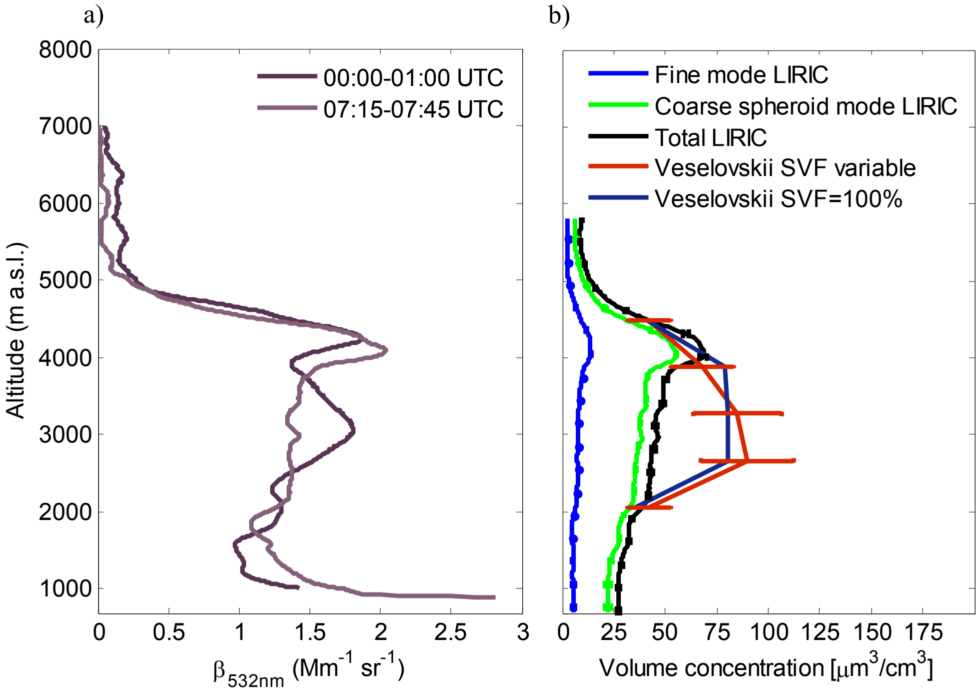

Figure 5.21. a) β_{532nm} *retrieved with Raman technique at 00:00-01:00 UTC and Klett-Fernald method at 07:15-07:45 UTC on 27th June 2011. b) LIRIC volume concentration profiles for fine, coarse spheroid and total modes for the period 07:15-07:45 UTC and Veselovskii's retrieved volume concentration profiles for the period 00:00-01:00 UTC with (red line) and without (dark blue line) considering depolarization information.*

5.3 Evaluation of LIRIC performance using independent sun photometer data at two altitude levels

In this section, the availability of a special observational setup has been used for obtaining LIRIC retrievals from two different altitudes with independent sun photometer measurements. This provides a unique opportunity to check LIRIC methodology and the quality of LIRIC products in situations where there are changes in atmospheric aerosol properties along the vertical column. The experimental setup consisted in combining the tandem multiwavelength lidar and CIMEL sun photometer operated at Granada with a second sun photometer installed in the close vicinity at higher altitude in the Sierra Nevada slopes (Cerro Poyos AERONET station). First, two independent study cases using such measurement configuration are presented here. In the first case, LIRIC is applied to a situation with a dust layer well mixed along the column. In the second case, two different and clearly decoupled aerosol layers are investigated. Results allow comparing the profiles obtained from the two altitudes to evaluate the performance of the algorithm under different atmospheric conditions. In a second part, an extensive statistical analysis during the summer of 2012 comparing the retrievals from both altitude levels is presented in order to evaluate the general performance of the algorithm above Granada experimental site.

The experimental setup is shown in Figure 5.22. As previously indicated, it includes a second sun photometer at a different altitude located almost in the same atmospheric column as the experimental site in Granada. This setup has been previously explored in *Alados-Arboledas et al.*, [2008]. In this way, we can use the same lidar profiles to retrieve the volume concentration profiles starting at different heights, namely 680 m a.s.l and 1820 m a.l.s (therefore with $\Delta z = 1140$ m), using independent AERONET input data at each height. This allows for checking the coherence of both profiles over the upper mountain station. This can be specially challenging in cases when several layers of different aerosol types are present along the atmospheric column, since LIRIC assumes that properties such as the refractive index or the size distribution are height independent for each mode. Additionally, the retrievals using the second sun photometer in Cerro Poyos station overcome the incomplete lidar overlap, avoiding the assumption of a constant volume concentration value below z_{N0} which, in turn, reduces the uncertainties.

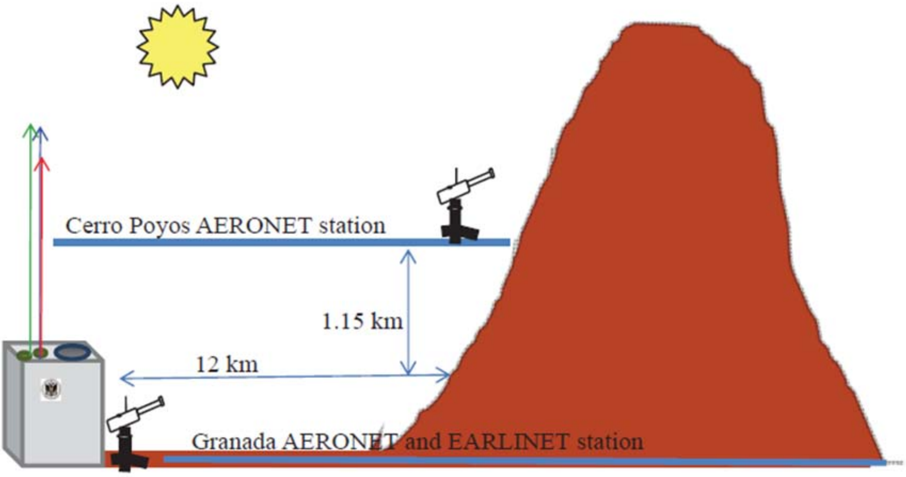

Figure 5.22. Experimental setup during summer with two AERONET stations at two different altitudes.

5.3.1 Study cases

5.3.1.1 Study case I: 30th July 2012

On 30th July 2012 three different aerosol layers were detected over Granada, as observed in the lidar range corrected signal time series (Figure 5.23a). 5-day backward trajectories obtained with HYSPLIT model indicated that the air masses came from North Africa above 2 km a.s.l. The Atlantic Ocean and the Iberian Peninsula were the source regions for the air masses at low altitudes (Figure 5.23b). BSC-DREAM8b and NAAPS models forecast the presence of mineral dust over the Southeastern Iberian Peninsula, although the forecast loads were not very large (Figure 5.23c and d).

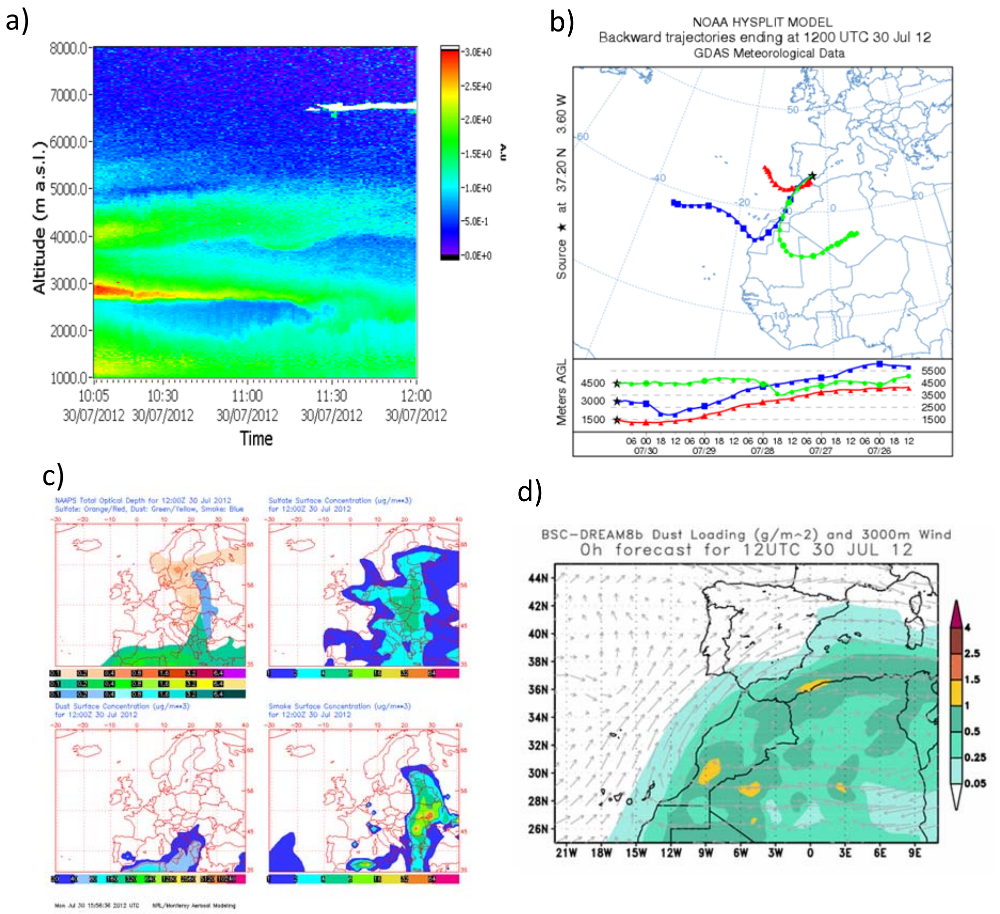

Figure 5.23. a) Time series of the lidar range corrected signal in arbitrary units at 532 nm for 30th July 2012. b) 5-day backward trajectories of the air masses arriving over Granada the same day at 10:00 UTC obtained with HYSPLIT model. c) NAAPS forecast for the same date at 12:00UTC over Europe.d) BSC-DREAM8b model forecast of dust loading for Spain and the North of Africa for the same date at 12:00 UTC.

Figure 5.24 shows the AERONET data for both stations (Granada and Cerro Poyos). Data indicated that there was a high aerosol load with τ_{440} increasing from 0.10 to 0.60 between 06:00 and 11:00 UTC. Low values of the AE(440-870), below 0.20, especially after 09:00 UTC indicated the predominance of coarse particles. Size distributions retrieved at 09:22 UTC showed a clear predominance of the coarse mode with quite high contributions at both altitudes. The single scattering albedo ω(λ) had lower values over Granada, indicating that the layer between the surface and 1820 m a.s.l. had comparably more absorbing particles than the lofted layers above this height. The spectral dependence at both altitudes is typical of situations with mineral dust [*Dubovik et al.,* 2002*; Alados-Arboledas et al.,* 2008*; Valenzuela et al.,* 2012a].

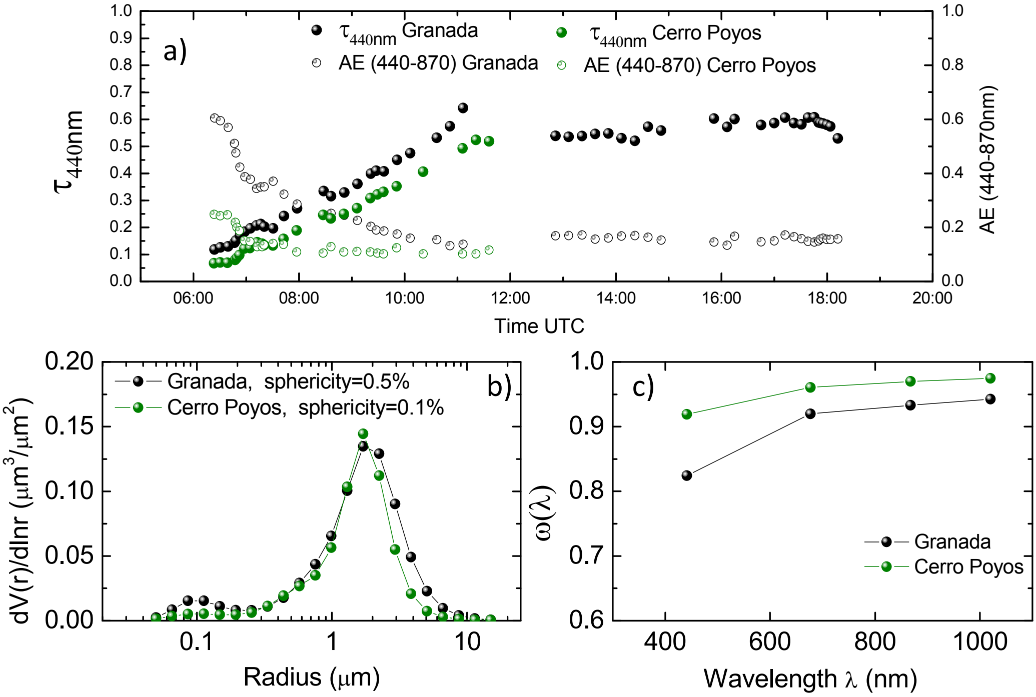

Figure 5.24. Time series of AERONET τ_{440nm} and AE(440-870nm) data on 30th July 2012. b) Volume size distribution retrieved by AERONET inversion algorithm Version 2 the same day at 06:25 UTC. c) Single scattering albedo ω(λ) versus wavelength λ retrieved by AERONET for the same date.

LIRIC volume concentration profiles were retrieved from lidar data between 10:00 and 10:30 UTC and the AERONET inversion at 09:22 UTC at both altitude levels (Figure 5.24).

Using AERONET data from Granada station and the user-defined input parameters in Table 5.2, the retrieved volume concentration profiles showed a clear predominance of the coarse spheroid mode, with values up to 80 μm^3/cm^3, and a slight contribution of the fine mode, reaching 10 μm^3/cm^3 from 3000 to 6600 m a.s.l. (Figure 5.25). The coarse spheroid mode vertical profile retrieved by LIRIC presents three maximum values corresponding to the three different layers observed, being the highest concentrations around 80 μm^3/cm^3 at 4200 m a.s.l. The error bars in Figure 5.25 were calculated as indicated in section 4.3.

The availability of the AERONET station in Cerro Poyos allowed to obtain the volume concentration profiles using an independent sun photometer measurement and the lidar signals from 1820 m a.s.l., avoiding the regions affected from incomplete overlap in the lower part of the lidar profiles. Comparison between the profiles retrieved from Granada and Cerro Poyos is shown in Figure 5.25. The agreement for the coarse spheroid mode was good with differences below 5%. The coarse spherical mode was identical and practically null from both altitude levels. However, the fine mode presents larger values between 1820 and 3000 m a.s.l. when retrieved from Cerro Poyos, although differences are still very low (smaller than 5 μm^3/cm^3). The good agreement between both retrievals is due to the strong contribution of the mineral dust along the whole atmospheric column above both altitude levels. So the assumption of a height independent aerosol model, based on height independent parameters for each mode such as the size distribution, the refractive index (1.6 and 1.52 at Granada and Cerro Poyos, respectively) and the sphericity (1.6 and 0.1% at Granada and Cerro Poyos, respectively), did not introduce large uncertainties.

According to the results from section 3.2., variations in the lower limit value z_{N0} leaded to the highest uncertainties in the performed tests. As the overlap do not affect the lidar signals from Cerro Poyos, z_{N0} is always set to 1820 m a.s.l. in LIRIC retrievals from this second AERONET station. This is the reason why error bars (computed as the standard deviations obtained by averaging the 12 retrievals described in section 3.3) were much lower when volume concentration profiles were retrieved from Cerro Poyos than when retrieved from Granada. The largest error bars which are obtained below 1500 m a.s.l. do not affect the retrieval from Cerro Poyos. In addition, the uncertainties in the retrieval from Cerro Poyos are a 50% lower than the ones obtained in the retrieval from Granada above 1820 m a.s.l.

Date	STUDY CASE I 30th July 2012	STUDY CASE II 24th July 2012
z_{N0}	1055	1080
z_N	6860	3350
z_U	7070	3500
k_{335}	$7.5 \cdot 10^{-4}$	$7.5 \cdot 10^{-4}$
k_{532}	$7.5 \cdot 10^{-4}$	$2.5 \cdot 10^{-4}$
k_{1064}	$2.5 \cdot 10^{-4}$	$2.5 \cdot 10^{-4}$
k_{532c}	$7.5 \cdot 10^{-5}$	$7.5 \cdot 10^{-5}$
f_{fine}	15	13
$f_{spherical}$	5	4
$f_{spheroid}$	10	12
d_{fine}	5	5
$d_{spherical}$	5	5
$d_{spheroid}$	5	5

Table 5.2. Initial sets of user-defined input parameters for LIRIC retrievals for the study cases I and II (z_{N0} = lower limit, z_N = reference height, z_U = upper limit, k_λ = lidar regularization parameters, f_v = sun photometer regularization parameters, d_v = smooth constraints regularization parameters. Heights are expressed in m a.s.l. and regularization parameters are dimensionless).

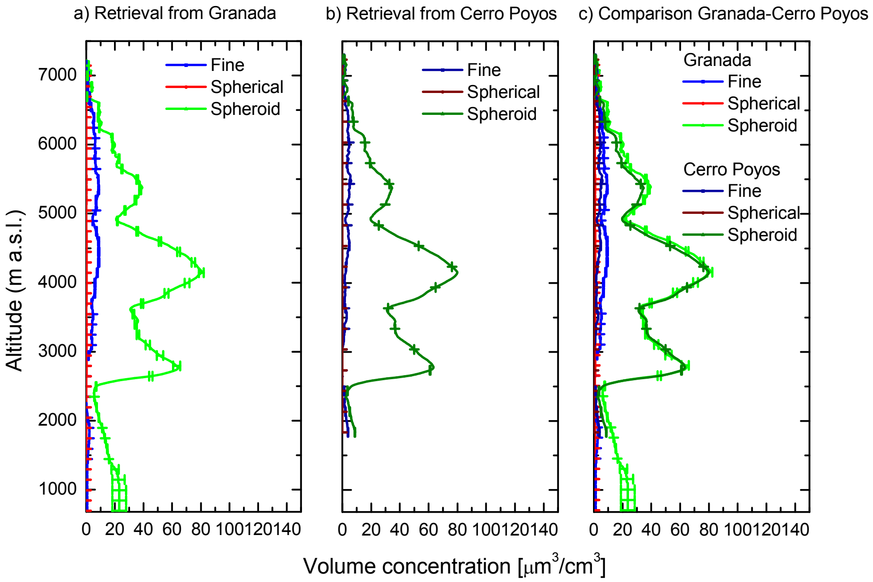

Figure 5.25. Volume concentration of the fine (blue), coarse spherical (red) and coarse spheroid (green) modes computed on 30th July 2012 between 10:00 and 10:30 UTC using LIRIC with a) AERONET retrieval corresponding to 09:22 UTC from Granada station and lidar signals from 1055 m a.s.l. (due to the incomplete overlap) b) AERONET retrieval corresponding to 09:22 UTC from Cerro Poyos station and lidar signals from 1820 m a.s.l. c) Comparison of a) and b) figures. Error bars indicate the standard deviations obtained by averaging the 12 retrievals described in section 3.2.

Figure 5.26 shows the β_λ^{aer} profiles from Granada station. Good agreement was found in this case for 532 nm. However, larger differences were observed for 355 nm and 1064nm, especially at the maximum values. For this case a clear increase of the LIRIC derived β_λ^{aer} with wavelength was also observed, being negative the associated Angström Exponent, as it occurred in the dust case presented in section 4.3.2.2. Values close to zero were obtained for the β-AE retrieved with Klett-Fernald and the α-AE obtained with LIRIC. As explained before, this could be related to the uncertainties in the spheroid model used by AERONET at Θ = 180°, which highly drives the LIRIC retrievals in predominance of coarse particles. This needs further attention in the future. As it can be observed, in this case the difference between the lidar ratio used for Klett-

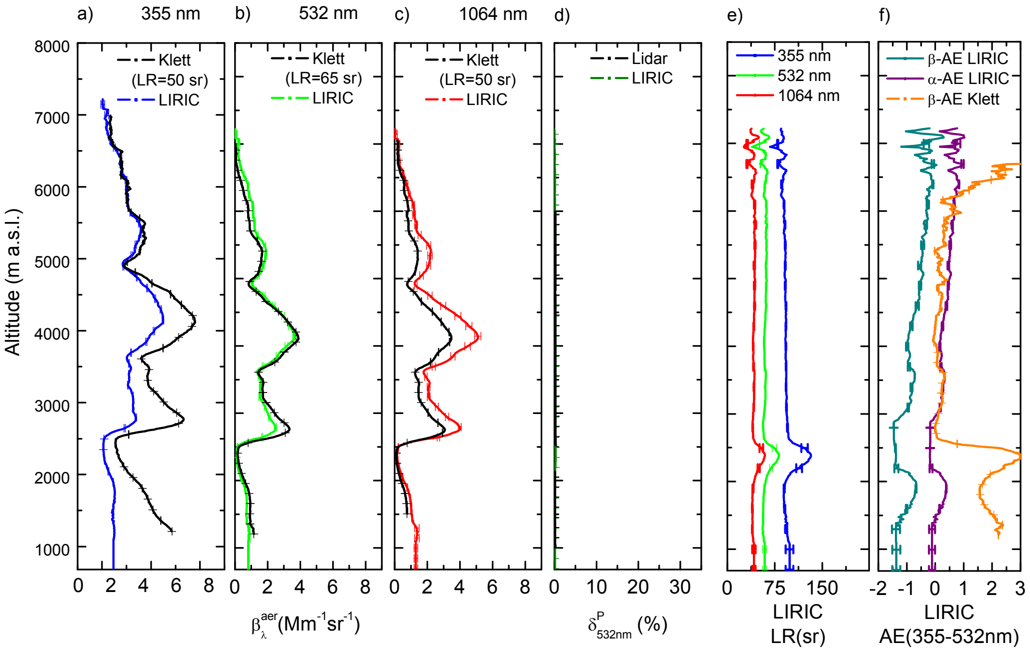

Figure 5.26. β_{λ}^{aer} profiles at a) 355 nm, b) 532 nm and c) 1064 nm retrieved from LIRIC output profiles (coloured lines) and Klett-Fernald (black lines) on 30th July 2012 between 06:00 and 06:30 UTC. d) δ_{532nm}^{P} profiles obtained from LIRIC (coloured line) and lidar data (black line) for the same period. e) Lidar ratio profiles obtained from LIRIC retrievals. f) Backscatter- and extinction-related Angtröm exponent between 355 and 532 nm profiles retrieved with LIRIC and backscatter-related Angström exponent obtained with Klett-Fernald. The error bars of LIRIC profiles indicate the standard deviations obtained from the 14 retrievals performed as indicated in section 4.1.

Fernald retrieval at 355 nm (50 sr) and the value provided by LIRIC for this wavelength (~90 sr) is quite large. δ_{532nm}^{P} profiles were very similar for both methods below 2 km a.s.l., but values provided by LIRIC were half of those obtained from the lidar data above 2.5 km a.s.l. δ_{532nm}^{P}obtained from lidar data reached values around 20%, indicating a predominance of coarse spheroid particles. This is in agreement with the typical value of δ_{532nm}^{P} under dust conditions obtained at Granada. As obtained in section 4, δ_{532nm}^{P}values retrieved from LIRIC were always lower than the obtained exclusively from lidar data according to *Bravo-Aranda et al.* [2013]. As explained in section 4.3.2, these differences are originated in the different procedures followed in each one of the retrievals. LIRIC is mainly based on AERONET information on the sphericity for the whole column. Meanwhile, our procedure uses cross and parallel β_{532nm} profiles including a careful calibration, which corrects misalignment between the polarization plane of the laser and the optical system and diattenuation effects of the lidar system, not included in LIRIC.

5.3.1.2 Study case II: 24th July 2012

On 24th July 2012 a smoke plume was detected over the CEAMA station between 2 and 3 km a.s.l. as observed in the lidar range corrected signal time series (Figure 5.27a). The combination of the 10-day backward trajectory analysis from HYSPLIT and MODIS FIRMS data indicated that the air masses advected smoke from North America, Portugal and the Northeast of the Iberian Peninsula above 2200 m a.s.l. and passed close to the North of Algeria below at 1200 m a.s.l., where some active fires were also observed, (Figure 5.27b and d). The NAAPS model (Figure 5.27c) also forecast the presence of smoke over the Southeastern of the Iberian Peninsula combined with sulphates, thus indicating the presence of anthropogenic pollution.

AERONET data in Figure 5.28. show that aerosol optical properties were quite variable along the morning over Granada, with higher values of τ_{440} from 06:00 to 10:00 UTC. During this period, τ_{440} was much larger over Granada than over Cerro Poyos, where τ_{440} was almost constant around 0.20, indicating that the aerosol load was mainly below 1820 m a.s.l. However, values were closer at both altitudes starting at midday. The AE(440-870nm) values were smaller over Granada (~1.0) station than over Cerro Poyos (~1.4), which indicated a higher influence of the coarse mode below Cerro Poyos altitude. AERONET inversion data were retrieved at the two heights at 15:22 UTC. At the time of the retrieval, 60% of the aerosol load was below Cerro Poyos. The size distributions showed

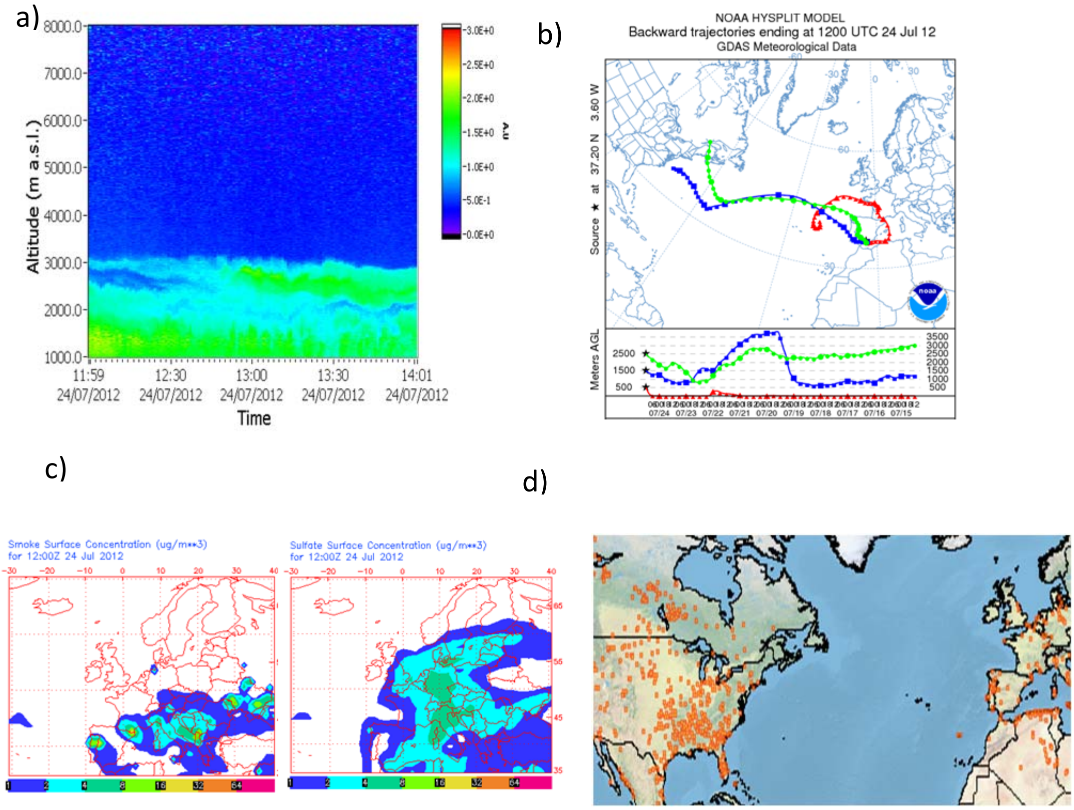

Figure 5.27. a) Time series of the lidar range corrected signal at 532 nm on 24th July 2012. b) 10-day backward trajectories of the air masses arriving over Granada the same day at 12:00 UTC obtained with HYSPLIT model. c) NAAPS forecast for the same date at 12:00 UTC over Europe. d) MODIS FIRMS image indicating the active fires during the five previous days to 24th July 2012.

very low values and very similar for both modes. Values for the coarse mode over Granada were higher than those over Cerro Poyos. ω(λ) above Granada was decreasing with wavelength as it is usually observed for cases of biomass burning and anthropogenic pollution [*Dubovik et al.,* 2002]. However, it was higher above Cerro Poyos and almost wavelength independent. This spectral dependence of ω(λ) can be explained in terms of the ageing processes suffered by the smoke since it is affected by a long range transport at altitudes over 4 km a.s.l. [*Eck et al.,* 2003].

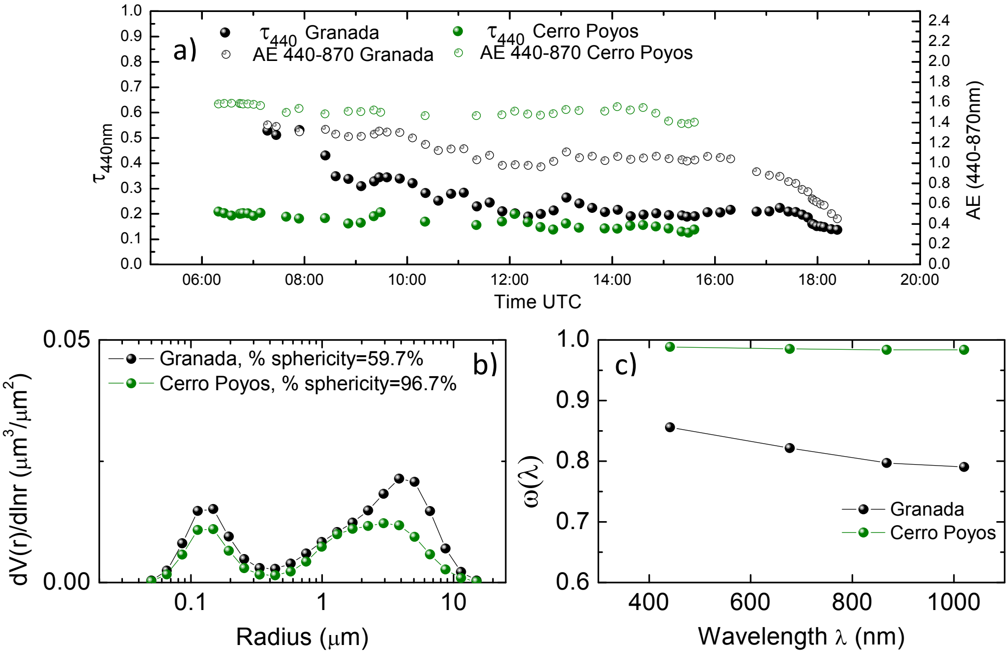

Figure 5.28. As Figure 5.24, but for 24 July 2012.

For the retrieval with LIRIC, lidar data between 13:30 and 14:00 and AERONET inversion at 15:22 were used. LIRIC volume concentration profiles retrieved from Granada are shown in Figure 5.29a. User-defined input parameters are included in Table 5.2. There was a slight predominance of the coarse spherical mode in the whole profile, with maximum values in the layer between 2 and 3 km a.s.l., reaching 20 $\mu m^3/cm^3$. Below 2.5 km the coarse spheroid mode was also considerable with volume concentration values of 10 $\mu m^3/cm^3$, but above this height it was drastically reduced. The fine mode presented a small contribution (~5 $\mu m^3/cm^3$) up to 2 km a.s.l and then increased having a maximum value of 15 $\mu m^3/cm^3$ around 2.9 km a.s.l. Relative errors were below 25% for the fine mode and below 15% for coarse spheroid mode. For the coarse spherical mode relative errors were very low, being less than 10% except at the overlap region, reaching 15%.

Figure 5.29c shows a direct comparison between the volume concentration profiles obtained from Granada and from Cerro Poyos stations. Some remarkable discrepancies were observed in this case. Coarse spheroid particles were not observed at all by the second sun photometer at Cerro Poyos station, whereas according to the retrieval from Granada they reached almost 3 km a.s.l. Maximum concentration of the coarse spherical mode was obtained at both altitude levels around 2.5 km a.s.l., but values of the maximum were 18 and 33 μm^3/cm^3 for the retrievals from Granada and from Cerro Poyos, respectively. For the fine mode, similar values were obtained but the maximum was located much higher when data from Cerro Poyos station were used. The unrealistic offset introduced by LIRIC in the molecular region was affecting much more the fine mode in the retrieval from Cerro Poyos and variation in z_U values introduced large uncertainties, as it is observed in the error bars. For this specific situation, there was a good mixing in the lower part of the profile with very constant values of the aerosol optical properties and the assumption of constant volume concentrations below z_{N0} did not substantially affect the retrievals. The reason for the large discrepancies between the retrievals at both altitudes is not clear. They may be caused by uncertainties of the measurements or the spheroid model that drives AERONET aerosol retrievals and, therefore, LIRIC results too. In this sense, τ_{440} is quite low (~ 0.13) over Cerro Poyos being the retrieval accuracy of ω(λ) in the range 0.02-0.07 [*Dubovik et al.,* 2006]. Furthermore, it is necessary to take into account that the sphericity (40.2 and 96.7% at Granada and Cerro Poyos, respectively) and size distributions are assumed to be independent of the altitude when using LIRIC. According to the remote sensing data, for this case there were two layers of different aerosol types, so this assumption may introduce some important errors when using data from AERONET Granada station. Therefore, it is necessary to take into account these limitations of LIRIC under specific situations. When lidar retrievals and the corresponding derived intensive properties profiles presents a complex vertical structure, LIRIC profiles should be taken as a first approach of the microphysical properties profiles affected by large uncertainties. A more detailed analysis with more datasets would be required to quantify the uncertainties they can introduce in the retrievals.

Figure 5.30 shows the comparison between aerosol optical properties derived from Klett-Fernald and LIRIC retrieved volume concentration profiles from Granada station. In this case, the best agreement was found for 532 nm. However, larger discrepancies appeared for 1064 nm and 355 nm profiles. For the β-AE retrieved with LIRIC, the spectral dependence was almost negligible in the lower part, where the coarse mode predominated. Values of the Angström exponent were around unity in the upper part, where the increase in the fine mode volume concentration was observed. Again, β-AE retrieved following Klett-Fernald algorithm and LIRIC retrieved α-AE, values were larger and closer to the column-integrated ones. The δ^{P}_{532nm} profiles obtained from LIRIC presented very low values, below 5%, indicating the predominance of spherical particles. As in

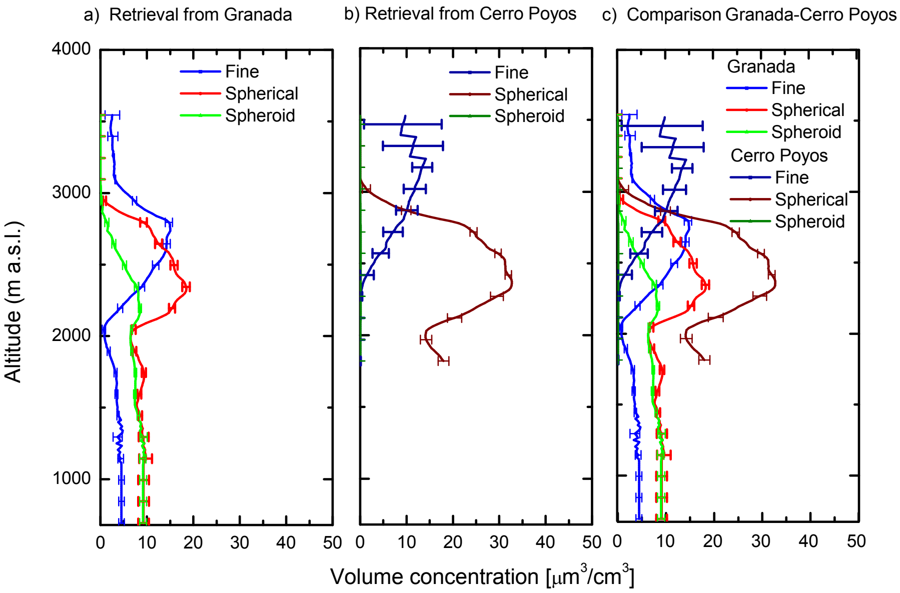

Figure 5.29. As Figure 5.25 but for 24th July 2012.

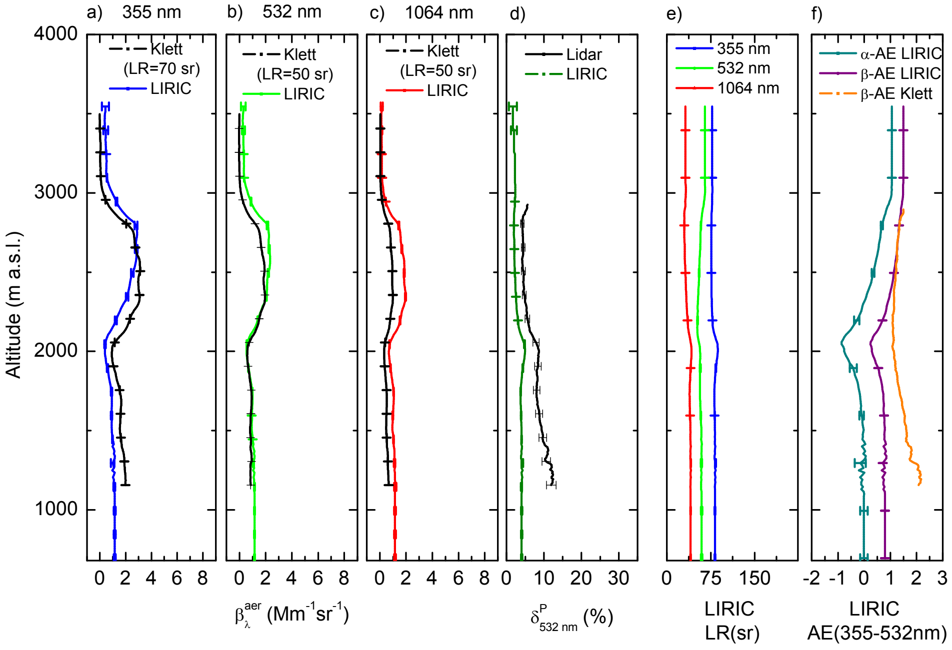

Figure 5.30. As Figure 5.26 but for 24th July 2012.

the previous cases, $\delta^{P}_{532\mathrm{nm}}$values obtained from the lidar data were slightly larger, especially below 2 km a.s.l, where the volume concentration obtained with LIRIC was lower. In this case, $\delta^{P}_{532\mathrm{nm}}$ values obtained from the lidar data are more coherent with the sphericity values retrieved by AERONET at the two altitude levels than those retrieved with LIRIC. Discrepancies in $\delta^{P}_{532\mathrm{nm}}$ profiles can be explained as in previous cases.

From the analysis of these two study cases we can conclude that when the aerosol load is large and the predominant aerosol type is the same over both stations, there is a rather good agreement between the retrieved volume concentration profiles over Granada and over Cerro Poyos, using independent AERONET data at two altitudes. When layers with different aerosol types are present the agreement is lower, because the algorithm uses different aerosol models in the retrievals at different altitudes and it is necessary to take into account this effect in the interpretation of the results. This is related to the assumption of constant values with altitude of the Angström exponent, lidar ratio, percentage of sphericity and refractive index. Therefore, more vertical information from the lidar system may be used to improve the results providing more information about optical and microphysical properties, as proposed in GARRLIC algorithm [*Lopatin et al.,* 2013]. While LIRIC is based on AERONET retrieved data, GARRLIC proposes a stronger synergy between lidar and sun photometer data. It takes into account both the vertical information of the lidar system and the sun photometer direct measurements combining both datasets in the retrieval of column-integrated and vertically resolved optical and microphysical properties. Particularly, in contrast to LIRIC, GARRLIC also provides information about vertical distribution of refractive index, which improves the calculations of the lidar ratio and, therefore, β_{λ}^{aer} profiles.

5.3.2 Summer 2012 statistical analysis

Following the EARLINET measurement strategy, regular lidar measurements are performed at Granada station since 2006. In addition to the EARLINET protocol, supplementary measurements are performed in coincidence with CALIPSO overpasses and under special conditions, such as biomass burning, pollution or dust events. In order to establish a more extensive climatology, additional measurements are also performed around noon during weekdays. As a consequence, an extensive lidar database is available, especially for daytime measurements.

This lidar database can be combined with the sun photometer measurements that are continuously gathered at the station during daytime according to AERONET protocol measurements. In this way we have gathered a wide dataset of simultaneous and collocated lidar-sun photometer measurements above Granada station. As previously explained, the availability of a second sun photometer located at Cerro Poyos AERONET station during summertime since 2011, allows obtaining simultaneous measurements at two different altitude levels and in the same atmospheric.

Thanks to this experimental setup, a statistical analysis of microphysical properties profiles retrieved from two different levels by means of LIRIC was performed during summer 2012 using AERONET data from both stations. A total of 112 microphysical properties profiles retrievals were performed simultaneously above Granada and Cerro Poyos stations. The available database is limited by the number of AERONET inversion retrievals provided by the sun photometer at Cerro Poyos station, since it is the most restrictive due to the lower aerosol load above this station and to the frequent cloud development in Sierra Nevada slopes along the day.

The statistical analysis presented here includes the months of July (35 retrievals during 7 days) and August (77 retrievals during 10 days). The number of retrievals is variable for each day depending on the number of AERONET retrievals and the availability of lidar data.

For the analysed cases, a classification of aerosol types based on criteria similar to that suggested by *Basart et al.*, [2012] is performed. Namely, cases corresponding to dust are those with an AE(440-870nm)<0.75 and the sphericity below 30%. The mixed dust presents values of AE(440-870nm) in the range 0.75-1 and sphericity 30-60%. Finally, for the cases labelled as mixture of different aerosol types, the AE(440-870nm) varies between 1 and 1.5 and the sphericity is larger than 60% . However, some cases do not fit in this classification and needs to be applied carefully. AERONET retrieved τ_{440nm}, AE(440-870nm) and sphericity data used for the classification are presented in figure Figure 5.31. For the classification, data from Granada AERONET station were used. In general, similar values of the AE(440-870nm) and sphericity were obtained for both stations. As expected, τ_{440nm} presented larger values above Granada station. Results according to the aerosol type classification are shown in Figure 5.32. A great majority of the cases (70%) corresponded to mineral dust in our analysed period. This is in agreement with the previous study by *Navas-Guzmán et al.*, [2013], that also indicated, based on lidar-retrieved aerosol optical properties, a strong presence of mineral dust above Granada experimental site during the period from April to September.

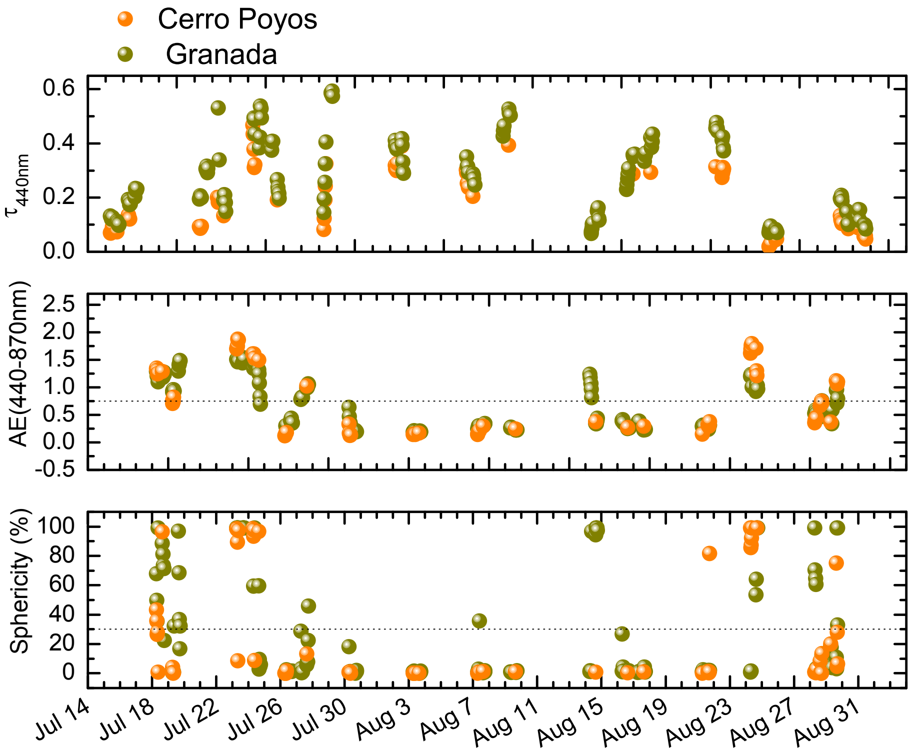

Figure 5.31. AERONET retrieved τ_{440nm}, AE(440-870nm) and sphericity corresponding to the analysed days during summer 2012.

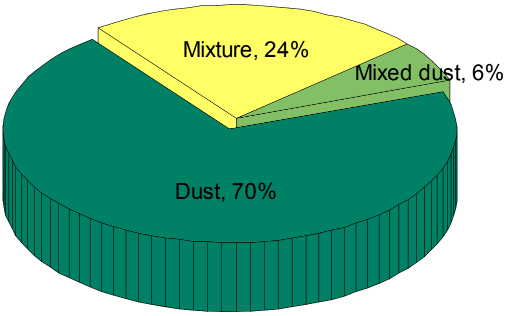

Figure 5.32. Information on the aerosol type classification during summer 2012. See text for the category definition.

First, in order to characterize the aerosol microphysical properties above the experimental site, a statistical analysis is presented in Figure 5.33. A box-whiskers diagram is obtained with the main statistical parameters for the 112 retrievals obtained from each AERONET station considering 500-m layers. 500-m layers were chosen since they have proven to provide enough number of points to perform the statistical analysis and they were small enough to detect vertical structures. As we can see, there was a clear predominance of the coarse spheroid mode. This result is in agreement with the aerosol type classification, since the 70% of the cases corresponds to mineral dust and the sphericity was below 30% according to our classification. The fine and coarse spherical modes presented very low concentration values, with both median and mean values below 10 $\mu m^3/cm^3$. Maximum values up to 20 $\mu m^3/cm^3$ for the fine mode and 60 $\mu m^3/cm^3$ for the coarse spherical mode were observed. These maximum values were found only in the retrieval from Granada in the lowermost layers, but not in the retrieval from Cerro Poyos. Considering the retrieval from Cerro Poyos, maximum values for the fine and the spherical mode were 15 and 40 $\mu m^3/cm^3$, respectively. The slightly larger values of the fine and especially the coarse spherical mode observed below 2000 m a.s.l. may be related to the contribution from local sources located at the surface, such as traffic emissions or local fires. Since the mixing layer remains usually below the altitude of Cerro Poyos station [*Granados-Muñoz et al.,* 2012], these particles hardly reached the second station and their contribution was not detected by the second sun photometer. Nonetheless, it is worthy to consider also the effects of the incomplete overlap and the larger uncertainties affecting LIRIC retrievals in this height range. The predominant coarse spheroid mode presented mean values ~30 $\mu m^3/cm^3$. Slightly larger values were obtained in the lowermost height ranges. An important decrease was observed above 5500 m a.s.l., where the volume concentration dropped towards zero. Maximum values were 120 and 130 $\mu m^3/cm^3$ in the retrievals from Granada and Cerro Poyos, respectively. The large standard deviation (from 5 to 25 μm^3/cm^3 depending on the height range), interquartile range (up to 48 μm^3/cm^3) and extreme values indicated a strong variability. This results from the variability in the frequency of dust events as indicated by *Navas-Guzmán et al.* [2013]. Comparing the mean values of the retrievals from both stations, we observe a quite large agreement, with differences below 5 μm^3/cm^3. However, it is noticeable that from Granada station no volume concentrations are observed above 6000 m a.s.l, whereas from Cerro Poyos some data are observed above this altitude. However, the number of data available over 6000 m a.s.l. is quite reduced (11 data points) and, therefore, the statistic is not significant. As discussed in *Navas-Guzmán et al.* [2013], during summer aerosol particles reach quite high altitudes (up to 6000 m a.s.l.) due mainly to two factors: the large values of the planetary boundary layer height [*Granados-Muñoz et al.*, 2012] and the frequent long-range transport of aerosol particles in the free troposphere [*Alados-Arboledas et al.*, 2011; *Guerrero-Rascado et al.*, 2009].

In order to compare the retrievals from Granada and from Cerro Poyos, only the height range corresponding to altitudes above 1820 m a.s.l. of the profiles retrieved from Granada were considered. Figure 5.34 shows the distribution of the volume concentrations by height levels in percentage. To obtain the relative contribution in percentage, the total volume concentration was obtained by summing the total volume concentration values of the 112 retrievals and the volume concentration values at every point of the profiles (every 15 m). Therefore, the length of the bars in Figure 5.34 indicates the contribution of every 250-m layer to the total volume concentration for the whole period. Inside each bar, the different colors indicate the apportionment to the total volume concentration in the corresponding height range by the fine, coarse spherical and coarse spheroid modes. As we can see, the largest aerosol loads were located at 2000-3000 m a.s.l. and a very low portion was observed above 5000 m a.s.l.

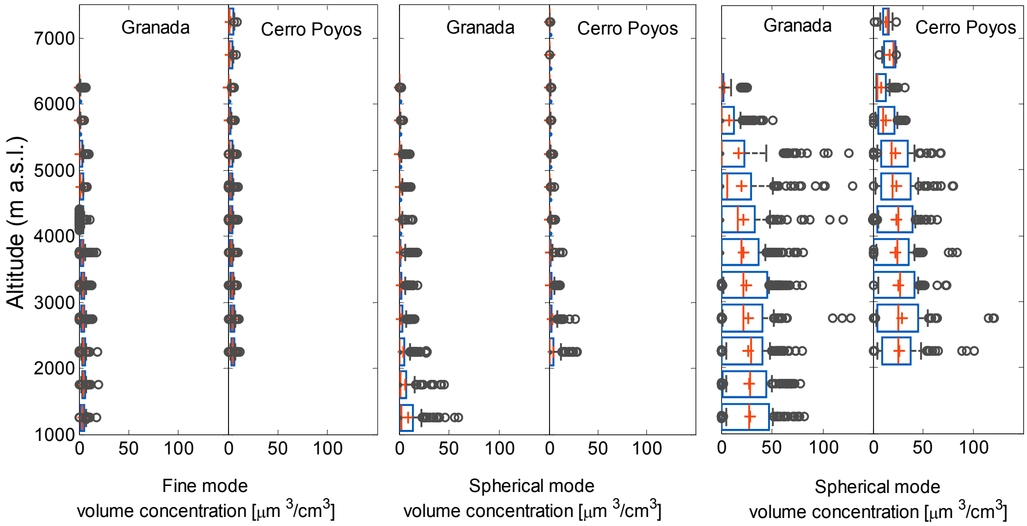

Figure 5.33. Box-whisker plots of the volume concentration of every mode in layers of 500 m. The red cross indicates the mean value and the central line in the box is the median. The extremes of the box correspond to the first and third quartile and the bars indicate the standard deviation. The grey dots correspond to the outliers which are those data with values larger (lower) than the mean plus (minus) standard deviation.

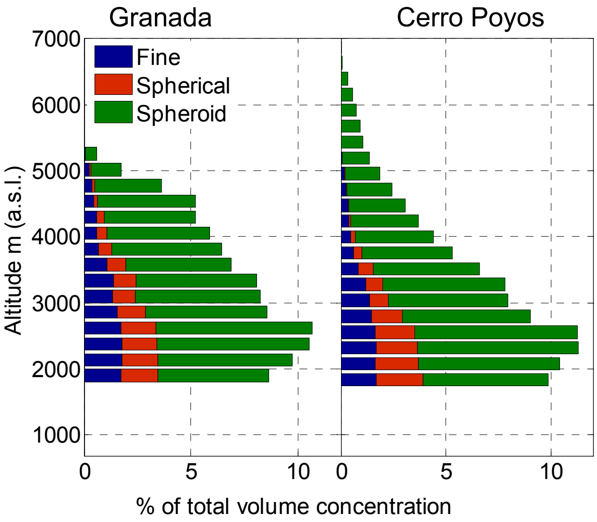

Figure 5.34. Percentage of the total volume concentration distributed by layers of 250 m. The length of the bars indicates the contribution of every 250-m layer to the total volume concentration. The total volume concentration is calculated as the sum of the 112 profiles during the whole analysed period and the sum of the values for the entire vertical profiles. Inside each bar, the different colors (blue, red, green) indicate the apportionment to the total volume concentration in the corresponding height range by the fine, coarse spherical and coarse spheroid modes, respectively.

However, it seems that the retrieval from Cerro Poyos tended to distribute above 5000 m some of the aerosol load that the retrieval from Granada located in the layers between 4000 and 5000 m a.s.l. The apportionment of the fine mode to each layer was very similar at both stations. However, larger differences are observed for the coarse spherical mode. For Granada station, the contribution is almost constant up to 3500 m a.s.l. and some values are observed up to 5000 m a.s.l. On the other hand, for Cerro Poyos a larger apportionment of the spherical mode is observed for the lower layers up to 2750 m, and no contribution is observed above 4500 m a.s.l. The spheroid mode is clearly predominant in every layer, representing always more than 60% of the total volume concentration.

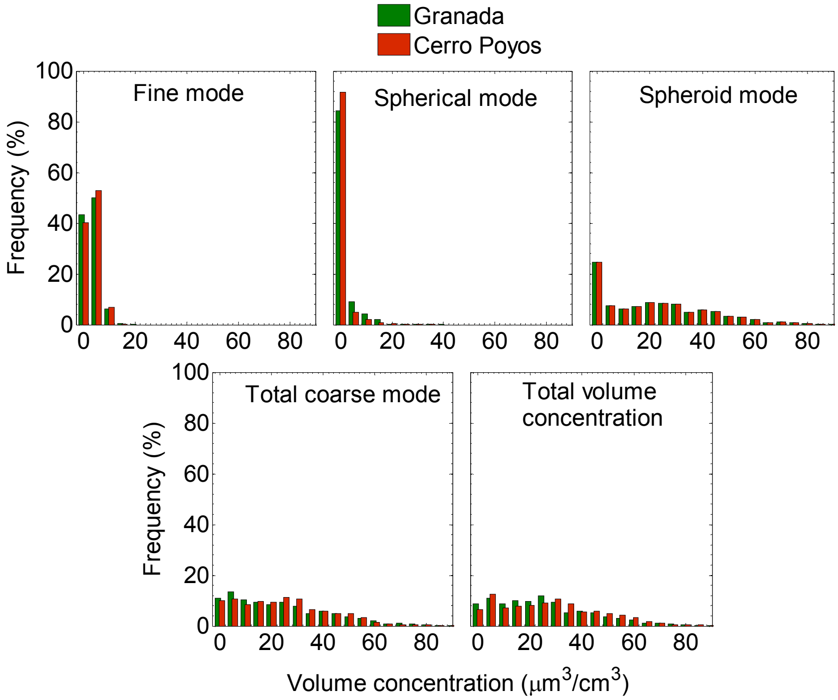

Figure 5.35. Frequency distribution of the volume concentration for every mode, the total coarse mode and the total volume concentration for summer 2012. Each point of the 15-m vertically resolved profiles was considered as an independet data to retrieve the frequency distributions. In the retrievals from Granada station, only those data corresponding to heights above 1820 m a.s.l. were considered in order to compare with the retrievals from Cerro Poyos.

Figure 5.35 shows the frequency distributions of the volume concentration values obtained with LIRIC retrievals from both stations. To make the frequency distribution, volume concentration data each point of the 15-m vertically resolved profiles was considered as a data. The frequency distributions were very similar for every mode at both stations, as it could be expected from the comparison of the mean profiles. Nonetheless, some small discrepancies were observed. According to the histogram of the total volume concentration, it seems that the retrieval from Granada from 1820 m a.s.l. presented lower values of the volume concentration compared to the retrieval from Cerro Poyos. This result could be explained by the effect of the incomplete overlap in the lower part of the profiles retrieved from Granada. The underestimation of the volume concentration above 1820 m a.s.l. could be associated to an overestimation in the lower height range. According to the frequency distribution of the fine mode, 90% of the data corresponded to volume concentrations below 10 $\mu m^3/cm^3$. For the coarse spherical mode a small fraction of the data reached values up to 40 $\mu m^3/cm^3$, but 90% of the values were below 5 $\mu m^3/cm^3$. The coarse spheroid mode presented a much more homogeneous distribution, with 95% of the data in the range 0-60 $\mu m^3/cm^3$. The total coarse mode and the total volume concentration presented distributions similar to the one of the coarse spheroid mode, although the fraction of data corresponding to the bin 0-5 $\mu m^3/cm^3$ was much lower.

The deviations between the profiles retrieved from both stations are also presented here. These deviations were calculated by subtracting the 15-m vertically resolved volume concentration profiles from Granada above 1820 m a.s.l. to those retrieved from Cerro Poyos station for each mode. Besides the fine, coarse spherical and coarse spheroid mode, the calculations were also performed for the total coarse mode (spherical plus spheroid) and the total volume concentration (sum of the three modes). Figure 5.36 shows the histograms corresponding to the deviations. For the fine mode the deviations were always below 5 μm^3/cm^3, since the volume concentrations for this mode were very low. The negative values indicated a general slight underestimation of the profiles calculated from Cerro Poyos for the fine mode. In the case of the spherical mode, 95% of the values presented an absolute deviation lower than 5 μm^3/cm^3. However, deviations as large as -15 μm^3/cm^3 were also obtained. The deviations for the spheroid mode exhibited a larger range of variation, with the 90% of the data distributed between -5 and 15 μm^3/cm^3. Nonetheless, 50% of the data presented deviations close to 0, indicating very good agreement between both retrievals. For the total coarse mode, the histogram was basically the same as the one obtained for the coarse spheroid mode, since it was the predominant mode, as observed in Figure 5.33. The total volume concentration presented deviations lower than 5 μm^3/cm^3 (in absolute value) for 70% of the data and below 10 μm^3/cm^3 for the 90% of the data. This is indicative of the good agreement between both retrievals, especially taking into account the values of the uncertainties obtained in section 4.1.2. A 70% of the data points exhibited positive deviations, what indicates that the total volume concentration retrieved from Cerro Poyos were larger than those retrieved from Granada. This is in agreement with the results in Figure 5.33 and, as previously stated, may be related to the effect of the incomplete overlap in the lowermost height region of the profiles retrieved from Granada.

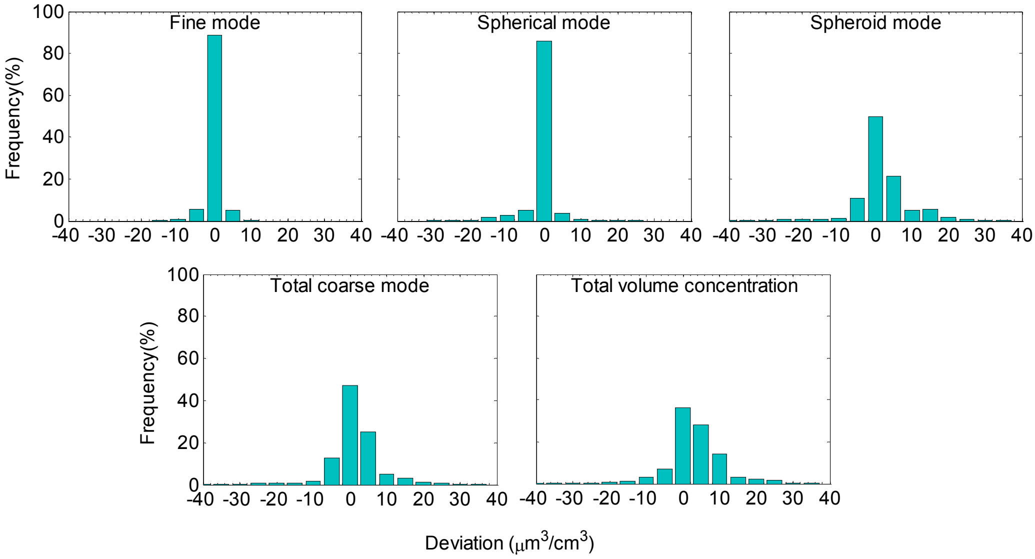

Figure 5.36. Histogram of the frequency distribution of the deviations for the whole dataset corresponding to summer 2012. Deviations were obtained by subsctracting the profiles from Granada above 1820 m a.s.l. to the profiles retrieved from Cerro Poyos at every height level (15 m vertical resolution).

In order to further investigate the variation of the deviations with height, a box-whiskers plot corresponding to the absolute deviation in layers of 500 m is represented in Figure 5.37. For the fine and spherical modes, the mean values of the deviation were always close to zero, and the standard deviations were mainly in the range ±5 $\mu m^3/cm^3$, since the profiles corresponding to these modes presented usually very low values. However, for the coarse spheroid mode, the deviations were larger, with mean values between -2 and 4 $\mu m^3/cm^3$ and standard deviations ranging from -17 to 16 $\mu m^3/cm^3$. The interquartile range also exhibited larger values than in the fine and spherical modes, indicating larger variability of the spheroid mode during the analysed period. Since the spheroid mode is usually related to mineral dust, this may be due to the variability in the frequency of the dust events affecting the different experimental sites. The deviation values were mainly positive, indicating that for the spheroid mode, the volume concentration profiles values retrieved are usually larger in the retrieval from Cerro Poyos, as observed also in Figure 5.35. The largest variability in the absolute deviations was observed between 4 and 6 km a.s.l. This is in agreement with the results in Figure 5.33, where larger standard deviation values were observed in the retrieval from Granada than in that from Cerro Poyos station. The total coarse mode and the total volume concentration profile plots were very similar to the plot of the coarse spheroid mode since it was clearly predominant, as inferred from the previous results. The limits of the boxes corresponding to the total volume concentration presented always positive values, confirming that the volume concentration retrieved from Cerro Poyos station was slightly larger. This may be an indicator than in the retrieval from Granada the aerosol volume concentration in the layer between the surface and 1820 m a.s.l. (below Cerro Poyos) is being slightly overestimated, as it was previously indicated. It is worthy to notice that this region is affected by the incomplete overlap of the lidar system and more affected by the uncertainties as discussed in section 4.1.2. This overestimation of the volume concentration profiles retrieved from Granada in the lowermost height region and the consequent underestimation above 1820 m a.s.l. was also confirmed by the height-integrated volume concentration values. The volume concentration profiles retrieved from Granada were integrated in the height range between 1820 m a.s.l. and the top of the profiles. When compared to the integrated volume concentration profiles retrieved using Cerro Poyos AERONET data, 85% of the values were lower in the case of Granada retrieval.

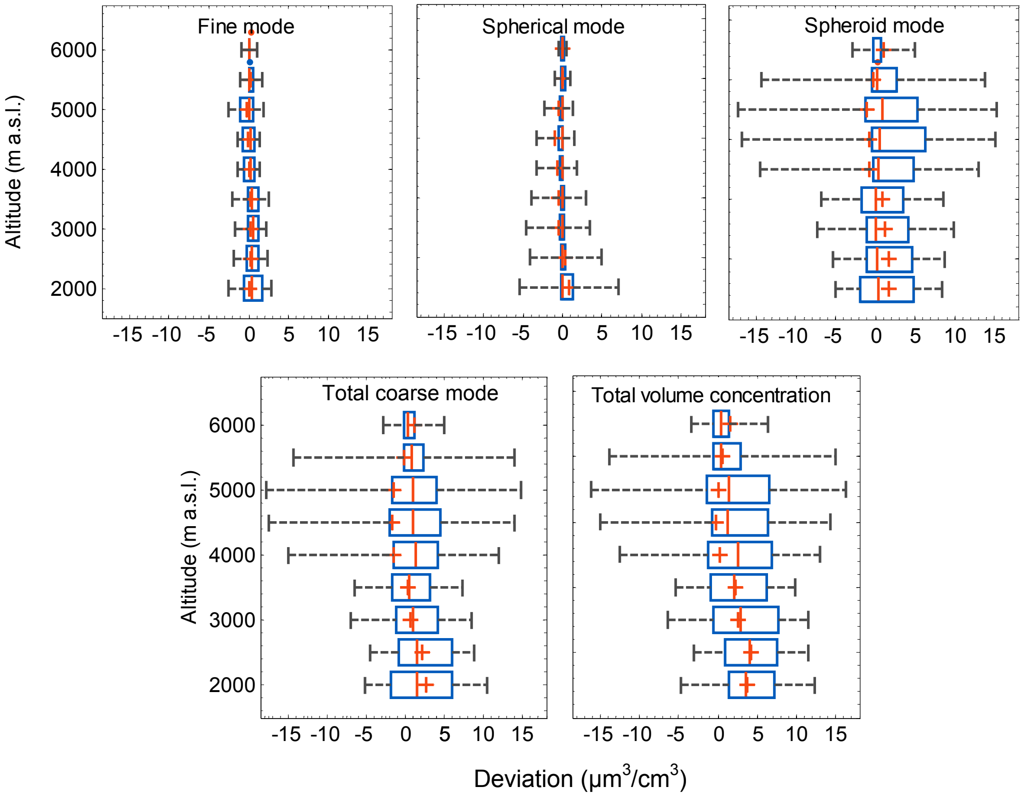

Figure 5.37. Box-whisker plots of the deviation profiles distributed in 500-m layers for fine, coarse spherical, coarse spheroid, total coarse mode and the total volume concentration. Deviations are obtained by subtracting the retrieved volume concentration profiles from Granada above 1820 m a.s.l. to those retrieved from Cerro Poyos at every height level (15 m vertical resolution).

Scatter plots of the 15-m vertically resolved profiles retrieved simultaneously above Granada and above Cerro Poyos stations were performed for the 112 retrievals. An example corresponding to 9th August 2012 in the perriod from 15:30 to 16:00 UTS is shown in Figure 5.38. As previosly indicated, in the retrieval from Granada only those data above 1820 m a.s.l. were considered.

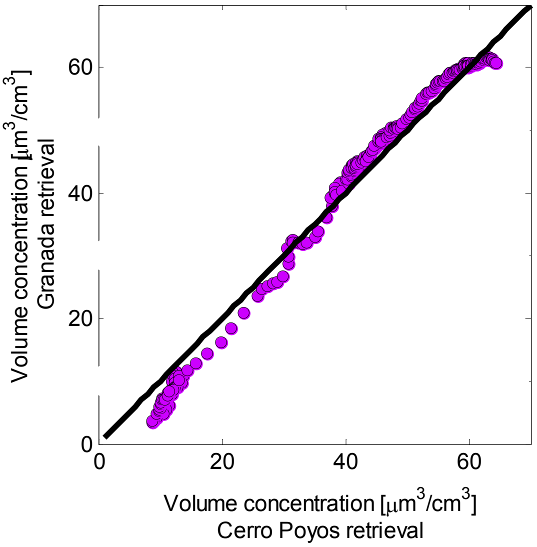

Figure 5.38. Scatter plot of the total volume concentration profiles retrieved from Granada vs Cerro Poyos stations corresponding to the 9th August 2012 between 15:30 and 16:00 UTC. The black line corresponds to the 1:1 line.

Linerar fits were calculated and 112 correlation coefficients (R) corresponding to these linear fits between both retrievals were obtained. The frequency distribution of R is shown in (Figure 5.39). As it can be observed, R values greater than 0.6 were obtained for the 80% of the 112 retrievals for all the modes. Therefore, high correlations were obtained. For the coarse spheroid mode and the total volume concentration profiles correlation values of 1 were obtained in 73% and 77% of the profiles, respectively. Negative values of R were also observed, although only for 12% of the cases for the fine and the spherical modes. These cases were reviewed in detail and it was observed that this occurred mainly in those profiles where the volume concentration was below 7 $\mu m^3/cm^3$. For these profiles the variations with height are more related to noise than to real aerosol vertical distribution and, therefore, R is not a good parameter to study the agreement between both retrievals.

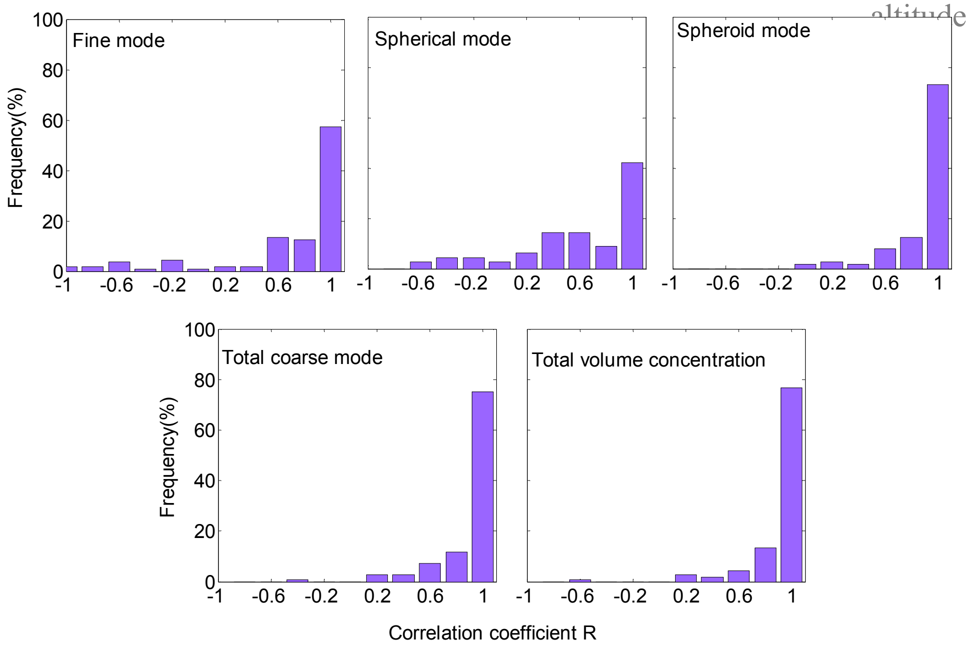

Figure 5.39. Frequency distribution of the correlation coefficient R retrieved from the 112 linear fits of the profiles retrieved simultaneously from Granada and from Cerro Poyos in the coincident height range. In the case of Granada, only heights above 1820 m a.s.l. were considered.

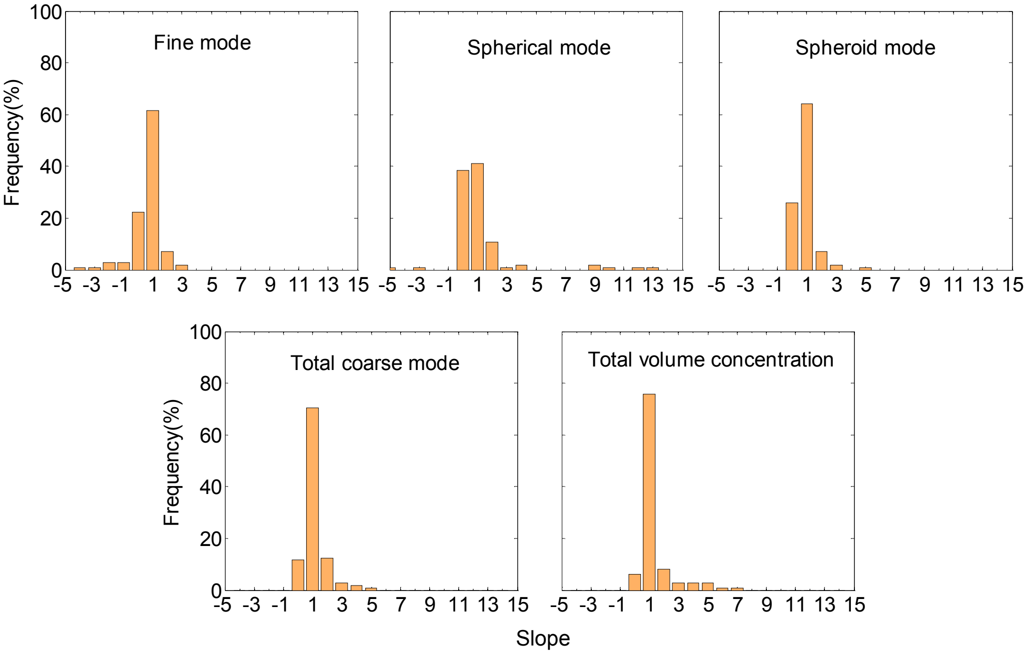

Figure 5.40. Frequency distribution of the slope retreieved from the 112 linear fits of the simultaneous profiles for every mode. The linear fits were obtained for the profiles retrieved simultaneously from Granada and from Cerro Poyos in the coincident height range. Therefore, only heights above 1820 m a.s.l. were considered in the retrieval from Granada.

The slope values corresponding to the linear fits are shown in Figure 5.40. For the different modes analysed most of the data presented values of the slope around unity. Specifically, the slopes of at least 65% of the profiles for all the modes are around unity. This value decreased down to 50% for the spherical mode. It is also remarkable that as much as 40% of the data for this mode were grouped around zero. After reviewing this 40% of the cases in detail it was observed that there were three possible scenarios. Around 85% of them corresponded to situations where the volume concentration of the spherical mode was very low (usually close to zero) in comparison to the total volume concentration. A small fraction (~4 %) corresponded to situations similar to that explained in section 5.3.1.2, where different aerosol types were observed above and below Cerro Poyos station. These situations were not very often during summer 2012 and it seems that, even though the methodology presents some weakness in this especial cases and they should be excluded, they do not introduce much uncertainty in this statistical analysis. Finally, the third scenario corresponds to those cases when the aerosol load was very low above Cerro Poyos station (~10% of the cases). For these cases, the retrieval of the sphericity parameter is affected by high uncertainties (especially if it has extreme values) and there are enormous differences between the sphericity assumed at Granada station and that assumed at Cerro Poyos station. Consequently, for these cases also the spheroid mode presented slope values close to zero. However, for the total coarse mode the agreement and the slope are quite good. Therefore, the sphericity parameter needs to be carefully reviewed when making this kind of statistical comparisons. According to *Chaikovsky* [personal communication], the distinction between spherical and spheroid particles within the coarse mode is not reliable in those cases with extreme values of the sphericity, precisely due to the large uncertainties in the sphericity parameter. Therefore, for further statistical analysis, these cases should be either rejected or the depolarization should not be considered, therefore retrieving only the total coarse mode.

To sum up, from the statistical analysis we can conclude that during the summer of 2012 a large number of long-range transport dust events affected the experimental site. As a consequence, the predominant mode in the retrieval of microphysical properties was the coarse spheroid mode. For this mode, a large variability was observed due to the variations in the frequency of the dust events above Granada station.

Because of the use of the second sun photometer at Cerro Poyos, the comparison between the retrievals from two different heights was possible. Differences were expected because of the effects of the incomplete overlap in the retrieval from Granada and the very low aerosol load above Cerro Poyos in some cases. In addition, the horizontal distance (even though very short) and the orography between both stations may introduce some small discrepancies in the results. In order to make the comparison, the profiles retrieved using Granada AERONET data were only considered above 1820 m a.s.l., which is the coincident height range for both retrievals. Taking into account these constraints, the deviations values obtained indicated a quite good agreement, with discrepancies within the uncertainty limits obtained in section 4.3.2 for almost 90% of the analysed cases. A more detailed analysis considering the variations in the different layers revealed a quite good agreement also with height, except in the upper part of the profiles. In this uppermost part, the retrievals from Cerro Poyos tended to distribute some of the aerosol load up to higher altitudes than the retrievals from Granada in some cases. The number of these cases was quite reduced though. Comparing the different modes, the agreement was also quite good especially for the fine and coarse spheroid modes. The spherical mode agreed also quite well, but larger discrepancies than for the other two modes were observed in the height range close to Cerro Poyos station.

In spite of the good agreement, larger values of the total volume concentration were obtained above 1820 m a.s.l. in the retrieval from Cerro Poyos than in the retrieval from Granada. The underestimation of the volume concentration values above 1820 m a.s.l. in the retrieval from Granada may be associated to an overestimation of the profiles in the lowermost part. According to these results, the way the incomplete overlap effects are considered in this region by LIRIC and the assumption of constant volume concentration values below z_{N0} should be reviewed in order to improve the algorithm results.

Besides the analysis of the deviations, 112 linear fits were performed for the profiles retrieved simultaneously from Granada and from Cerro Poyos stations. From the detailed analysis of the correlation coefficient R and the slope obtained from the linear fits, good agreement was also inferred, with most of the data presenting values close to one. From this analysis we can conclude that those cases with large discrepancies correspond to three possible situations: i) situations with very low volume concentration values; ii) situations with different aerosol types above and below Cerro Poyos station height and iii) situations with very low aerosol load above Cerro Poyos which lead to large uncertainties in the retrieval of the sphericity parameter. Situations corresponding to case (ii) did not occur very often during summer 2012 (~2% of the total cases) and therefore the errors introduced are almost negligible. For the three exposed situations, some assumptions need to be carefully reviewed, i.e., the height independency of the size distribution or the sphericity and the performance of LIRIC algorithm under very low aerosol load conditions.

6 Hygroscopic growth effects on the backscatter coefficient measured above Granada station

Results presented in this chapter correspond to the period 2011-2013, when several radiosounding campaigns were performed at the experimental site. A total of 50 radiosondes were launched mainly during summer and winter. Additional launches were also performed under certain specific conditions when hygroscopic growth was foreseen. During these periods, lidar measurements were always running in coincidence with the radiosounding launches. These lidar measurements have been exhaustively analysed together with the relative humidity (RH) profiles provided by the radiosoundings in order to detect potential cases of aerosol hygroscopic growth following the methodology described in section 4.4. According to this methodology, adequate conditions for the analysis of hygroscopic properties under ambient conditions were rarely encountered at the experimental site. However, the analysis of two study cases corresponding to 22nd July 2011 and 22nd July 2013 evidenced that hygroscopic growth was highly possible at certain height ranges for these dates. The analysis of these cases is presented in the following subsections.

6.1 Case I: 22nd July 2011

On 22nd July 2011 a radiosounding was launched at 20:30 UTC in coincidence with night-time lidar measurements. The analysis of the lidar data and the ancillary information according to the procedures described in section 4.4 suggested the likelihood that some atmospheric layers were affected by aerosol hygroscopic growth.

As explained in chapter 2, atmospheric aerosol hygroscopic properties are highly dependent on the aerosol chemical composition. Due to the lack of aerosol chemical composition data, the information provided by the models with respect to the aerosol type was quite relevant for the discussion of the results in the analysis of hygroscopic growth properties. According to NAAPS and BSC-DREAM8b models, 22nd July 2011 at 18:00 UTC was characterized by the presence of mineral dust above Granada (Figure 6.1). Models outputs corresponding to 23rd July 2011 at 00:00 UTC (not shown), which are also close to the time corresponding to the radiosonde launch, were almost identical to the ones presented in Figure 6.1.

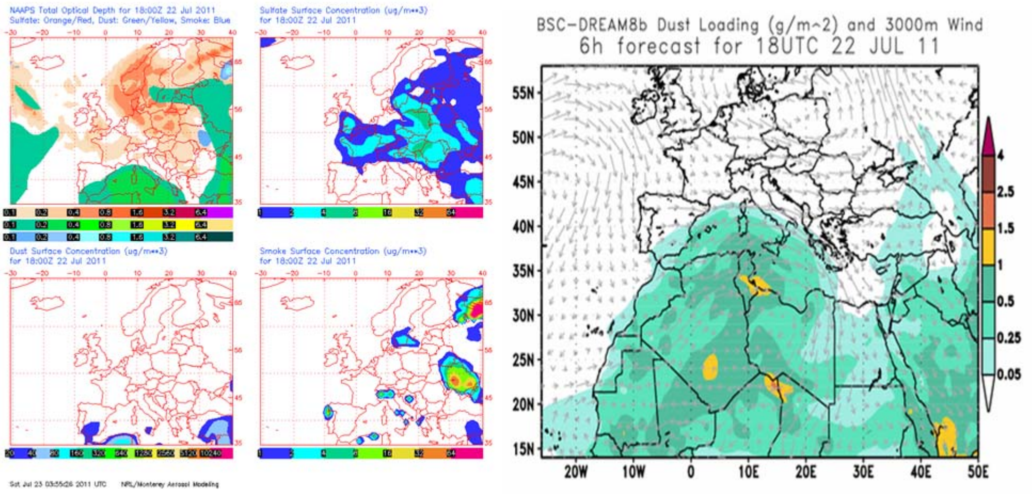

Figure 6.1. NAAPS and BSC-DREAM8b model forecasts for 22nd July 2011 at 18:00 UTC.

Sun photometer experimental data were also used for this analysis, since they provide information about the aerosol type. For this specific day, sun photometer data were in agreement with the models during the morning and afternoon hours, indicating the presence of mineral dust above the station. However, sun photometer data from 15:00 to 18:30 UTC indicated an important contribution of fine particles (Figure 6.2). As it can be seen, τ_{440nm} was decreasing during the afternoon, changing from 0.30 in the morning to values of 0.20 at 18:30 UTC. The AE(440-870nm) was increasing from 0.5 to 1.1, indicating an enhancement in the contribution of fine particles from midday onwards. The size distribution retrieved at 18:30 UTC (shown in Figure 6.2b) indicated a balanced presence of both fine and coarse particles. This is confirmed by the fine mode fraction, determined through the SDA (spectral deconvolution algorithm) [*O'Neill et al.,* 2003], that increases from 0.35 in the early morning up to 0.55 in the late evening. The ω(λ) values, around 0.93, and its spectral dependence indicated a mixing of mineral dust with aerosol from anthropogenic origin [*Dubovik et al.*, 2002].

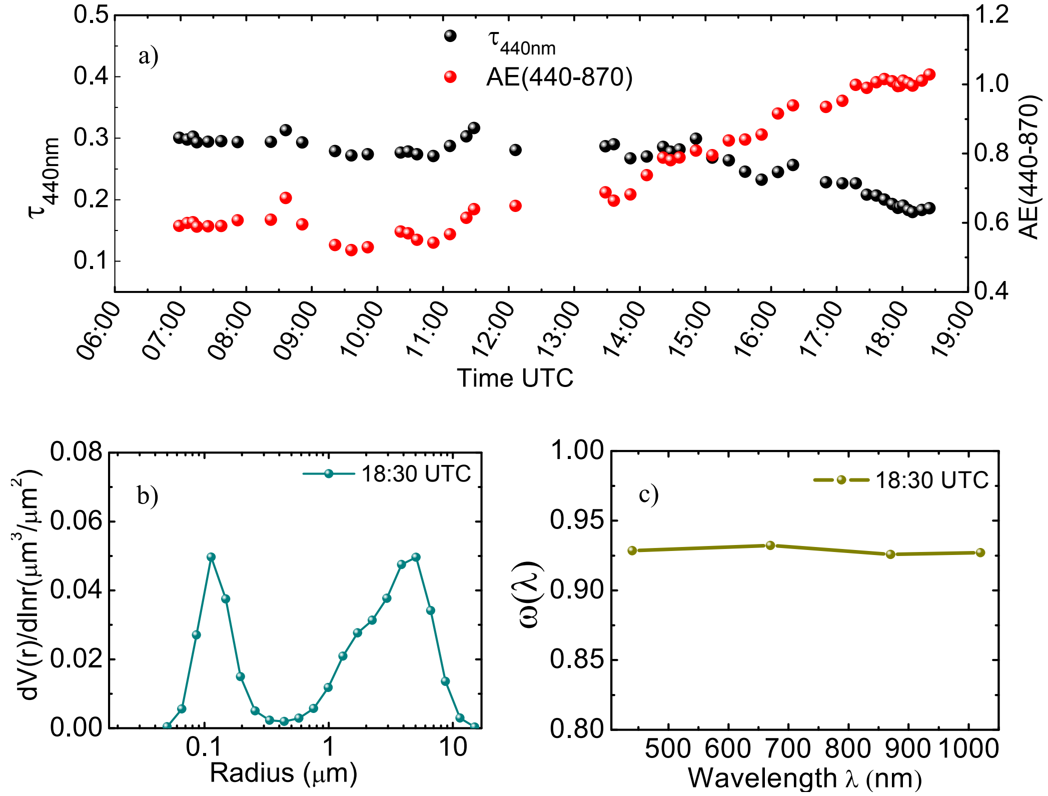

Figure 6.2. a) AERONET τ_{440} and AE(440-870) daily time series on 22nd July 2011. b) AERONET retrieved volume size distribution at 18:30 UTC for the same date. c) ω(λ) for the same time and date.

Lidar RCS time series (Figure 6.4) indicated the presence of atmospheric aerosol up to 3000 m a.s.l. Moreover, a strong increase of the RCS was observed inside this height range around 2400 m a.s.l. between 20:30 and 21:00 UTC. This increase in the RCS could be related to the aerosol water uptake due to the increase in RH. The increase of RH with altitude is clearly observed in Figure 6.3, where detailed information from radiosounding data is presented in a skew-T diagram.

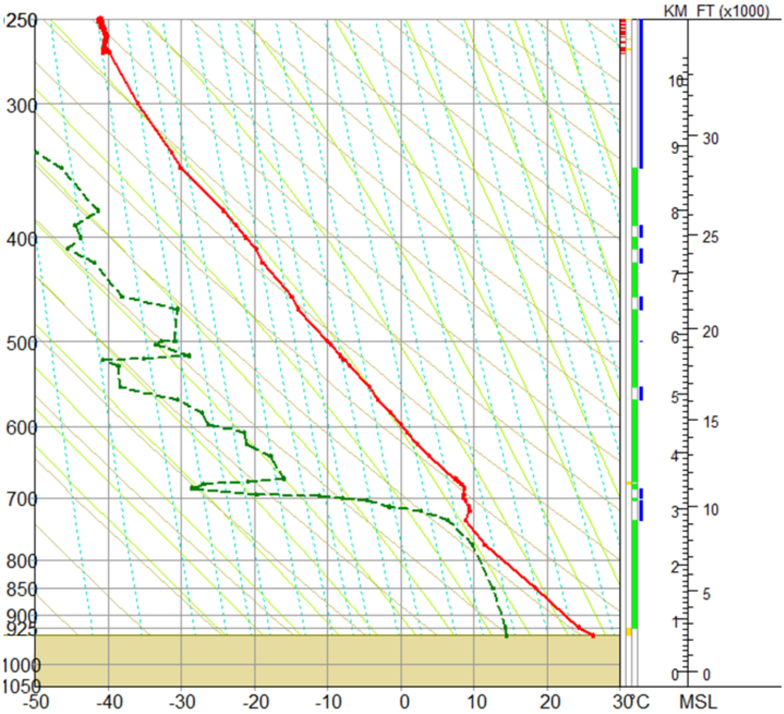

Figure 6.3. Skew-T diagram of the radiosounding launched on 22nd July 2011 at 20:30 UTC. The red line represents the temperature profile and the green dashed line is the dew point temperature (in °C).

The analysis of lidar data by means of the Klett-Fernald inversion algorithm during the period 20:30-21:00 UTC revealed a marked increase in β_{532} in the height range from 1330 to 2330 m a.s.l. (Figure 6.5). For the same height range, the RH profile measured from the radiosounding increases from 60 to 90%.

Opposite to β_{532}, β-AE(355-532nm) decreased with altitude in the aforementioned height range with values from 1.3 to 0.8. The decrease in β-AE(355-532nm) indicated a change in the size of particles from bottom to top in this height range, being stronger the contribution of larger particles at higher altitudes. The δ^P_{532nm} also decreased with altitude being 0.10 at 1330 m a.s.l. and decreasing down to 0.05 at 2330 m a.s.l. The positive correlation between β-AE(355-532nm) and δ^P_{532nm} indicated that the increasing contribution of larger particles corresponded to an increase in particle sphericity. This behaviour suggested hygroscopic growth, since aerosol particles become larger and more spherical due to water uptake. The δ^P_{532nm} profiles retrieved from lidar data are rather low in comparison with the values associated to pure mineral dust particles (δ^P_{532nm} = 0.35) [*Freudenthaler et al.*, 2009]. Therefore, it comes to confirm that during the analysed period the atmospheric aerosol over Granada was not only mineral dust, in spite of the models. Values of δ^P_{532nm} lower than 0.1, the AE(440-870nm) values larger than unity and the low spectral dependence of ω(λ) indicated by AERONET data suggests a mixture of mineral dust with a strong contribution of anthropogenic aerosol [*Dubovik et al.*, 2002].

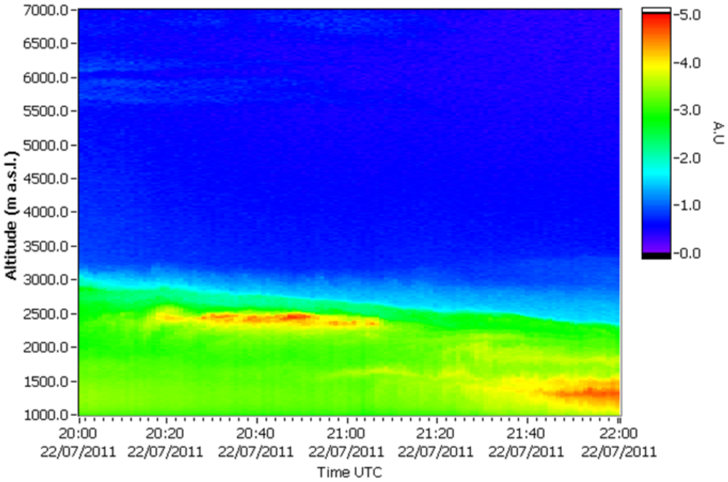

Figure 6.4. a) Lidar RCS time series at 532 nm (arbitrary units) on 22nd July 2011 from 20:30 to 21:00 UTC.

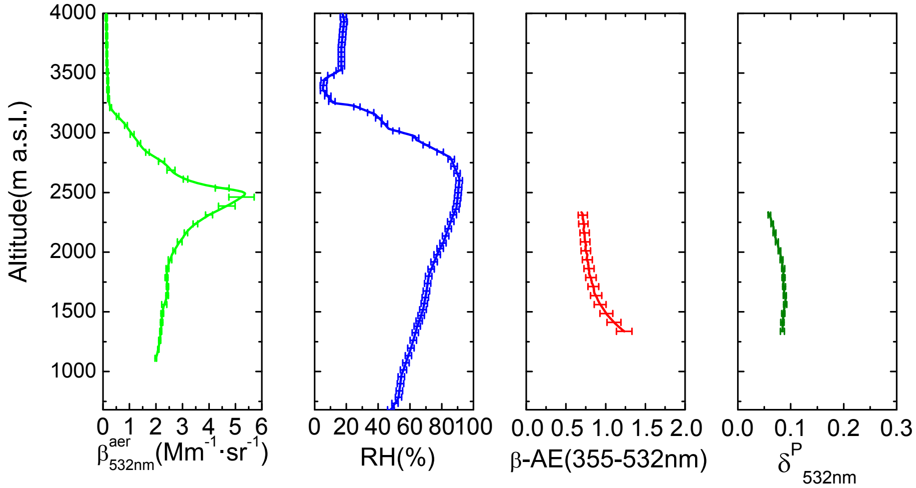

Figure 6.5. a) β_{532} *retrieved with Klett-Fernald algorithm from 20:30 to 21:00 UTC on 22*nd *July 2011 b) RH profiles from the radiosounding launched at 20:30 UTC on the same date. c) β-AE(355-532nm) retrieved with Klett-Fernald algorithm from 20:30 to 21:00 UTC on 22*nd *July 2011. d)* δ^{P}_{532nm} *retrieved from lidar data for the same period.*

According to all the previous results, this case could be considered representative of hygroscopic growth since there is an enhancement in β_{532} coincidence with an increase in RH in the selected height range. In order to check that this enhancement of β_{532} is due to water uptake and not to changes in the aerosol load or composition, it is necessary to check that the conditions described in the methodology in section 4.2 are fulfilled.

The 5-day backward trajectories analysis performed with HYSPLIT model revealed that the air masses came from the Northwest of Europe, going through the Northern Iberian Peninsula, finally arriving over Granada after overpassing the Iberian Peninsula Mediterranean Coast (Figure 6.6). The backward trajectories analysis was performed only for heights corresponding to the height range analysed for studying hygroscopic growth (1330 to 2330 m a.s.l.). The trajectories were almost the same regardless the altitude level in the height range considered. Therefore, the same aerosol type might have been advected over Granada in the investigated height range. These air masses might have transported anthropogenic aerosol from Europe above the experimental site, particularly considering that they were travelling at very low altitudes, located probably within the planetary boundary layer.

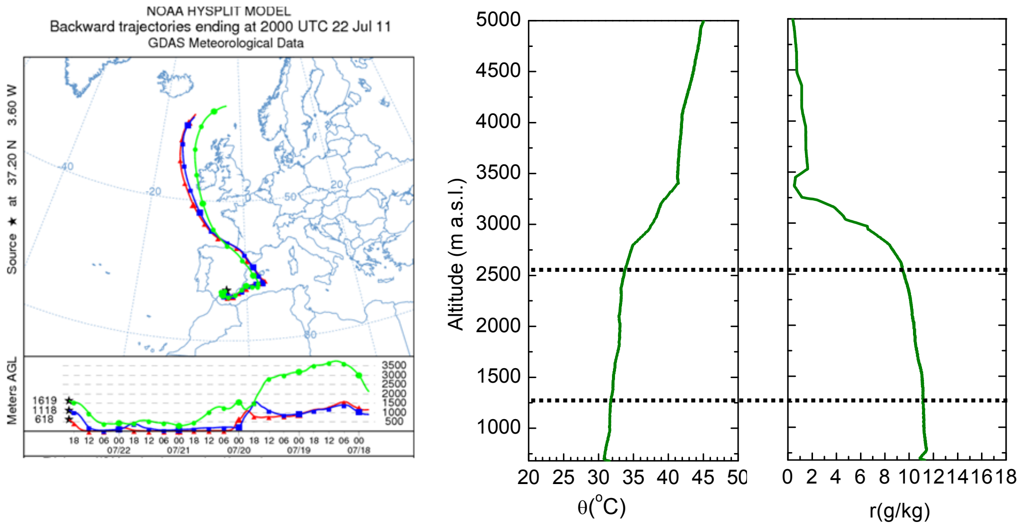

Figure 6.6. a) 5-day backtrajectories analysis ending on 22nd July 2011 at 20:00 performed with HYSPLIT model. b) Vertical profiles of θ(in °C) and r (in g/kg) from radiosounding data on 22nd July 2011 at 20:30 UTC.

Vertical profiles of θ and r measured with radiosounding data were also obtained in order to corroborate good mixing conditions within the analysed height range. Both θ and r profiles presented almost constant values between 1200 and 2500 m a.s.l. (Figure 6.6) and thus it can be inferred that the analysed layer was well mixed. Once these conditions are fulfilled, vertical homogeneity in the analysed height range can be assumed. Therefore, hygroscopic growth is foreseen for this case since there is a high likelihood that changes in the aerosol properties were not due to variations in the aerosol load or the aerosol composition but to water uptake.

From the combination of the β_{532nm}^{aer} and RH profiles in Figure 6.5, the aerosol backscatter coefficient enhancement $f_\beta(RH)$ was obtained as indicated in Eq. 4.24.

$$f_\beta(RH) = \frac{\beta(RH)}{\beta(RH_{ref})}$$

The RH_{ref} in this case is 60%, which is the lower value measured in the investigated height range. The resultant humidogram is shown in Figure 6.7.

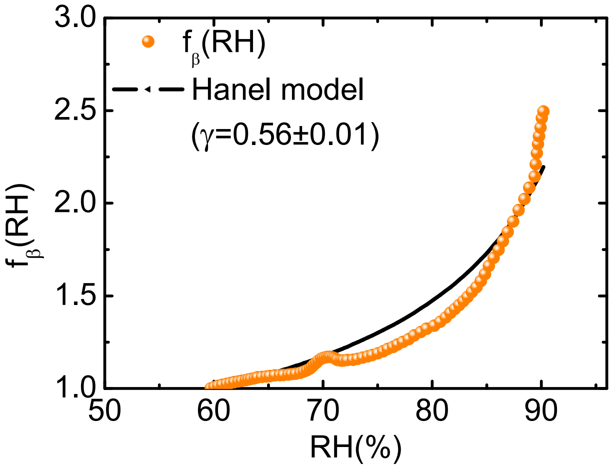

Figure 6.7. f_β(RH) retrieved on 22nd July 2011 from 20:30 to 21:00 UTC for the height range between 1330 and 2330 m a.s.l.

It is evident that β_{532nm}^{aer} increased 2.5 times ($f_\beta(90\%) = 2.5$) in the range of humidity between 60 and 90%. In a similar study performed by *Veselovskii et al.* [2009] in the East Coast of the United States, using the aerosol extinction coefficient profile retrieved with lidar data, they got a value of $f_\beta(90\%) = 5$ in the presence of the typical continental haze using the same RH_{ref} (60%). .

Besides the study by *Veselovskii et al.* [2009], not many lidar-based hygroscopic growth studies with comparable results have been published in recent years. A comparison with in-situ studies would be useful in order to contextualize these results. These studies frequently are based on the retrieval of the scattering coefficient factor $f_{\sigma}(RH)$ and not on the $f_{\beta}(RH)$ used here and usually provide values for f(85%) using RH_{ref} values of 40% or lower (dry conditions). In order to compare results to these in-situ studies using a RH_{ref} of 40%, the Hänel model described in section 4.4 was used. The parameterization of the data using the Hänel model provided a value of $\gamma = 0.56 \pm 0.01$ (black solid line in*Figure 6.7*). Using the value obtained for γ, $f_{\beta}(40\%)$ is calculated by means of the Hänel equation (Eq. 4. 25). The values of f_{β}(RH) represented on Figure 6.7 obtained with the equation $f_{\beta}(RH) = \frac{\beta(RH)}{\beta(60\%)}$ were divided by the $f_{\beta}(40\%)$ value obtained from the Hänel equation. The normalized resulting humidogram is represented in Figure 6.8. Then $f_{\beta}(RH) = \frac{\beta(RH)}{\beta(40\%)}$ is obtained and consequently it is possible to compare with the diverse values of $f_{\beta}(85\%)$ provided by in-situ studies. Although the enhancement factors refer to different optical properties, namely the aerosol scattering coefficient and the aerosol backscatter coefficient, *Feingold and Morley* [2003] stated that $f_{\beta}(RH)$ and $f_{\sigma}(RH)$ presents very good agreement in the range of RH from 85 to 95%.

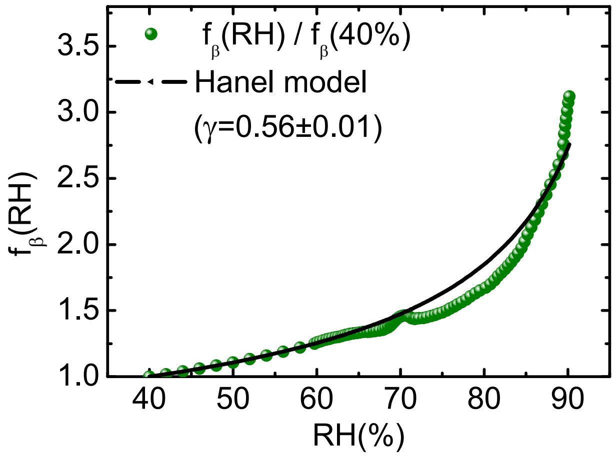

Figure 6.8. $f_{\beta}(RH)$ referred to a $RH_{ref} = 40\%$ obtained by normalizing to the $f_{\beta}(40\%)$ value obtained from the Hänel model. As in Figure 6.7, the humidogram corresponds to 22^{nd} July 2011 from 20:30 to 21:00 UTC for the height range between 1330 and 2330 m a.s.l.

After the normalization to $f_\beta(40\%)$, the value of $f_\beta(90\%)$ increased from 2.5 to 3.2. The obtained $f_\beta(85\%)$ was 2.1, which is within the range of values obtained in previous studies with in-situ measurements for aerosol light scattering. For example, in the study by *Zieger et al.*, [2013], $f_\beta(85\%)$ values were obtained for several aerosol types at different measurement sites. These values ranged between 1.28 for Saharan dust influenced aerosol and 3.41 for Arctic aerosol.

The γ value obtained for the Hänel parameterization in this study case was also in the range of values obtained in previous studies. *Randriamiarisoa et al.* [2006] found values between 0.47 and 1.35 for urban aerosols over Paris using the same parameterization but for the aerosol scattering coefficient. *Gasso et al.* [2000] reported values between 0.27 and 0.6 for polluted and clean marine aerosols respectively, based also on $f_\sigma(RH)$. *Raut and Chazette* [2007] applied the Hänel parameterization to the scattering cross-section and obtained values of $\gamma = 0.55 \pm 0.05$ for urban aerosol in Paris, very similar to the value obtained in this study.

The availability of the AERONET inversion retrieval data at 18:30 UTC shown in Figure 6.9 allowed for retrieving volume concentration profiles by means of LIRIC algorithm [*Chaikovsky et al.,* 2008; 2012]. Figure 6.9a represents these volume concentration profiles obtained by the combination of lidar data from 20:30 to 21:00 UTC and the closer sun photometer retrieval (at 18:30 UTC). As it can be observed, there were mainly coarse spherical and fine particles along the whole profile. Very low concentration of coarse spheroid particles was retrieved for this period in agreement with AERONET retrieved sphericity values (84.6%). The total volume concentration was increasing with height reaching a maximum around 2500 m a.s.l. Figure 6.9b shows the volume concentration enhancement factor (f_{VC}(RH)) for the fine mode and the total volume concentration against RH. As it is observed, the fine mode presented a strong increase with RH. Conversely, the coarse mode was decreasing with RH. The total volume concentration smoothly increased with RH, mainly due to the increase in the fine mode. According to *Zieger et al,* [2013], both size and chemical composition are crucial when determining *f*(RH). Therefore, the relative contribution of the fine and the coarse modes and the specific chemical composition for each mode are very important for determining *f*(RH). In this particular case, it seems that the fine mode was dominated by high hygroscopic particles whereas the coarse mode was dominated by substances with very low hygroscopic growth. *Di Girolamo et al.* [2012] observed similar behavior analyzing aged dust particles partially mixed with maritime, urban and organic aerosols. Their results showed the presence of a hydrophobic coarse mode and hygroscopic fine mode. However, this is not a general result. The interaction between size and chemical composition can lead to compensation effects for *f*(RH), and smaller and less hygroscopic particles may have the same magnitude of *f*(RH) as larger and more hygroscopic particles [*Zieger et al.*, 2010].

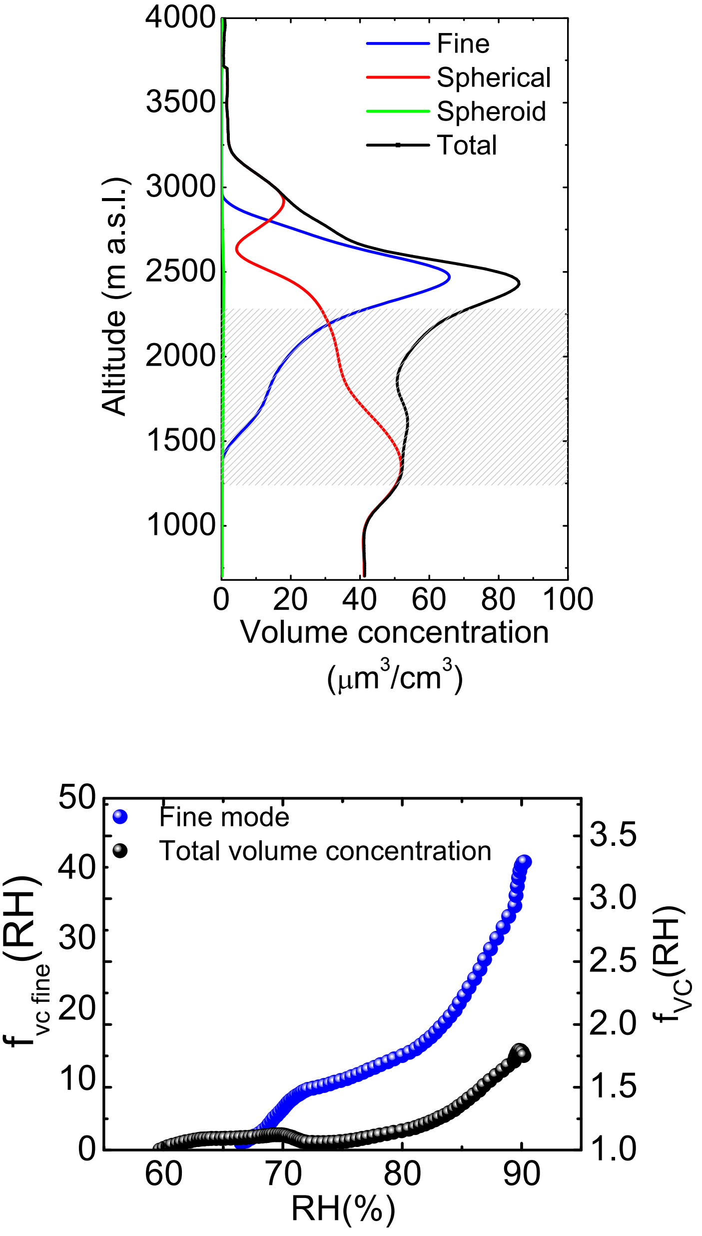

Figure 6.9. a) LIRIC retrieved volume concentration profiles on 22nd July 2011 from 20:30 to 21:00 UTC. The shaded area indicates the height range where hygroscopic growth was investigated. b) $f_{VC}(RH)$ retrieved for the fine mode and the total volume concentration profiles for the same period and the layer corresponding to heights between 1330 and 2330 m a.s.l.

6.2 Case II: 22nd July 2013

Another case of potential hygroscopic growth was detected on 22nd July 2013 during the summer radiosounding campaign. For this specific day, the radiosounding was launched at 20:00 UTC in coincidence with simultaneous lidar measurements. The observed increase in RH with height and the analysis of the lidar data, together with the ancillary information which revealed good mixing conditions indicated a high probability of hygroscopic growth. As a first approach in order to identify the aerosol chemical composition, the NAAPS model was used. For this case, it indicated the presence of sulphates and smoke above the experimental site (Figure 6.10).

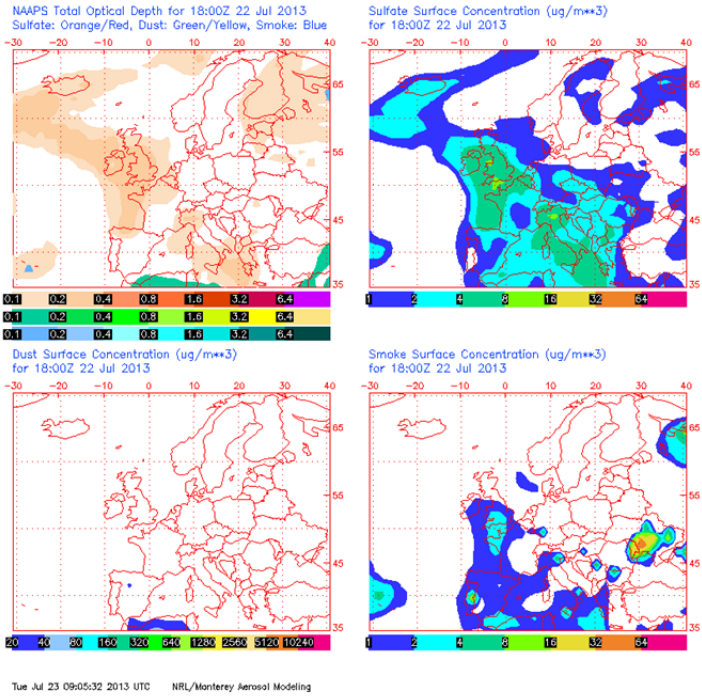

Figure 6.10. NAAPS model output on 22nd July 2013 at 18:00 UTC, which is the closest time to the radiosounding launch.

Figure 6.11 shows data provided by AERONET sun photometer. As it can be observed, τ_{440nm} values indicated high aerosol loads reaching values above 0.40 from 17:00 UTC. The AE(440-870nm) exhibited values larger than 1.2 during the whole day reaching 1.4 at 18:30 UTC, thus indicating a strong presence of fine particles. The AERONET inversion retrieval closer to the radiosonde launch was obtained at 18:10 UTC. For this retrieval, the size distribution showed similar volume concentrations for fine and coarse modes. Both, the $\omega(\lambda)$ values close to 0.9, and their spectral dependence, with a decreasing trend with wavelength, evidenced the presence of anthropogenic pollution and smoke over Granada [*Dubovik et al.*, 2002], in agreement with NAAPS forecast model.

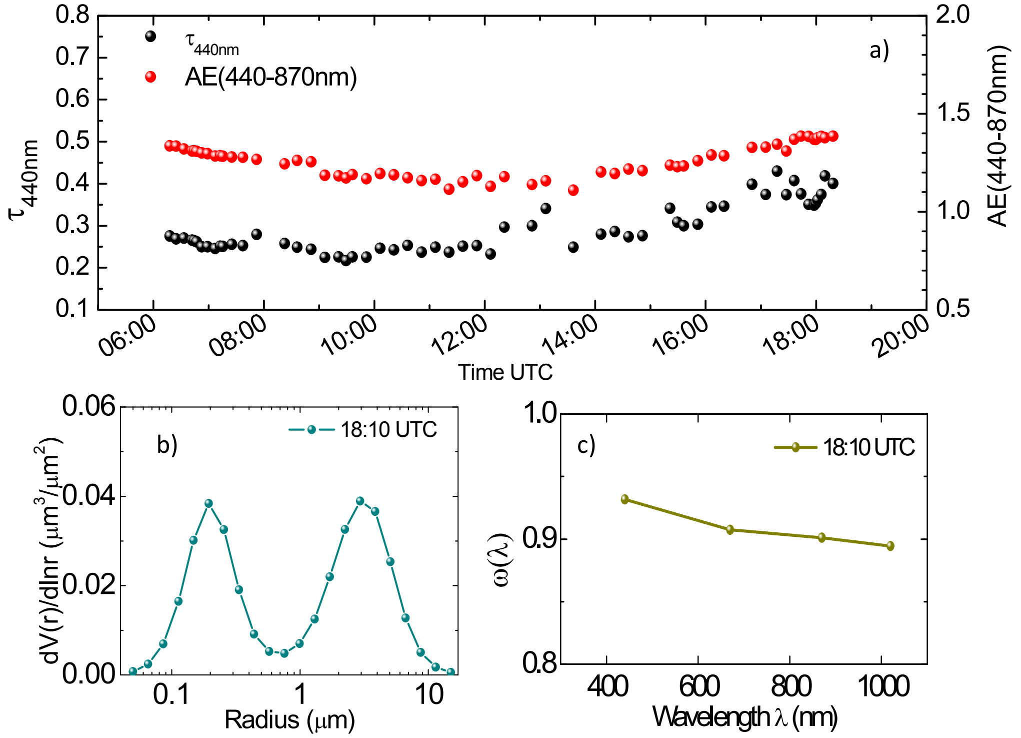

Figure 6.11. a) AERONET τ_{440} and AE(440-870) daily time series on 22nd July 2013. b) AERONET retrieved volume size distribution at 18:10 UTC for the same date. c) $\omega(\lambda)$ for the same time and date.

Lidar measurements were running from 20:00 to 22:00 UTC. The time series of the lidar RCS (Figure 6.13) indicated that atmospheric aerosol reached altitudes up to 3500 m a.s.l. with the strongest backscattered signal around 3000 m a.s.l. Since the radiosounding launch took place at 20:00 UTC, lidar data from 20:00 to 20:30 UTC are used for the hygroscopicity analysis. In the lidar RCS time series, some clouds were observed from 21:30 UTC. The occurrence of these clouds might be related to the ability of hygroscopic aerosol to act as cloud condensation nuclei (CCN).

The detailed information from the simultaneous radiosounding data is shown in the skew-T diagram in Figure 6.12. As in the previous case, an increase in RH with height was observed.

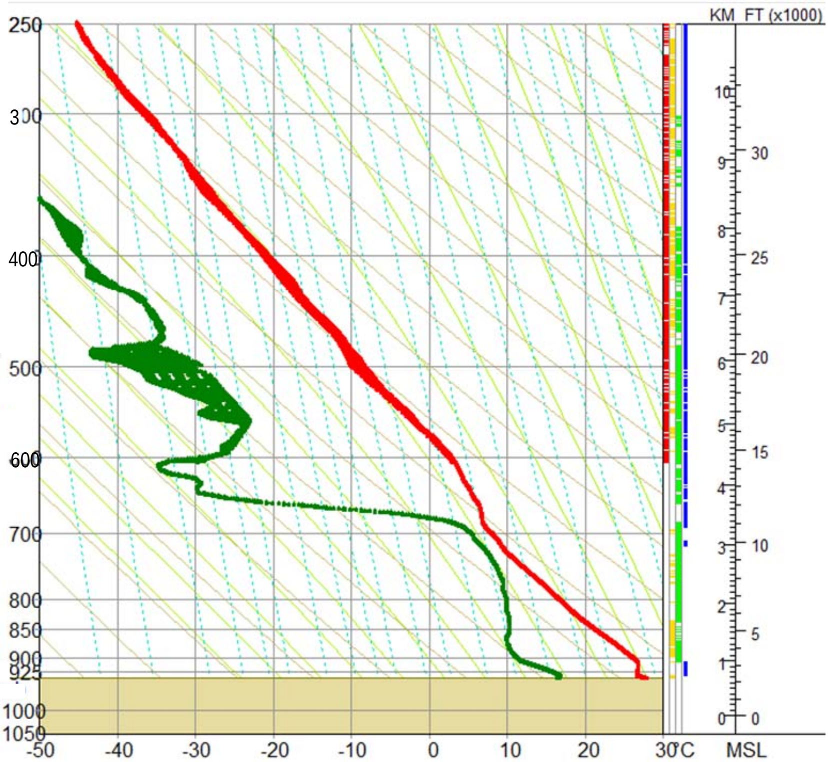

Figure 6.12. Skew-T diagram of the radiosounding launched on 22nd July 2013 at 20:30 UTC. The blue line represents the temperature profile and the yellow line is the dew point temperature (°C).

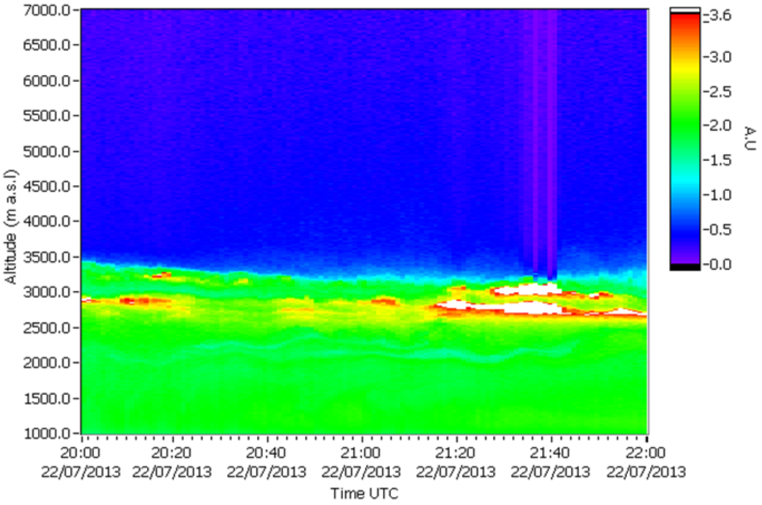

Figure 6.13. Lidar RCS time series at 532 nm (arbitrary units) on 22th July 2011 from 20:00 to 20:30 UTC.

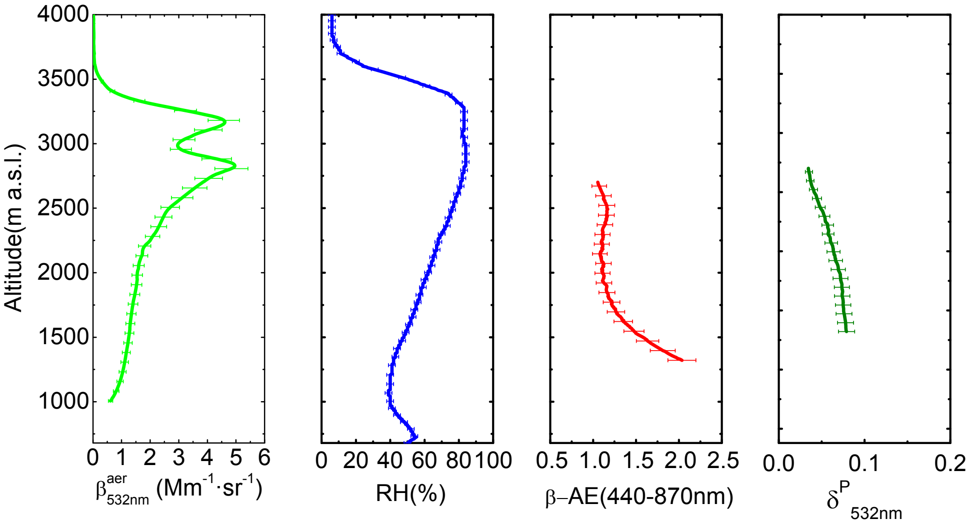

Figure 6.14. a) β_{532} retrieved with Klett-Fernald algorithm from 20:00 to 20:30 UTC on 22nd July 2013 b)RH profiles from the radiosounding launched at 20:00 UTC on the same date. c) β-AE(355-532 nm) retrieved with Klett-Fernald algorithm from 20:00 to 20:30 UTC on 22nd July 2013. d) δ^{P}_{532nm} retrieved from lidar data for the same period.

As it can be observed in Figure 6.14, the RH increased from 40 to 85% in the height range from 1300 to 2700 m a.s.l. In addition, the Klett-Fernald analysis applied to the lidar signals from 20:00 to 20:30 UTC showed a clear increase in β_{532nm} at the same height range. Conversely, β-AE(355-532nm) presented a strong decrease from 2.0 at 1300 m a.s.l. to 1.0 at 2700 m a.s.l. δ^{P}_{532nm} also decreased with altitude in the height range from 0.07 to 0.03, indicating that particles become more spherical as their size increased. The simultaneous increase in β_{532} and RH from 1300 to 2700 m a.s.l. together with the simultaneous reduction in β-AE(355-532nm) and δ^{P}_{532nm} in the same height range evidenced conditions of hygroscopic growth.

As in the previous case, to verify the aerosol vertical homogeneity 5-day backward trajectories were calculated only for those heights between 1300 and 2700 m a.s.l. (Figure 6.15). The analysis revealed that the origin and trajectories of the air masses were identical for the different altitudes considered. Therefore, likely the same aerosol type was advected to the investigated atmospheric height range above the experimental site. The air masses came from the Mediterranean region at the three altitude levels considered and they were travelling very close to the surface up to 24 hours before the analysed period, so they are likely loaded with sulphates and smoke as indicated by the NAAPS model. The trajectories were very similar to those on 22nd July 2011, but for this case they presented a shorter path. For this case, the vertical profiles of θ and r presented also very constant values in the investigated height range (Figure 6.15). Hence, good mixing conditions can be assumed according to the ancillary information.

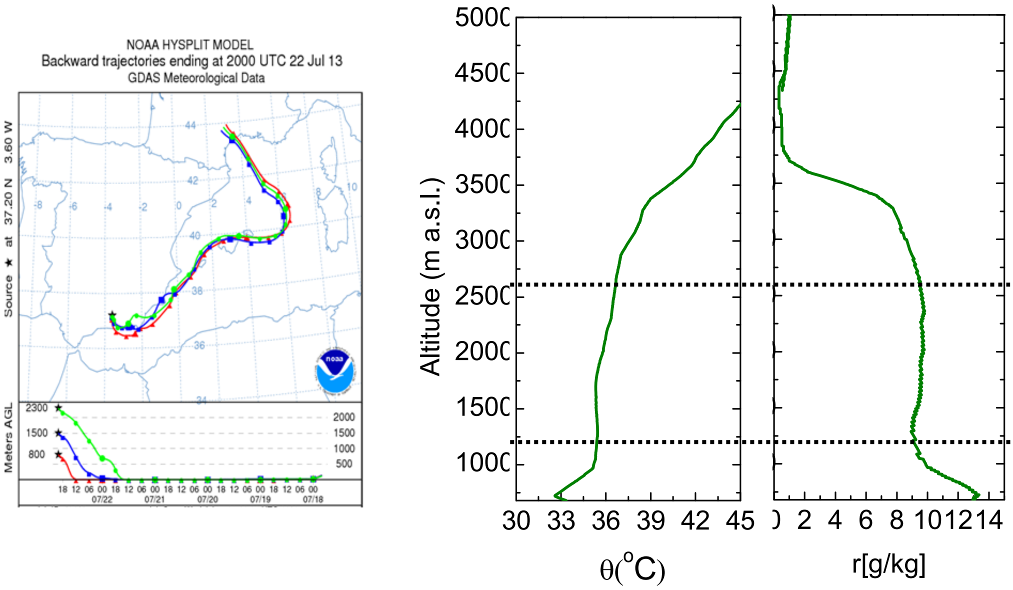

Figure 6.15. a) 5-day backtrajectories analysis ending on 22nd July 2013 at 20:00UTC performed with HYSPLIT model. b) Vertical profiles of θ and r from radiosounding on 22nd July 2013 at 20:00 UTC.

Once the requirements for homogeneity in the aerosol layer were verified, β_{532nm} profiles were combined with RH at the same height range, providing $f_\beta(RH)$ values (Figure 6.16). For this second case, $f_\beta(83\%) = 3.5$, in the range of RH between 40 and 83%. RH_{ref} is 40% in this case, since it is the lowest RH value reached in the analysed height range.

Since RH_{ref} in this case is 40%, the normalization performed in the previous case was not necessary in order to compare with in-situ studies. In this case, the Hänel equation was used in order to obtain $f_\beta(85\%)$, since RH values above 83% are not reached in the RH profile. For this case, $\gamma = 1.07 \pm 0.01$, which is closer to the value retrieved by *Veselovskii et al.* [2009] ($\gamma = 0.9$) than the results obtained for the case on 22nd July 2011. The γ value was also within the range 0.47-1.35 reported by *Randriamiarisoa et al.* [2006] for the Hänel parameterization of $f_\sigma(RH)$, but is larger than the values obtained by *Gasso et al.* [2000] for polluted and clean marine aerosols. The value of $f_\beta(85\%) = 3.9$ is slightly larger than the values obtained for the light scattering in the study by *Zieger et al.*, [2013], who obtained maximum values of 3.41 ± 0.66 for Arctic aerosol at Ny-Ålesund experimental site.

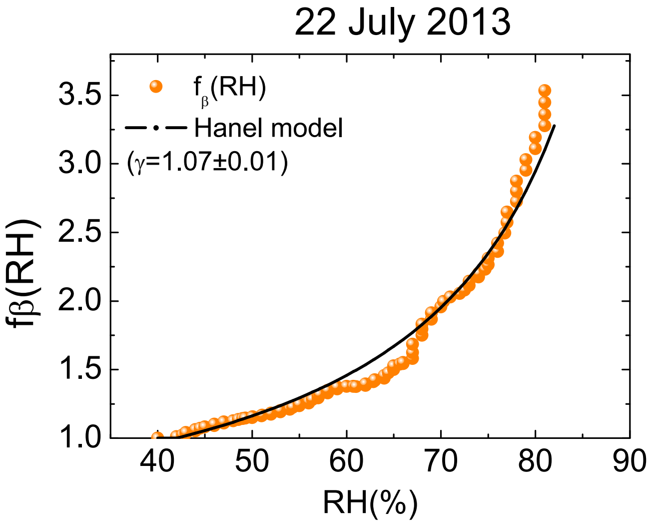

Figure 6.16. $f_\beta(RH)$ retrieved on 22^{nd} July 2013 from 20:00 to 20:30 UTC for the layer corresponding to heights between 1300 and 2700 m a.s.l.

As previously stated, in the study made by *Veselovskii et al.* [2009] using lidar data, RH_{ref} was 60%. In order to compare results from this case with those obtained in that study, $f_\beta(RH)$ was obtained also for $RH_{ref} = 60\%$. Varying the RH_{ref} from 40 to 60%, the new value of $f_\beta(85\%)$ went down to 2.65. This value was very similar to the one obtained by *Veselovskii et al.* [2009] for the aerosol regional haze using the aerosol extinction coefficient ($f_\alpha(85\%) = 2.3$).

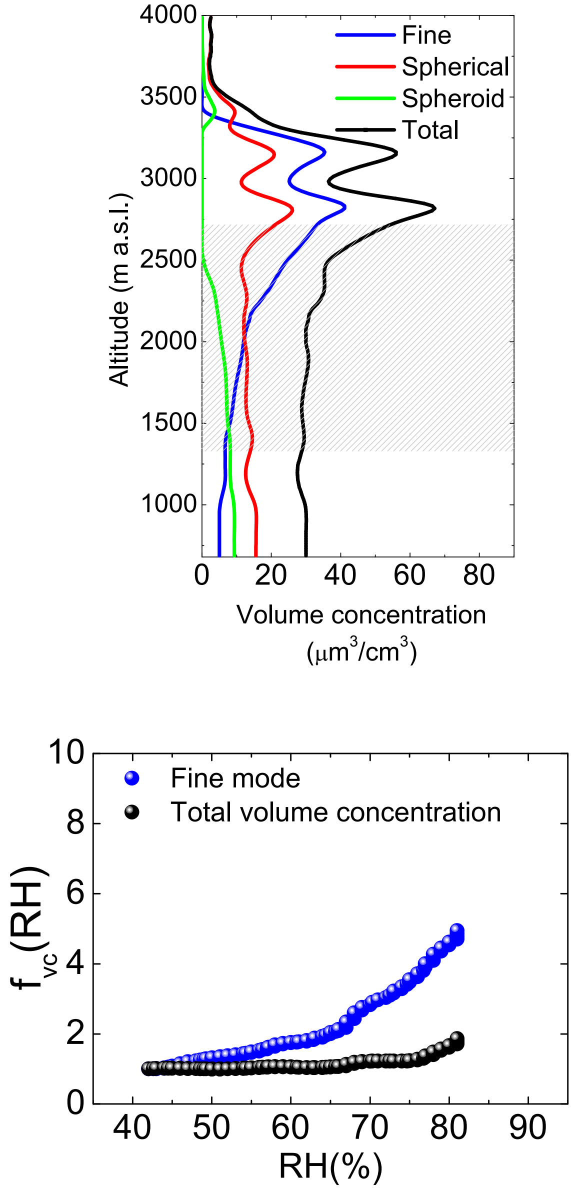

Figure 6.17. a) LIRIC retrieved volume concentration profiles on 22nd July 2013 from 20:00 to 20:30 UTC. The shaded area indicates the investigated height range. b) f_{VC}(RH) retrieved for the fine mode and the total volume concentration profiles for the same period and the layer corresponding to heights between 1300 and 2700 m a.s.l.

For this second case of hygroscopic growth above the experimental site, microphysical properties profiles were also retrieved by combining lidar data from 20:00 to 20:30 UTC and the AERONET inversion data at 18:10 UTC by means of LIRIC algorithm (Figure 6.17a). As it can be observed, there was a clear predominance of the fine mode above 2000 m a.s.l., whereas the coarse spherical mode presented the largest volume concentration values below this altitude. In addition, some spheroid particles were observed below 2500 m a.s.l. Figure 6.17b shows f_{VC}(RH) values for the fine mode and the total volume concentration. It was observed an increase with RH for both profiles, with f_{VC}(83%) = 2.0 for the total concentration. However, the increase was stronger for the fine mode (f_{VC}(83%) = 5.1). Therefore, according to these results, the fine mode was the one dominating the hygroscopic growth in the analysed layer as in the previous case.

6.3 Summary: 22nd July 2011 vs. 22nd July 2013.

A comparison between the two cases affected by hygroscopic growth was performed in this section for evaluating similarities and differences in order to better characterize the aerosol hygroscopic properties.

For the Case I corresponding to 22nd July 2011, the RH values ranged from 60 to 90%, whereas for the Case II on 22nd July 2013 they ranged from40 to 83%. For this reason, the values of RH_{ref} were different for each case (60% and 40% respectively). Consequently, before performing the comparison, it was necessary to use a common RH_{ref} = 40% for both cases in order to obtain equivalent humidograms. For this purpose, data from Case I were normalized to the value of $f_{\beta}(40\%)$ obtained using the Hänel parameterization, as previously explained. Humidograms corresponding to both cases are plotted together in Figure 6.18

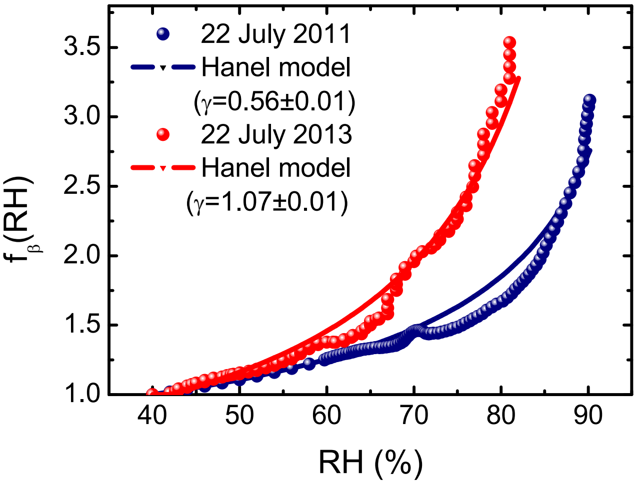

Figure 6.18. Comparison between f_β(RH) obtained on 22nd July 2011 and that on 22nd July 2013 using RH_{ref} = 40%. Solid lines represent the Hänel model.

A summary of the parameters obtained for both cases using 40% as RH_{ref} is presented in Table 6.1.

	Case I	**Case II**
$f_\beta(80\%)$	1.60 ± 0.03	3.00 ± 0.02
γ	0.56 ± 0.01	1.07 ± 0.01
$f_\beta(85\%)$	2.10 ± 0.06	3.90 ± 0.03

Table 6.1. Values of $f_\beta(80\%)$, $f_\beta(85\%)$ and γ for the two cases of hygroscopic growth corresponding to the 22nd July of 2011 and 2013, respectively.

As it can be inferred from Table 6.1 and Figure 6.18, the atmospheric aerosol presented a stronger hygroscopic growth for Case II. $f_\beta(80\%)$ was 1.60 ± 0.03 for the Case I whereas it was 3.00 ± 0.02 for the Case II. Also, the values of γ (0.56 ± 0.01 for Case I and 1.07 ± 0.01 for Case II) indicated that the aerosol was more hygroscopic for the second case. According to the combination of

AERONET data with the modelling tools, this is mostly due to the fact that during the second case a larger contribution of fine particles was observed (the AE(440-870nm) was 1.0 for case I and 1.4 for Case II), mainly related to the presence of sulphates. However, for the first case mineral dust was present in the atmospheric aerosol composition, being mineral dust usually less hygroscopic than sulphates.

As previously stated, the calculation of $f_\beta(85\%)$ allowed for the comparison with in-situ hygroscopicity studies. *Fierz-Schmidhauser et al.* [2010] reported values of $f_\sigma(85\%)$ from 1.2 (for mineral dust) to 3.3 (for marine aerosol) at Jungfraujoch experimental site. The mean value obtained at this site was 2.23 for free tropospheric aerosol. At different European sites, *Zieger et al.* [2013] obtained values of $f_\beta(85\%)$ for several aerosol types ranging from 1.28 for Saharan dust influenced aerosol to 3.41 for Arctic aerosol. *Kim et al.,* [2006] found that $f_\sigma(85\%) = 2.75$ for polluted aerosol of East Asia. A much lower value ($f_\sigma(85\%) = 1.71$) was obtained by *Adam et al.* [2012] at Ispra, Italy, indicating the predominance of very low hygroscopic aerosol. For the first case of this study, $f_\beta(85\%) = 2.1$ is within the range of values reported in these studies. However, for the second case $f_\beta(85\%) = 3.9$ but RH = 85% was not reached and, therefore, it was necessary to use the Hänel parameterization (Eq. 4.25.) in order to calculate it. The $f_\beta(85\%)$ value obtained for Case II was larger than the values previously reported in the literature for in situ measurements. However, differences are not very large. In addition, it is worthy to remind that in situ studies are usually based on light-scattering and the aerosol sample is usually dried and then re-exposed to high relative humidity conditions. Therefore, discrepancies with these results are expected since they are based on aerosol backscatter coefficient and the aerosol sample is measured under ambient and unperturbed conditions.

The enhancement factor total uncertainty is very difficult to determine since it is highly dependent on the uncertainties of the optical data, the range of RH considered as well as the hygroscopic growth of the particle itself and therefore it is not well characterized yet. *Adam et al.*, [2012] provided estimation based on a sensitivity test and Mie calculations. According to their study, this uncertainty varies between 4% (for RH < 40%) and 38% (at RH > 95%). Considering these uncertainties, differences between $f_\beta(85\%)$ values obtained in this study cases and in the literature are not significant. The uncertainties of $f_\beta(RH)$ provided in Table 6.1 were obtained by error propagation applied to Eq. 4. 24. Therefore, only the uncertainty introduced by the aerosol backscatter coefficient was considered.

To sum up, aerosol hygroscopic properties were analysed using a lidar system in combination with radiosounding RH profiles. Two cases of hygroscopic growth were detected within the available dataset consisting on 50 radiosounding profiles and their simultaneous lidar measurements. Different conditions were observed in these two cases. Enhancement factors (related to aerosol backscatter coefficient), $f_\beta(RH)$, of 2.5 for a RH increase from 60 to 90% and 3.5 for RH from 40 to 83% were retrieved under ambient conditions. In order to compare the two analysed cases, the Hänel parameterization was used and data were recalculated using a common RH_{ref} value of 40%. From this comparison, it was observed that the atmospheric aerosol presents a stronger hygroscopic growth during the second case corresponding to 22nd July 2013, as indicated by $f_\beta(80\%)$, $f_\beta(85\%)$ and γ values. This is mainly due to a presence of mineral dust during Case I and the larger sulphate load during Case II according to AERONET data and modelling tools. The values obtained for $f_\beta(85\%)$ are quite coherent with in situ studies for both cases, considering the uncertainty affecting $f_\beta(RH)$ and differences in methodologies as well as optical properties used for the different studies.

7 Conclusions and outlook

7.1 Conclusions

This section presents the main conclusions reached in the development of this thesis. Considering the interest on the retrieval of vertical profiles of the atmospheric aerosol microphysical properties, the Lidar Radiometer Inversion Code (LIRIC) is used throughout this thesis. LIRIC is applied to different datasets measured under different conditions. As a first step, the study of the uncertainties of the retrieval code associated to the choice of the different input parameters is done. Thus, selected cases representative of different atmospheric conditions, are analysed and the retrievals of the volume concentration profiles are performed varying the different user-defined input parameters in LIRIC within their expected uncertainty range. The considered input parameters include the lower limit height z_{N0}, the reference height z_N, the upper limit height z_U and the regularization parameters *k, f* and *d.* It is obtained that the uncertainty associated to the uncertainty in the user-defined input parameters is usually lower than 15%. Uncertainties due to the regularization parameters, the reference height and the upper height limit are usually very low, with values below 2%. The parameter which introduces the largest uncertainty is the lower limit height. This uncertainty specially affects the lowermost part of the profiles, and it is found to be highly dependent on the aerosol vertical structure (varying between 10 and 30%). Larger uncertainties are related to complex structures. A reliable correction of the incomplete overlap effect in this lowermost region could significantly reduce the uncertainty in this height range. In addition, it is evident an unrealistic offset, usually lower than 5 $\mu m^3/cm^3$ but highly variable depending on the specific case, which overestimates the aerosol volume concentration in the molecular region.

This offset, which is more noticeable in those cases with low volume concentrations and especially in the modes presenting the lowest volume concentrations, could be associated to the underestimation of the molecular extinction in LIRIC. According to our evaluation, the optical properties obtained during the LIRIC retrieval procedure present some differences with those retrieved using Klett-Fernald algorithm. Thus, LIRIC retrieves negative β-AE in those cases with predominance of the coarse mode, likely due to the limitations of AERONET spheroids model at scattering angles Θ~180°. Furthermore, absolute differences in the linear particle depolarization profiles, δ^{P}_{532nm}, computed from LIRIC present lower values than those obtained using Klett-Fernald algorithm, evidencing the challenge in getting accurate depolarization values. Moreover, δ^{P}_{532nm} profiles from LIRIC are smoother due to the use of height independent input parameters in LIRIC such as the sphericity. According to the results obtained throughout this thesis, this seems to be still a weak point in LIRIC which needs to be improved and carefully considered in the analysis of the results, even though LIRIC is a very useful and robust tool for the analysis of microphysical properties profiles in two dimensions i.e. temporal and vertical coordinates.

Once the uncertainties of LIRIC algorithm are delimited, it is applied to different scenarios. Data corresponding to several experimental campaigns, including a comprehensive instrumental setup, are used. Thus, data corresponding to CHARMEX campaign on 2012 and CLIMARENO-GRA on 2011 are analysed. During both campaigns, dust events affect Granada station. CHARMEX presents the main advantage that it is a 72-h intensive measurement exercise and a study of the temporal evolution of the dust event is possible. The measurement period was much shorter during CLIMARENO-GRA, so a detailed analysis of the temporal evolution is not possible. However, it presents the main advantage that data from a simultaneous flight above Granada station are available. Furthermore, availability of night-time Raman data during the previous night allows for the retrieval of aerosol microphysical properties profiles with a different inversion scheme (Veselovskii's algorithm).

As expected in presence of mineral dust, a clear predominance of the coarse spheroid mode is obtained for both cases. During CHARMEX, the analysis of the temporal evolution of LIRIC output profiles shows a decrease of the intensity in the dust concentration, with values of the total volume concentration from 35 $\mu m^3/cm^3$ on 9th July to 15 $\mu m^3/cm^3$ on 11th July. The analysis of the variations in the concentration of the different modes suggests possible aging and mixing processes affecting the mineral dust advected over Granada station. During CLIMARENO-GRA on 2011 the intensity of the observed dust event is similar to that on 9th July 2012, with volume concentration values around 30 $\mu m^3/cm^3$. In both cases, some fine particles are observed in low concentrations (~6 $\mu m^3/cm^3$) at high altitudes, which suggests that they could have been advected from the industrial areas in the North of Africa together with the mineral dust or they might be part of the fine mode of the mineral dust. From the analysis of these two cases, LIRIC proves to be a very useful tool for the monitoring of the atmospheric aerosol, allowing for the analysis of the evolution of atmospheric aerosol profiles of microphysical properties.

Both datasets are also used to perform a comparison of LIRIC retrieved mass concentration profiles with BSC-DREAM8b model output values since they correspond to mineral dust events. From the results from CHARMEX, it is clearly inferred that BSC-DREAM8b model strongly underestimates LIRIC retrievals during this particular event, with deviations reaching values up to 70 $\mu g/m^3$. This result is in agreement with previous studies which indicated that BSC-DREAM8b model underestimates the aerosol optical depth at 550nm, τ_{550nm}, when compared to AERONET data above the Iberian Peninsula. However, when comparing the profiles normalized to their maximum values from both LIRIC and BSC-DREAM8b outputs, it was observed that the BSC-DREAM8b reproduces much better the aerosol vertical structure than the aerosol load for this particular dust event, as indicated by low deviation values. However, the results from the comparison during CLIMARENO-GRA indicates good agreement for the mass concentration values (with differences in the total column-integrated mass concentration of only 30%), whereas BSC-DREAM8b model does not correctly forecast vertical structure of the dust layers. The different results obtained in these two campaigns may be attributed to the different stages of the dust event at the time of the measurements or to a non-homogeneous horizontal distribution of the dust.The dust event was already well developed during the measurements in CHARMEX whereas it was at the beginning during CLIMARENO-GRA. In order to get more conclusive results a more extensive analysis would be needed using a wider dataset which covers a more extensive and varied number of cases.

The CASA C-212-200 aircraft measurements and simultaneous LIRIC retrieved profiles obtained during this CLIMARENO-GRA campaign present some discrepancies for both fine and total coarse modes. These discrepancies can be easily explained due to the different techniques used (remote sensing techniques for LIRIC and in-situ measurements from the aircraft), together with the different assumptions made, i. e. the sphericity of the particles in the case of the aircraft for Mie calculations. Nonetheless, the profiles retrieved by means of these two different approaches presents very similar vertical aerosol layering and also very similar volume concentration values, with discrepancies within the uncertainties.

The use of Veselovskii's retrieval algorithm applied to the Raman lidar data during the night previous to the flight allows to assess the performance of LIRIC by comparison with this different inversion scheme. The retrievals of total volume concentration profiles at night (with Veselovskii's algorithm) and in the early morning (with LIRIC) indicate a decrease in the volume concentration from maximum values of 75 $\mu m^3/cm^3$ to 50 $\mu m^3/cm^3$. The aerosol backscatter coefficient, β_{532nm}^{aer}, profiles also present larger values during the night than in the early morning (1.8 and 1.4 $Mm^{-1}\cdot sr^{-1}$ respectively), indicating changes in the aerosol properties due to the temporal evolution of the dust event during the night. According to the results, discrepancies in the volume concentration values obtained with both retrieval algorithms are easily explained by the temporal evolution of the dust event and do not imply disagreement between both techniques. Results obtained indicate that their combined use might be very appropriate for the continuous monitoring of aerosol microphysical properties during both day and night time.

Besides the two field campaigns, the availability of a unique experimental setup based on the use of a second sun photometer located in Cerro Poyos AERONET station, allows for performing a comparison between LIRIC retrievals from two different heights. The analysis of two study cases shows that when the aerosol load is large and the predominant aerosol type is the same above both stations, the agreement between the retrieved volume concentration profiles above Granada and above Cerro Poyos is fairly good. However, when complex layering with different aerosol types is present above the stations the assumption of constant values with altitude of the Angström exponent, lidar ratio, percentage of sphericity and refractive index introduces more discrepancies and results need to be carefully discussed. Nevertheless, according to the statistical analysis performed during the summer of 2012 with this experimental setup, these cases are not very often (only 2% during summer 2012), so the applicability of LIRIC algorithm is quite extended. From this statistical analysis, based on 112 retrievals, it is obtained that the agreement between the retrievals from both stations is really high. Discrepancies are within the uncertainty limits (below 15%) for almost 90% of the analysed cases. Furthermore, the slopes and the correlation coefficients R corresponding to the linear fits indicates also very good agreement, with most of the values close to one (60 and 80% of the data for the slope and R, respectively) for all the modes. The cases with larger discrepancies are analysed in detail and they corresponded to three possible situations: (i) situations with very low volume concentration values; (ii) situations with different aerosol types above and below Cerro Poyos station height and (iii) situations with very low aerosol load above Cerro Poyos which lead to large uncertainties in the retrieval of the sphericity parameter. A careful interpretation of LIRIC output profiles needs to be performed in these cases considering the limitations of the algorithm.

In spite of the good agreement, in general larger values of the total volume concentration are obtained in the retrieval from Cerro Poyos than in the retrieval from Granada. This underestimation of the volume concentration profiles from Granada above 1820 m a.s.l. implies an overestimation of the profiles in the lowermost part region, related to the incomplete overlap effects and the assumption of constant volume concentration values below z_{N0}. This assumption should be reviewed in order to improve the algorithm results.

Another important part of this dissertation focuses on the analysis of the effects of the aerosol hygroscopic growth on the aerosol optical and microphysical properties. During the first case analysed, hygroscopic growth is detected in an aerosol layer between 1300 and 2300 m a.s.l. and a backscatter enhancement factor $f_{\beta}(RH)$ of 2.5 for a RH increase from 60 to 90% is obtained. In the second case analysed, the hygroscopic growth is detected between 1300 and 2700 m a.s.l. and $f_{\beta}(RH)$ is 3.5 for RH between 40 and 83%. From the comparison of the two cases using a common RH_{ref} = 40% by means of the Hänel parameterization it is observed that the atmospheric aerosol is more hygroscopic during the second case. This can be explained by the different atmospheric conditions in the two cases, since the first one is affected by a mixing of mineral dust with anthropogenic pollution and the second one corresponds mainly two sulphates, as indicated by AERONET data and the modelling tools. The values obtained for the backscatter enhancement factor $f_\beta(85\%)$ are within the range obtained with in-situ studies for the two study cases, especially considering the uncertainties affecting the retrieval of the enhancement factors for optical properties, $f_\zeta(RH)$, which can reach up to 38%.

7.2 Outlook

Future research will be necessary in order to continue with the advancement in the aspects developed in this thesis, making emphasis in some topics:

- A main goal for the future research will be to evaluate the uncertainties of LIRIC algorithm due to the uncertainties of the input optical data and not only the uncertainties due to the use-defined input parameters.
- An important aspect for future research is the collaboration with lidar microphysical algorithms developers in order to improve the provided results and solve the remaining weak points.
- Application of the already developed algorithm GARRLIC, which follows the same approach than LIRIC, to the analysed data will be performed.
- Analysis of the data during CHARMEX 2012 intensive measurement period will be extended to the other participating stations in order to characterize the mineral dust events in three dimensions and evaluate the performance and usefulness of LIRIC in this kind of situations.
- A more intensive analysis will be performed extending the database in order to characterize the hygroscopic properties of atmospheric aerosol under ambient and unperturbed conditions by means of active remote sensing. For this purpose, a way to retrieve relative humidity profiles with quite high accuracy and larger temporal resolution will be implemented in our station.

8 Conclusiones y perspectivas

8.1 Conclusiones

En esta sección se presentan las principales conclusiones de esta tesis. Debido al interés en la obtención de perfiles verticales de propiedades microfísicas del aerosol atmosférico, el algoritmo LIRIC (Lidar Radiometer Inversion Code) se aplica a varios conjuntos de datos correspondientes a diferentes condiciones atmosféricas. En primer lugar, se realiza un estudio de la incertidumbre asociada a la elección de los diferentes parámetros de entrada definidos por el usuario. Para tal fin, se analizan varios casos representativos de diferentes condiciones atmosféricas, variando dichos parámetros de entrada dentro de su rango de incertidumbre esperada. Los parámetros de entrada considerados incluyen la altura límite inferior z_{N0}, la altura de referencia z_N, la altura límite superior z_U y los parámetros de regularización *k, f* y *d*. De este análisis se obtiene que la incertidumbre asociada a la elección de estos parámetros de entrada definidos por el usuario suele ser inferior al 15 %. Las incertidumbres debidas a los parámetros de regularización, la altura de referencia y el límite de altura superior suelen ser muy bajas, con valores inferiores al 2%. El parámetro que introduce la mayor incertidumbre es la altura límite inferior. Se ha observado que la incertidumbre afecta especialmente a la parte inferior de los perfiles, y es altamente dependiente de la estructura vertical de las capas de aerosol, variando entre el 10 y el 30 %. Las estructuras más complejas conllevan mayores valores de incertidumbre. Una corrección del efecto de solapamiento incompleto en la región inferior de los perfiles podría reducir significativamente la incertidumbre en este rango de altura. Además, en este análisis se ha observado una sobreestimación en los perfiles de concentración en volumen del aerosol en la región molecular, por lo general inferior a 5 $\mu m^3/cm^3$, pero muy variable dependiendo del caso específico. Esta sobreestimación, que es más notable en los casos de concentraciones en volumen bajas, parece estar asociada a una subestimación de la extinción molecular en LIRIC.

De acuerdo con nuestra evaluación, las propiedades ópticas obtenidas con LIRIC presentan algunas diferencias con las obtenidas a partir del algoritmo de Klett-Fernald, empleado ampliamente en la inversión de perfiles elásticos. Estas diferencias están relacionas con el hecho de que LIRIC proporciona valores negativos de β -AE en los casos con predominio del modo grueso, probablemente debido a las limitaciones del modelo de esferoides de AERONET para ángulos de dispersión Θ~180°. Además, los perfiles de despolarización lineal de partículas, δ^P_{532nm}, obtenidos con LIRIC presentan valores más bajos que los obtenidos utilizando el algoritmo de Klett- Fernald, lo que evidencia las dificultades para conseguir valores de despolarización precisos con LIRIC. Asimismo, los perfiles de δ^P_{532nm} de LIRIC presentan una estructura vertical más suavizada debido a que parámetros de entrada del modelo (tales como la esfericidad) se consideran independientes de la altura. De acuerdo con los resultados obtenidos a lo largo de esta tesis, este parece ser un punto débil del algoritmo que necesita ser mejorado y que debe de considerarse atentamente en el análisis de resultados. A pesar de ello, LIRIC se muestra como una herramienta muy útil y robusta para el análisis de perfiles de propiedades microfísicas del aerosol en dos dimensiones, es decir, en las coordenadas temporal y vertical.

Una vez que las incertidumbres de LIRIC se han delimitado, el algoritmo se aplica a datos correspondientes a diferentes escenarios. Para ello se utilizan los datos correspondientes a varias campañas experimentales, en las que hay disponible una amplia información adicional. Dichas campañas son CHARMEX, desarrollada en el verano de 2012, y CLIMARENO-GRA, que tuvo lugar en el verano de 2011. Durante ambas campañas, la estación experimental de Granada estuvo afectada por sendos eventos de polvo mineral proveniente de África. Durante la campaña CHARMEX se realizaron 72 horas de medidas continuas con el sistema lidar, de modo que se puede estudiar la evolución temporal del evento de polvo mineral. Durante CLIMARENO-GRA el periodo de medidas es mucho más corto, por lo que un análisis detallado de la evolución temporal no es factible. Sin embargo, existen datos de un vuelo instrumentado sobre la estación de Granada simultáneo a las medidas lidar. Además, la disponibilidad de datos lidar Raman durante la noche anterior a la campaña ofrece la posibilidad de obtener perfiles de propiedades microfísicas del aerosol mediante el algoritmo de inversión de Veselovskii.

Como era de esperar, la presencia de polvo mineral en ambas campañas da lugar a un claro predominio del modo grueso esferoide. Durante CHARMEX, el análisis de la evolución temporal de los perfiles de salida de LIRIC muestra una disminución en la concentración de polvo, con valores en torno a 35 $\mu m^3/cm^3$ el día 9 de julio bajando hasta 15 $\mu m^3/cm^3$ el 11 de julio. El análisis de las variaciones en la concentración de los diferentes modos sugiere la acción de procesos de mezcla, así como un posible envejecimiento del polvo mineral sobre la estación de Granada. Durante CLIMARENO-GRA en 2011 la intensidad del evento de polvo observado es similar a la del día 9 de julio de 2012, con valores de concentración de volumen de alrededor de 30 $\mu m^3/cm^3$. En ambos casos, se observan partículas finas en bajas concentraciones (~ 6 $\mu m^3/cm^3$) a gran altura, lo que sugiere que podrían tener su origen en las zonas industriales del norte de África y ser transportadas junto con el polvo mineral, o bien que se trate polvo mineral incluido en ese modo fino.

En conclusión, a partir del análisis de estos dos casos, podemos inferir que LIRIC se presenta como una herramienta muy útil para el seguimiento del aerosol atmosférico, lo que permite el análisis de la evolución de sus perfiles de propiedades microfísicas.

Los datos de CHARMEX y CLIMARENO-GRA también se utilizan para llevar a cabo una comparación de los perfiles de concentración en masa de polvo mineral proporcionados por el modelo BSC-DREAM8b con los perfiles obtenidos a partir LIRIC. A partir de los resultados de CHARMEX, se deduce claramente que el modelo BSC-DREAM8b subestima los valores proporcionados por LIRIC durante este evento en particular, con desviaciones que alcanzan valores de hasta 70 $\mu g/m^3$. Este resultado es similar a los obtenidos en estudios previos que ya indicaban que el modelo BSC-DREAM8b subestima los valores de profundidad óptica de aerosol a 550 nm, τ_{550nm}, al compararlo con datos de AERONET en la Península Ibérica. Sin embargo, si se comparan los perfiles normalizados (al valor máximo) de LIRIC y el BSC-DREAM8b, se observa que los perfiles del modelo BSC-DREAM8b reproducen mejor la estructura vertical que la carga de aerosol. Por el contrario, los resultados de la comparación durante CLIMARENO-GRA indican buen acuerdo para la carga de aerosol (con diferencias para los valores integrados en columna de concentración másica de tan solo un 30 %), mientras que el modelo BSC- DREAM8b no pronostica correctamente la estructura vertical de las capas de polvo. Los diferentes resultados obtenidos en estas dos campañas se pueden atribuir principalmente a las diferentes etapas de desarrollo de los eventos de polvo en el momento en el que se realizaron las medidas experimentales, o bien a las diferencias en la distribución horizontal de la pluma de polvo mineral, o a una combinación de ambas. Así, el evento se encontraba en una fase avanzada durante la campaña CHARMEX. Por el contrario, durante CLIMARENO-GRA se monitorizó la fase inicial de llegada del polvo mineral sobre Granada. Con el fin de obtener resultados más concluyentes sería necesario realizar un análisis más extenso, basado en un conjunto de datos más amplio que abarcase una mayor diversidad de casos y un seguimiento de los mismos desde las fases iniciales hasta la conclusión del evento.

Los perfiles proporcionados por el vuelo del avión CASA C-212-200, operado por el INTA, y los obtenidos con LIRIC, durante la campaña CLIMARENO–GRA, presentan algunas discrepancias, tanto para el modo fino como para el modo grueso, aunque se mantienen dentro de los márgenes de incertidumbre. Estas discrepancias pueden explicarse fácilmente, considerando las diferentes técnicas utilizadas (técnicas de teledetección en el caso de LIRIC y mediciones in-situ en el caso del avión), junto con las diversas hipótesis formuladas para la obtención de los resultados, entre las que se incluye la esfericidad de las partículas para los cálculos de Mie en el caso del avión. A pesar de las discrepancias, los perfiles obtenidos presentan una estratificación vertical del aerosol muy similar y valores de concentración de volumen también bastante semejantes (~30 $\mu m^3/cm^3$).

El uso del algoritmo de Veselovskii aplicado a los datos Raman durante la noche anterior al vuelo permite evaluar el funcionamiento de LIRIC en comparación con un esquema de inversión diferente. Los perfiles de concentración en volumen total de la noche (obtenidos con el algoritmo de Veselovskii) y los de la mañana (obtenidos con LIRIC) indican una disminución de los valores máximos de 75 a 50 $\mu m^3/cm^3$. Los perfiles del coeficiente de retrodispersión de aerosol, β_{532nm}, también presentan valores más altos por la noche que durante mañana (1.8 y 1.4 $Mm^{-1} \cdot sr^{-1}$, respectivamente), lo que indica cambios en las propiedades del aerosol debidos a la evolución temporal del evento durante la noche. Por consiguiente, las discrepancias en los valores de concentración en volumen obtenidos con ambos algoritmos se pueden explicar fácilmente en base a dicha evolución temporal y sugieren un grado de acuerdo razonable entre ambas técnicas. Es más, los resultados obtenidos indican que el uso combinado de LIRIC y el algoritmo de Veselovskii puede ser muy adecuado para el seguimiento continuo de las propiedades microfísicas del aerosol durante el día y la noche.

Además de las dos campañas de medidas, la disponibilidad de una configuración experimental única basada en el uso de un segundo fotómetro solar situado en la estación AERONET Cerro Poyos, permite realizar una comparación de los perfiles LIRIC obtenidos desde dos alturas diferentes, con datos de fotometría independientes. El análisis detallado de dos casos de estudio muestra que el acuerdo entre los perfiles de concentración en volumen es bastante alto cuando la carga de aerosol es grande y el tipo de aerosol predominante es el mismo por encima de Granada y CerroPoyos. Sin embargo, cuando hay una estratificación compleja, con diferentes tipos de aerosol en a vertical atmosférica, la suposición de que los valores del exponente Angström, razón lidar, esfericidad e índice de refracción son independientes de la altura, produce diferencias considerables y los resultados deben ser analizados con atención. No obstante, según el análisis estadístico realizado sobre datos medidos durante el verano de 2012 con esta configuración experimental, estos casos no son muy frecuentes (sólo un 2% durante el verano de 2012), por lo que la aplicabilidad del algoritmo LIRIC es bastante plausible. A partir de este análisis estadístico, basado en 112 perfiles, se obtiene que el acuerdo entre los perfiles calculados a partir de los datos de ambas estaciones es muy alto. Las discrepancias se encuentran dentro de los límites de incertidumbre (por debajo del 15 %) para casi el 90 % de los casos analizados. Además, las pendientes y los coeficientes de correlación R obtenidos a partir de ajustes lineales indican también muy buen acuerdo, con la mayoría de los valores cercanos a uno para todos los modos (para el 60 y el 80 % de los datos para la pendiente y R, respectivamente). Del análisis detallado de los casos que presentan mayores diferencias se concluye que pueden corresponder a tres posibles situaciones: i) situaciones con valores de concentración en volumen muy bajo; ii) situaciones con diferentes tipos de aerosol por encima y por debajo de la altura de la estación Cerro Poyos, y iii) situaciones con muy poca carga de aerosol por encima de Cerro Poyos, que normalmente conllevan grandes incertidumbres asociadas al parámetro de esfericidad. Para estos casos, la interpretación de los perfiles de salida de LIRIC requiere una especial atención considerando las limitaciones del algoritmo.

A pesar del buen acuerdo obtenido, en general se observan valores mayores de la concentración en volumen total en los datos obtenidos a partir de Cerro Poyos que en los de Granada. Esta subestimación de los perfiles de concentración en volumen de Granada por encima 1820 m s.n.m. implica una sobreestimación de los perfiles en la región inferior, asociada a efectos de solapamiento incompleto del lidar y la consideración de valores constantes de concentración en volumen por debajo de z_{N0}. Esta hipótesis necesita ser revisada con el fin de mejorar los resultados del algoritmo.

Otra parte importante de esta tesis doctoral se centra en el análisis de los efectos del crecimiento higroscópico del aerosol sobre sus propiedades ópticas y microfísicas. Se presentan los resultados correspondientes a varios casos. En el primer caso, el crecimiento higroscópico del aerosol es detectado en una capa entre 1300 y 2300 m s.n.m. y se obtiene un factor de crecimiento del coeficiente de retrodispersión, $f_{\beta}(HR)$ de 2.5 para un aumento de la humedad relativa (RH) del 60 al 90%. En el segundo caso, el crecimiento higroscópico es detectado entre 1300 y 2700 m s.n.m. y el $f_{\beta}(HR)$ obtenido es de 3.5 para una HR entre el 40 y el 83%. De la comparación de los dos casos, usando una humedad relativa de referencia común, $RH_{ref} = 40\%$, realizando una extrapolación de los resultados tras la aplicación de la parametrización de Hänel, se observa que el aerosol atmosférico es más higroscópico durante el segundo caso. Esto es debido a las diferentes condiciones atmosféricas en los dos casos, ya que el primero se ve afectado por una mezcla de polvo mineral con contaminación antropogénica mientras que el segundo corresponde principalmente a sulfatos, como indican tanto los datos de AERONET como los modelos de transporte de aerosol considerados. El factor de crecimiento del coeficiente de retrodispersión del aerosol al 85% de humedad relativa, $f_\beta(85\%)$, presenta valores dentro del rango de los que se encuentran en la bibliografía para otras propiedades determinadas mediante instrumentación in-situ, considerando las incertidumbres que afectan a los valores de $f_\zeta(HR)$, que puede alcanzar hasta un 38%.

8.2 Perspectivas

Para continuar con el avance de los aspectos desarrollados en esta tesis, será necesaria realizar en el futuro una investigación más exhaustiva de ciertos aspectos puestos de manifiesto en este estudio. Así::

- → Un objetivo principal en próximas investigaciones será evaluar las incertidumbres del algoritmo LIRIC debidas a las incertidumbres asociadas a los datos ópticos de entrada, completando el estudio de las incertidumbres relacionadas con los parámetros de entrada definidos por el usuario, realizado en esta tesis.
- → Un aspecto importante para futuras investigaciones será la intensificación de la colaboración con los creadores de los algoritmos de inversión, para la obtención de propiedades microfísicas a partir de datos lidar, iniciada en el desarrollo de esta tesis. Esto será un aspecto clave para mejorar los resultados y trabajar en los puntos débiles de los algoritmos.
- → Por otro lado, se espera implementar el algoritmo GARRLIC, que ha sido desarrollado recientemente y que presenta una aproximación similar a LIRIC, pero con interesantes mejoras en su concepción,
- → El análisis de los datos medidos durante la campaña CHARMEX2012 se extenderá al resto de estaciones participantes con el fin de caracterizar el evento de polvo mineral detectado en

tres dimensiones y evaluar el funcionamiento y la utilidad de LIRIC en este tipo de situaciones.

→ Se realizará una ampliación de la base de datos de perfiles de humedad relativa necesarios para caracterizar las propiedades higroscópicas del aerosol atmosférico en condiciones ambientales y sin alterar el medio mediante técnicas de teledetección activa. Para tal fin, se trabajará en la implementación de una metodología para obtener perfiles de humedad relativa con alta resolución temporal y valores más precisos en nuestra estación.

→List of acronyms and symbols

ADNET	Asian Dust NETwork
AE(λ_1-λ_2)	Ångström Exponent
AERONET	Aerosol Robotic Network
a.s.l.	Above sea level
CEAMA	Centro Andaluz de Medio Ambiente
CNN	Cloud Condensation Nuclei
DREAM	Dust Regional Atmospheric Model
EARLINET	European Aerosol Research Lidar Network
BC	Black Carbon
GFAT	Atmospheric Physics Group
HYSPLIT	Hybrid single-particle Lagrangian integrated trajectories
IPCC	Intergovernmental Panel on Climate Change
lidar	light detection and ranging
LR	Lidar Ratio
MPLNET	Micro-Pulsed Lidar NETwork
NAAPS	Navy Aerosol Prediction System
Nd:YAG	Neodymium-doped yttrium-aluminium-garnet
OT	Optical Thickness
RCS	Range Corrected Signal
RH	Relative Humidity
SPALINET	Spanish and Portuguese Aerosol Lidar Network
LALINET	Latin American Lidar Network
GALION	Global Atmospheric Watch Aerosol Lidar Observation
LIRIC	Lidar Radiometer Inversion Code
AR4	Fourth Assessment Report of the IPCC
AR5	Fifth Assessment Report of the IPCC

BSC	Barcelona Supercomputing Center
CAPS	Cloud, Aerosol, and Precipitation Spectrometer
CAS	Cloud and Aerosol Spectrometer
PCASP-100X	Passive Cavity Aerosol Spectrometer Probe
DRH	Deliquescence relative humidity
ERH	Efflorescence relative humidity
IS	International system
INTA	National Institute of Aerospace Technique in Spain
FNL/NCEP	Final Analysis/National Centers for Environmental Prediction
$\sigma_{a\lambda}$	Monochromatic absorption coefficient
$\sigma_{s\lambda}$	Monochromatic scattering coefficient
$\sigma_{e\lambda}$	Monochromatic extinction coefficient
τ_{λ}	Aerosol optical depth
m	Refractive index
$f_{\zeta}(RH)$	Enhancement factor of ζ
$g(RH)$	Hygroscopic growth factor
Φ_{λ}	Monochromatic radiant flux
Q	Radiant energy
Φ_{λ}	Radiant flux
E_{λ}	Radiant flux density (irradiance)
I_{λ}	Radiant intensity
L_{λ}	Radiance
$\widetilde{\upsilon}$	Frequency
λ	Wavelength
c_0	Speed of light at the vacuum
x	Size parameter
n	Real part of the complex refractive index
Θ	Scattering angle
Q_e	Extinction efficiency factor

$n(r)$	Numeric size distribution
N	Concentration of particles
$s(r)$	Surface size distribution
$v(r)$	Volume size distribution
$s_c(r)$	Column-integrated surface size distribution
$v_c(r)$	Column-integrated volume size distribution
m_0	Relative optical air mass
θ_0	Solar zenith angle
$\omega(\lambda)$	Single scattering albedo
$P(\Theta)$	Phase function
D_{dry}	Dry diameter
e	Water vapor pressure
e_0	Vapor pressure for a flat surface
S	Saturation ratio
χ_w	Mole fraction of water
n_w	Number of water molecules
γ_w	Water activity coefficient
a_w	Water activity
σ_{sol}	Surface tension
M_w	Molecular weight of water
ρ_w	Density of water
R	Ideal gas constant
T	Temperature
e_K	Equilibrium vapor pressure over a curved surface
$P(z_n)$	Received power from a distance z_n
P_B	Background noise
$O(z_n)$	Overlap function
K	System factor for range-independent parameters of the lidar
$\beta(z)$	Atmospheric backscatter coefficient

$\beta_{\lambda}^{aer}(z_n)$	Lidar-retrieved aerosol backscatter coefficient
$\alpha(z_n)$	Lidar-retrieved extinction coefficient
$T(z_n)$.	Transmission term
P_L	Average power of a single laser pulse
A	Area of the receiver optics in the lidar system
η	Lidar system efficiency
f_{rep}	Pulse repetition frequency of the laser
β-AE(λ_1-λ_2)	Backscatter related Angstöm exponent
α- AE(λ_1- λ_2)	Extinction related Angstöm exponent
δ^{P}_{532nm}	Particle linear depolarization ratio at 532 nm
$K_i(r,m,\lambda,s)$	Kernel efficiencies for the i data
$B_j(r)$	triangular base functions
w_j	Weight factors
$V(\lambda)$	Signal measured by the sun photometer
b	Sun-photometer integrated backscatter coefficients
a_v	Mean value of the extinction coefficients per unit of column-integrated volume concentration
b_v	Mean value of the backscatter coefficients per unit of column-integrated volume concentration
$C_v(z_n)$.	Volume concentration profiles
$L^{*,j}(z_n)$	Normalized measured lidar signal at λ_j
$L^j(\, C_v^j(z_n), m_j, z_n)$	LIRIC-calculated nonlinear function
W_v^*	Total column integrated content of the aerosol fraction from sun photometer measurements
$W\big(C_v(z_n)\big)$	Total column integrated content of the aerosol fraction from LIRIC calculations
$F_{11.v}(\lambda_i, 180°)$	First diagonal element of the scattering matrix at 180°
k, f, d	Regularization parameters in LIRIC
z_N,	Reference height in LIRIC

z_{N0},	Lower limit height in LIRIC
z_U	Upper limit height in LIRIC
g_{asym}	Asymmetry factor

→References

AERONET-Homepage (2011b), AERONET Inversion Products, Tech. rep., NASA,http://aeronet.gsfc.nasa.gov/new web/publications.html.

Alados-Arboledas, L., A. Alcántara, F. J. Olmo, J. A. Martínez-Lozano, V. Estellés, V. Cachorro, A. M. Silva, H. Horvath, M. Gangl, and A. Díaz (2008), Aerosol columnar properties retrieved from CIMEL radiometers during VELETA 2002, *Atmospheric Environment*, *42*(11), 2654-2667.

Alados-Arboledas, L., D. Müller, J. L. Guerrero-Rascado, F. Navas-Guzmán, D. Pérez-Ramírez, and F. J. Olmo (2011), Optical and microphysical properties of fresh biomass burning aerosol retrieved by Raman lidar, and star-and sun-photometry, *Geophysical Research Letters*, *38*(1).

Albrecht, B. A. (1989), Aerosols, cloud microphysics, and fractional cloudiness, *Science*, *245*(4923), 1227-1230.

Andreae, M. (1991), Biomass burning- Its history, use, and distribution and its impact on environmental quality and global climate, *Global biomass burning- Atmospheric, climatic, and biospheric implications(A 92-37626 15-42). Cambridge, MA, MIT Press, 1991*, 3-21.

Andrey, J., E. Cuevas, M. C. Parrondo, S. Alonso-Pérez, A. Redondas, and M. Gil-Ojeda (2014), Quantification of ozone reductions within the Saharan air layer through a 13-year climatologic analysis of ozone profiles, *Atmospheric Environment*, *84*, 28-34.

Ångström, A. (1964), The parameters of atmospheric turbidity, *Tellus*, *16*(1), 64-75.

Ansmann, A., and D. Müller (2005), *Lidar and atmospheric aerosol particles*, Springer.

Ansmann, A., M. Riebesell, and C. Weitkamp (1990), Measurement of atmospheric aerosol extinction profiles with a Raman lidar, *Optics Letters*, *15*(13), 746-748.

Ansmann, A., U. Wandinger, M. Riebesell, C. Weitkamp, and W. Michaelis (1992a), Independent measurement of extinction and backscatter profiles in cirrus clouds by using a combined Raman elastic-backscatter lidar, *Applied Optics*, *31*(33), 7113-7113.

Ansmann, A., M. Riebesell, U. Wandinger, C. Weitkamp, E. Voss, W. Lahmann, and W. Michaelis (1992b), Combined Raman elastic-backscatter lidar for vertical profiling of moisture, aerosol extinction, backscatter, and lidar ratio, *Applied Physics B*, *55*(1), 18-28.

Ansmann, A., H. Baars, M. Tesche, D. Müller, D. Althausen, R. Engelmann, T. Pauliquevis, and P. Artaxo (2009), Dust and smoke transport from Africa to South America: Lidar profiling over Cape Verde and the Amazon rainforest, *Geophysical Research Letters*, *36*(11), L11802.

Ansmann, A., J. Bösenberg, A. Chaikovsky, A. Comerón, S. Eckhardt, R. Eixmann, V. Freudenthaler, P. Ginoux, L. Komguem, and H. Linné (2003), Long-range transport of

Saharan dust to northern Europe: The 11–16 October 2001 outbreak observed with EARLINET, *Journal of geophysical research*, *108*(D24), 4783.

Antón, M., J. E. Gil, J. Fernández-Gálvez, H. Lyamani, A. Valenzuela, I. Foyo-Moreno, F. J. Olmo, and L. Alados-Arboledas (2011), Evaluation of the aerosol forcing efficiency in the UV erythemal range at Granada, Spain, *Journal of geophysical research*, *116*(D20), D20214.

Balis, D. S., V. Amiridis, S. Nickovic, A. Papayannis, and C. Zerefos (2004), Optical properties of Saharan dust layers as detected by a Raman lidar at Thessaloniki, Greece, *Geophysical Research Letters*, *31*(13), L13104.

Barth, C. A., R. W. Sanders, R. J. Thomas, G. E. Thomas, B. M. Jakosky, and R. A. West (1983), Formation of the El Chichon aerosol cloud, *Geophysical Research Letters*, *10*(11), 993-996.

Basart, S., C. Pérez, S. Nickovic, E. Cuevas, and J. M. Baldasano (2012), Development and evaluation of the BSC-DREAM8b dust regional model over Northern Africa, the Mediterranean and the Middle East, *Tellus B*, *64*.

Baumgardner, D., G. B. Raga, J. C. Jimenez, and K. Bower (2005), Aerosol particles in the Mexican East Pacific Part I: processing and vertical redistribution by clouds, *Atmospheric Chemistry and Physics*, *5*(11), 3081-3091.

Bluth, G. J. S., W. I. Rose, I. E. Sprod, and A. J. Krueger (1997), Stratospheric loading of sulfur from explosive volcanic eruptions, *Journal of Geology*, *105*(6), 671-683.

Böckmann, C. (2001), Hybrid regularization method for the ill-posed inversion of multiwavelength lidar data in the retrieval of aerosol size distributions, *Applied Optics*, *40*(9), 1329-1342.

Böckmann, C., I. Mironova, D. Müller, L. Schneidenbach, and R. Nessler (2005), Microphysical aerosol parameters from multiwavelength lidar, *JOSA A*, *22*(3), 518-528.

Bohren, C. F., and D. R. Huffman (1983), Absorption and scattering by a sphere, *Absorption and Scattering of Light by Small Particles*, 82-129.

Bösenberg, J. et al. (2001), *EARLINET: A European Aerosol Research Lidar Network, laser remote sensing of the atmosphere*, Selected Papers of the 20th International Laser Radar Conference, Dabas, A., C. Loth and J. Pelon (Eds.), Edition Ecole Polytechnique, Palaissea, France, pp. 155-158.

Brasseur, G. P., J. J. Orlando, and G. S. Tyndall (1999), *Atmospheric chemistry and global change*, Oxford University Press New York.

Bréon, F.-M. (2006), How do aerosols affect cloudiness and climate?, *Science*, *313*(5787), 623-624.

Cairo, F., Di Donfrancesco, G., Adriani, A., Pulvirenti, L., & Fierli, F. (1999). Comparison of various linear depolarization parameters measured by lidar. Applied optics, 38(21), 4425-4432.

Campanelli, M., V. Estellés, C. Tomasi, T. Nakajima, V. Malvestuto, and J. A. Martínez-Lozano (2007), Application of the SKYRAD Improved Langley plot method for the in-situ calibration of CIMEL Sun-sky photometers, *Applied Optics*, *46*(14), 2688-2702.

Claquin, T., M. Schulz, Y. Balkanski, and O. Boucher (1998), Uncertainties in assessing radiative forcing by mineral dust, *Tellus B*, *50*(5), 491-505.

Cook, J., and E. J. Highwood (2004), Climate response to tropospheric absorbing aerosols in an intermediate general-circulation model, *Quarterly Journal of the Royal Meteorological Society*, *130*(596), 175-191.

Cooney, J. (1972), Measurement of atmospheric temperature profiles by Raman backscatter, *Journal of Applied meteorology*, *11*, 108-112.

Córdoba-Jabonero, C., M. Sorribas, J. L. Guerrero-Rascado, J. A. Adame, Y. Hernández, H. Lyamani, V. Cachorro, M. Gil, L. Alados-Arboledas, and E. Cuevas (2011), Synergetic monitoring of Saharan dust plumes and potential impact on surface: a case study of dust transport from Canary Islands to Iberian Peninsula, *Atmospheric Chemistry and Physics*, *11*(7), 3067-3091.

Costa, M. J., V. Levizzani, and A. M. Silva (2004), Aerosol characterization and direct radiative forcing assessment over the ocean. Part II: Application to test cases and validation, *Journal of Applied meteorology*, *43*(12), 1818-1833.

Chaikovsky, A., O. Dubovik, P. Goloub, D. Tanre, and G. Pappalardo, Wandinger, U., Chaikovskaya, L., Denisov, S., Grudo, Y., Lopatsin, A., Karol, Y., Lapyonok, T., Korol, M., Osipenko, F., Savitski, D., Slesar, A., Apituley, A., Arboledas, L. A., Binietoglou, I., Kokkalis, P., Granados Muñoz, M. J., Papayannis, A., Perrone, M. R., Pietruczuk, A., Pisani, G., Rocadenbosch, F., Sicard, M., De Tomasi, F., Wagner, J., and Wang, X. (2012), Algorithm and software for the retrieval of vertical aerosol properties using combined lidar/radiometer data: Dissemination in EARLINET,, paper presented at 26th International Laser and Radar Conference, Porto Heli, Greece.

Chaikovsky, A., O. Dubovik, P. Goloub, N. Balashevich, A. Lopatsin, Y. Karol, S. Denisov, and T. Lapyonok (2008), Software package for the retrieval of aerosol microphysical properties in the vertical column using combined lidar/photometer data (test version), *Technical Report.*, Institute of Physics, National Academy of Sciences of Belarus Minsk, Belarus.

Charlson, R. J., S. E. Schwartz, J. M. Hales, R. D. Cess, J. A. Coakley Jr, J. E. Hansen, and D. J. Hofmann (1992), Climate forcing by anthropogenic aerosols, *Science*, *255*(5043), 423-430.

Di Girolamo, P., D. Summa, R. Bhawar, T. Di Iorio, M. Cacciani, I. Veselovskii, O. Dubovik, and A. Kolgotin (2012), Raman lidar observations of a Saharan dust outbreak event: characterization of the dust optical properties and determination of particle size and microphysical parameters, *Atmospheric Environment*, *50*, 66-78.

Draxler, R. R., and G. D. Rolph (2003), HYSPLIT (HYbrid Single-Particle Lagrangian Integrated Trajectory) model access via NOAA ARL READY website (http://www. arl. noaa. gov/ready/hysplit4. html). NOAA Air Resources Laboratory, Silver Spring, edited, Md.

Dubovik, O. (2005), Optimization of numerical inversion in photopolarimetric remote sensing, in *Photopolarimetry in remote sensing*, edited, pp. 65-106, Springer.

Dubovik, O., and M. D. King (2000), A flexible inversion algorithm for retrieval of aerosol optical properties from Sun and sky radiance measurements, *Journal of Geophysical Research: Atmospheres (1984–2012)*, *105*(D16), 20673-20696.

Dubovik, O., A. Smirnov, B. N. Holben, M. D. King, Y. J. Kaufman, T. F. Eck, and I. Slutsker (2000), Accuracy assessments of aerosol optical properties retrieved from Aerosol Robotic Network (AERONET) Sun and sky radiance measurements, *Journal of Geophysical Research: Atmospheres (1984–2012)*, *105*(D8), 9791-9806.

Dubovik, O., B. N. Holben, T. Lapyonok, A. Sinyuk, M. I. Mishchenko, P. Yang, and I. Slutsker (2002), Non-spherical aerosol retrieval method employing light scattering by spheroids, *Geophysical Research Letters*, *29*(10), 54-51.

Dubovik, O., B. Holben, T. F. Eck, A. Smirnov, Y. J. Kaufman, M. D. King, D. Tanré, and I. Slutsker (2002), Variability of absorption and optical properties of key aerosol types observed in worldwide locations, *Journal of the Atmospheric Sciences*, *59*(3), 590-608.

Dubovik, O., A. Sinyuk, T. Lapyonok, B. N. Holben, M. Mishchenko, P. Yang, T. F. Eck, H. Volten, O. Muñoz, and B. Veihelmann (2006), Application of spheroid models to account for aerosol particle nonsphericity in remote sensing of desert dust, *Journal of Geophysical Research: Atmospheres (1984–2012)*, *111*(D11).

Eadie, W. T., and F. James (2006), *Statistical methods in experimental physics*, World Scientific Publishing Company.

Eck, T. F., B. N. Holben, J. S. Reid, O. Dubovik, A. Smirnov, N. T. O'Neill, I. Slutsker, and S. Kinne (1999), Wavelength dependence of the optical depth of biomass burning, urban, and desert dust aerosols, *Journal of Geophysical Research: Atmospheres (1984–2012)*, *104*(D24), 31333-31349.

Eichinger, W. E., and V. A. Kovalev (2004), Elastic Lidar: Theory, Practice, and Analysis Methods, edited, Wiley Publishers.

Estellés, V., M. P. Utrillas, J. L. Gómez-Amo, R. Pedrós, and J. A. Martinez-Lozano (2004), Aerosol size distributions and air mass back trajectories over a Mediterranean coastal site, *International Journal of Remote Sensing*, *25*(1), 39-50.

Feingold, G., and B. Morley (2003), Aerosol hygroscopic properties as measured by lidar and comparison with in situ measurements, *Journal of geophysical research*, *108*(D11), 4327.

Feingold, G., R. Furrer, P. Pilewskie, L. A. Remer, Q. Min, and H. Jonsson (2006), Aerosol indirect effect studies at Southern Great Plains during the May 2003 intensive operations period, *Journal of geophysical research*, *111*(D5), D05S14.

Fernald, F. G. (1984), Analysis of atmospheric lidar observations- Some comments, *Applied Optics*, *23*(5), 652-653.

Fernald, F. G., B. M. Herman, and J. A. Reagan (1972), Determination of aerosol height distributions by lidar, *Journal of Applied meteorology*, *11*(3), 482-489.

Ferrare, R. A., S. H. Melfi, D. N. Whiteman, K. D. Evans, M. Poellot, and Y. J. Kaufman (1998), Raman lidar measurements of aerosol extinction and backscattering: 2. Derivation of aerosol real refractive index, single-scattering albedo, and humidification factor using Raman lidar and aircraft size distribution measurements, *Journal of Geophysical Research: Atmospheres (1984–2012)*, *103*(D16), 19673-19689.

Fierz-Schmidhauser, R., P. Zieger, M. Gysel, L. Kammermann, P. F. DeCarlo, U. Baltensperger, and E. Weingartner (2010), Measured and predicted aerosol light scattering enhancement factors at the high alpine site Jungfraujoch, *Atmospheric Chemistry and Physics*, *10*(5), 2319-2333.

Flores, J., R. Z. Bar-Or, N. Bluvshtein, A. Abo-Riziq, A. Kostinski, S. Borrmann, I. Koren, and Y. Rudich (2012), Absorbing aerosols at high relative humidity: linking hygroscopic growth to optical properties, *Atmospheric Chemistry and Physics*, *12*(12), 5511-5521.

Forster, P., V. Ramaswamy, P. Artaxo, T. Berntsen, R. Betts, D. W. Fahey, J. Haywood, J. Lean, D. C. Lowe, and G. Myhre (2007), Changes in atmospheric constituents and in radiative forcing, *Climate change*, *20*.

Freudenthaler, V., M. Esselborn, M. Wiegner, B. Heese, M. Tesche, A. Ansmann, D. Müller, D. Althausen, M. Wirth, and A. Fix (2009), Depolarization ratio profiling at several wavelengths in pure Saharan dust during SAMUM 2006, *Tellus B*, *61*(1), 165-179.

Gasso, S., D. A. Hegg, D. S. Covert, D. Collins, K. J. Noone, E. Öström, B. Schmid, P. B. Russell, J. M. Livingston, and P. A. Durkee (2000), Influence of humidity on the aerosol scattering coefficient and its effect on the upwelling radiance during ACE-2, *Tellus B*, *52*(2), 546-567.

Ginoux, P. (2003), Effects of nonsphericity on mineral dust modeling, *Journal of Geophysical Research: Atmospheres (1984–2012)*, *108*(D2).

Goody, R., R. West, L. Chen, and D. Crisp (1989), The correlated-k method for radiation calculations in nonhomogeneous atmospheres, *Journal of Quantitative Spectroscopy and Radiative Transfer*, *42*(6), 539-550.

Goudie, A. S., and N. J. Middleton (2001), Saharan dust storms: nature and consequences, *Earth-Science Reviews*, *56*(1), 179-204.

Grams, G. W., I. H. Blifford Jr, B. G. Schuster, and J. S. DeLuisi (1972), Complex Index of Refraction of Airborne Fly Ash Determined by Laser Radar and Collection of Particles at 13 km, *Journal of Atmospheric Sciences*, *29*, 900-905.

Granados-Muñoz, M. J., F. Navas-Guzmán, J. A. Bravo-Aranda, J. L. Guerrero-Rascado, H. Lyamani, J. Fernández-Gálvez, and L. Alados-Arboledas (2012), Automatic determination of the planetary boundary layer height using lidar: One-year analysis over southeastern Spain, *Journal of Geophysical Research: Atmospheres (1984–2012)*, *117*(D18).

Guerrero-Rascado, J. L., F. J. Olmo, I. Avilés-Rodríguez, F. Navas-Guzmán, D. Pérez-Ramírez, H. Lyamani, and L. Alados-Arboledas (2009), Extreme Saharan dust event over the southern Iberian Peninsula in September 2007: Active and passive remote sensing from surface and satellite, *Atmos. Chem. Phys*, *9*(21), 8453-8469.

Guerrero Rascado, J. L. (2008), Técnica Lidar para caracterización atmosférica mediante dispersión elástica y Raman.

Gysel, M., E. Weingartner, S. Nyeki, D. Paulsen, U. Baltensperger, I. Galambos, and G. Kiss (2004), Hygroscopic properties of water-soluble matter and humic-like organics in atmospheric fine aerosol, *Atmospheric Chemistry and Physics*, *4*(1), 35-50.

Hamilton, J. F., P. J. Webb, A. C. Lewis, J. R. Hopkins, S. Smith, and P. Davy (2004), Partially oxidised organic components in urban aerosol using GCXGC-TOF/MS, *Atmospheric Chemistry and Physics*, *4*(5), 1279-1290.

Hamonou, E., P. Chazette, D. Balis, F. Dulac, X. Schneider, E. Galani, G. Ancellet, and A. Papayannis (1999), Characterization of the vertical structure of Saharan dust export to the Mediterranean basin, *Journal of Geophysical Research: Atmospheres (1984–2012)*, *104*(D18), 22257-22270.

Hänel, G. (1976), The Properties of Atmospheric Aerosol Particles as Functions of the Relative Humidity at Thermodynamic Equilibrium with the Surrounding Moist Air, in *Advances in Geophysics*, edited by H. E. Landsberg and J. V. Mieghem, pp. 73-188, Elsevier.

Haywood, J., and O. Boucher (2000), Estimates of the direct and indirect radiative forcing due to tropospheric aerosols: A review, *Reviews of Geophysics*, *38*(4), 513-543.

Hegg, D. A., R. J. Ferek, and P. V. Hobbs (1993), Aerosol size distributions in the cloudy atmospheric boundary layer of the North Atlantic Ocean, *Journal of Geophysical Research: Atmospheres (1984–2012)*, *98*(D5), 8841-8846.

Hegg, D. A., D. S. Covert, M. J. Rood, and P. V. Hobbs (1996), Measurements of aerosol optical properties in marine air, *Journal of Geophysical Research: Atmospheres (1984–2012)*, *101*(D8), 12893-12903.

Hitschfeld, W., and J. Bordan (1954), Errors inherent in the radar measurement of rainfall at attenuating wavelengths, *Journal of Meteorology*, *11*(1), 58-67.

Holben, B. N., et al. (1998), AERONET—A Federated Instrument Network and Data Archive for Aerosol Characterization, *Remote Sensing of Environment*, *66*(1), 1-16.

Horvath, H. (1998), Influence of atmospheric aerosols upon the global radiation balances, in *Atmospheric Particle*, edited by R. M. H. a. R. v. Grieken, pp. 543-596, John Wiley & Sons.

Huang, J., Q. Fu, J. Su, Q. Tang, P. Minnis, Y. Hu, Y. Yi, and Q. Zhao (2009), Taklimakan dust aerosol radiative heating derived from CALIPSO observations using the Fu-Liou radiation model with CERES constraints, *Atmospheric Chemistry and Physics*, *9*(12), 4011-4021.

IPCC (2007), Contribution of Working Group I to the Fourth Assessment Report of the Intergovernmental Panel on Climate Change, edited by S. Solomon, D. Qin, M. Manning, Z. Chen, M. Marquis, K.B. Averyt, M. Tignor and H.L. Miller Cambridge University Press.

IPCC (2013), Contribution of Working Group I to the Fifth Assessment Report of the Intergovernmental Panel on Climate Change, in *Summary for Policymakers in Climate Change*, edited by T. F. Stocker, D. Qin, G.K. Plattner, M. Tignor, S. Allen, J. Boschung, A. Nauels, Y. Xia, V. Bex, and P. Midgley, Cambrigde University Press.

Iqbal, M. (1983), *An introduction to solar radiation*, Access Online via Elsevier.

Johnson, B. T., K. P. Shine, and P. M. Forster (2004), The semi-direct aerosol effect: Impact of absorbing aerosols on marine stratocumulus, *Quarterly Journal of the Royal Meteorological Society*, *130*(599), 1407-1422.

Junge, C. E. (1963), Air chemistry and radioactivity, *1963*, 382.

Kasten, F., and A. T. Young (1989), Revised optical air mass tables and approximation formula, *Appl. Opt*, *28*(22), 4735-4738.

Kaufman, Y. J., D. Tanré, J. F. Léon, and J. Pelon (2003), Retrievals of profiles of fine and coarse aerosols using lidar and radiometric space measurements, *Geoscience and Remote Sensing, IEEE Transactions on*, *41*(8), 1743-1754.

Kaufman, Y. J., O. Boucher, D. TanrÃ©, M. Chin, L. A. Remer, and T. Takemura (2005), Aerosol anthropogenic component estimated from satellite data, *Geophysical Research Letters*, *32*(17), 1-4.

Klett, J. D. (1981), Stable analytical inversion solution for processing lidar returns, *Applied Optics*, *20*(2), 211-220.

Klett, J. D. (1985), Lidar inversion with variable backscatter/extinction ratios, *Applied Optics*, *24*(11), 1638-1643.

Kokkalis, P., A. Papayannis, V. Amiridis, R. E. Mamouri, I. Veselovskii, A. Kolgotin, G. Tsaknakis, N. I. Kristiansen, A. Stohl, and L. Mona (2013), Optical, microphysical, mass and geometrical properties of aged volcanic particles observed over Athens, Greece, during the Eyjafjallajökull eruption in April 2010 through synergy of Raman lidar and sunphotometer measurements, *Atmospheric Chemistry & Physics Discussions*, *13*, 5315-5364.

Kotchenruther, R. A., and P. V. Hobbs (1998), Humidification factors of aerosols from biomass burning in Brazil, *Journal of Geophysical Research: Atmospheres (1984–2012)*, *103*(D24), 32081-32089.

Kotchenruther, R. A., P. V. Hobbs, and D. A. Hegg (1999), Humidification factors for atmospheric aerosols off the mid-Atlantic coast of the United States, *Journal of Geophysical Research: Atmospheres (1984–2012)*, *104*(D2), 2239-2251.

LaFontaine, C. V., R. A. Bryson, and W. M. Wendland (1990), Airstream regions of North Africa and the Mediterranean, *Journal of climate*, *3*(3), 366-372.

Lelieveld, J., H. Berresheim, S. Borrmann, P. J. Crutzen, F. J. Dentener, H. Fischer, J. Feichter, P. J. Flatau, J. Heland, and R. Holzinger (2002), Global air pollution crossroads over the Mediterranean, *Science*, *298*(5594), 794-799.

Léon, J.-F., D. Tanré, J. Pelon, Y. J. Kaufman, J. M. Haywood, and B. Chatenet (2003), Profiling of a Saharan dust outbreak based on a synergy between active and passive remote sensing, *Journal of geophysical research*, *108*(D18), 8575.

Lohmann, U., and J. Feichter (2005), Global indirect aerosol effects: a review, *Atmospheric Chemistry and Physics*, *5*(3), 715-737.

Lopatin, A., O. Dubovik, A. Chaikovsky, P. Goloub, T. Lapyonok, D. Tanré, and P. Litvinov (2013), Enhancement of aerosol characterization using synergy of lidar and sun photometer coincident observations: the GARRLiC algorithm, *Atmospheric Measurement Techniques Discussions*, *6*, 2253-2325.

Lyamani, H., F. J. Olmo, and L. Alados-Arboledas (2005), Saharan dust outbreak over southeastern Spain as detected by sun photometer, *Atmospheric Environment*, *39*(38), 7276-7284.

Lyamani, H., F. J. Olmo, and L. Alados-Arboledas (2009), Physical and optical properties of aerosols over an urban location in Spain: seasonal and diurnal variability, *Atmospheric Chemistry and Physics Discussions*, *9*(5), 18159-18199.

Lyamani, H., F. J. Olmo, and L. Alados-Arboledas (2010), Physical and optical properties of aerosols over an urban location in Spain: seasonal and diurnal variability, *Atmos. Chem. Phys.*, *10*(1), 239-254.

Mattis, I., A. Ansmann, D. Müller, U. Wandinger, and D. Althausen (2004), Multiyear aerosol observations with dual-wavelength Raman lidar in the framework of EARLINET, *Journal of Geophysical Research: Atmospheres (1984–2012)*, *109*(D13).

McCormick, M. P., P. H. Wang, and L. R. Poole (1993), Stratospheric aerosols and clouds, Aerosol-Cloud-Climate Interactions, *PV Hobbs*, 205-222.

McFiggans, G., P. Artaxo, U. Baltensperger, H. Coe, M. C. Facchini, G. Feingold, S. Fuzzi, M. Gysel, A. Laaksonen, and U. Lohmann (2006), The effect of physical and chemical aerosol properties on warm cloud droplet activation, *Atmospheric Chemistry and Physics*, *6*(9), 2593-2649.

McInnes, L., M. Bergin, J. Ogren, and S. Schwartz (1998), Apportionment of light scattering and hygroscopic growth to aerosol composition, *Geophysical Research Letters*, *25*(4), 513-516.

McInnes, L. M., P. K. Quinn, D. S. Covert, and T. L. Anderson (1996), Gravimetric analysis, ionic composition, and associated water mass of the marine aerosol, *Atmospheric Environment*, *30*(6), 869-884.

Measures, R. M. (1984), Laser remote sensing: Fundamentals and applications(Book), *New York, Wiley-Interscience, 1984, 521 p*.

Melfi, S. H. (1972), Remote measurements of the atmosphere using Raman scattering, *Applied Optics*, *11*(7), 1605-1610.

Menon, S., J. Hansen, L. Nazarenko, and Y. Luo (2002), Climate effects of black carbon aerosols in China and India, *Science*, *297*(5590), 2250-2253.

Mie, G. (1908), Beiträge zur Optik trüber Medien, speziell kolloidaler Metallösungen, *Annalen der physik*, *330*(3), 377-445.

Mishchenko, M. I., L. D. Travis, R. A. Kahn, and R. A. West (1997), Modeling phase functions for dustlike tropospheric aerosols using a shape mixture of randomly oriented polydisperse spheroids, *Journal of geophysical research*, *102*(D14), 16831-16816.

Mona, L., A. Amodeo, M. Pandolfi, and G. Pappalardo (2006), Saharan dust intrusions in the Mediterranean area: Three years of Raman lidar measurements, *Journal of Geophysical Research: Atmospheres (1984–2012)*, *111*(D16).

Mona, L.; M. Sicard, A. Amodeo, A. Apituley, L. Alados-Arboledas, and D. Balis (2012), EARLINET and the international ChArMEx and PEGASOS measurement campaigns in summer 2012, paper presented at European Aerosol Conference, Granada.

Moulin, C., C. E. Lambert, F. Dulac, and U. Dayan (1997), Control of atmospheric export of dust from North Africa by the North Atlantic Oscillation, *Nature*, *387*(6634), 691.

Müller, D., U. Wandinger, and A. Ansmann (1999), Microphysical particle parameters from extinction and backscatter lidar data by inversion with regularization: theory, *Applied Optics*, *38*(12), 2346-2357.

Müller, D., Mattis, I., Ansmann, A., Wandinger, U., Ritter, C., & Kaiser, D. (2007). Multiwavelength Raman lidar observations of particle growth during long-range transport of forest-fire smoke in the free troposphere. Geophysical research letters, 34(5), L05803.

Müller, D., I. Veselovskii, A. Kolgotin, M. Tesche, A. Ansmann, and O. Dubovik (2013), Vertical profiles of pure dust and mixed smoke–dust plumes inferred from inversion of multiwavelength Raman/polarization lidar data and comparison to AERONET retrievals and in situ observations, *Applied Optics*, *52*(14), 3178-3202.

Nakajima, T., G. Tonna, R. Rao, P. Boi, Y. Kaufman, and B. Holben (1996), Use of sky brightness measurements from ground for remote sensing of particulate polydispersions, *Applied Optics*, *35*(15), 2672-2686.

Navas-Guzmán, F., J. L. G. Rascado, and L. A. Arboledas (2011), Retrieval of the lidar overlap function using Raman signals, *Opt. Pura Apl*, *44*(1), 71-75.

Navas-Guzmán, F., J. A. Bravo-Aranda, J. L. Guerrero-Rascado, M. J. Granados-Muñoz, and L. Alados-Arboledas (2013), Statistical analysis of aerosol optical properties retrieved by Raman lidar over Southeastern Spain, *Tellus B*, *65*.

Navas-Guzmán, F. J. (2012), Atmospheric vertical profiling by Raman Lidar, *PhD Dissertation*.

Navas-Guzmán, F., D. Müller, J. A. Bravo-Aranda, J. L. Guerrero-Rascado, M. J. Granados-Muñoz, D. Pérez-Ramírez, F. J. Olmo, and L. Alados-Arboledas (2013), Eruption of the Eyjafjallajökull Volcano in spring 2010: Multiwavelength Raman lidar measurements of sulphate particles in the lower troposphere, *Journal of Geophysical Research: Atmospheres*.

Nickovic, S., G. Kallos, A. Papadopoulos, and O. Kakaliagou (2001), A model for prediction of desert dust cycle in the atmosphere, *Journal of geophysical research*, *106*(D16), 18113-18118.

O'Neill, N. T., T. F. Eck, A. Smirnov, B. N. Holben, and S. Thulasiraman (2003), Spectral discrimination of coarse and fine mode optical depth, *Journal of geophysical research*, *108*(D17), 4559.

Olmo, F. J., A. Quirantes, A. Alcántara, H. Lyamani, and L. Alados-Arboledas (2006), Preliminary results of a non-spherical aerosol method for the retrieval of the atmospheric aerosol optical properties, *Journal of Quantitative Spectroscopy and Radiative Transfer*, *100*(1), 305-314.

Papayannis, A., D. Balis, V. Amiridis, G. Chourdakis, G. Tsaknakis, C. Zerefos, A. D. A. Castanho, S. Nickovic, S. Kazadzis, and J. Grabowski (2005), Measurements of Saharan dust aerosols over the Eastern Mediterranean using elastic backscatter-Raman lidar, spectrophotometric and satellite observations in the frame of the EARLINET project, *Atmospheric Chemistry and Physics*, *5*(8), 2065-2079.

Pappalardo, G., A. Amodeo, M. Pandolfi, U. Wandinger, A. Ansmann, J. Bösenberg, V. Matthias, V. Amiridis, F. De Tomasi, and M. Frioud (2004), Aerosol lidar intercomparison in the framework of the EARLINET project. 3. Raman lidar algorithm for aerosol extinction, backscatter, and lidar ratio, *Applied Optics*, *43*(28), 5370-5385.

Pérez, C., S. Nickovic, G. Pejanovic, J. M. Baldasano, and E. Özsoy (2006a), Interactive dust-radiation modeling: A step to improve weather forecasts, *Journal of geophysical research*, *111*(D16), D16206.

Pérez, C., S. Nickovic, J. M. Baldasano, M. Sicard, F. Rocadenbosch, and V. E. Cachorro (2006b), A long Saharan dust event over the western Mediterranean: Lidar, Sun photometer observations, and regional dust modeling, *Journal of Geophysical Research: Atmospheres (1984–2012)*, *111*(D15).

Petters, M. D., and S. M. Kreidenweis (2007), A single parameter representation of hygroscopic growth and cloud condensation nucleus activity, *Atmospheric Chemistry and Physics*, *7*(8), 1961-1971.

Preißler, J., F. Wagner, J. L. Guerrero-Rascado, and A. M. Silva (2013), Two years of free-tropospheric aerosol layers observed over Portugal by lidar, *Journal of Geophysical Research: Atmospheres*.

Prospero, J. M., P. Ginoux, O. Torres, S. E. Nicholson, and T. E. Gill Environmental characterization of global sources of atmospheric soil dust derived from the NIMBUS7 TOMS absorbing aerosol product, Rev, Citeseer, 2002.

Pruppacher, H. R., J. D. Klett, and P. K. Wang (1998), Microphysics of clouds and precipitation, *Taylor&Francis,* pp. 381-382.

Raes, F., T. Bates, F. McGovern, and M. Van Liedekerke (2000), The 2nd Aerosol Characterization Experiment (ACE-2): General overview and main results, *Tellus, Series B: Chemical and Physical Meteorology*, *52*(2), 111-125.

Ramaswamy, V., O. Boucher, J. Haigh, D. Hauglustine, J. Haywood, G. Myhre, T. Nakajima, G. Y. Shi, and S. Solomon (2001), Radiative forcing of climate, *Climate change*, 349-416.

Randriamiarisoa, H., P. Chazette, P. Couvert, J. Sanak, and G. Mégie (2006), Relative humidity impact on aerosol parameters in a Paris suburban area, *Atmospheric Chemistry and Physics*, *6*(5), 1389-1407.

Raut, J. C., and P. Chazette (2007), Retrieval of aerosol complex refractive index from a synergy between lidar, sunphotometer and in situ measurements during LISAIR experiment, *Atmospheric Chemistry and Physics*, *7*(11), 2797-2815.

Reagan, J. A., J. D. Spinhirne, D. M. Byrne, D. W. Thomson, R. G. De Pena, and Y. Mamane (1977), Atmospheric particulate properties inferred from lidar and solar radiometer observations compared with simultaneous in situ aircraft measurements: A case study, *Journal of Applied meteorology*, *16*, 911-928.

Rodríguez, S., A. Alastuey, S. Alonso-Pérez, X. Querol, E. Cuevas, J. Abreu-Afonso, M. Viana, M. Pandolfi, and J. Rosa (2011), Transport of desert dust mixed with North African industrial pollutants in the subtropical Saharan Air Layer, *Atmospheric Chemistry and Physics Discussions*, *11*(3), 8841-8892.

Sabatier, P. C. (1987), Basic concepts and methods of inverse problems, *Basic Methods of Tomography and Inverse Problems*.

Sasano, Y., and E. V. Browell (1989), Light scattering characteristics of various aerosol types derived from multiple wavelength lidar observations, *Applied Optics*, *28*(9), 1670-1679.

Sasano, Y., E. V. Browell, and S. Ismail (1985), Error caused by using a constant extinction/backscattering ratio in the lidar solution, *Applied Optics*, *24*(22), 3929-3932.

Sawamura, P., J. P. Vernier, J. E. Barnes, T. A. Berkoff, E. J. Welton, L. Alados-Arboledas, F. Navas-Guzmán, G. Pappalardo, L. Mona, and F. Madonna (2012), Stratospheric AOD after the 2011 eruption of Nabro volcano measured by lidars over the Northern Hemisphere, *Environmental Research Letters*, *7*(3), 034013.

Seinfeld, J. H., and S. N. Pandis (2012), *Atmospheric chemistry and physics: from air pollution to climate change*, John Wiley & Sons.

Shifrin, K. S. (1995), Simple relationships for the Ångström parameter of disperse systems, *Applied Optics*, *34*(21), 4480-4485.

Shimizu, A., N. Sugimoto, I. Matsui, K. Arao, I. Uno, T. Murayama, N. Kagawa, K. Aoki, A. Uchiyama, and A. Yamazaki (2004), Continuous observations of Asian dust and other aerosols by polarization lidars in China and Japan during ACE-Asia, *Journal of Geophysical Research: Atmospheres (1984–2012)*, *109*(D19).

Sinyuk, A., O. Dubovik, B. Holben, T. F. Eck, F.-M. Breon, J. Martonchik, R. Kahn, D. J. Diner, E. F. Vermote, and J.-C. Roger (2007), Simultaneous retrieval of aerosol and surface properties from a combination of AERONET and satellite data, *Remote Sensing of Environment*, *107*(1), 90-108.

Smirnov, A., B. N. Holben, T. F. Eck, O. Dubovik, and I. Slutsker (2000), Cloud-screening and quality control algorithms for the AERONET database, *Remote Sensing of Environment*, *73*(3), 337-349.

Sokolik, I. N., and O. B. Toon (1999), Incorporation of mineralogical composition into models of the radiative properties of mineral aerosol from UV to IR wavelengths, *Journal of Geophysical Research: Atmospheres (1984–2012)*, *104*(D8), 9423-9444.

Sokolik, I. N., D. M. Winker, G. Bergametti, D. A. Gillette, G. Carmichael, Y. J. Kaufman, L. Gomes, L. Schuetz, and J. E. Penner (2001), Introduction to special section: Outstanding problems in quantifying the radiative impacts of mineral dust, *Journal of Geophysical Research: Atmospheres (1984–2012)*, *106*(D16), 18015-18027.

Takamura, T., and T. Nakajima (2004), Overview of SKYNET and its activities, *Opt. Pura Apl*, *37*(3), 3303-3308.

Tanré, D., J. Haywood, J. Pelon, J. F. Léon, B. Chatenet, P. Formenti, P. Francis, P. Goloub, E. J. Highwood, and G. Myhre (2003), Measurement and modeling of the Saharan dust radiative impact: Overview of the Saharan Dust Experiment (SHADE), *Journal of geophysical research*, *108*(D18), 8574.

Tegen, I., and I. Fung (1994), Modeling of mineral dust in the atmosphere: Sources, transport, and optical thickness, *Journal of Geophysical Research: Atmospheres (1984–2012)*, *99*(D11), 22897-22914.

Tegen, I., M. Werner, S. P. Harrison, and K. E. Kohfeld (2004), Relative importance of climate and land use in determining present and future global soil dust emission, *Geophysical Research Letters*, *31*(5).

Textor, C., M. Schulz, S. Guibert, S. Kinne, Y. Balkanski, S. Bauer, T. Berntsen, T. Berglen, O. Boucher, and M. Chin (2007), The effect of harmonized emissions on aerosol properties in global models–an AeroCom experiment, *Atmospheric Chemistry and Physics*, *7*(17), 4489-4501.

Thomas, G. E., and K. Stamnes (2002), *Radiative transfer in the atmosphere and ocean*, Cambridge University Press.

Tikhonov, A. N., and V. Y. Arsenin (1979), Methods for solving ill-posed problems, edited, Nauka, Moscow.

Twomey, S. (1977), Atmospheric aerosols, *OSTI ID: 6747246*.

Uthe, E. E. (1982), Particle size evaluations using multiwavelength extinction measurements, *Applied Optics*, *21*(3), 454-459.

Valenzuela, A., F. J. Olmo, H. Lyamani, M. Antón, A. Quirantes, and L. Alados-Arboledas (2012a), Classification of aerosol radiative properties during African desert dust intrusions over southeastern Spain by sector origins and cluster analysis, *Journal of Geophysical Research: Atmospheres (1984–2012)*, *117*(D6).

Valenzuela, A., F. J. Olmo, H. Lyamani, M. Antón, A. Quirantes, and L. Alados-Arboledas (2012b), Aerosol radiative forcing during African desert dust events (2005–2010) over Southeastern Spain, *Atmospheric Chemistry and Physics*, *12*(21), 10331-10351.

Veselovskii, I., A. Kolgotin, V. Griaznov, D. Müller, U. Wandinger, and D. N. Whiteman (2002), Inversion with regularization for the retrieval of tropospheric aerosol parameters from multiwavelength lidar sounding, *Applied Optics*, *41*(18), 3685-3699.

Veselovskii, I., D. N. Whiteman, A. Kolgotin, E. Andrews, and M. Korenskii (2009), Demonstration of aerosol property profiling by multiwavelength lidar under varying relative humidity conditions, *Journal of Atmospheric and Oceanic Technology*, *26*(8), 1543-1557.

Veselovskii, I., O. Dubovik, A. Kolgotin, T. Lapyonok, P. Di Girolamo, D. Summa, D. N. Whiteman, M. Mishchenko, and D. Tanré (2010), Application of randomly oriented spheroids for retrieval of dust particle parameters from multiwavelength lidar measurements, *Journal of Geophysical Research: Atmospheres (1984–2012)*, *115*(D21).

Veselovskii, I., D. N. Whiteman, M. Korenskiy, A. Kolgotin, O. Dubovik, and D. Perez-Ramirez (2013), Retrieval of height-temporal distributions of particle parameters from multiwavelength lidar measurements using linear estimation technique and comparison results with AERONET, *Atmospheric Measurement Techniques Discussions*, *6*(2), 3059-3088.

Volten, H., O. Munoz, E. Rol, J. F. De Haan, W. Vassen, J. W. Hovenier, K. Muinonen, and T. Nousiainen (2001), Scattering matrices of mineral aerosol particles at 441.6 nm and 632.8 nm, *Journal of geophysical research*, *106*(D15), 17375-17317.

Wagner, J., (2012), Microphysical aerosol properties retrieved from combined lidar and sun photometer measurements, *Master Thesis presented at the Faculty of Physics and Earth Sciencesof Leipzig University*.

Wagner, J., A. Ansmann, U. Wandinger, P. Seifert, A. Schwarz, M. Tesche, A. Chaikovsky, and O. Dubovik (2013a), Evaluation of the Lidar/Radiometer Inversion Code (LIRIC) to determine microphysical properties of volcanic and desert dust, *Atmos. Meas. Tech.*, *6*(7), 1707-1724.

Wandinger, U., A. Ansmann, J. Reichardt, and T. Deshler (1995), Determination of stratospheric aerosol microphysical properties from independent extinction and backscattering measurements with a Raman lidar, *Applied Optics*, *34*(36), 8315-8329.

Wandinger, U., A. Hiebsch, I. Mattis, G. Pappalardo, L. Mona, and F. Madonna (2010), Aerosols and clouds: Longterm database from spaceborne lidar measurements*Rep. ESTEC Contract 21487/08/NL/HE, FinalReport.*, Leipzig, Germany and Potenza, Italy.

Washington, R., M. Todd, N. J. Middleton, and A. S. Goudie (2003), Dust-storm source areas determined by the total ozone monitoring spectrometer and surface observations, *Annals of the Association of American Geographers*, *93*(2), 297-313.

Weitkamp, C. (2005), *Lidar: range-resolved optical remote sensing of the atmosphere*, Springer.

Welton, E. J., J. R. Campbell, T. A. Berkoff, S. Valencia, J. D. Spinhirne, B. Holben, and S.C. Tsay (2005), 5.2 The Nasa Micro-Pulse Lidar Network (MPLNET): co-location of lidars with AERONET sunphotometers and related Earth Science applications.

Wulfmeyer, V., and G. Feingold (2000), On the relationship between relative humidity and particle backscattering coefficient in the marine boundary layer determined with differential absorption lidar, *Journal of Geophysical Research: Atmospheres (1984–2012)*, *105*(D4), 4729-4741.

Yu, H., Y. J. Kaufman, M. Chin, G. Feingold, L. A. Remer, T. L. Anderson, Y. Balkanski, N. Bellouin, O. Boucher, and S. Christopher (2006), A review of measurement-based assessments of the aerosol direct radiative effect and forcing, *Atmospheric Chemistry and Physics*, *6*(3), 613-666.

Zender, C. S., H. Bian, and D. Newman (2003), Mineral Dust Entrainment and Deposition (DEAD) model: Description and 1990s dust climatology, *Journal of geophysical research*, *108*(D14), 4416.

Zieger, P., R. Fierz-Schmidhauser, E. Weingartner, and U. Baltensperger (2013), Effects of relative humidity on aerosol light scattering: results from different European sites, *Atmospheric Chemistry and Physics Discussions*, *13*(4), 8939-8984.

Zieger, P., R. Fierz-Schmidhauser, M. Gysel, J. Ström, S. Henne, K. E. Yttri, U. Baltensperger, and E. Weingartner (2010), Effects of relative humidity on aerosol light scattering in the Arctic, *Atmospheric Chemistry and Physics*, *10*(8), 3875-3890.

→List of publications

ARTICLES

A1. AUTHORS (in order of authorship): A.Valenzuela, F.J. Olmo, H. Lyamani, **M.J. Granados Muñoz**, M. Antón, J.L. Guerrero-Rascado, A. Quirantes, C. Toledano, A. Smirnov and L. Alados-Arboledas
TITLE: Aerosol transport over the western Mediterranean basin: evidence of anthropogenic contribution to desert dust plumes over the Alborán island
JOURNAL/BOOK TITLE: Journal of Geophysical Research
DATE OF PUBLICATION: submitted
MOST OUTSTANDING ASPECTS: Category: Geosciences, Multidisciplinary; Impact Factor: 3.174; Ranking in category: 23/170 (in 2012)

A2. AUTHORS (in order of authorship): J.L. Corredor-Ardoy, J.A. Bravo-Aranda, **M.J Granados-Muñoz**, J.L. Guerrero-Rascado, J. Fernández-Gálvez, A. Cazorla and L. Alados-Arboledas
TITLE: Active and passive remote sensing for monitoring the planetary boundary layer height
JOURNAL/BOOK TITLE: Óptica Pura y Aplicada KEY: A
DATE OF PUBLICATION: under review
MOST OUTSTANDING ASPECTS: Category: Atomic & Molecular Physics & Optics; Impact Factor SJR: 0.162; Ranking in category: 67/77 (in 2012)

A3. AUTHORS (in order of authorship): N. Rogelj, J. L. Guerrero-Rascado, F. Navas-Guzmán, J. A. Bravo-Aranda, **M. J. Granados-Muñoz** and L. Alados-Arboledas
TITLE: Experimental determination of UV- and VIS- lidar overlap function
JOURNAL/BOOK TITLE: Óptica Pura y Aplicada
DATE OF PUBLICATION: under review
MOST OUTSTANDING ASPECTS: Category: Atomic & Molecular Physics & Optics; Impact Factor SJR: 0.162; Ranking in category: 67/77 (in 2012)

A4. AUTHORS (in order of authorship): P. Ortiz-Amezcua, J. L. Guerrero-Rascado, **M. J. Granados-Muñoz**, J. A. Bravo-Aranda and L. Alados-Arboledas
TITLE: Characterization of atmospheric aerosols for a long range transport of biomass burning particles from Canadian forest fires over the southern Iberian Peninsula in July 2013
JOURNAL/BOOK TITLE: Óptica Pura y Aplicada
DATE OF PUBLICATION: under review
MOST OUTSTANDING ASPECTS: Category: Atomic & Molecular Physics & Optics; Impact Factor SJR: 0.162; Ranking in category: 67/77 (in 2012)

A5. AUTHORS (in order of authorship): **M. J. Granados- Muñoz**, J. L. Guerrero-Rascado, J. A. Bravo-Aranda, F. Navas-Guzmán, A. Valenzuela, H. Lyamani, A. Chaikovsky, U. Wandinger, A. Ansmann, O. Dubovik and L. Alados-Arboledas
TITLE: Retrieving aerosol microphysical properties by LIdar-Radiometer Inversion Code (LIRIC) for different aerosol types
JOURNAL/BOOK TITLE: Journal of Geophysical Research
DATE OF PUBLICATION: accepted
MOST OUTSTANDING ASPECTS: Category: Geosciences, Multidisciplinary; Impact Factor: 3.174; Ranking in category: 23/170 (in 2012)

A6. AUTHORS (in order of authorship): F. Navas-Guzmán, J. Fernández-Gálvez, **M. J. Granados-Muñoz**, J. L. Guerrero-Rascado, J. A. Bravo-Aranda and L. Alados-Arboledas
TITLE: Tropospheric water vapour and relative humidity profiles from lidar and microwave radiometry
JOURNAL/BOOK TITLE: Atmospheric Measurement Techniques Discussions, 6, 10481–10510
DATE OF PUBLICATION: 2013
MOST OUTSTANDING ASPECTS: Category: Meteorology & Atmospheric Sciences; Impact Factor: 3.205; Ranking in category: 15/74 (in 2012)

A7. AUTHORS (in order of authorship): F. Navas-Guzmán, J. A. Bravo-Aranda, J.L. Guerrero-Rascado, **M.J. Granados-Muñoz** and L. Alados-Arboledas
TITLE: Statistical analysis of aerosol optical properties retrieved by Raman lidar over Southeastern Spain
JOURNAL/BOOK TITLE: Tellus B, 65, 21234, http://dx.doi.org/10.3402/tellusb.v65i0.21234
DATE OF PUBLICATION: 2013
MOST OUTSTANDING ASPECTS: Category: Meteorology and Atmospheric Sciences; Impact Factor: 3.197; Ranking in category: 16/74 (in 2012)

A8. AUTHORS (in order of authorship): J. Fernández-Gálvez, J. L. Guerrero-Rascado, F. Molero, H. Lyamani, M. A. Revuelta, F. Navas-Guzmán, M. Sastre, J. A. Bravo-Aranda, A. J. Fernández, **M. J. Granados-Muñoz**, F. J. Gómez-Moreno, F. J. Olmo, M. Pujadas, and L. Alados-Arboledas
TITLE: Aerosol size distribution from inversion of solar radiances and measured at ground-level during SPALI10 campaign
JOURNAL/BOOK TITLE: Atmospheric Research, 127, 130-140, doi:10.1016/j.atmosres.2012.03.015
DATE OF PUBLICATION: 2013
MOST OUTSTANDING ASPECTS: Category: Meteorology and Atmospheric Sciences; Impact Factor: 2.200; Ranking in category: 29/74 (en 2012)

A9. AUTHORS (in order of authorship): J. A. Bravo-Aranda, F. Navas-Guzmán, J. L. Guerrero-Rascado, D. Pérez-Ramírez, **M. J. Granados-Muñoz**, and L. Alados-Arboledas
TITLE: Analysis of lidar depolarization calibration procedure and application to the atmospheric aerosol characterization
JOURNAL/BOOK TITLE: International Journal of Remote Sensing, Vol. 34, Nos. 9-10, 3543-3560 http://dx.doi.org/10.1080/01431161.2012.716546

DATE OF PUBLICATION: 2013
MOST OUTSTANDING ASPECTS: Category: Remote Sensing; Impact Factor: 1.138; Ranking in category: 16/27 (in 2012)
Category: Imaging Science and Photographic Technology; Impact Factor: 1.138; Ranking in category: 10/23 (in 2012)

A10. AUTHORS (in order of authorship): F. Navas-Guzmán, D. Müller, J. A. Bravo-Aranda, J. L. Guerrero-Rascado, **M. J. Granados-Muñoz**, D. Pérez-Ramírez, F. Olmo-Reyes and L. Alados-Arboledas
TITLE: Eruption of the Eyjafjallajökull Volcano in spring 2010: Multiwavelength Raman Lidar Measurements of Sulphate Particles in the Lower Troposphere
JOURNAL/BOOK TITLE: Journal of Geophysical Research, 118, doi:10.1002/jgrd.50116
DATE OF PUBLICATION: 2013
MOST OUTSTANDING ASPECTS: Category: Geosciences, Multidisciplinary; Impact Factor: 3.174; Ranking in category: 23/170 (in 2012)

A11. AUTHORS (in order of authorship)): F. Molero, M. Sicard, F. Navas-Guzmán, J. Preißler, A. Amodeo, V. Freudenthaler, A. J. Fernández, S. Tomás, **M. J. Granados-Muñoz**, F. Wagner, A. Giunta, I. Mattis, M. Pujadas, A. Comerón, L. Alados-Arboledas, J. L. Guerrero-Rascado, G. D'Amico, D. Lange, J. A. Bravo, D. Kumar, G. Pappalardo, J. Giner, C. Muñoz, and F. Rocadenbosch
TITLE: Study on aerosol properties over Madrid (Spain) by multiple instrumentation during SPALI10 lidar campaign
JOURNAL/BOOK TITLE: Óptica Pura y Aplicada, 45(4), 405-413
DATE OF PUBLICATION: 2012
MOST OUTSTANDING ASPECTS: Category: Atomic & Molecular Physics & Optics; Impact Factor SJR: 0.162; Ranking in category: 67/77 (in 2012)

A12. AUTHORS (in order of authorship): F. Molero, A. j. Fernández, M. Pujadas, M. Sicard, S. Tomás, A. Comerón, D. Lange, D. Kumar, J. Giner, C. Muñoz, F. Rocadenbosch, F. Navas-Guzmán, **M. J. Granados-Muñoz**, L. Alados-Arboledas, J. A. Bravo-Aranda, J. Preißler, F. Wagner, and J. L. Guerrero-Rascado
TITLE: Study on aerosol properties over Madrid (Spain) by multiple instrumentation during SPALI10 lidar campaign
JOURNAL/BOOK TITLE: Revista Boliviana de Física, 20, 16-18
DATE OF PUBLICATION: 2011

BOOK CHAPTERS

CB1. AUTHORS (in order of authorship): L. Alados-Arboledas, I. Foyo, H. Lyamani, J. L. Guerrero-Rascado, F. Navas-Guzmán, J. A. Bravo-Aranda, A. Cazorla, J. Fernández-Gálvez, G. Titos, **M. J. Granados-Muñoz**, I. Alados, A. Valenzuela and F. J. Olmo
TITLE: Monitoring daily evolution of the atmospheric aerosol in an urban environment by means of remote sensing and in-situ methodologies
REF. REVISTA/LIBRO: Juan Antonio Morente Chiquero: in memoriam, 75-80, ISBN: 978-84-338-5540-4, Editorial Universidad de Granada, D.L.: GR./1.152-2013
DATE OF PUBLICATION: 2013

CB2. AUTHORS (in order of authorship): J. Fernández-Gálvez, J. L. Guerrero-Rascado, F. Molero, H. Lyamani, M. A. Revuelta, F. Navas-Guzmán, M. Sastre, J. A. Bravo-Aranda, A. J. Fernández, **M. J. Granados-Muñoz**, F. J. Gómez-Moreno, F. J. Olmo, M. Pujadas, and L. Alados-Arboledas
TITLE: Aerosol size distribution from inversion of solar radiances and measured at ground-level during SPALI10 campaign
JOURNAL/BOOK TITLE: Proceedings of the Global Conference on Global Warming 2011 edited by A. M. Silva, A. H. Reis, D. Bortoli, J. Carneiro, M. J. Costa, M. Bezzeghoud and R. Salgado, 199-208, ISBN: 978-989-95091-3-9
DATE OF PUBLICATION: 2011

CB3. AUTHORS (in order of authorship): **M. J. Granados-Muñoz**, D. Pozo-Vázquez, L. Alados-Arboledas, and J. L. Guerrero-Rascado
TITLE: Study of aerosol optical properties over the Iberian Peninsula based on 9-year MODIS dataset
JOURNAL/BOOK TITLE: Proceedings of the Global Conference on Global Warming 2011 edited by A. M. Silva, A. H. Reis, D. Bortoli, J. Carneiro, M. J. Costa, M. Bezzeghoud and R. Salgado, 815-824, ISBN: 978-989-95091-3-9
DATE OF PUBLICATION: 2011

CB4. AUTHORS (in order of authorship): F. Molero, A. Amodeo, M. Sicard, J. Preißler, F. Navas-Guzmán, V. Freudenthaler, A. J. Fernández, A. Giunta, S. Tomás, F. Wagner, **M.J. Granados-Muñoz**, I. Mattis, M. Pujadas, G. D'Amico, A. Comeron, J. L. Guerrero-Rascado, L. Alados-Arboledas, D. Lange, J.A. Bravo, D. Kumar, G. Pappalardo, J. Giner, C. Muñoz, and F. Rocadenbosch
TITLE: Study on aerosol properties over Madrid (Spain) by multiple instrumentation during EARLINET lidar intercomparison campaign: SPALI10
JOURNAL/BOOK TITLE: Book of extended abstracts of “Quinta Reunión Española de Ciencia y Tecnología de Aerosoles”, B4-1 – B4-6, ISBN: 978-84-7834-662-2
DATE OF PUBLICATION: 2011

CB5. AUTHORS (in order of authorship): **M. J. Granados-Muñoz**, F. Navas-Guzmán, J. A. Bravo-Aranda, J. L. Guerrero-Rascado, J. Fernández-Gálvez, and L. Alados-Arboledas
TITLE: Multi-instrumental detection of the mixing layer height over Granada

JOURNAL/BOOK TITLE: Book of extended abstracts of “Quinta Reunión Española de Ciencia y Tecnología de Aerosoles”, B5-1 – B5-6, ISBN: 978-84-7834-662-2
DATE OF PUBLICATION: 2011

CB6. AUTHORS (in order of authorship): F. Navas-Guzmán, J. A. Bravo-Aranda, J. L. Guerrero-Rascado, **M. J. Granados-Muñoz**, and L. Alados-Arboledas
TITLE: Study of ground-based vertical profiles of tropospheric aerosol in coincidence with CALIPSO overpasses at Granada, Spain
JOURNAL/BOOK TITLE: Book of extended abstracts of “Quinta Reunión Española de Ciencia y Tecnología de Aerosoles”, D3-1 – D3-6, ISBN: 978-84-7834-662-2
DATE OF PUBLICATION: 2011

CB7. AUTHORS (in order of authorship): J. A. Bravo Aranda, F. J. Navas-Guzmán, **M. J. Granados-Muñoz**, J. L. Guerrero-Rascado, and L. Alados-Arboledas
TITLE: Atmospheric aerosol characterization by dual lidar depolarization
JOURNAL/BOOK TITLE: Book of extended abstracts of “Quinta Reunión Española de Ciencia y Tecnología de Aerosoles”, H2-1 – H2-5, ISBN: 978-84-7834-662-2
DATE OF PUBLICATION: 2011

CB8. AUTHORS (in order of authorship): F. Navas-Guzmán, J. A. Bravo-Aranda, **M. J. Granados-Muñoz**, J. L. Guerrero-Rascado, and L. Alados-Arboledas
TITLE: Study on the planetary boundary layer top with Raman lidar
JOURNAL/BOOK TITLE: Book of extended abstracts of “Cuarta Reunión Española de Ciencia y Tecnología de Aerosoles”, C9-1-6, ISBN: 978-84-693-4839-0
DATE OF PUBLICATION: 2010

CB9. AUTHORS (in order of authorship): **M. J. Granados-Muñoz**, D. Pozo-Vazquez, L. Alados Arboledas
TITLE: Variability of aerosol optical properties derived from MODIS over the Iberian Peninsula.
JOURNAL/BOOK TITLE: Book of extended abstracts of “Cuarta Reunión Española de Ciencia y Tecnología de Aerosoles”, ISBN: 978-84-693-4839-0
DATE OF PUBLICATION: 2010

CB10. AUTHORS (in order of authorship): D. Pérez-Ramírez, J. Fernández-Gálvez, H. Lyamani, **M. J. Granados-Muñoz**,F.J.Olmo-Reyes, L. Alados-Arboledas
TITLE: Water vapour from sun and star photometer as compared with passive microwave radiometry: modified K-CICLO for correcting sun photometer calibration.
JOURNAL/BOOK TITLE: Book of extended abstracts of “Quinta Reunión Española de Ciencia y Tecnología de Aerosoles”, ISBN: 978-84-693-4839-0
DATE OF PUBLICATION: 2011
MOST OUTSTANDING ASPECTS (**):

PRESENTATIONS IN CONGRESSES

C1. AUTHORS: P. Ortiz-Amezcua, J. L. Guerrero-Rascado, **M. J. Granados-Muñoz**, J. A. Bravo-Aranda and L. Alados-Arboledas
TITLE: Characterization of atmospheric aerosols for a long range transport of biomass burning particles from Canadian forest fires over the southern Iberian Peninsula in July 2013
TYPE OF PRESENTATION: Poster
CONGRESS: VII Workshop on Lidar Measurements in Latin America
PUBLICATION: Handbook of VII Workshop on Lidar Measurements in Latin America, 39
MEETING PLACE: Pucón, Chile
YEAR: 2013

C2. AUTHORS: J.A. Bravo-Aranda, **M.J. Granados-Muñoz**, F. Navas-Guzmán, J.L. Guerrero-Rascado, J. Fernández-Gálvez, F. J. Olmo and L. Alados-Arboledas
TITLE: Improvements on planetary boundary layer height estimates using lidar depolarization during CHARMEX 2012 campaign
TYPE OF PRESENTATION: Poster
CONGRESS: VII Workshop on Lidar Measurements in Latin America
PUBLICATION: Handbook of VII Workshop on Lidar Measurements in Latin America, 38
MEETING PLACE: Pucón, Chile
YEAR: 2013

C3. AUTHORS: J.L. Corredor-Ardoy, J.A. Bravo-Aranda, **M.J. Granados-Muñoz**, J.L. Guerrero-Rascado, J. Fernández-Gálvez, A. Cazorla and L. Alados-Arboledas
TITLE: Active and passive remote sensing for monitoring the planetary boundary layer height
TYPE OF PRESENTATION: Poster
CONGRESS: VII Workshop on Lidar Measurements in Latin America
PUBLICATION: Handbook of VII Workshop on Lidar Measurements in Latin America, 19
MEETING PLACE: Pucón, Chile
YEAR: 2013

C4. AUTHORS: N. Rogelj, J. L. Guerrero-Rascado, F. Navas-Guzmán, J. A. Bravo-Aranda, **M. J. Granados-Muñoz** and L. Alados-Arboledas
TITLE: Experimental determination of UV- and VIS- lidar overlap function
TYPE OF PRESENTATION: Poster
CONGRESS: VII Workshop on Lidar Measurements in Latin America
PUBLICATION: Handbook of VII Workshop on Lidar Measurements in Latin America, 13
MEETING PLACE: Pucón, Chile
YEAR: 2013

C5. AUTHORS: B. Torres, L. Blarel, P. Goloub, M. Mallet, T. Bourrianne, D. Tanré, F. Dulac, O. Dubovik, C. Verwaerde, T. Podvin, A. Mortier, Y. Derimian, J. L. Guerrero-Rascado, L. Alados-Arboledas, **M. J. Granados-Muñoz**, J. A. Bravo-Aranda, G. Roberts, G, Monboisse, P. Chazette, J. Totems, M. L. Boytard and D. Fuertes
TITLE: First Retrievals Of Aerosol Properties Derived From Measurements Of The New Airborne Sunphotometer PLASMA During The Campaigns SHADOWS And ChArMEx

TYPE OF PRESENTATION: Poster
CONGRESS: 7th International Workshop on Sand/Duststorms and Associated Dustfall
PUBLICATION: Handbook of 7th International Workshop on Sand/Duststorms and Associated Dustfall
C6. MEETING PLACE: Frascati, Rome, Italy
YEAR: 2013

C7. AUTHORS: A.Valenzuela, F.J. Olmo, H. Lyamani, **M.J. Granados-Muñoz**, J. L. Guerrero-Rascado, A. Quirantes and L. Alados-Arboledas
TITLE: Air masses types over the remote Alborán Island
TYPE OF PRESENTATION: Poster
CONGRESS: European Aerosol Conference 2013
PUBLICATION: Handbook of EAC013, A193
MEETING PLACE: Prague, Czech Republic
YEAR: 2013

C8. AUTHORS: A. Quirantes, F.J. Olmo, A. Valenzuela, **M.J. Granados-Muñoz**, J.L. Guerrero-Rascado, J.A. Bravo-Aranda, F. Navas-Guzmán and L. Alados-Arboledas
TITLE: Bimodal particle concentration profile retrieved from ground-based Lidar and CIMEL measurements
TYPE OF PRESENTATION: Poster
CONGRESS: European Aerosol Conference 2013
PUBLICATION: Handbook of EAC013, A141
MEETING PLACE: Prague, Czech Republic
YEAR: 2013

C9. AUTHORS: **M. J. Granados-Muñoz**, F. Navas-Guzmán, J.A. Bravo-Aranda, J.L. Guerrero-Rascado, A. Valenzuela, J. Fernández-Gálvez and L. Alados-Arboledas
TITLE: Analysis of aerosol hygroscopic properties by combination of lidar, microwave radiometer and radiosounding data
TYPE OF PRESENTATION: Poster
CONGRESS: European Aerosol Conference 2013
PUBLICATION: Handbook of EAC013, A078
MEETING PLACE: Prague, Czech Republic
YEAR: 2013

C10. AUTHORS: J.A. Bravo-Aranda, **M. J. Granados-Muñoz**, F. Navas-Guzmán, J.L. Guerrero-Rascado, F. J. Olmo and L. Alados-Arboledas
TITLE: Lidar depolarization evolution during the CHARMEX intensive field campaign
TYPE OF PRESENTATION: Poster
CONGRESS: European Aerosol Conference 2013
PUBLICATION: Handbook of EAC013, A033
MEETING PLACE: Prague, Czech Republic
YEAR: 2013

C11. AUTHORS: A. Valenzuela, F. Olmo, H. Lyamani, **M.J. Granados-Muñoz**, J.L. Guerrero-Rascado, A. Quirantes and L. Alados-Arboledas
TITLE: Characterization of the aerosol properties over the remote Alborán island
TYPE OF PRESENTATION: Poster
CONGRESS: 1st Iberian Meeting on Aerosol Science and Technology (RICTA2013)
PUBLICATION: Abstract Book of RICTA2013, 72
MEETING PLACE: Évora, Portugal
YEAR: 2013

C12. AUTHORS: J. A. Bravo-Aranda, **M.J. Granados-Muñoz**, F. Navas-Guzmán, J.L. Guerrero-Rascado, F. Olmo and L. Alados-Arboledas
TITLE: 72h-temporal evolution of lidar depolarization during CHARMEX
TYPE OF PRESENTATION: Poster
CONGRESS: 1st Iberian Meeting on Aerosol Science and Technology (RICTA2013)
PUBLICATION: Abstract Book of RICTA2013, 61
MEETING PLACE: Évora, Portugal
YEAR: 2013
Awarded as the best poster in RICTA2013

C13. AUTHORS:, F. Navas-Guzmán, J. A. Bravo-Aranda, J.L. Guerrero-Rascado, A. Valenzuela, J. Fernández-Gálvez and L. Alados-Arboledas
TITLE: Application of active and passive remote sensing to study aerosol hygroscopic growth
TYPE OF PRESENTATION: Oral
CONGRESS: 1st Iberian Meeting on Aerosol Science and Technology (RICTA2013)
PUBLICATION: Abstract Book of RICTA2013, 39
MEETING PLACE: Évora, Portugal
YEAR: 2013

C14. AUTHORS: A. Quirantes, F. J. Olmo, A. Valenzuela, **M. J. Granados-Muñoz**, J. L. Guerrero-Rascado, J. A. Bravo-Aranda, F. Navas-Guzmán, and L. Alados-Arboledas
TITLE: Layer-by-layer concentration retrieval of an airborne two-component particle mixture from ground-based lidar and Cimel measurements
TYPE OF PRESENTATION: Oral
CONGRESS: 1st Iberian Meeting on Aerosol Science and Technology (RICTA2013)
PUBLICATION: Abstract Book of RICTA2013, 36
MEETING PLACE: Évora, Portugal
YEAR: 2013

C15. AUTHORS: Anatoli Chaikovsky, Oleg Dubovik, Philipper Goloub, Didier Tanré, Gelsomina Pappalardo, Ulla Wandinger, Ludmila Chaikovskaya, Sergei Denisov, Yan Grudo, Anton Lopatsin, Yana Karol, Tatyana Lapyonok, Michail Korol, Fiodor Osipenko, Dzmitry Savitski, Alexander Slesar, Arnoud Apituley, Lucas Alados Arboledas, Ioannis Binietoglou, Adolfo Comeron, Panayotis Kokkalis, **María José Granados Muñoz**, Alexandros Papayannis, Maria Rita Perrone, Aleksander Pietruczuk, Ferdinando De Tomasi, Janet Wagner, Xuan Wang.
TITLE: Algorithm and software for the retrieval of vertical aerosol properties using combined lidar/radiometer data: dissemination in EARLINET network

TYPE OF PRESENTATION: Poster
CONGRESS: 26 th International Laser Radar Conference (26 th ILRC)
PUBLICATION: Book of abstracts
MEETING PLACE: Porto Heli, Greece
YEAR: 2012

C16. AUTHORS: J. Preißler, J. A. Bravo-Aranda, F. Wagner, **M. J. Granados-Muñoz**, F. Navas-Guzmán, J. L. Guerrero-Rascado, H. Lyamani and L. Alados-Arboledas
TITLE: Optical Properties of Free Tropospheric Aerosol from Multi-wavelength Raman Lidars over the Southern Iberian Peninsula
TYPE OF PRESENTATION: Poster
CONGRESS: 9th International Symposium on Tropospheric Profiling (ISTP2012)
PUBLICATION: Proceedings of 9th International Symposium on Tropospheric Profiling (ISTP2012), P09
MEETING PLACE: L'Aquila, Italy
YEAR: 2012

C17. AUTHORS: J. Preißler, J.A. Bravo-Aranda, F. Wagner, **M.J. Granados-Muñoz**, F. Navas-Guzmán, J.L.Guerrero-Rascado, H. Lyamani, and L. Alados-Arboledas
TITLE: Combined observations with multi-wavelength Raman lidars and sun photometers on the southern Iberian Peninsula
TYPE OF PRESENTATION: Poster
CONGRESS: Europena Aerosol Conference 2012
PUBLICATION: European Aerosol Conference 2012 Handbook, A-WG01S1P18
MEETING PLACE: Granada, Spain
YEAR: 2012

C18. AUTHORS: **M.J. Granados-Muñoz**, J.A. Bravo-Aranda, F. Navas-Guzmán, J.L. Guerrero-Rascado, H. Lyamani, A.Chaikovsky, J. Wagner, U. Wandinger, F.J.Olmo and L. Alados-Arboledas
TITLE: Retrieval of aerosol microphysical properties profiles by combination of Lidar and sun photometer measurements. Application to mineral dust and volcanic aerosols.
TYPE OF PRESENTATION: Oral
CONGRESS: Europena Aerosol Conference 2012
PUBLICATION: European Aerosol Conference 2012 Handbook, SS01S1O05
MEETING PLACE: Granada, Spain
YEAR: 2012

C19. AUTHORS: J.A.Bravo-Aranda, F. Navas-Guzmán, J. Andrey, M.J. Granados-Muñoz, J.L. Guerrero-Rascado, M.Gil, H. Lyamani, A. Valenzuela, G. Titos, J. Fernández-Gálvez, F.J. Olmo and L. Alados-Arboledas
TITLE: CLIMARENO-GRA 2011 campaign: Aerosol optical properties characterization from ground-based instrumentation
TYPE OF PRESENTATION: Oral
CONGRESS: Europena Aerosol Conference 2012
PUBLICATION: European Aerosol Conference 2012 Handbook, WG01S3O02
MEETING PLACE: Granada, Spain

YEAR: 2012

C20. AUTHORS: J.L. Guerrero-Rascado, J.A. Bravo-Aranda, F. Wagner, C. Córdoba-Jabonero, F. Molero, D. Lange, **M. J. Granados-Muñoz**, J. Preißler, D. Toledo, A.J. Fernández, M. Sicard, F. Navas-Guzmán, Y. Hernández, A.M. Silva, M. Pujadas, A. Comerón, S. Pereira, F. Rocadenbosch and L. Alados-Arboledas
TITLE: Detection of the stratospheric volcanic aerosol plume from the Nabro eruption in summer 2011 in the framework of SPALINET
TYPE OF PRESENTATION: Poster
CONGRESS: Europena Aerosol Conference 2012
PUBLICATION: European Aerosol Conference 2012 Handbook, B-WG01S2P08
MEETING PLACE: Granada, Spain
YEAR: 2012

C21. AUTHORS: J.L. Guerrero-Rascado, **M. J. Granados-Muñoz**, F. Navas-Guzmán, J. A. Bravo-Aranda, F. J. Olmo, J. Andrey, M. Gil, A. Chaikovsky, U. Wandinger and L. Alados-Arboledas
TITLE: CLIMARENO-GRA 2011 campaign: retrieval of vertically-resolved aerosol microphysical properties by lidar at daytime
TYPE OF PRESENTATION: Poster
CONGRESO: Europena Aerosol Conference 2012
PUBLICATION: European Aerosol Conference 2012 Handbook, B-WG01S2P09
MEETING PLACE: Granada, Spain
YEAR: 2012

C22. AUTHORS: F. Navas-Guzmán, J. Bravo-Aranda, **M.J. Granados-Muñoz**, J.L. Guerrero-Rascado, J. Fernández-Gálvez, A.J. Fernández and L. Alados-Arboledas
TITLE: Towards a remote sensing tool for aerosol hygroscopicity studies combining lidar and passive microwave radiometry
TYPE OF PRESENTATION: Poster
CONGRESS: Europena Aerosol Conference 2012
PUBLICATION: European Aerosol Conference 2012 Handbook, B-WG01S2P24
MEETING PLACE: Granada, Spain
YEAR: 2012

C23. AUTHORS: F. Dulac and an international ChArMEx Team: T. Agacayak, L. Alados Arboledas, A. Alastuey, Z. Ameur, G. Ancellet, E.-M. Assamoi, J.-L. Attié, S. Becagli, M. Beekmann, G. Bergametti, M. Bocquet, F. Bordier, T. Bourrianne, J.A. Bravo-Aranda, P. Chazette, I. Chiapello, P. Coddeville, A. Colomb, A. Comerón, G. D'Amico, B. D'Anna, K. Desboeufs, J. Descloitres, M. Diouri, C. Di Biagio, G. Di Sarra, P. Durand, L. El Amraoui, R. Ellul, L. Fleury, P. Formenti, E. Freney, E. Gerasopoulos, P. Goloub, **M.J. Granados-Muñoz**, J.L. Guerrero Rascado, C. Guieu, D. Hadjimitsis, E. Hamonou, H.C. Hansson, M. Iarlori, S. Ioannou, E. Jaumouillé, M. Jeannot, W. Junkermann, C. Keleshis, S. Kleanthous, P. Kokkalis, D. Lambert, B. Laurent, J.-F. Léon, C. Liousse, M. Lopez Bartolome, R. Losno, M. Mallet, R.-E. Mamouri, N. Marchand, L. Menut, N Mihalopoulos, R. Morales Baquero, P. Nabat, F. Navas-Guzmán, D. Nicolae, J. Nicolas, G. Notton, C. Paoli, A. Papayannis, G. Pappalardo, S. Pandis, J. Pelon, J. Pey, V. Pont, X. Querol, F. Ravetta, J.-B. Renard, V. Rizi,

G. Roberts, K. Sartelet, J.-L. Savelli, J. Sciare, K. Sellegri, D.M. Sferlazzo, M. Sicard, A. Smyth, F. Solmon, D. Tanré, A. Tovar Sánchez, N. Verdier, F. Wagner, Y. Wang, J. Wenger, N. Yassaa, et al
TITLE: An update on ChArMEx (the Chemistry-Aerosol Mediterranean Experiment) activities and plans for aerosol studies in the Mediterranean region
TYPE OF PRESENTATION: Poster
CONGRESS: Europena Aerosol Conference 2012
PUBLICATION: European Aerosol Conference 2012 Handbook, B-LP01S1P24
MEETING PLACE: Granada, Spain
YEAR: 2012

C24. AUTHORS: .J. Ferrnández-Gálvez, **M.J. Granados-Muñoz**, F.J. Olmo and L. Alados-Arboledas TITLE: Mixing height from passive remote sensing at high temporal resolution
TYPE OF PRESENTATION: Poster

CONGRESS: European Aerosol Conference (EAC 2012)

PUBLICATION: Book of abstracts
MEETING PLACE: Granada, Spain.
YEAR: 2012

C25. AUTHORS: F. Navas-Guzmán, L. Osterloh, C. Böckmann, **M.J. Granados-Muñoz**, and L. Alados Arboledas.
TITLE: Optical and Microphysical properties from Raman lidar and depolarization data.
TYPE OF PRESENTATION: Poster
CONGRESS: European Aerosol Conference (EAC 2012)
PUBLICATION: Book of abstracts
MEETING PLACE: Granada, Spain.
YEAR: 2012

C26. AUTHORS: F. Molero, A. J. Fernández, M. Pujadas, M. Sicard, S. Tomás, A. Comerón, D. Lange, D. Kumar, J. Giner, C. Muñoz, F. Rocadenbosch, F. Navas-Guzmán, **M.J. Granados-Muñoz**, L. Alados-Arboledas, J.A. Bravo-Aranda, J. Preißler, F. Wagner, and J.L. Guerrero-Rascado
TITLE: Study on aerosol properties over Madrid (Spain) by multiple instrumentation during SPALI10 lidar campaign
TYPE OF PRESENTATION: Poster
CONGRESS: VI Workshop on lidar measurements in latin America
PUBLICATION: Proceedings of the VI Workshop on lidar measurements in latin America, 1-3
MEETING PLACE: La Paz, Bolivia
YEAR: 2011

C27. AUTHORS: F. Molero, F. J. Andrey, J. Preißler, F. Navas-Guzmán, A. Giunta, M. Sicard, A. J. Fernández, M. C. Parrondo, F. Wagner, **M.J. Granados-Muñoz**, G. D'Amico, S. Tomás, M. Pujadas, C. Córdoba-Jabonero, J. L. Guerrero-Rascado, L. Alados-Arboledas, A. Amodeo, A. Comerón, J.A. Bravo, G. Pappalardo, D. Kumar, I. Mattis, V. Freudenthaler, D. Lange, J. Giner, C. Muñoz, and F. Rocadenbosch

TITLE: Aerosol size distribution study by airborne and ground-level in-situ measurements and remote sensing during EARLINET lidar intercomparison campaign: SPALI10
TYPE OF PRESENTATION: Poster
CONGRESS: European Aerosol Conference 2011
PUBLICATION: European Aerosol Conference Handbook, 8P144
MEETING PLACE: Manchester, England
YEAR: 2011

C28. AUTHORS: L. Alados-Arboledas, F. Navas-Guzmán, J.A. Bravo-Aranda, H. Lyamani, D. Pérez-Ramírez, J. L. Guerrero-Rascado, I. Foyo, I. Alados, **M. J. Granados-Muñoz**, G. Titos, J. Fernández-Gálvez, A. Valenzuela, M. Antón, A. Quirantes, X. Querol, A. Alastuey, and F. J. Olmo
TITLE: Multi-instrumental characterization of the mixing of Eyjafjallajökull volcanic aerosols and boundary layer aerosols at Granada, Spain
TYPE OF PRESENTATION: Oral
CONGRESS: European Aerosol Conference 2011
PUBLICATION: European Aerosol Conference Handbook, 10B4
MEETING PLACE: Manchester, England
YEAR: 2011

C29. AUTHORS: F. Navas-Guzmán, J. A. Bravo-Aranda, J. L. Guerrero-Rascado, **M. J. Granados-Muñoz**, and L. Alados-Arboledas
TITLE: Three years of Raman lidar measurements in correspondence with CALIPSO overpasses over the South of the Iberian Peninsula
TYPE OF PRESENTATION: Poster
CONGRESS: European Aerosol Conference 2011
PUBLICATION: European Aerosol Conference Handbook, 8P145
MEETING PLACE: Manchester, England
YEAR: 2011

C30. AUTHORS: J. Andrey, Y. Bennouna, **M.J. Granados-Muñoz**, J.L. Gomez-amo, B. Piguet, A. Minikin, J. Jensen, R. Krejci
TITLE: Intercomparison of aerosols airborne size distribution measurements
TYPE OF PRESENTATION: Poster
CONGRESS: European Aerosol Conference 2011 (EAC 2011)
PUBLICATION: Book of abstracts
MEETING PLACE: Manchester, United Kingdom.
YEAR: 2011

C31. AUTHORS: D. Pérez-Ramírez, J. Fernández-Gálvez, H. Lyamani, M.J. Granados-Muñoz, F.J. Olmo-Reyes, L. Alados-Arboledas
TITLE: Water vapour from sun and star photometer as compared with passive microwave radiometry: modified K-CICLO for correcting sun photometer calibration.
TYPE OF PRESENTATION: Poster
CONGRESS: V Reunión Española de Ciencia y Tecnología de Aerosoles
PUBLICATION: Book of abstracts
MEETING PLACE: Madrid, Spain.
YEAR: 2011

C32. AUTHORS: Y. Bennouna, J.Andrey, **M. J. Granados-Muñoz**, J. L. Gomez-amo, B. Piguet, A. Minikin, J. Jensen, R. Krejci
TITLE: An aircraft intercomparison for the measurement of aerosol size distribution during the ICARE 2010 intercalibration flights.
TYPE OF PRESENTATION: Poster
CONGRESS: V Reunión Española de Ciencia y Tecnología de Aerosoles
PUBLICATION: Book of abstracts
MEETING PLACE: Madrid, Spain.
YEAR: 2011

C33. AUTHORS: D. Pozo-vázquez, S. Wilbert, C. A. Gueymard, L. Alados-ArboledasF.J. Santos-Alamillos, **M. J. Granados-Muñoz**
TITLE: Interannual variability of long time series of DNI and GHI at PSA, Spain.
TYPE OF PRESENTATION: Poster
CONGRESS: SolarPACES
PUBLICATION: Book of abstracts
MEETING PLACE: Granada, Spain.
YEAR: 2011

C34. AUTHORS: J. Fernández-Gálvez, J. L. Guerrero-Rascado, F. Molero, H. Lyamani, M. A. Revuelta, F. Navas-Guzmán, M. Sastre, J. A. Bravo-Aranda, A. J. Fernández, **M. J. Granados-Muñoz**, F. J. Gómez-Moreno, F. J. Olmo, M. Pujadas, and L. Alados-Arboledas
TITLE: Aerosol size distribution from inversion of solar radiances and measured at ground-level during SPALI10 campaign
TYPE OF PRESENTATION: Poster
CONGRESS: Global Conference on Global Warming 2011
PUBLICATION: Abstract Booklet, 33
MEETING PLACE: Lisbon, Portugal
YEAR: 2011

C35. AUTHORS: **M. J. Granados-Muñoz**, D. Pozo-Vázquez, L. Alados-Arboledas, and J. L. Guerrero-Rascado
TITLE: Study of aerosol optical properties over the Iberian Peninsula based on 9-year MODIS dataset
TYPE OF PRESENTATION: Oral
CONGRESS: Global Conference on Global Warming 2011
PUBLICATION: Abstract Booklet, 78
MEETING PLACE: Lisbon, Portugal
YEAR: 2011

C36. AUTHORS: F. Molero, A. Amodeo, M. Sicard, J. Preißler, F. Navas-Guzmán, V. Freudenthaler, A. J. Fernández, A. Giunta, S. Tomás, F. Wagner, **M.J. Granados-Muñoz**, I. Mattis, M. Pujadas, G. D'Amico, A. Comeron, J. L. Guerrero-Rascado, L. Alados-Arboledas, D. Lange, J.A. Bravo, D. Kumar, G. Pappalardo, J. Giner, C. Muñoz, and F. Rocadenbosch

TITLE: Study on aerosol properties over Madrid (Spain) by multiple instrumentation during EARLINET lidar intercomparison campaign: SPALI10
TYPE OF PRESENTATION: Poster
CONGRESS: Quinta Reunión Española de Ciencia y Tecnología de Aerosoles (2011)
PUBLICATION: Book of abstracts, B4
MEETING PLACE: Madrid, Spain
YEAR: 2011

C37. AUTHORS: **M. J. Granados-Muñoz**, F. Navas-Guzmán, J. A. Bravo-Aranda, J. L. Guerrero-Rascado, J. Fernández-Gálvez, and L. Alados-Arboledas
TITLE: Multi-instrumental detection of the mixing layer height over Granada
TYPE OF PRESENTATION: Poster
CONGRESS: Quinta Reunión Española de Ciencia y Tecnología de Aerosoles (2011)
PUBLICATION: Book of abstracts, B5
MEETING PLACE: Madrid, Spain
YEAR: 2011

C38. AUTHORS: F. Navas-Guzmán, J. A. Bravo-Aranda, J. L. Guerrero-Rascado, **M. J. Granados-Muñoz**, and L. Alados-Arboledas
TITLE: Study of ground-based vertical profiles of tropospheric aerosol in coincidence with CALIPSO overpasses at Granada, Spain
TYPE OF PRESENTATION: Poster
CONGRESS: Quinta Reunión Española de Ciencia y Tecnología de Aerosoles (2011)
PUBLICATION: Book of abstracts, D3
MEETING PLACE: Madrid, Spain
YEAR: 2011

C39. AUTHORS: J. A. Bravo Aranda, F. J. Navas-Guzmán, **M. J. Granados-Muñoz**, J. L. Guerrero-Rascado, and L. Alados-Arboledas
TITLE: Atmospheric aerosol characterization by dual lidar depolarization
TYPE OF PRESENTATION: Poster
CONGRESS: Quinta Reunión Española de Ciencia y Tecnología de Aerosoles (2011)
PUBLICATION: Book of abstracts, H2
MEETING PLACE: Madrid, Spain
YEAR: 2011

C40. AUTHORS: F. Navas-Guzmán, J. A. Bravo-Aranda, **M. J. Granados-Muñoz**, J. L. Guerrero-Rascado, and L. Alados-Arboledas
TITLE: Study on the planetary boundary layer top with Raman lidar
TYPE OF PRESENTATION: Poster
CONGRESS: Cuarta Reunión Española de Ciencia y Tecnología de Aerosoles (2010)
PUBLICATION: Book of abstracts, C9
MEETING PLACE: Granada, Spain
YEAR: 2010

C41. AUTHORS: Bravo-Aranda, Juan Antonio; Navas-Guzman, Francisco Jesus; **Granados-Muñoz,** María José; Alados-Arboledas, Lucas
TITLE: Atmospheric Aerosol Characterization by lidar depolarization profiles.
TYPE OF PRESENTATION: Poster
CONGRESS: 3RD International Symposium on Recent Advances in Quantitative Remote Sensing.
PUBLICATION:
MEETING PLACE: Torrent, Spain.
YEAR: 2010

C42. AUTHORS: **Granados-Muñoz**, María José; Alados-Arboledas, Lucas
TITLE: Analyses of MODIS aerosol productos over the Iberian Peninsula
TYPE OF PRESENTATION: Poster
CONGRESS: European Aerosol Conference (EAC 2009)
PUBLICATION: Book of abstracts
MEETING PLACE: Karlsruhe, Germany
YEAR: 2009

C43. AUTHORS: **Granados-Muñoz**, María José; Alados-Arboledas, Lucas
TITLE: Analyses of MODIS aerosol productos over the Iberian Peninsula
TYPE OF PRESENTATION: Poster
CONGRESS: III Reunión Española de Ciencia y Tecnología de Aerosoles (RECTA)
PUBLICATION: Book of abstracts
MEETING PLACE: Bilbao, Spain.
YEAR: 2009
